学位論文

Study of Exoplanet Migration Mechanisms with the Direct Imaging Method

（太陽系外惑星の惑星軌道移動に関する直接撮像法を用いた研究）

平成２５年１２月博士（理学）
申請

東京大学大学院理学系研究科

天文学専攻

髙橋　安大

Study of Exoplanet Migration Mechanisms with the Direct Imaging Method

Yasuhiro Takahashi

Abstract

Since the discovery of the first extrasolar planet (exoplanet) in 1995, about one thousand have subsequently been identified. Most exoplanets have been detected using the radial velocity (RV) or the transit method. The RV method allows the minimum mass and the eccentricity of a planet to be determined, whereas the transit method can yield the radius of a planet but not its mass. For a transiting planet, the true mass can be evaluated by a combination of the two methods. An RV anomaly, known as the Rossiter-McLaughlin effect, arises when a planet transits a star and partially occults its photosphere. Investigating the shape of the RV anomaly allows the direction of the planet across the photosphere to be determined, in addition to the parameter λ, which is the projected angle between the stellar spin axis and the planetary orbital axis. Indirect observational methods have identified a large number of Jovian-mass planets orbiting with periods of a few days (hot Jupiters), planets with highly eccentric orbits (eccentric planets), and planets with orbital planes that are inclined to the stellar equatorial planes (tilted planets; $|\lambda| > 0$ deg). Recently, significant advances have been made in direct imaging of faint objects with very small angular separations from a bright star, and this has enabled detection of planets in orbits with large semi-major axes of several tens of AU (wide-orbit planets).

Long before the discovery of exoplanets, planet formation theories were constructed in an attempt to explain the origin of the Solar system. Planet formation is currently believed to occur in a protoplanetary disk, which rotates around a star in a circular orbit and in the same direction as the stellar spin (so-called prograde) due to its viscosity. Planet formation scenarios are mainly divided into two categories: gravitational instability and core accretion. In the gravitational instability model, planets are directly produced in local regions of a gravitationally unstable protoplanetary disk. This theory can account for the formation of giant gaseous planets in very wide orbits. According to the core accretion model, dust particles in a protoplanetary disk collide to produce planetesimals, which then accrete to become protoplanets. Rocky planets are thought to be the survivors of such protoplanets, or the result of giant impacts. Depending on how much gas is accumulated during the planet formation period, either a gaseous planet or an icy planet will be produced. Planetary systems including the Solar system are currently believed to have been formed mainly by core accretion, except for planets that have been directly imaged in very wide orbits, which may be the result of gravitational instability.

However, these formation models cannot explain the existence of eccentric or tilted planets. This is because planets formed in a circularly rotating prograde protoplanetary disk should also have circular prograde orbits. In order to explain eccentric or tilted planets, in addition to planets extremely close to their parent stars, planetary migration mechanisms have been invoked. In these models, planets are not formed *in situ* at their present locations but migrate there from their birthplaces. Two principal models have been proposed to account for eccentric or tilted planets. The first is planet-planet scattering, which predicts that if more than two giant planets exist in a system, gravitational interactions and orbital intersections will result in one being ejected or driven into the central star. The remaining planets will have a wide distribution of orbital eccentricities and inclinations. The second model is based on the Kozai mechanism, by which orbital oscillations are induced due to secular perturbations caused by an

outer object such as a stellar companion. These oscillations can explain the existence of planets with highly eccentric orbits or oblique orbital axes. At present, however, there is insufficient observational evidence to determine which if any of these models is most effective.

In this thesis, we describe the results of high-contrast observations aimed at detecting companion objects around planetary systems that may give rise to planetary migration. We focus on the binary rate for stars hosting eccentric or tilted planets. In systems containing a single planet, it is likely that planet-planet scattering can be ignored, so that the Kozai mechanism is the only feasible means of producing eccentric or tilted planets. In such a case, a correlation should exist between the number of systems with eccentric or tilted planets and the binary rate. If such a correlation is not found, then the Kozai mechanism can be considered to be ineffective and unknown scattering counterparts may instead exist. We employed the HiCIAO high-contrast imaging instrument and the AO188 adaptive optics system on the Subaru telescope to conduct direct imaging observations at near-infrared wavelengths of planetary systems hosting eccentric ($e \geq 0.7$) planets or tilted ($|\lambda| > 0$ deg) planets. The image contrast was sufficient to detect faint objects around target stars with masses typical of red dwarfs. This is the first high-contrast direct imaging study of planet migration mechanisms and is expected to form an important basis for future discussions, even though the sample sizes are limited. For systems with eccentric planets, candidate companions were observed in 2 out of 8 cases. The common proper motion test confirmed the existence of a physical companion in these cases, and one was identified as a background star. Including a known binary system, the final binary rate was found to be 3 out of 8. For systems with tilted planets, the binary rate was found to be 4-12 out of 15 based on direct observations. Due to their small proper motion, only a few of these systems could be subjected to the common proper motion test, so that the final binary rate was unclear. All of the identified candidate companions are expected to be capable of inducing Kozai effects for hypothetical planets beyond the snow line in each system.

Although the binary rates for both types of planetary system are statistically identical to that for Solar-type stars in the Solar neighborhood ($\sim 46\%$), the rate for stars with tilted planets except for the least case is significantly higher than the general rate for planet - hosting stars ($\sim 12\%$). In addition, the accuracy of the rate for stars with eccentric planets is limited due to the small sample size. Our high binary rates possibly indicate that tilted planets (and perhaps also eccentric planets) may have been formed by the Kozai mechanism. Our results likely suggest that the influence of Kozai mechanism is not statistically negligible. However, Morton and Johnson (2011a) pointed out that the λ distribution for all of their samples could be explained in terms of planet-planet scattering and an aligned model, which conflicts with the high binary rate obtained for stars with tilted planets in the present study. The inconsistency between the high binary rate and the λ distribution will be a subject for future experimental and theoretical studies. A larger number of targets is necessary to verify the robustness of our results. In addition, in order to precisely estimate the influence of the Kozai mechanism, it will be necessary to determine the fraction of planets with circular ($e \sim 0$) or aligned ($|\lambda| \sim 0$ deg) orbits.

Acknowledgments

Contents

List of Figures

List of Tables

Chapter 1

Introduction

Does "the second Earth" really exist? And, does intelligent life exist there? These questions, which have been universally wondered from ancient times, are no longer philosophical problems, but being already dealt with science, commencing with astronomy. The questions are exceedingly important for considering what is the *raison d'être* of the human beings, and will occupy a crucial position in the future civilized society as before. In order to answer the questions, researches of extrasolar planets (or exoplanets) have been advanced in present astronomical field.

What at first sprang up were theoretical mechanisms for planet formation, which at that time tried to explain the formation scenario of the only known planetary system at that time, the Solar system. Based on the theories, we learned the knowledge that planets are formed in a disk consisting of gas and dust and rotating around a central star, so-called a protoplanetary disk. Dust accretes to be planetesimals, the planetesimals sequentially coalesce to grow up into protoplanets and some especially massive ones of which gather surrounding gas. In this wise, astronomers appeared to succeed in building up the Solar system only by employing one planet formation scenario to elucidate the diversity of planets, such as rocky planets and gaseous planets.

However, 51 Pegasi b, the first discovered exoplanet around a Solar-type star (Mayor and Queloz, 1995), completely metamorphosed circumstances. Namely, the planet with about a half of the Jupiter mass orbits a star in a period of only 4.2 days. The discovery surprised us a lot, who assumed the Solar system as the most typical one in the universe. The fact that the Solar system as the standard in the universe is a likely irregular one may suggest that Earth, on which the only planet the human beings live, has an extremely rare existence. A large number of hot Jupiters (hot planets with a Jovian-sized mass orbiting irradiating stars in periods of a few days) and eccentric planets (planets in highly eccentric orbits) discovered subsequently seem to support that.

Moreover, the direct imaging method, delineated a new aspect of exoplanets. Direct imaging is an exceedingly difficult technique, but is suited to detect very faint objects close to central stars. Due to the technical requirements, it is appropriate to detect objects separated by a few tens AU from a star, and in the first directly imaged planetary system of the Solar system scale, HR 8799 (Marois et al., 2008), plural planets are present in such positions. Considering planet formation timescales, such planets could be hardly explained.

However, there are also fortunate facts in contrast. The results obtained with the *Kepler* satellite, launched in 2009, are also altering the situations. It has discovered a lot of Earth-sized and slightly larger planets. Indeed, most of them are too hot or too cold because they are located too close to or too separated from central stars, but a planet in an adequate orbit, like Kepler-22b (Borucki et al., 2012), possibly has liquid water on its surface. A planet in such an adequate region for holding liquid water on

a planetary surface, called as a habitable zone, is named as a habitable planet, and several examples have been already known. In addition, Kepler-16b is a circumbinary planet, which is revolving around a close binary (Doyle et al., 2011). Hence, the *Kepler* satellite played a profound role toward finding the second Earth.

As shown above, the fact that planetary systems have variety, from similar ones to completely different ones from the Solar system, have come to light, and consequently a unified planet formation theory to explain such various states has been required. Then, how efficient is each planet formation model? According to the models, how many planets are predicted to be inhabited by extraterrestrial life? We here repeatedly assert that these questions are no longer philosophical but astronomical as mentioned in the beginning of the sentences. To answer the fundamental questions, in this thesis, we aim to investigate from observational aspects how actually effective the planet formation mechanisms are. Because, practically, the formation mechanisms themselves have been well studied, let us focus on the planet migration theories, which connect theoretically predicted planetary systems and various actually-observed planetary systems.

In order to explain the motivation of this thesis, we introduce the planet migration models as the background knowledge in this chapter. All the migration models anticipate that planets are not built via *in situ* formation but move from their birthplaces after formation. However, it is unclear how effective they are to explain observed planets due to their variety. Of main migration models, type II migration model is hard to be examined with direct imaging. Thus, we focus on two of migration models, planet-planet scattering and Kozai migration. Because the latter requires stellar companions (strictly speaking, outer planets can occur Kozai mechanism), the companions' presence is an important factor for discussing Kozai mechanism. To approach the models, we here employ the direct imaging method with a high-contrast direct imaging instrument to detect additional objects around planetary systems. Targets are chosen from known planetary systems with eccentric or tilted planets, which have been formed via Kozai mechanism or planet-planet scattering. Our strategy, i.e. a large high-contrast direct imaging survey of planetary systems hosting eccentric or tilted planets, is the first attempt, in contrast to that many previous surveys have already been made toward general nearby stars. Therefore the number of targets so far conducted is still limited. However, our results will be a profound foundation for investigating planet migration models.

1.1   Thesis Outline

We here explain the outline of this thesis. In this chapter, we start with showing theoretical background to illuminate our motivations of this thesis. After reviewing planet formation models, we introduce planetary migration models, which propose that planetary orbits change from their birthplaces. Finally we state our motivations.

Next, in Chapter 2, we illustrate indirect methods to discover planets, which have clued us in considering the migration mechanisms. As shown later, we observed and discussed planetary systems hosting eccentric planets and tilted planets. We expound how to find these planets in this chapter.

Moreover, in Chapter 3, we explain manners and reduction techniques for the direct imaging method, which are employed in our study as a main technique. We also mention what we can learn from objects discovered with the method. We introduce atmospheric models we adopt to the objects to estimate masses, and a common proper motion test to examine whether the objects are physically associated with their central stars.

In Chapter 4, we show observations and results of a retrograde planetary system HAT-P-7 as an example of our methodology. We actually report the presence of a companion around HAT-P-7 and,

therefore, exemplify the possibility of the object being a source of the sequential Kozai migration.

In Chapter 5, we report a direct imaging survey of discovering companions around eccentric or tilted planetary systems and its results. Our survey of 23 targets is a large-scaled observation in direct imaging surveys oriented to finding stellar objects around planetary systems. We measure the coordinates and magnitudes of companion candidates and estimate their masses with the atmospheric models if companions detected. In addition, though in a simple manner, we discriminate actual candidate sources of Kozai mechanism from unrelated stars. In this study, we assume the possible sources as real companions.

In Chapter 6, we present comparison of our binary rate derived from our results with that in literatures. Using this result, we propose new observational constraints on the planet migration scenarios. We also investigate whether the binary rate and stellar effective temperature have a significant correlation or not.

Finally we summarize our study and state conclusion in Chapter 7. Future works are also mentioned in this chapter.

1.2 Review of a Planet Formation and Migration Scenarios

1.2.1 Planet Formation Scenarios

The earliest studies of exoplanets started with explaining how to form the Solar system. As the planets are on the almost identical orbital plane in the Solar system, planets are believed to form in protoplanetary disks. However, astronomers did not know how to make protostars and protoplanetary disks from interstellar nebulae before 1980s. As observations had revealed that stars are born in molecular clouds, it had been clarified that gas and dust in the molecular clouds collapse together due to their gravity to be a so-called first core with angular momentum. A first core again partially collapse into a spinning protostar and the residuals to be a rotating protoplanetary disk holding gas and dust in it. Only recent studies can approach calculations integrating planet formation with protoplanetary disk formation (e.g. Inutsuka et al. 2010).

Let us get back to the history. Since Miyama et al. (1984) showed that various protoplanetary disks can be formed depending on initial conditions of molecular clouds, initial protoplanetary disks have been set to build planets in the disks without any robust theoretical backing. Especially, a planet formation model given by members of Kyoto University (e.g. Mizuno et al. 1978; Hayashi 1981; Hayashi et al. 1985) succeeded in explaining the Solar system, and therefore the model is often called as the Kyoto model. Their model and another model proposed by Safronov (1969) postulated protoplanetary disks with minimum mass expected from the current Solar system of $0.01 - 0.04 M_{\odot}$, where $M_{\odot}$ is the Solar mass, while Cameron (1962) presumed a massive disk of $\sim 1 M_{\odot}$. Resulting from the initial disk mass difference, current planet formation models can be separated in mainly two; one is called as the gravitational instability, the other is the core accretion model. The following sentences introduce the two prominent planet formation models.

The gravitational instability (hereafter GI) model (e.g. Durisen et al. 2007), which began with Cameron (1962), is a model that planets are directly built through collapse caused by gravitational instability of a disk with an initial disk mass of $\sim 1 M_{\odot}$. The instability can be investigated with Toomre's Q,

$$Q = \frac{c_{\mathrm{s}} \Omega_K}{\pi G \Sigma} \tag{1.1}$$

(Toomre, 1964), where c_{s}, Ω_K, G, and Σ are the sound speed, the Keplarian angular velocity, the gravitational constant, and the surface density, respectively, and $Q \lesssim 1$ indicates an instability. Here, Ω_K is

defined as

$$\Omega_K = \sqrt{\frac{GM_*}{a^3}}, \tag{1.2}$$

where M_* and a are the stellar mass and the semi-major axis, respectively. An unstable disk is estimated to be divided into some fragments with critical wave numbers of $k_{\text{crit}} = \Omega_K^2/\pi G\Sigma$ in both a radial and an azimuthal direction. They have masses of

$$m = \pi\Sigma \left(\frac{2\pi}{k_{\text{crit}}}\right)^2 = (2\pi)^2 \left(\frac{\Sigma\pi a^2}{M_*}\right)^3 M_* \tag{1.3}$$

and result in planets in theory. Figure 1.1 shows evolution of a disk based on GI. The figure indicates that the disk got to be suddenly unstable 100 years after the calculation and made massive planets in wide orbits in $\sim 10^3$ years. Recently some planets have been directly imaged and they appear to be massive and wide-orbit ones. It is likely that such planets are built via GI because they are difficult to be explained by the core accretion model, which is illustrated later on. Constraints on a mass of β Pictoris b derived from radial velocity also support the GI hypothesis for the planet (Lagrange et al., 2012). Furthermore, as the figure clearly shows, the GI model is capable of concurrently making many planets in a disk.

Because those gaseous clumps are too hot to shrink, cooling is necessary to reduce pressure. With a timescale, t_{cool}, planets can be formed when the following condition is satisfied:

$$t_{\text{cool}}\Omega_K < \beta, \tag{1.4}$$

where β is the parameter indicating the cooling limit. The value of this parameter is supposed to be about 3-18 (Meru and Bate, 2011). Based on the cooling limit, planets are estimated to be formed in outer regions than $a \gtrsim 30$ AU from central stars. Planetary masses understandably depend on a disk mass, and, for example, a relatively massive disk with a mass of $M_{\text{disk}} = 0.1 - 0.2M_\odot$ is able to produce planets with their masses of about 1-5M_J (M_J is the Jovian mass). In addition, moderately eccentric planets ($e \lesssim 0.35$) can be also built via GI (Boss, 2011).

One problem of the GI model is the higher metallicity of planets. According to GI, planets naturally have the same metallicity as a central star because they are directly formed from a disk. However, even Jupiter, whose metallicity is the lowest in the Solar system, has more metal than the Sun. Another problem is rocky planet formation. Namely, rocky planets cannot be explained by GI since planets are directly built from gas in a disk. Hence, it is unlikely for planets to be elucidated by GI alone, except for planets discovered with direct imaging observations.

On the other hand, the core accretion (CA) model (e.g. Pollack et al. 1996; Wuchterl et al. 2000) is a model using a light disk with a mass of $\sim 0.01M_\odot$ which cannot cause gravitational instability. Figure 1.2 illustrates a conceptual image of CA. In the disk, dust accretes and grows up into planetesimals, and they sequentially collide and coalesce with each other to be protoplanets. As for the dust accretion, two influential models have been proposed; the gravitational instability hypothesis (e.g. Goldreich and Ward 1973) and the direct accretion hypothesis (e.g. Weidenschilling 1977). The former is a theory that passably grown dust precipitates onto the midplane of a disk and induces gravitational instability to collide and accrete. The latter predicts direct combination of planetesimals without passing through the instability. Each model has difficulties of wreathing up caused by the Kelvin-Helmholtz instability and of falling down onto central stars. Moreover it has been pointed out that both models have a problem that collision of dust and planetesimals leads to destruction to prevent progress in growing up. However, recent researches have proposed solutions to these problems by considering transformation of dust structures (Kataoka et al., 2013a,b).
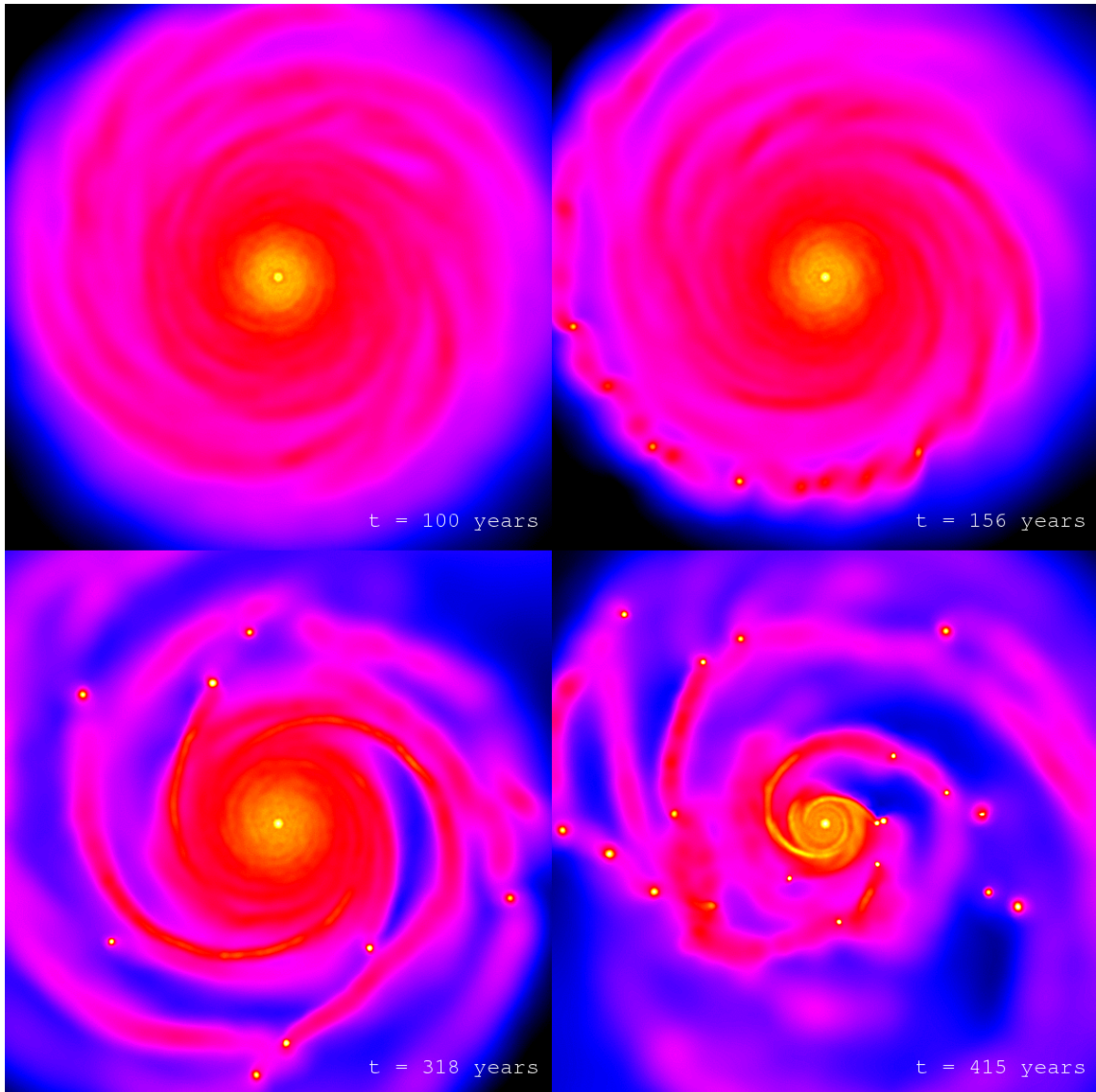
Figure 1.1: A sequence of snapshots of planet formation through gravitational instability (Lufkin et al., 2004). The central star with a mass of $1M_\odot$ hosts an unstable protoplanetary disk with a mass of $0.2M_\odot$ and the minimum Q of $Q_{min} = 0.8$. After 150 yr from the simulation start, a spiral arm collapse into some segments to be giant planets. Comparing with the widths of each panel of 55 AU and considering the time, the simulation clearly suggests that GI is capable of forming planets in widely separated orbits with taking only $\lesssim 10^3$ yr.

Here, we introduce the snow line, which is a border between outer regions containing water ice and inner regions where water evaporates. In outer regions the surface density of dust can be three to four times as high as that of inner regions due to the ice. The high density is responsible for large planetesimals and consequently large protoplanets, so the line is an important concept in the CA model. A position of the snow line is estimated as

$$r_{\text{snowline}} \simeq 2.7 \left(\frac{L_*}{L_\odot}\right)^{1/2} \text{AU} \simeq 2.7 \left(\frac{M_*}{M_\odot}\right)^2 \text{AU}, \tag{1.5}$$

where $L_\odot$ and L_* are the luminosities of the Sun and a star, respectively (Ida and Lin, 2004). The proportional relation of $L_* \propto M_*^4$ is available in $0.5M_\odot \lesssim M_* \lesssim 3M_\odot$. Although a destruction problem in a collision phase has been pointed out (Ida et al., 2008), planetesimals grow up through run-away growth (e.g. Kokubo and Ida 2002) into protoplanets. Then gas rapidly flows in a protoplanet (i.e. a core) to be a gaseous planet if a core's mass exceeds $\gtrsim 10M_\oplus$ (Ikoma et al., 2000), where $M_\oplus$ is the Earth mass. Mercury, Mars, Uranus and Neptune in the Solar system are thought to be survivals of protoplanets (in addition to some gas capture). Venus and Earth are deliverables of giant impact events, and Jupiter and Saturn had captured gas to be gaseous planets. Gaseous planets shrink following the Kelvin-Helmholtz contraction on a timescale of

$$\tau_{\text{KH}} \sim 10^b \left(\frac{M_{\text{core}}}{M_\oplus}\right)^{-c} \left(\frac{\kappa}{1 \text{ g cm}^{-2}}\right) \text{yr}. \tag{1.6}$$

The parameters are calculated to be $b \simeq 8$, $c \simeq 2.5$ (Ikoma et al., 2000), but they possibly change into $\simeq 10$, $\simeq 3.5$ (Ida and Lin, 2004). Here, there is a serious problem that planets must be formed before disk dissipation, whose timescale was observationally estimated to be ~ 6 Myr (Haisch et al., 2001). According to Ida and Lin (2004), it takes $\sim 10^7$ years for a planet at a current Jupiter's position to obtain $10M_\oplus$, which is necessary to be a gas giant as explained above. It suggests that the timescale problem is not easy to be mitigated because the growing-up timescale is comparable to the timescale of disk dissipation.

On the other side, once gas falls onto a core, the gas contributes to increasing the core mass and decreasing τ_{KH}, resulting in a run-away growth. However, the core stops its growth due to exhaustion of the finite amount of gas. The planet then opens a gap in the disk in the planet's orbit. A critical mass of a planet with a gap incompletely opened is expressed as

$$M_{\text{gas}}^{\text{crit}} \sim \pi a^2 \Sigma_g \simeq 290 f_g \left(\frac{a}{1 \text{ AU}}\right)^2 M_\odot \tag{1.7}$$

(Ida and Lin, 2004), where a is the semi-major axis of the planet, f_g is the normalization constant of surface density. The parameter f_g is set to be $f_g = 0.7$ for the Hayashi model (Hayashi, 1981), and typically has values of 0.1-10. Hence, a planetary mass, m_p, cannot exceed the critical mass (i.e. $m_p \lesssim M_{\text{gas}}^{\text{crit}}$) based on the CA model. Besides, it is hard to build a planet in regions outer than ~ 30 AU due to the formation timescale problem. Because the CA model is capable of systematically explaining formation of all kinds of planets such as rocky, gaseous, and icy planets, the model is the mainstream in planet formation scenarios. Planetary orbits are circular as a result of interactions with a disk, corresponding to the Solar planets, as well.

In summary, planets are predicted to be formed as followed. The GI model creates wide-orbit ($\gtrsim 30$ AU) and massive ($\gtrsim M_J$) gaseous planet(s) in a circular or moderately eccentric orbit, while the CA model forms various planets in regions within $\lesssim 30$ AU, and especially Jovian planets are built beyond the snow line (~ 2.7 AU for Sun-like stars). Their planetary orbits are circular.
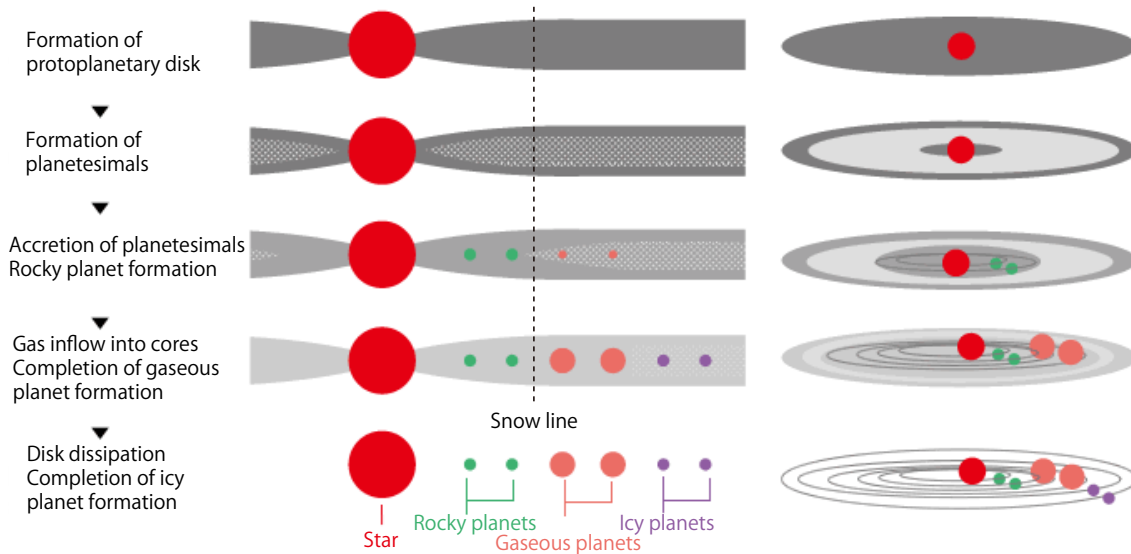
Figure 1.2: A schematic illustration of a concept of the core accretion model. At first, planetesimals form in a protoplanetary disk. Then they accrete to be protoplanets. Some protoplanets experience giant impacts to grow up into massive rocky planets. Massive protoplanets, i.e. cores of giant gaseous planets, capture gas around the protoplanets. Protoplanets in outer regions are too far to grow up into massive planets before a disk dissipates. Courtesy of Shigeru Ida and revised by us.

1.2.2 Migration Scenarios

However, the first discovered planet orbiting a Solar-type star, 51 Pegasi b, actually has an orbital period of only 4.2 days and a mass of $0.47M_J$ (the lower limit) (Mayor and Queloz, 1995). The planet is markedly different from the planets in the Solar system, and therefore, it is definitely difficult to explain the planet only with the conventional planet formation models. A massive ($\gtrsim M_J$) planet orbiting in a period of a few days is called as a hot Jupiter. In addition, planets in highly eccentric orbits, such as 70 Virginis b ($e = 0.40$; Marcy and Butler 1996) and 16 Cygni B b ($e = 0.68$; Cochran et al. 1997), have been reported. Those planets are called as eccentric planets. Furthermore, HAT-P-7 (Narita et al., 2009; Winn et al., 2009), the first-discovered retrograde planet (see §2.2), thrusted a problem of planet formation as well. This is because a protoplanetary disk circularly rotates in the same direction as its host star's spin due to its origin and viscosity, and consequently planets formed in the disk are also supposed to have a circular orbit with the same direction of the stellar spin. Thus eccentric planets and retrograde planets cannot be formed in typical disks, though some models that an interaction with a disk raises a planetary eccentricity have been proposed (Goldreich and Sari, 2003; Sari and Goldreich, 2004). To solve the questions some new models have been proposed which predict that a planet has migrated from its birthplace to a current position. The planet migration models are divided in mainly two. One is caused by interaction with a protoplanetary disk, while the other is induced by interaction with other objects after disk dissipation. In this section, we introduce the planet migration theories.

Type I/II Migration

As for migration models induced by interactions with a disk, principally two kinds of models, called as type I and type II migrations, have been proposed. At first we introduce the latter one, type II migration. Type II migration (e.g. Lin and Papaloizou 1985) can be explained with the gap induced by a giant planet, which is mentioned in the previous section. If a gaseous giant planet opens a gap in a disk, it is confined in the gap due to its reaction. Then a disk gradually carries its angular momentum outward due to the viscosity, leading to its accretion onto a central star. Also a planet sequentially falls inward with being confined in the gap. The process is named as type II migration, which makes giant planets fall inward. A timescale of the migration is described as

$$\tau_{\mathrm{mig,II}} = \left| \frac{a}{\dot{a}} \right| \simeq 0.6 \times 10^5 \left(\frac{\alpha}{10^{-3}} \right)^{-1} \left(\frac{a}{1 \text{ AU}} \right) \left(\frac{M_*}{M_\odot} \right) \tag{1.8}$$

for a typically modeled disk and a Jovian planet, where α is the parameter indicating a strength of viscosity. Because type II migration has a timescale proportional to a semi-major axis, a planet falls inward with increasing speed. A planet migrating inward eventually stops at an inner edge of the disk. The edge is determined by a corotation radius, r_{corot}, of ionized gas in the disk and a spinning period of a star with a magnetic field. The r_{corot} is expressed as

$$r_{\mathrm{corot}} = 0.04 \left(\frac{P}{3 \text{ days}} \right)^{2/3} \left(\frac{M_*}{M_\odot} \right)^{-1/3} \text{ AU}. \tag{1.9}$$

Since a planet formed beyond the snow line is estimated to migrate inward on a timescale of 10^5 to 10^6 yr, it may be delicate to judge whether a timescale of type II migration or of disk dissipation is shorter. As a planetary orbit gradually changes, a planet possibly gets to be in a resonance state with another planet, resulting in a stable orbit. Type II migration is available only for a massive planet which can open a gap in a disk, but ineffective for a light planet with a mass of $\lesssim 10 M_\oplus$. As a result, type II migration produces a close-in planet in a circular orbit whose orbital axis is aligned with a stellar spin axis due to the interaction with a disk.

A planet whose mass is too light to open a gap in a disk causes type I migration (Ward, 1986). A planet in a disk receives angular momentum from inner components, which rotate more rapidly, and conversely deliver to outer components, which rotates more slowly (so-called a Lindblad torque). A timescale of migration driven by a Lindblad torque in a locally isothermal disk is written as

$$\tau_{\mathrm{mig,I}} \simeq 1.6 \times 10^5 C_1^{-1} f_g^{-1} \left(\frac{M_{\mathrm{core}}}{M_\oplus} \right)^{-1} \frac{a}{1 \text{ AU}} \left(\frac{M_*}{M_\odot} \right)^{3/2} \text{ yr}, \tag{1.10}$$

where C_1 is the parameter denoting a delay of migration due to a non-linear effect. The timescale is sufficiently shorter than the planet formation timescale, and planets quickly descend inward after the formation as a result. However, it has been reported that a planet does not always migrate inward if a disk has a negative slope of entropy in radial direction (Baruteau and Masset, 2008; Paardekooper and Papaloizou, 2008). Hence, the situation surrounding type I migration is unpredictable.

Planet-Planet Scattering

Although hot Jupiters can be explained by type I/II migrations since the migrations transfer the planet in a protoplanetary disk with interacting with the disks, eccentric planets and retrograde planets are hard to form. Thus, we here explain other migration models after disk dissipation, beginning with an

introduction of planet-planet scattering. Planet-planet scattering (see Figure 1.3) is an event that orbits of giant planets are gravitationally affected by other planets to intersect, leading to planets with high eccentricities and with inclined orbital planets. In a two-planetary system, the instability requires that a difference of semi-major axes, Δa, is less than $2\sqrt{3}$ times long as the Hill radius (a typical radius of a sphere dominated by planetary gravity),

$$r_H = \left(\frac{m_{p,1} + m_{p,2}}{3M_*}\right)^{1/3} a_{1,2},$$ (1.11)

where $m_{p,i}$ is the i-th planetary mass and $a_{1,2}$ is defined as $a_{1,2} = (m_{p,1}a_1 + m_{p,2}a_2)/(m_{p,1} + m_{p,2})$. However, since it is unlikely that planets form with such close distances, systems with two giant planets are stable in general and it is difficult to explain the observed systems with the scampering (Ford et al., 2001).

In contrast, planetary systems with three giants can suddenly become unstable and change into elliptic orbits (Marzari and Weidenschilling, 2002). Figure 1.3 shows a concept of planet-planet scattering in a three-planetary system. A timescale of the instability is approximately described as

$$\tau_{\text{cross}} \sim 10^{2.5K - 4.5} \text{ yr},$$ (1.12)

where K is defined as $K = \Delta a/r_H$. The coefficients in the exponent are easily changeable (Chambers et al., 1996), but the strong dependence of K on Δa and M_* is robust. Based on N-body simulations (Nagasawa et al., 2008; Chatterjee et al., 2008), it is likely that one of three giant planets is ejected from the system or drops down to the central star in most of three-giant planetary systems, resulting in two remaining planets or rarely in only one. The products of the scattering are wide distributions of eccentricity for both planets in addition to semi-major axes distributed over wide ranges for inner planets and over restricted ranges of merely 0.5-1 times as large as initial semi-major axes. The scattering has been reported to incline orbital planes with a distribution of inclination over 0 to 180 deg; in other words, tilted planets (including retrograde planets) can be formed, where a tilted planet is defined as a planet with spin-orbit misalignment of $|\lambda| > 0$ deg (see §2.2 in detail). A timescale of instability is typically calculated to be $\sim 10^6$ yr. Furthermore, some studies have investigated the migrating planets in mean motion resonance (Raymond et al., 2008).

Hence, planet-planet scattering plausibly contribute to forming eccentric planets and tilted planets. As illustrated above, N-body simulations predict two planets in a system which has caused the scattering. However, it is frequent that only one planet has been discovered even in a system hosting an extremely eccentric planet or a tilted planet. The situation suggests that another mechanism occurs in such systems though it is possible to explain that an additional planet has not been discovered yet.

Kozai Mechanism

Next, we introduce another mechanism capable of raising planetary eccentricity. If an additional object (e.g. a planet and a stellar/substellar companion) exists in outer regions of a planetary system, it oscillates the planetary orbit around a longitude of pericenter ω of 90 or 270 deg with preserving the z-component of angular momentum, i.e.

$$\sqrt{GMa(1 - e^2)} \cos i = \text{const.},$$ (1.13)

where i denotes the mutual inclination between the planetary and the companion's orbit, because of a secular perturbation of the additional object (Kozai, 1962). The oscillation is named as Kozai oscillation, and a sequential migration theory caused by Kozai oscillation is called as Kozai mechanism (Holman et al., 1997). Figure 1.4 represents a concept of Kozai mechanism. The oscillation induces repetitious
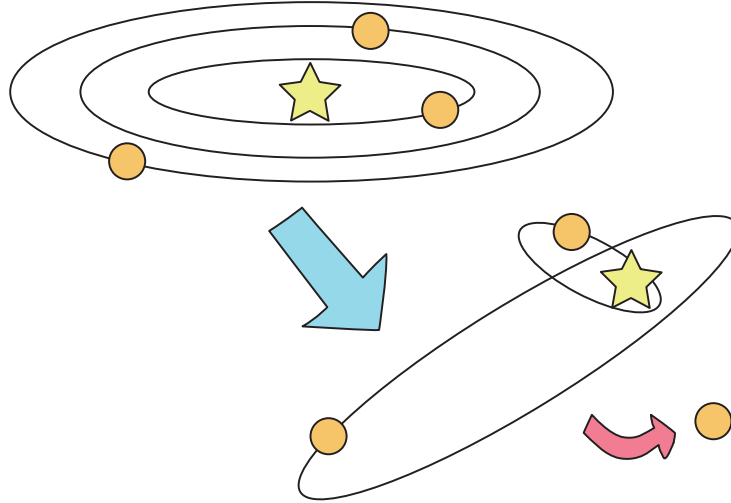
Figure 1.3: A conceptual image of planet-planet scattering. More than two giant planets in a planetary system easily cause a scattering due to their gravitational interaction, frequently resulting in two remaining planets with high eccentricities and high inclinations in addition to one ejected planet from the system.

transitions between a situation with high eccentricity and low inclination and another one with low eccentricity and high inclination. To cause Kozai mechanism, the mutual inclination i necessarily satisfies the equation:

$$i > i_{\mathrm{crit}} = \arccos\sqrt{\frac{3}{5}} = 39.2°.\tag{1.14}$$

For example, a planet bound to a star in a wide binary is possibly affected by the stellar companion as a source of Kozai mechanism if $i > i_{\mathrm{crit}}$ is satisfied. The influence of Kozai mechanism may not be negligible because especially nearly 50% of Solar-type stars in the Solar neighborhood were reported to constitute multiple systems (Raghavan et al., 2010). One of eccentric planets, HD 80606b, is a representative sample; HD 80606 indeed constitutes a binary system together with HD 80607, which was estimated to have caused Kozai mechanism to the planet b to make it eccentric (Wu and Murray, 2003). A Kozai timescale (or period) in a system consisting of a main star A and a stellar companion (or an outer planet) B is approximated as

$$P_{\mathrm{Kozai}} \sim \frac{M_{\mathrm{A}}}{M_{\mathrm{B}}}\frac{P_{\mathrm{B}}^2}{P_{p,0}}(1 - e_{\mathrm{B}}^2)^{3/2},\tag{1.15}$$

where M_{A} and M_{B} are the masses of the objects, P_{B} denotes B's orbital period, $P_{p,0}$ represents the initial period of the planet, and e_{B} indicates the B's eccentricity (Holman et al., 1997). As the equation explicitly shows, the timescale strongly depends on the companion's period. If the timescale is sufficiently shorter than the system's age, Kozai migration can occur. Moreover, "sequential" Kozai migration, which predicts that an outermost object gravitationally affect an outer planet in a planetary system and consequently the outer affects the inner one, has been proposed (Takeda et al., 2008; Kita et al., 2010).

We here note pericenter precession induced by relativistic effect, which perturbs Kozai oscillation.
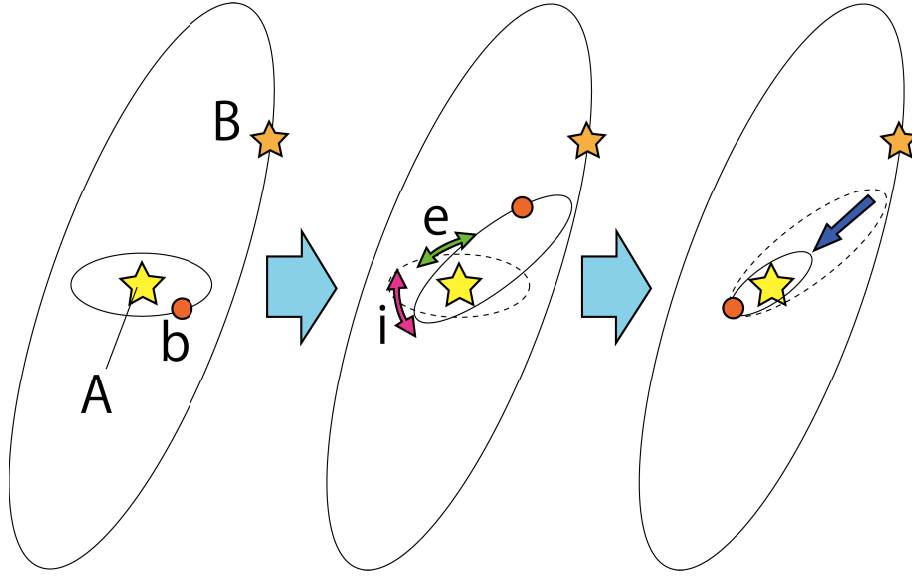
Figure 1.4: A conceptual image of Kozai mechanism. An outer companion (or an outer planet) B hosted by a planetary system affects a planet b orbiting a central star A via a secular perturbation. The planet's eccentricity and inclination oscillates and consequently its orbital energy decreases to be a close-in planet due to a tidal dissipation if a planet has an extremely small pericenter distance.

A timescale of the effect is estimated to be written as

$$P_{\mathrm{GR}} \sim \frac{2\pi c^2 (1 - e_{\mathrm{p},0}^2) a_{\mathrm{p},0}^{5/2}}{3(GM_{\mathrm{A}})^{3/2}}, \tag{1.16}$$

where $e_{\mathrm{p},0}$ and $a_{\mathrm{p},0}$ are the initial eccentricity and semi-major axis of the planet (Wu and Murray, 2003). The timescales are calculated to be ~ 30 Myr for 1 AU, ~ 500 Myr for 3 AU and ~ 2 Gyr for 5 AU around a $1M_\odot$ star with an assumption of $e_{\mathrm{p},0} = 0$. Because the timescales for planets within the snow line are adequately shorter than the typical Kozai timescales, it is reasonably necessary to well consider the effect.

Kozai mechanism is capable of explaining an eccentric planet and a tilted planet in a single-planetary system hosting a widely-separated stellar companion, which cannot be fully illustrated by planet-planet scattering, though, the mechanism will be ineffective in a too-wide binary even if a companion is present. However, a recent study proposed that a large semi-major axis of a companion possibly changes due to the Galactic tide (Kaib et al., 2013). Based on the model, even a widely-separated companion may have caused Kozai migration.

Tidal Dissipation

What to be considered with combining with planet-planet scattering and Kozai mechanism is a theory named as tidal dissipation. Tidal dissipation predicts a loss of orbital energy due to tidal friction caused by a deformation of a planet when the planet grazes a central star with an extremely small pericenter distance, q. In this process, q is almost preserved because of the angular momentum preservation. Thus a relation of the final semi-major axis a_{fin} with the initial semi-major axis a_{ini} and eccentricity e_{ini}, which

is expressed as

$$a_{\text{fin}} = \frac{1 + e_{\text{ini}}}{1 + e_{\text{fin}}} q_{\text{ini}} = (1 + e_{\text{ini}}) q_{\text{ini}}, \tag{1.17}$$

arises, where we substitute $e_{\text{fin}} = 0$ (therefore $a_{\text{fin}} = q_{\text{fin}}$) due to the dissipation. The event that the tide makes an orbit circular is called as tidal circularization. Timescales of the circularization, $\tau_e = |e/\dot{e}|$, for a planet at 0.01, 0.02, and 0.04 AU are estimated as $\tau_e \sim 10^2, 10^5$, and 10^{12} yr, respectively, with considering only the normal vibration of a planet (Ivanov and Papaloizou, 2004; Nagasawa et al., 2008). Corresponding timescales of decreasing the semi-major axis τ_a are $\sim 10, 10^2$, and 10^{11} yr, respectively, in case of a no-spinning $1M_{\text{J}}$ planet with a radius of $2R_{\text{J}}$ orbiting a $1M_{\odot}$, where R_{J} denotes the Jovian radius.

If a planet has an exceedingly small pericenter distance induced by planet-planet scattering or Kozai mechanism, the influence of tidal dissipation cannot be negligible. The slingshot model (Rasio and Ford, 1996) actually predicts that a planet migrating inward due to the scattering is altered to be a hot Jupiter by tidal dissipation. Besides, there is another hypothesis that Kozai mechanism can make a hot Jupiter as well with the dissipation by increasing eccentricity and coincidently decreasing the pericenter distance q (Fabrycky and Tremaine, 2007; Wu et al., 2007). In any case, hot Jupiters are able to be formed by interaction not only with a protoplanetary disk but also with other objects after disk dissipation. Moreover, a population synthesis model (e.g. Ida et al. (2013), a representative figure is shown in Figure 6.1), which predicts distributions of the parameters based on the core accretion model and the migration models (especially the scattering), has been proposed.

1.3   Our Goals: Observational Constraints on Migration Theory

So far, we introduce the theoretical models which explain how to form hot Jupiters, eccentric planets and tilted planets. Many hot Jupiters observed so far can be expounded by both type II migration and tidal dissipation combined with planet-planet scattering or Kozai mechanism, as explained above. Hence, it is difficult to prove what model has formed an individual hot Jupiter at the present time. A possible way to verify that is to discover a wide-orbit planet around a hot Jupiter, supporting the slingshot model. In order to detect the planet, it is possible to monitor targets which has a long term trend in radial velocity with the RV method (explained in §2.1) or to directly image the system hosting the hot Jupiter (see Chapter 3), but direct imaging is difficult due to contrast limited by older ages of the systems. If a companion object more massive than a planet is found around the system, Kozai mechanism may have occurred. The stellar companion is easily detected because of its brightness (cf. Chapter 5). On the other side, type II migration reasonably explain a hot Jupiter in case that no other object is discovered, but it is significantly hard to classify formation mechanisms for single hot Jupiters into the scattering and type II migration, with considering current detection limits.

Because eccentric planets and tilted planets cannot be explained by type II migration as mentioned above, they are believed to be outputs of planet-planet scattering or Kozai mechanism. Especially for a planetary system with only one discovered planet, Kozai mechanism is more reasonable than planet-planet scattering to explain the cause because the scattering needs a counterpart planet. In order to verify that, it is important to examine whether a companion is indeed present or not by employing direct imaging. However, though direct imaging observations of planetary systems were carried out so far (e.g. Bergfors et al. 2013; Adams et al. 2013), they did not especially focus on systematically investigating the formation mechanisms for eccentric planets and tilted planets.

Hence, in this study we conducted direct imaging observations of systems hosting eccentric and tilted planets in order to detect candidate sources of Kozai mechanism with a specific motivation to approach

the formation mechanism. Figure 1.5, shows which model can explicate each type of planets. The region circled with a green ellipse indicates relations remaining ambiguous. As you can find, the most substantial component is the presence of companions (i.e. whether a single star or a binary). Moreover, in single planet systems, we can sharply distinguish Kozai effects from planet-planet scattering with the companion's presence. Therefore, we aim at acquiring binary rates of planet host stars with a single eccentric planet or a tilted planet (targets are surrounded by the red rectangle). The main purport of this thesis is to quantitatively approach the degrees of each planet migration mechanism by comparing the binary rates to others. In case that a system with an eccentric or a tilted planet frequently hosts a companion, we can interpret the binary rate as statistical results of Kozai mechanism. If, contrarily, the binary rate is not sufficiently high, the influence of Kozai effects is unlikely significant and we are able to comprehend accordingly that planet-planet scattering dominates causes of the migrations.

Here, we simply introduce our methodology and procedure. Data sets taken with high-contrast imaging are reduced with specific reduction techniques to efficiently detect faint objects. After the data reduction and measurements of positions and magnitudes of detected objects, although a theoretical analysis is properly necessary to judge whether Kozai mechanism truly occurs, we estimate Kozai timescales using Equation 1.15 and simply compare it instead with the system's age, because it is unfortunately difficult to calculate the orbit of the wide-separated companion. In this thesis, companions with a shorter Kozai timescale than their system's age are presumed to be companions which have caused Kozai mechanism to planets. Then we compare our binary rates with published other rates to estimate how high our binary rates are with a statistical confidence, though our sample sizes are still not so large resulting from the first attempt.
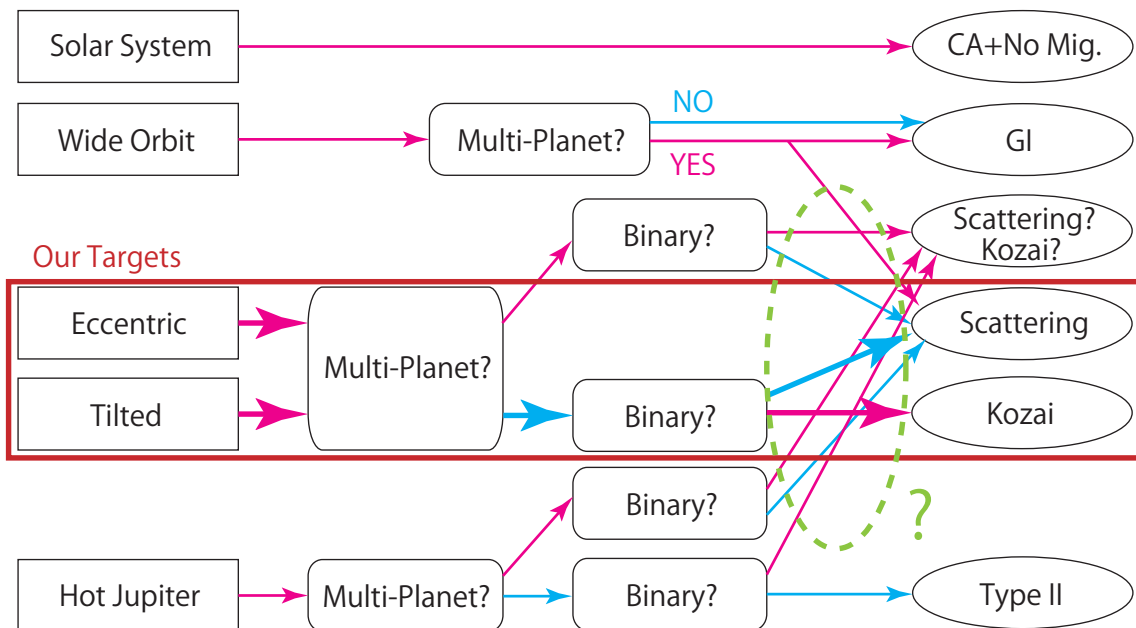
Figure 1.5: A flowchart to find the best migration scenario to explain various "irregular" planets. Because a companion orbiting a planetary system can change planets' orbits, it is important to investigate the presence of companions around planetary systems. Our study mainly focuses on single eccentric or tilted planetary systems (targets surrounded with a red rectangle). The relations circled with a green ellipse remain unclear.

Then we elucidate how to discover eccentric and tilted planets in the next chapter.

1.4   SEEDS Project and My Original Contributions to This Study

This observational study was implemented as a part of the Strategic Explorations of Exoplanets and Disks with Subaru (SEEDS) project (PI: Motohide Tamura, see Tamura 2009). The SEEDS project aims to directly image faint companion objects or disks around bright stars by employing a high-contrast imaging instrument HiCIAO together with an adaptive optics instrument AO188 on the Subaru telescope. The SEEDS project is also organized by National Astronomical Observatory of Japan (NAOJ), Princeton University, Max-Planck-Institut für Astronomie (MPIA), and other institutes, in which NAOJ and the University of Tokyo are leading the project. SEEDS has five main categories divided by targets' estimated ages; Debris Disk (DD), Open Cluster (OC), Moving Group (MG), Nearby Star (NS) and Young Star Object (YSO) to cover a wide age range from $\sim$ Myr to $\sim$ Gyr. One hundred twenty Subaru observation nights in total have been allocated to SEEDS. These significant planetary candidates, GJ 758B (Thalmann et al., 2009), GJ 504b (Kuzuhara et al., 2013), κ Andromedae b (Carson et al., 2013), and many disk structures were discovered by the project.

In particular, I belong to the NS category and lead the NS-RV subcategory, whose targets host known planets detected with the radial velocity (RV) method or the transit method (these techniques are described in the next chapter). The targets of this study, introduced in Chapter 5, were chosen after discussions with my collaborators Norio Narita and Motohide Tamura, but all data sets of this study only except for images of HAT-P-7 taken with IRCS and relating data in Chapter 4 were reduced by the author and the discussions in this thesis are led by the author. Though observations were carried out mainly by the SEEDS observation team, I conducted most of the observations in direct manners at the summit of Mauna Kea or remotely from Mitaka. Although the reduction pipelines I adopted in this study were originally constructed by my collaborators, I have added several improvements. Calibration data sets were also reduced by myself and these are extensively used by the team members.

Chapter 2

Indirect Observational Techniques for Exoplanets

In this chapter, we explain observational techniques for detecting and investigating extrasolar planets. There are various techniques mainly including the radial velocity method, the transit method, the microlensing method, the astrometry and the direct imaging method. We introduce the indirect methods in this section, followed by the next chapter describing the direct imaging method. Our targets for this thesis consist of stars hosting exoplanets discovered with the radial velocity method or the transit method.

2.1 Radial Velocity Method

The radial velocity method is a technique to discover exoplanets by detecting variations in radial velocity (RV) of a star. The first exoplanet orbiting a Solar-type star, 51 Pegasi b, was discovered with this method (Mayor and Queloz, 1995). If a planet exists in a planetary system, because the centroid of the system slightly shifts from the center of the star, the star orbits and shows a RV variation written as:

$$\mathrm{RV} = \frac{2\pi a_* \sin i}{P\sqrt{1-e^2}}[\cos(f+\omega)+e\cos\omega], \tag{2.1}$$

where a_*, i, P, e, f and ω are the semi-major axis of the star, the inclination of the orbital plane, the period, the eccentricity of the orbit, the true anomaly and the longitude of periastron, respectively (see Figure 2.1). The amplitude K, defined as

$$K \equiv \frac{2\pi a_* \sin i}{P\sqrt{1-e^2}}, \tag{2.2}$$

can be rewritten as

$$K = \left(\frac{2\pi G}{P}\right)^{1/3} \frac{1}{\sqrt{1-e^2}} \frac{m_p \sin i}{(M_* + m_p)^{2/3}}, \tag{2.3}$$

where M_* and m_p are the masses of the star and the planet, respectively, by adopting the Keplarian law,

$$P = 2\pi\sqrt{\frac{a^3}{G(M_* + m_p)}}, \tag{2.4}$$

where $a = a_* \times (M_* + m_p)/m_p$ is the semi-major axis of the system. Therefore, we can obtain the planet's mass, though not m_p but $m_p \sin i$, by measuring the RV and assuming a mass of the star, M_*, in

addition to the period and the eccentricity. Figures 2.2 and 2.3 show the difference of the shapes of the RV curves, which is induced by different eccentricities. This is a principle of the RV method, and we measure RV variations of a star, or shifts of stellar absorption lines in wavelengths. A system which has a small component of the orbital motion in the direction of a line of sight is difficult to detect. Since an amplitude of RV varies typically from several tens m/s to less than 1 m/s, the detection requires extremely high precision. In order to attain the goal, the gas absorption cell method (Campbell and Walker, 1979) or the simultaneous reference method (Baranne et al., 1979) is employed.
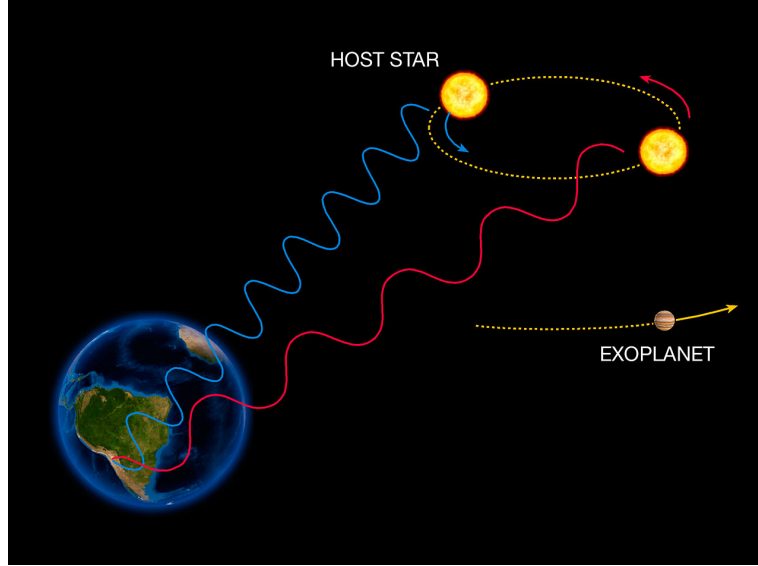
Figure 2.1: A conceptual image of the radial velocity method. (c) ESO.

In the I_2 cell method (e.g. Butler et al. 1996), we obtain stellar spectra engraved with iodic spectra through a standard high dispersion spectrograph and an I_2 cell. By analyzing how the stellar spectra shift with respect to the iodic spectra, we procure highly-precise RV. The method is easily implemented only with preparing the cell, but data reduction is difficult because the spectra are broken by the iodic spectra. The taken spectra, $I(\lambda)$, can be described as

$$I(\lambda) = k[A(\lambda)S(\lambda + \Delta\lambda)] * IP, \qquad (2.5)$$

where k, $A(\lambda)$, $S(\lambda)$, $\Delta\lambda = \lambda v/c$ and IP denote the normalization factor, the iodic spectra, the stellar spectra, the Doppler shift, and the instrumental profile, respectively (Sato et al., 2002). The mark $*$ represents convolution. Moreover, though I_2 cells supply good reference spectra in the optical regions (500-620nm; Marcy and Butler 1992) due to their many absorption lines, they are insufficient in the infrared regions, where late type stars are bright, because of the lack of the lines. New gaseous cells for infrared wavelengths have been developed (e.g. Bean et al. 2010).

On the other hand, the simultaneous reference method (e.g. Baranne et al. 1996) is a means of acquiring both stellar spectra and spectra of reference light (typically provided by a Th-Ar lamp) simultaneously. The light spectra are installed through fibers and placed on detectors side by side with the stellar spectra also fed by fibers. Here, the differences of wavelengths can be described as

$$\lambda_S(f_1, t_1) - \lambda_T(f_2, t_1), \qquad (2.6)$$
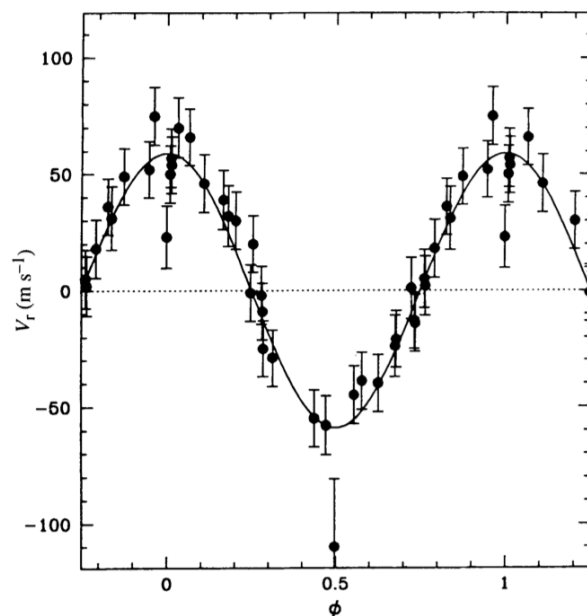
Figure 2.2: A radial velocity curve of 51 Pegasi (Mayor and Queloz, 1995). The horizontal axis and the vertical axis represent the radial velocity and the phase. A circular orbit ($e = 0$) of the planet 51 Pegasi b indicates a pure sine curve.
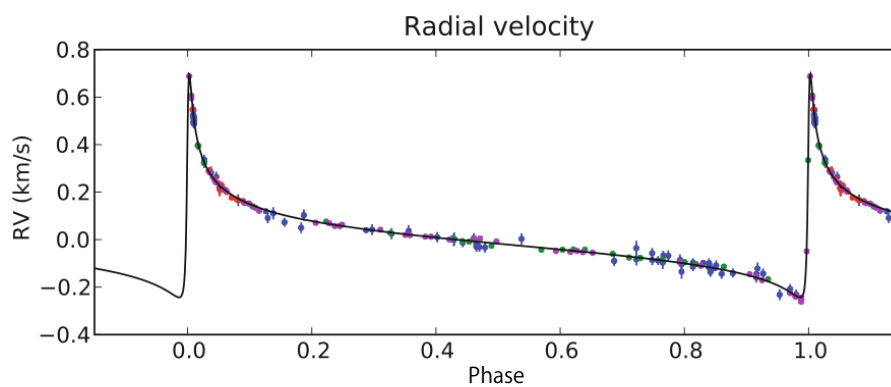
Figure 2.3: A radial velocity curve of HD 80606 (Pont et al., 2009). The horizontal axis and the vertical axis represent the radial velocity and the phase. The planet orbiting it with an extremely high eccentricity of $e = 0.9332 \pm 0.0008$ induces a characteristic curve.

where λ_S and λ_T are the wavelengths of stellar spectra and of a reference light, and f_i and t_i represent the fibers and time, respectively. In order to estimate the systematic errors, we obtain

$$\lambda_T(f_1, t_2) - \lambda_T(f_2, t_2). \tag{2.7}$$

Consequently, the shifts in wavelengths can finally be written as

$$[\lambda_S(f_1, t_1) - \lambda_T(f_2, t_1)] - [\lambda_T(f_1, t_2) - \lambda_T(f_2, t_2)]. \tag{2.8}$$

Because stellar spectra do not need to be broken, data are easy to be reduced. However, the instruments must be stable and require minute control. For example HARPS on ESO's 3.6m telescope in a vacuum chamber with temperature control at a 10^{-3} K level (Mayor et al., 2003). Studies of using the method in the infrared regions are ongoing, for example IRD (Tamura et al., 2012), which employs a laser frequency comb.

Then obtained RV is converted through the Fourier transform into the frequency space, and we find periods and fit the Keplarian motion (i.e. Equation 2.1) to detect planets. The method has succeeded in discovering the largest number of exoplanets. Although a planetary mass is determined in the $m_p \sin i$ form, its real mass, m_p, is statistically not so different from $m_p \sin i$ due to the equation of

$$\langle m_p \sin i \rangle = \frac{\int_0^\pi 2\pi m_p \sin i \sin i \, di}{\int_0^\pi \sin i \, di} = \frac{\pi}{4} m_p \sim 0.8 m_p. \tag{2.9}$$

However, there is a problem of existing plural solutions in multiple planetary systems (e.g. the GJ 581 system; Tuomi and Jenkins 2012).

In this thesis, we employ planetary systems detected with the RV method (Chapter 5).

2.2   Transit Method

The transit method, which was first succeeded in HD 209458 by Charbonneau et al. (2000), is a way to detect temporal dimmings in brightness of a star seen from Earth when a planet transits the stellar surface. The *Kepler* satellite, launched in 2009 and monitoring the Cygnus-Lyra regions, found more than 3,500 planet candidates with this methods. Because Earth, a planet and its host star must be aligned, the number of planets detected with the method is limited in principle. A probability that a planet in a circular orbit transits is given by

$$\text{Prob.} = \frac{\int_0^{\theta_{\rm crit}} \cos\theta \, d\theta}{\int_0^{\pi/2} \cos\theta \, d\theta} = \frac{\sin\theta|_0^{\theta_{\rm crit}}}{\sin\theta|_0^{\pi/2}} = \frac{R_*}{a}, \tag{2.10}$$

where $\theta_{\rm crit}$, R_* and a are the angle between a line of sight and a line from the stellar center to the planetary center, the stellar radius, and the orbital semi-major axis of the planet, respectively. The equation are described more precisely as

$$\text{Prob.} = \frac{R_* \pm R_p}{a} \frac{1 + e\sin\omega}{1 - e^2}, \tag{2.11}$$

where R_p is the planetary radius, e is the eccentricity of the planet. The $+$ sign allows a grazing eclipse and the $-$ sign denies (Winn, 2010). Many short period planets have been detected with this method.

Since transit depths are extremely shallow, specifically of a few % to less than 100 ppm, precise photometry is required. In order to achieve the aim, we often conduct relative photometry with defocusing
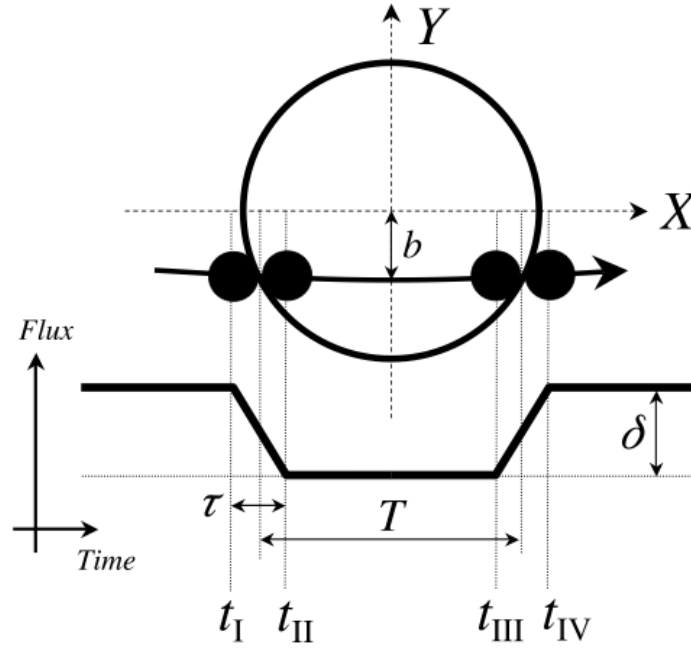
Figure 2.4: A conceptual image of the transit method. Quoted from Winn (2010).

to minimize influence of non-uniformity in sensitivity by placing the stars at the same positions of CCDs or infrared arrays. Large apertures are usually employed to cover all photons the stars emit. Because periodic dimmings in stellar light curves are caused not only by planets but also by dark spots on stellar photospheres and eclipsing binaries in the apertures (so-called "false positives"), it is important to check stability of dimmings, remove trends on light curves induced by stellar activities and examine whether theoretical curves are well fitted to observed curves (see Appendix B).

Basically, the transit method reveals planets' orbital periods, orbital inclinations and radii by using the following relations with δ, T and τ (definitions are shown in Figure 2.4). Here, the transit depth δ can be translated as $\delta = (R_p/R_*)^2$. The parameter τ represents the ingress and the egress duration and $T \equiv T_{\text{total}} - \tau$, where T_{total} denotes the total transit duration ($t_{\text{IV}} - t_{\text{I}}$ in Figure 2.4). The relations in limits of $e \to 0$, $R_p \ll R_* \ll a$ and $b \ll 1 - R_p/R_* \equiv 1 - k$ are written as

$$T \simeq T_0 \sqrt{1 - b^2} \tag{2.12}$$

and

$$\tau \simeq \frac{T_0 k}{\sqrt{1 - b^2}}, \tag{2.13}$$

where T_0 is the characteristic timescale defined as

$$T_0 \equiv \frac{R_* P}{\pi a}, \tag{2.14}$$

and b is the impact parameter,

$$b \equiv \frac{a \cos i}{R_*} \frac{1 - e^2}{1 + e \sin \omega} \to \frac{a \cos i}{R_*} \quad (e \to 0). \tag{2.15}$$

We note that a mass cannot be uncovered with the equations. However, true masse of the planets, m_p, can be obtained by combining resultative inclinations i with results of the RV method (i.e. $m_p \sin i$). Therefore, we can calculate bulk densities for transiting planets from planetary masses and radii. Moreover, even if RV induced by planets cannot be acquired, there is a chance to know the masses in addition to the existence of additional planets in multi-planetary systems. This is because time of transit centers can stir from the precisely periodical time by shifts of the center of gravity from a position of a single-planetary system (TTVs; Agol et al. 2005). The first confirmation with a TTV was carried out in Kepler-9 (Holman et al., 2010).
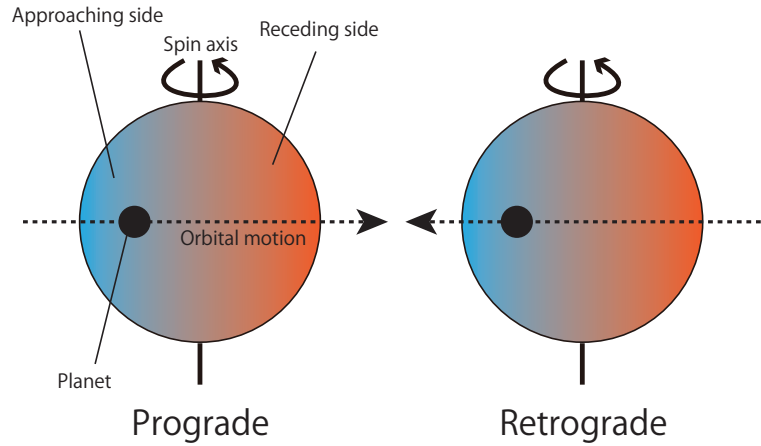
Figure 2.5: Concepts of a prograde and a retrograde planet. The planet occults the approaching side and the receding side.

Furthermore, the transiting planets tell us more information, for example orbital obliquities and planetary atmospheres. An orbital obliquity is measured by using the Rossiter-McLaughlin effect (Rossiter 1924; McLaughlin 1924, who proposed it for eclipsing binaries. see Ohta et al. 2005, 2009 for transiting planets). When a prograde planet transits a photosphere of its host star, it first occults the approaching side of the sphere and next the receding side. Conversely, a retrograde planet first screens the receding side and secondarily the approaching side (see Figure 2.5). Here, the approaching and the receding sides are blue- and red-shifted in RV due to the spin motion. If a planet occults the approaching side, the blue-shifted RV components are partially occulted and therefore total RV appears to be red-shifted, and vice versa. As a result, an anomaly arises in RV during a transit. Then, a shape of the anomaly depends on how a planet intersects a photosphere. Figure 2.6 illuminates the shape's dependence on an obliquity, λ, defined as the projected angle between the orbital axis of a planet and the spin axis of its host star. The first-reported retrograde planet, HAT-P-7, was discovered in this manner (Narita et al., 2009; Winn et al., 2009). The λs of more than 50 systems have been measured (cf. Albrecht et al. 2012). In our study, we chose planetary systems as targets which host planets with non-zero obliquities ($|\lambda| > 0$ deg).

Planetary atmospheres are often investigated with additional absorption lines or secondary eclipses. If a planet has atomic or molecular species in the airs, depths of absorption lines caused by the molecule deepen during a transit because of additional absorption induced by the same molecule in planetary atmosphere. The first detections of sodium and water were carried out by Charbonneau et al. (2002) and Tinetti et al. (2007). On the other hand, thermal inversion, an event that a hotter atmospheric layer lies above a cooler layer, has detected with dependence of depths of secondary eclipses on wavelengths (e.g. Burrows et al. 2007; Knutson et al. 2008), where the secondary eclipse means a phenomenon that a total
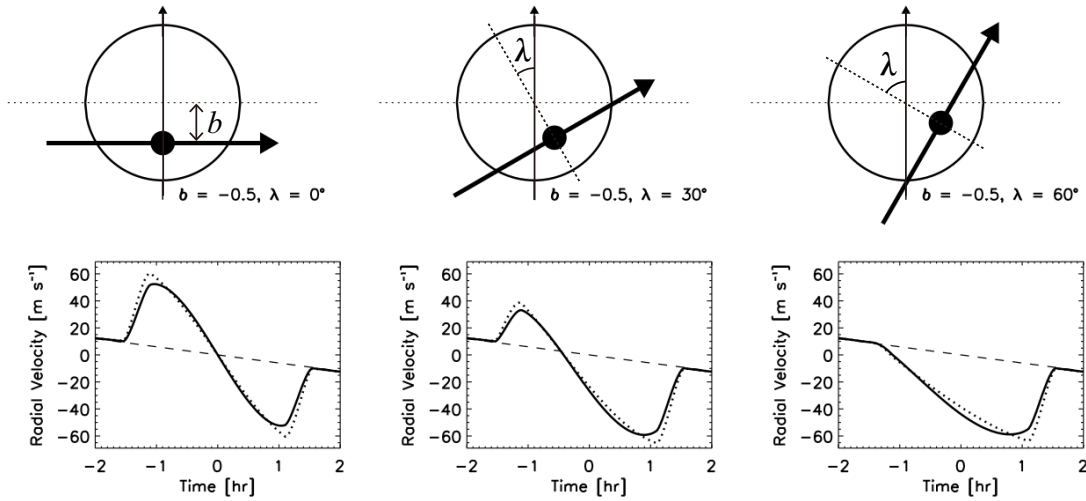
Figure 2.6: A definition of the obliquity λ. The shape of the Rossiter-McLaughlin effect (the bottom figures) strongly depends on λ. This is a revised image, originally quoted from Gaudi and Winn (2007).

flux of a star and a planet decreases while the planet passes behind the star. Secondary eclipses are used not only to investigate planetary atmospheres but also to precisely determine a planetary eccentricity e and the longitude of the periastron ω.

In this thesis, Appendix B deals with the light curve analysis, and Chapter 5 adopts transiting systems, especially with obliquities of $|\lambda| > 0°$.

2.3 Microlensing Method

The microlensing method (Gould and Loeb, 1992) is a technique detecting a microlensing effect, a kind of the general relativistic effect. When a star passes in front of a background object, the star collects light emitted from the background object like "a lens" due to its gravity and therefore amplifies the brightness of the object more than the sum of those of the object and the star ordinarily seen from Earth. Such an event is called as microlensing. If a planet is concomitant with the star, the planet also induce a microlensing event and we consequently detect two amplification (see Figure 2.7). Based on the method, we can acquire a separation on the lens plane between a star and a planet, and a planetary mass. Besides, the method has the advantage of being able to easily detect low-mass planets separated by $\sim$ 1-3 AU, where the other methods are poor at. In contrast, the difficulty of the microlensing method is related with follow-up observations. In order to avoid the demerit, verifiability is secured by collaborating with telescopes in the world on observing an event once the amplification is detected. The first detection was done by Bond et al. (2004). So far 25 planetary systems have been detected with the method.
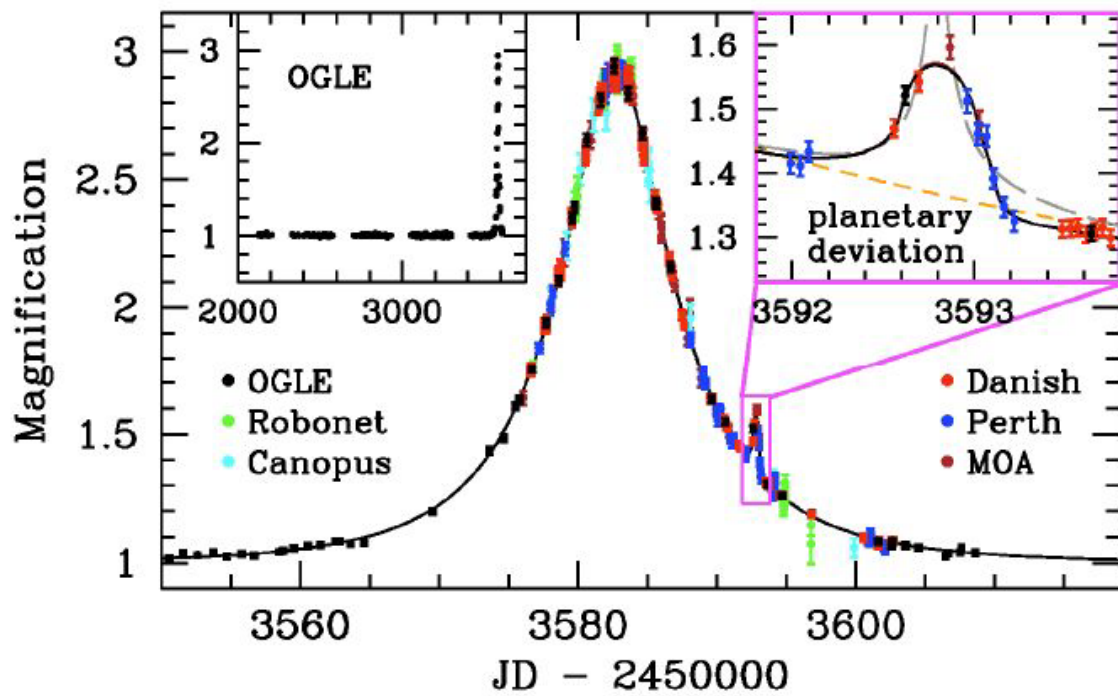
Figure 2.7: A light curve amplified by microlensing. The main peak at $JD - 2450000 \simeq 3583$ was caused by a star and the small peak at $JD - 2450000 \simeq 3593$ was induced by a planetary mass object (Beaulieu et al., 2006).

2.4 Astrometry Method and Timing Method

The astrometry method employs a stellar motion on the celestial sphere induced by a planet (similar to the RV method, but detection not in RV but in astrometry). The motion size in angle θ is estimated as

$$\theta \sim \frac{m_p a}{M_* d},\tag{2.16}$$

where d is the distance of the system from Earth. The size θ for a system with a $1M_\odot$ star and a $1M_J$ planet separated by 1 AU at 20 pc from Earth is calculated to be only 50 μas. This is why the method has not been in success yet though carried out since 1940s or even before (for Barnard's star; van de Kamp 1963). However, the astrometry method confirmed some already-known planetary systems (GJ 876b; Benedict et al. 2002, ε Eridani b; Benedict et al. 2006).

The pulsar timing method is a technique to detect timing shifts in pulsar's flashing period. A pulsar flashes at a precisely state period seen from Earth due to its rotation, but an orbiting planet barely shifts the period. The first discovery of exoplanets (PSR B1257+12b, c and d) was executed with this method by Wolszczan and Frail (1992); Wolszczan (1994), antecedent to planets around the main-sequence stars. Planets around pulsars are believed to form via different ways from those of planets around the main-sequence stars (e.g. Yan et al. 2013). The principle can be also adopted to eclipsing binaries (e.g. HW Virginis; Lee et al. 2009, NN Serpentis; Beuermann et al. 2010).

Chapter 3

Direct Imaging Method

In this chapter, we introduce the direct imaging (hereafter DI for short) method, which attempts to detect a planet in images, as its name suggests, in contrast to the indirect methods we mentioned above. In spite of its directness, this method had not been successful for Solar-system-scale planets until 2008 (HR 8799; Marois et al. 2008, Fomalhaut; Kalas et al. 2008) due to its technical difficulty: A giant planet is extremely faint with a high contrast ratio to its host star and orbits it very closely. A contrast ratio of a rocky planet is much more smaller. To escape from the difficultness, a high-contrast imaging instrument is required. Namely, it consists of an adaptive optics to sharpen images of a planet and its host star, a sensitive infrared array to detect a faint object, and a coronagraph to assuage bright light from the star. Figure 3.2 shows a figure of HiCIAO (Hodapp et al., 2008; Suzuki et al., 2010) on the Subaru telescope (see Figure 3.1), one of the high-contrast imaging instruments, and its concept (bottom). Our observations were mainly operated with HiCIAO (see Chapter 5 and Appendix B).

3.1 Representative Examples

Here we introduce three representative examples of planets DI discovered. The planets are massive and have wide orbits compared to planets discovered with the other techniques, and therefore unique and complementary.

3.1.1 HR 8799bcde

HR 8799 is an A5V star with a mass of $1.5 \pm 0.3 M_\odot$ and an age of 30-160 Myr. HR 8799 is one of the first discovered planetary systems with the DI method. The planets b, c and d were reported by Marois et al. (2008) and the additional planet, e, was announced by Marois et al. (2010) (see Figure 3.3). The planetary masses are estimated as 7-13M_J and 5-11M_J for the inner three planets and b with an atmospheric model (Baraffe et al., 2003), depending on the system's age. Semi-major axes are measured to be 68, 38, 24 and 15 AU for b, c, d and e, respectively. The wide-orbit massive planets cannot be explained by *in situ* formation via the core accretion model except for the innermost planet e. Although it is possible that the planets formed via the core accretion and migrated from the inner regions to the current positions (Currie et al., 2011), it is likely to have formed via the gravitational instability (GI) (e.g. Dodson-Robinson et al. 2009). The stability of the system has been discussed (e.g. Fabrycky and Murray-Clay 2010; Soummer et al. 2011), suggesting the 1:2:4 mean motion resonance for d, c and b, and leading to their eccentricities of ∼0-0.1, which can be explained by GI. Recently carbon monoxide and water absorption lines in the planetary atmosphere were reported by Konopacky et al. (2013).
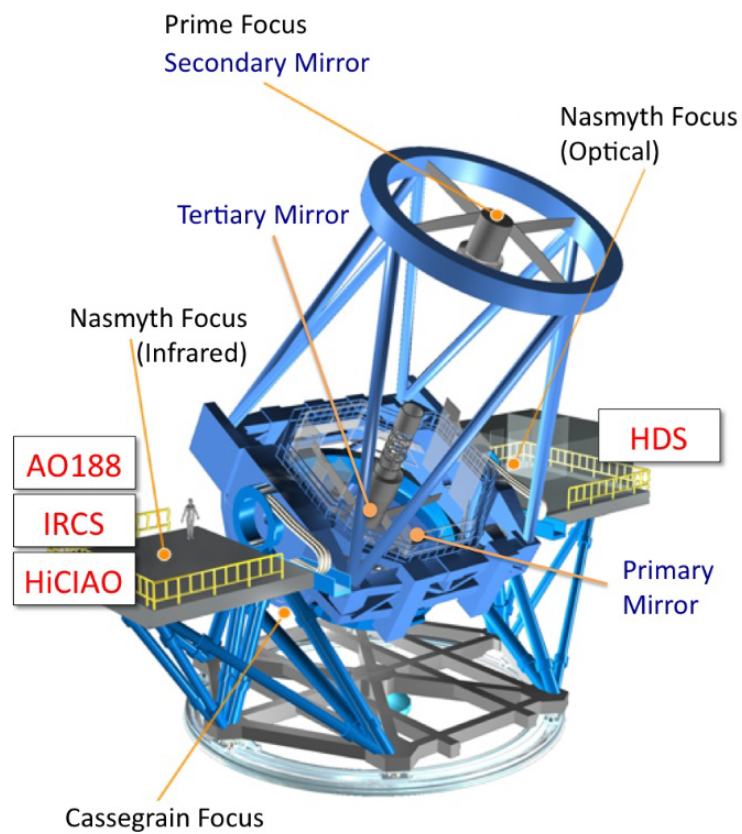
Figure 3.1: The Subaru telescope and its instruments. HiCIAO is placed at the Nasmyth focus together with an adaptive optics instrument, AO188, and the infrared camera and spectrograph, IRCS. Image courtesy of the Subaru telescope.
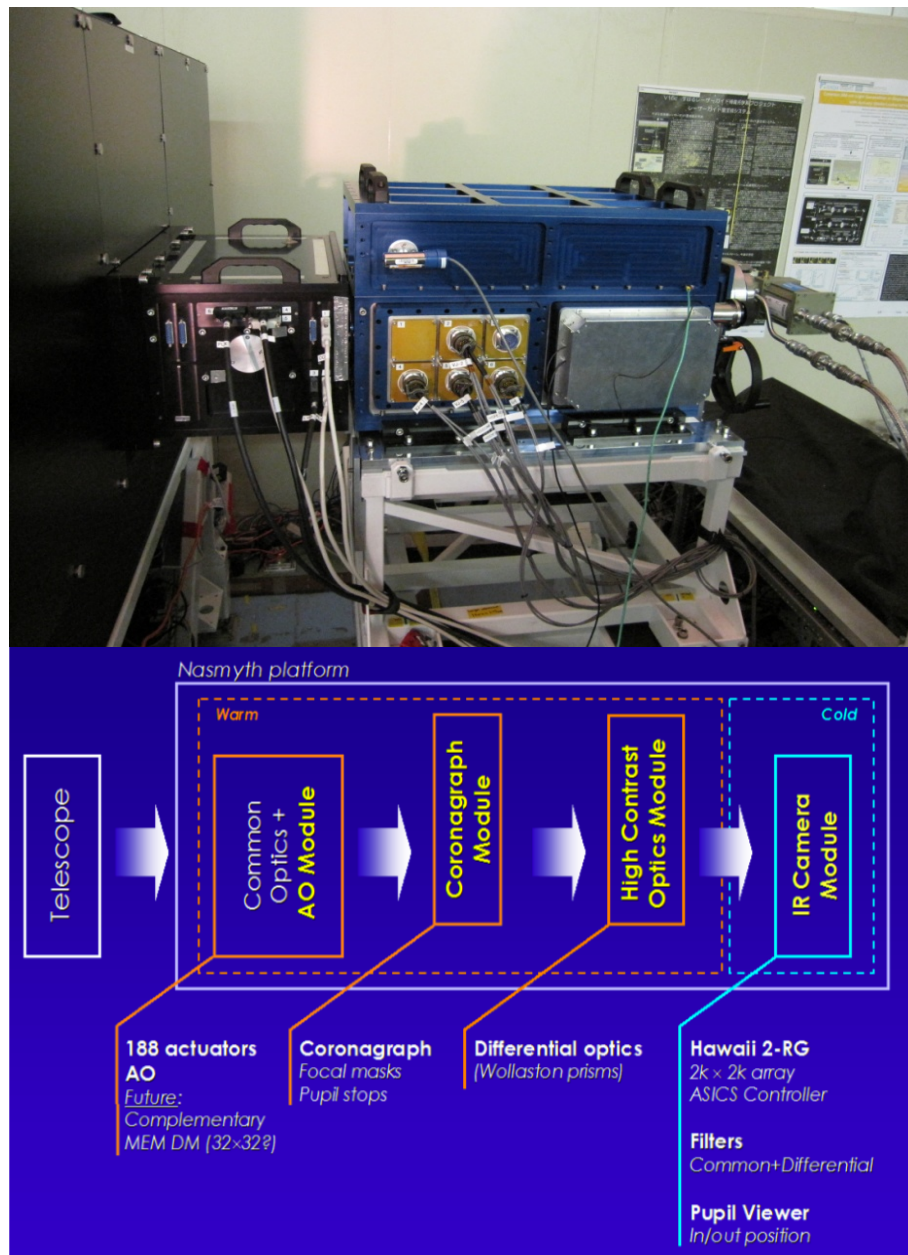
Figure 3.2: A figure of HiCIAO (top) and its concept (bottom). Light collected by the telescope is corrected by AO188 and passes through the coronagraph. The high contrast optics module is only used in the PDI and the SDI modes. Finally the light is detected with the IR camera module.
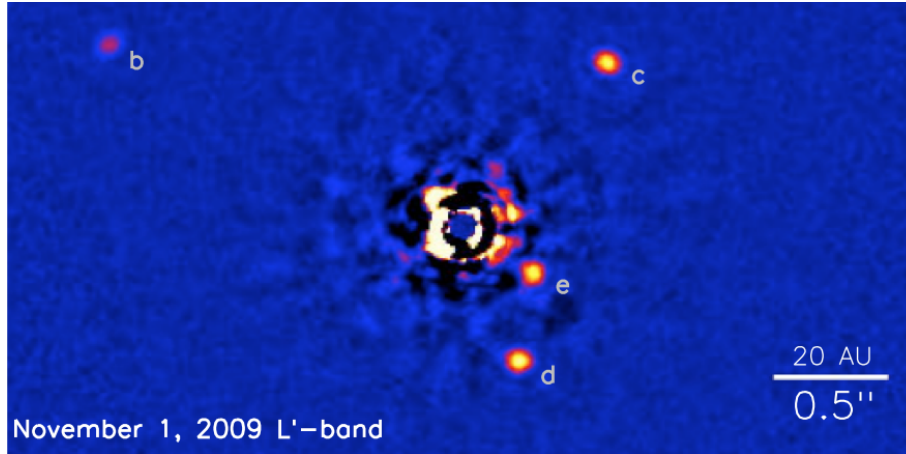
Figure 3.3: An image clearly showing the HR 8799 system (Marois et al., 2010).

3.1.2 β Pictoris b

A star β Pictoris is a young ($\sim 12^{+8}_{-4}$ Myr) and visible to the naked eye ($V = 3.9$) A-type star. It is also known for its debris disks (e.g. Tamura et al. 2006), which contains a cold disk (the outer component corresponds to the Kuiper belt in the Solar system) and a warm disk (the inner component like the main belt in the Solar system). Lagrange et al. (2010) reported that β Pictoris hosts a planetary companion with a separation of 8-13 AU and a mass of $\sim 9 \pm 3M_J$ based on Baraffe et al. (2003) (see Figure 3.4, the common proper motion test is discussed in §3.3). The planetary object, β Pictoris b, was also observed with the RV method, and its mass was dynamically limited ($m_p \lesssim$10-25M_J depending on its true semi-major axis; Lagrange et al. 2012). The dynamically-limited mass ruled out a high mass predicted by the cold-start model and, on the contrary, supports the hot-start model for the planet, in other words; β Pictoris b is likely to have been formed through GI. This is the first constraint on a mass of a directly-imaged planet. Like β Pictoris b, a planet whose mass is confined independently by an atmospheric model and indirect methods will be more important for comparing and examining the hot-start model and the cold-start model (the atmospheric models are introduced in §3.4 in detail). Furthermore, the planet may have caused a transit event in 1981 (Lecavelier Des Etangs and Vidal-Madjar, 2009). If the hypothesis is correct, some orbital parameters and a planetary radius will be more constrained.

3.1.3 GJ 504b

GJ 504b (Kuzuhara et al. 2013; see Figure 3.5) is a Jovian planet orbiting a G-type star GJ 504 and was discovered in the SEEDS project. Its significantly cool (510^{+30}_{-20} K) effective temperature and its blue color ($J - H = -0.23$) suggest its atmosphere being cloud free. The planet has a mass of $4^{+4.5}_{-1.0}M_J$, which is well confined in the planet mass region. A projected wide separation of 43.5 AU implies that this planet formed via GI. Janson et al. (2013) showed its atmosphere involving methane by adopting two filters whose wavelengths are designed at and slightly slipping out of methane absorption lines, and comparing their magnitudes. GJ 504b will be an important system for investigating atmospheric models and therefore planet formation models around Solar-type stars.
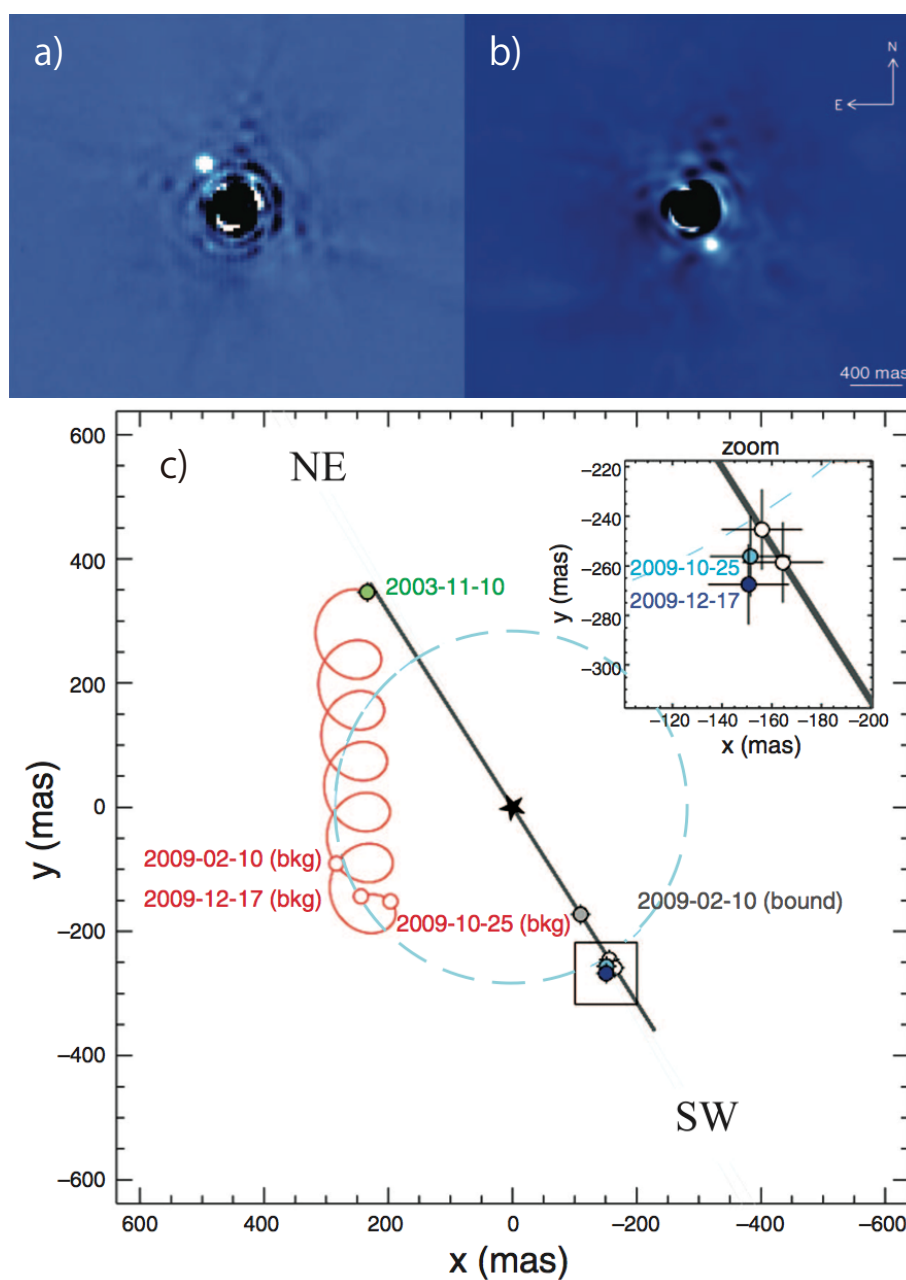
Figure 3.4: a) The β Pictoris main star (removed) and the planetary candidate on the northeastern side in November 2003 at L' band (3.78 μm). b) The same as a) but in the fall of 2009. The planet is at the opposite side. c) A track of a hypothetical back ground star (red line) and an expected orbital motion of a bound planet (black line). If the object is a background object, the object would be present at the positions indicated at the red circles. The difference between positions based on a background hypothesis and actually observed positions indicates that the object is physically bound (Lagrange et al., 2010).
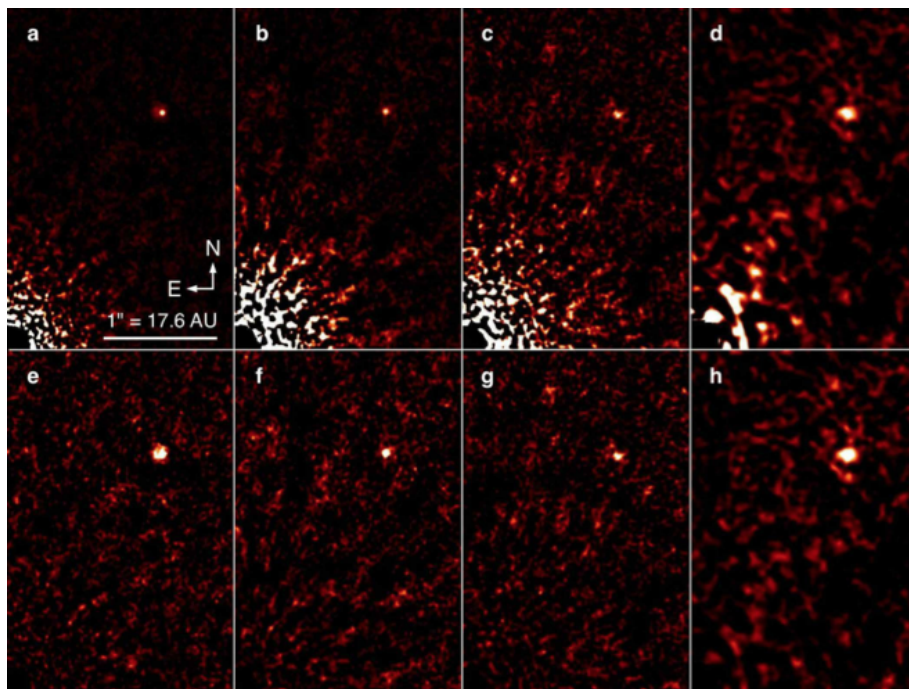
Figure 3.5: Images of GJ 504b (Kuzuhara et al., 2013). The images on the top row are final images at *J* (1.2μm), *H* (1.6μm), *Ks* (2.2μm) and *L'* band for the panel a, b, c and d, respectively. The bottom row indicates the corresponding signal-to-noise ratio (S/N) maps.

3.2 Reduction

In this section, we introduce how frames taken with the DI techniques are reduced. In the DI method, stars are observed frequently in a different manner from standard imaging observations. This observation technique is required mainly by a speckle noise and a spider noise. A speckle noise, which Figure 3.6 clearly shows, relates with light whose wave front is aligned by adaptive optics but is slightly deformed by a optical system. The light yields interference fringes to induce speckle noises. A spider noise, on the other hand, is caused also by interference fringes which is brought by the structure supporting a secondary mirror of a telescope. These quasi-static noises make us hard to detect a real faint object because they pretend faint objects or conceal real signals. In order to avoid the noise, many DI observations have been operated with the angular differential imaging (ADI) technique. ADI is carried out by rotating a target star on a detector using its diurnal motion but without changing an optics system. Figure 3.7 presents a conceptual image of the ADI technique. According to the art, the speckle noise and the spider noise stay at the same positions on the detector, while a real object rotates among frames due to its motion. Hence, we can distinguish the object from the noises.
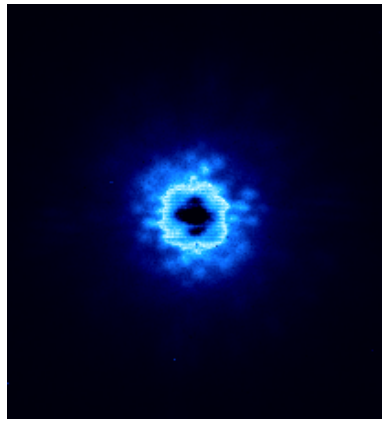
Figure 3.6: The blue star, whose center is saturated and therefore looks black, is surrounded by several signal-like noises. The noises are so-called speckle noises, which are caused by light aligned by an adaptive optics instrument but slightly deformed by an optics system. The noises preclude us from detecting a real object around a target star.

The images obtained with ADI are to be reduced in the following two ways. One is called as "classical ADI" (Marois et al., 2006) and the other "locally optimized combination of images (LOCI)." Figure 3.8 provides the principle of the classical ADI technique. According to classical ADI, we prepare a reference image made by median-combining all scientific frames whose rotation angles are not corrected. Then, speckle noise and spider noise remain in the reference frame together with a central star, while a companion candidate disappears because of its rotation. By subtracting the reference frame from each scientific frame, the central star and the noises are removed and only the companion is left, in principle. Finally we can acquire an image detecting only the companion object by combining reference-subtracted and rotation-corrected (in other words; derotated) frames to improve signal-to-noise ratio (S/N).

Thus the rotation angle ($\Delta\pi$) due to the diurnal motion is an important conception for the classical ADI reduction; for an observation with a small rotation, a planetary candidate does not move on a detector and is removed from observational frames because the planetary signal remains in a reference frame.
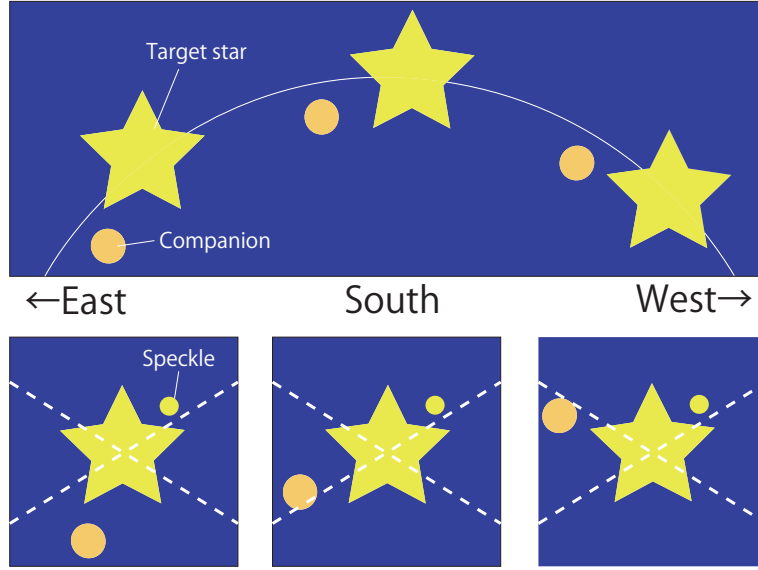
Figure 3.7: A schematic illustration of the principle of the angular differential imaging (ADI). (top) A target star hosting a companion rotates according to its diurnal motion. (bottom) the companion rotates on the frames due to the motion, while The fixed optics system makes the speckle noise and directions of the spider noise (denoted by the broken lines) (quasi-)static.

The problem specific to the ADI reduction is called as self-subtraction (see Figure 3.10). A large rotation angle can escape from the subtraction; typically $\Delta\pi \gtrsim 15-20°$ is desirable for sufficient reduction. The influence of the self-subtraction is estimated by photometrically measuring artificial signals embedded in raw scientific frames. After the reduction, it is popular to make a contrast curve, which indicates how faint objects the observations could detect. A 5σ contrast curve $C(r)$ as a function of the separation r is calculated as

$$C(r) = 5 \times \frac{N(r)S(r)^{-1}[\int_S dS]^{1/2}}{\int_S F_* dS}, \tag{3.1}$$

where $N(r), S(r), S$ and F_* are the noise and the degree of self-subtraction as a function of the separation, the area with photon counts of more than half maximum and stellar flux, respectively. A compensated flux of a planet, F_p, is generally converted into a magnitude, $\mathcal{M}_p$, using the equation:

$$\mathcal{M}_p = \mathcal{M}_* - 2.5\log\left(\frac{F_p}{F_*}\right), \tag{3.2}$$

where $\mathcal{M}_*$ denotes the magnitude of the star, respectively.

Although the classical ADI is an easy manner and does not need peculiar reduction techniques, however, there are two serious problems in actuality. One is caused by time variability in a central star. Namely, it is unrealistic to regard the flux and the point spread function (PSF) of a central star as exactly constant during an observation with a several tens minutes. Hence a star in the reference frame is not the best reference for all scientific frames. The other problem is that the noise can also alter according to the variation of the star and an optical systems. The reference frame based on the classical ADI, therefore, is also hard to be the best reference for the frames.
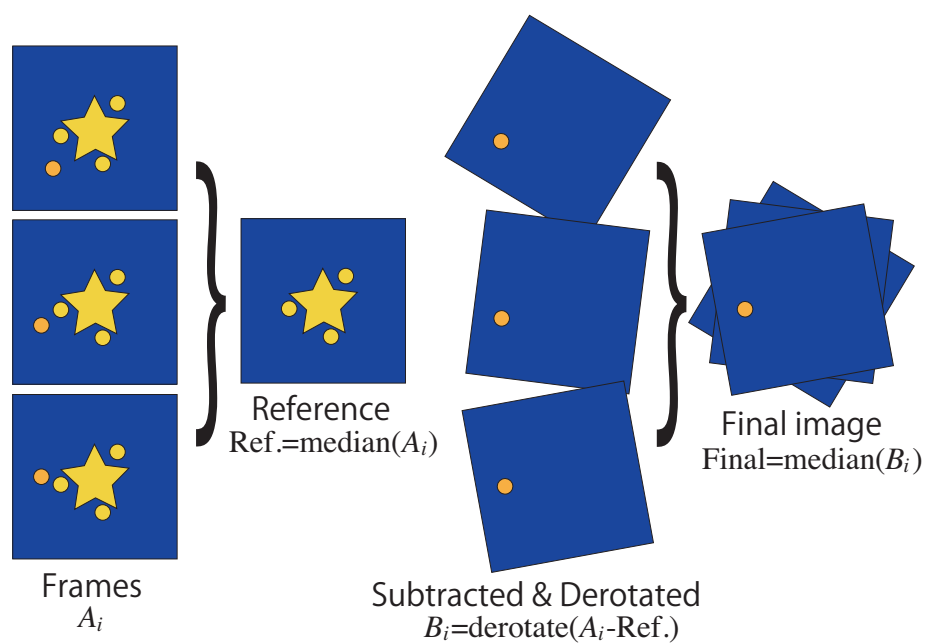
Figure 3.8: A manner of classical ADI reduction (Marois et al., 2006). Each obtained data frame (A_i) contains a main star, noise (the yellow circles) and a real companion candidate (the orange circles). A reference frame (Ref.) is made by combining the images (A_i) in median (Ref. = median(A_i)) and only includes the star and the noise. A final image is created from frames B_i which are produced by subtracting Ref. from A_i and derotated (i.e. $B_i = $ derotate($A_i - $ Ref.)).

Then, locally optimized combination of images (LOCI) method has been proposed by Lafrenière et al. (2007) to solve the above problems. LOCI also employs data frames taken with the ADI technique. LOCI divides each frame into many regions, and composes a reference frame for each scientific frame to reproduce corresponding regions. Figure 3.9 shows how LOCI makes each reference frame. LOCI starts with a inner part of an image. Excluding a saturated region (indicated by the cross-hatch), LOCI divides the image into the boxes bordered by thick black lines in radial and azimuthal directions. Each box is called as "an optimization region," and compared with corresponding regions in other scientific frames. Each reference region for the each optimization region is composed by combining the corresponding regions with the least squares method. Consequently, the each reference region is optimized for and therefore reproduces the each optimization region. However, only the grey-hatched regions (so-called "subtraction regions") in the optimization regions are actually used to be subtracted from the scientific frames because of minimizing ill effects caused by specific error-dominated regions. On the next stage, LOCI repeats to compose reference regions outside excluding the subtraction regions in addition to the saturated region. Because each reference frame is produced for each corresponding scientific frame, this algorithm is tough against the variability of a star and noise.

One point to be aware of composing reference frames are the self-subtraction problem as well as the classical ADI (see Figure 3.10). However, the problem is more serious for LOCI since the optimization is able to duplicate the optimization regions so minutely that subtraction can remove a planetary signal as well as harmful noise when rotation angles are small. Thus, not all scientific frames but frames temporally separated by adequate time interval are employed to compose reference frames as satisfying the following equation:

$$N_\delta \times \text{FWHM} \geq r\delta\theta, \tag{3.3}$$

where N_δ is the constant. The self-subtraction is compensated as well as the classical ADI reduction. Another point is related with the size of the optimization and subtraction regions. If the regions are too small, a planetary signal will be removed by reproducing the planet from noises. Conversely, the too large regions cancel out the advantage of LOCI. Hence, the appropriate size exists; Lafrenière et al. (2007) investigated the best parameters of LOCI. Our study adopts the same values as best values of (Lafrenière et al., 2007) except for N_δ of 0.75. Finally a contrast curve would be composed as well as for the classical ADI analysis. LOCI is the most popular way to reduce data sets obtained with the ADI observations and discovers many planets.

Apart from ADI, there are two observational techniques, polarized differential imaging (PDI) and spectral differential imaging (SDI). PDI is a method by obtaining images in two or four polarization directions simultaneously and subtracting each other to detect polarized signals. Based on this technique, variability of target stars are small due to the simultaneousness. Moreover, while the speckle noise and the spider noise are unpolarized because unpolarized light emitted from stars becomes sources the noises, objects reflecting light from stars, for example a disk surrounding a star, is easy to be polarized and detected with PDI observations. Hence, the strategic explorations of exoplanets and disks with Subaru (SEEDS) project (PI: Motohide Tamura, Tamura 2009), in which we participate, has successfully operated PDI observations to detect circumstellar disks in addition to ADI observations (e.g. Hashimoto et al. 2011).

SDI observations are performed by simultaneously obtaining multiple images with multiple filters. The wavelengths of the filters are designed at molecular absorption lines (on-filter; e.g. CH_4 at 1.57 μm) and at wavelengths slightly different from the absorption lines (off-filter; e.g. 1.55 μm). If the molecule species characterizes cool atmospheres and compose a part of a planetary atmosphere, its absorption line makes only the planet in an image taken with the on-filter fainter than that in an image with the off-filter. In contrast, fluxes of its host star in the image taken with both the on- and off-filter are almost the same
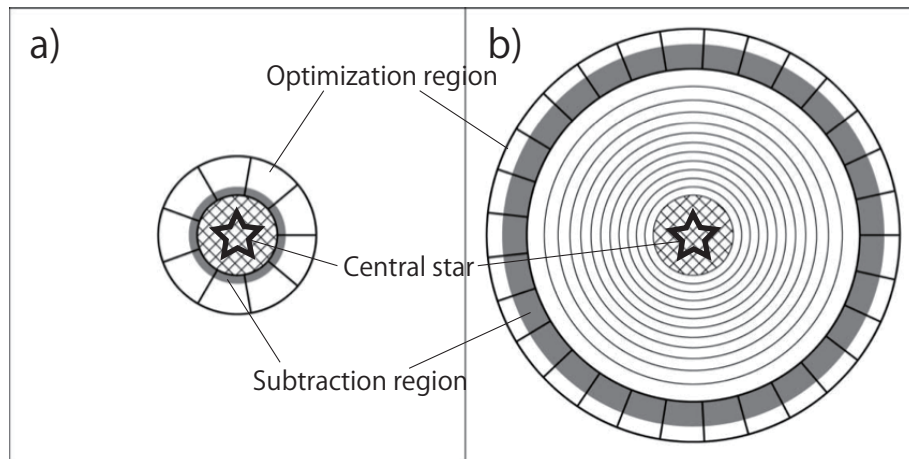
Figure 3.9: An illustration of how LOCI divides a scientific frame. The cross-hatched regions, the regions bordered by the thick black lines, and the grey-hatched regions represent the saturated regions (the positions of the central star are indicated), the optimization regions, and the subtraction regions, respectively. a) LOCI divides each image into optimization regions to make each reference region, but only subtraction regions are used to be subtracted. b) The regions are made outside gradually excluding subtraction regions already composed. See text in detail. The original image in Lafrenière et al. (2007) and revised by the author.
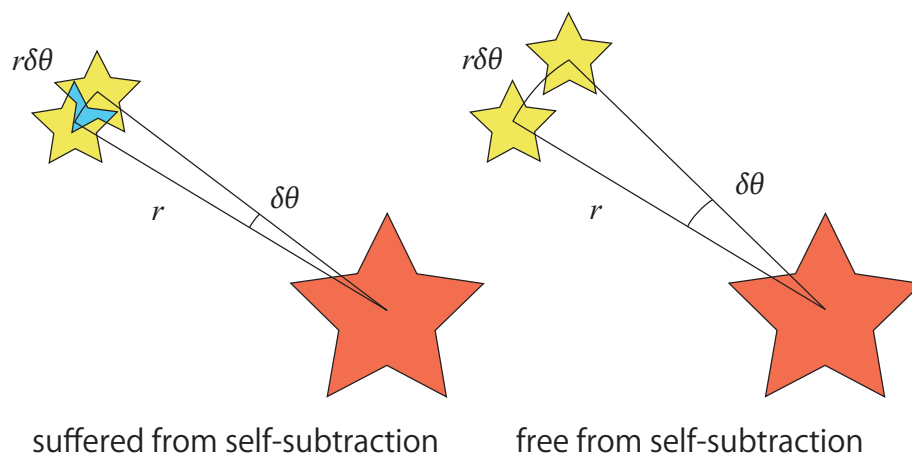
Figure 3.10: A concept of the self-subtraction. A star separated by r from a central star moves $r\delta\theta$ with a rotation angle of $\delta\theta$. (left) A small $\delta\theta$ induces a self-subtraction region (the overlapped regions colored in blue). (right) An adequate $\delta\theta$ does not cause it.

if the molecule species does not exist in the stellar atmosphere. By utilizing the contrast differences, subtraction of the on-image from the off-image leads to an image detecting only the planet, while the star practically disappears. Some observations employed the SDI technique (e.g. Biller et al. 2007).

3.3   Common Proper Motion Test

A detected planetary candidate with the DI method has a possibility of being a background object. Thus, follow-up observations are necessary to identify it as a physically-bound companion by the common proper motion (CPM) test. A star moves on the celestial sphere at speed of its proper motion of μ_α in right ascension (RA, α) and μ_δ in declination (Decl., δ). The μ_α is usually used in form of $\mu_\alpha \cos \delta$ to adjust its unit to that of μ_δ (mas/yr). Figure 3.11 shows a conceptual image of the CPM test. If a background object would stay at the same position and therefore the relative positions to a target star will change. Conversely, a candidate is physically associated with a star (i.e. a real companion), it would have the same proper motion (i.e. CPM). In this case, the relative positions will be constant in two observations. Actual results are shown in Chapter 5 with tracks driven by proper motions in addition to parallaxes of target stars. The CPM test is a deterministic test to distinguish a physical companion from a background object. Hence, all planetary candidates detected with the DI method have to be examined with the CPM test, and a candidate not examined with the test yet is "a companion candidate", not "a planet," strictly. In Chapter 5, our observations for each target were planed to be separated in time by Δt, written as

$$\Delta t \gtrsim \frac{5 \times \mathrm{PS}}{\sqrt{(\mu_\alpha \cos \delta)^2 + \mu_\delta^2}}, \tag{3.4}$$

where PS is the pixel scale (9.5 mas/pixel for HiCIAO), to test the CPM with high confidence. A candidate confirmed with the test is always regarded to have the same age and distance from Earth as those of its host star. A companion candidate around a star with a small proper motion is frequently examined with a color information.

3.4   Mass Estimates with Atmospheric Models

A giant planet imaged with the DI method enables us to measure its magnitudes and consequently infer its mass. Namely, a gaseous planet emits light produced by the Kelvin-Helmholtz contraction and gradually shrinks to be cooler. Thus, a planetary luminosity depends on its age. At a fixed radius, a massive planet has more potential energy in its interior to remain luminous, while a light planet immediately exhausts the energy to be dim. An object with a mass of $\gtrsim 13 M_\mathrm{J}$, where M_J represents the Jovian mass, experiences nuclear fusion of deuterium (Spiegel et al., 2011). It is reasonably robust to set a border between a planet and a brown dwarf at "the deuterium-burning limit." Therefore, the three parameters, the age (or the time), the mass, and the luminosity, are closely related with each other. The relation has been well investigated and summarized in the form of atmospheric models. In a DI analysis, the models are often employed to estimate a planetary mass with a given age (the host star's age normally substitutes for it) and magnitude(s). In this thesis, we mainly employ the COND model (Baraffe et al., 1998) for contrast curves and the NextGen model (Hauschildt et al., 1999a,b) for mass estimates as the atmospheric models, where the COND model is applicable to brown dwarfs or planets with a low effective temperature of $T_\mathrm{eff} < 1400$ K without irradiation and the NextGen model to low mass stars with $T_\mathrm{eff} > 2700$ K.
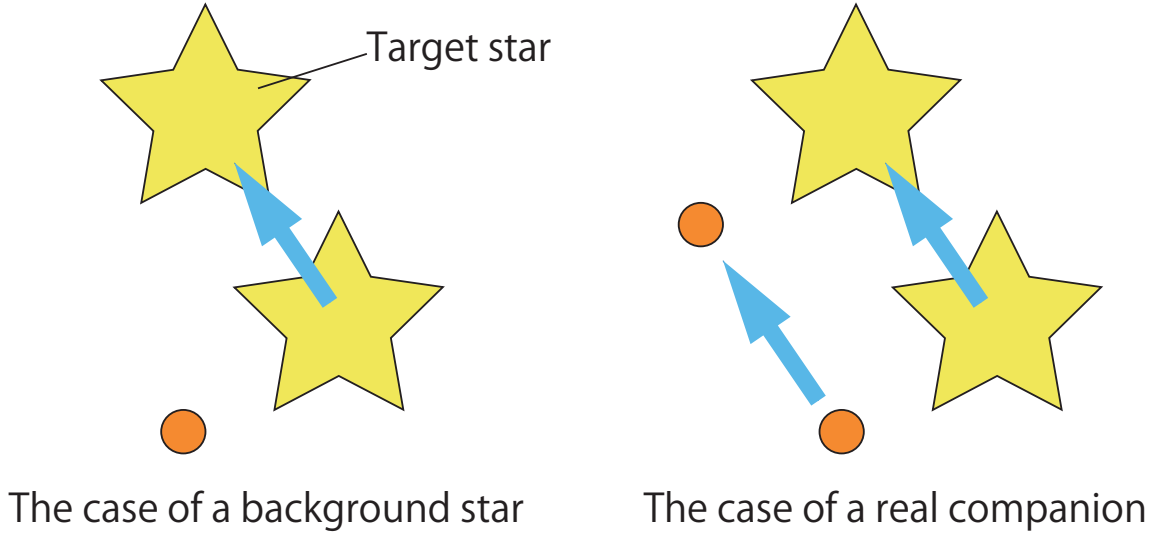
Figure 3.11: An illustration of a concept of the common proper motion test. (left) If the companion candidate (indicated by the orange circle) is a background star, the relative positions will change in two observations due to the star's proper motion and, actually, parallax. (right) If the companion candidate is a real companion, the relative positions will be constant because the companion has the same proper motion as its host star.

An age is estimated based on several techniques. The most fundamental way is to use isochrones (e.g. Y^2 isochrone; Yi et al. 2001); theoretical models to predict stellar evolutionary tracks in the Hertzsprung-Russel diagram (H-R diagram). Isochrones produce dependence of luminosity and temperature on age, but the parameters converge to the main-sequence. Hence, it is difficult to precisely estimate main sequence stars with adopting isochrone models. Another way depends on a relationship between age and chromospheric activity. Basically a star rapidly spins on its young stage and gradually slows down due to its mass loss. A rapid spin produces strong magnetic fields through the dynamo mechanism, and consequently gives rise to specific species in its chromosphere and characteristic emission lines, e.g. $H\alpha$ line at 6568 Å and Ca H and K lines at 3968 Å and 3933 Å. The $\log R'_{\mathrm{HK}}$ indicates a chromospheric activity by measuring Ca H and K lines and has a relation with age described as

$$\log(\mathrm{Age}) = -38.053 - 17.912 \log R'_{\mathrm{HK}} - 1.6675 (\log R'_{\mathrm{HK}})^2 \qquad (3.5)$$

(Mamajek and Hillenbrand, 2008). Although it is difficult to constrain its mass with only a magnitude at one wavelength mainly due to an uncertainty of age, a color, which is always defined as a difference of magnitudes at between two wavelengths, helps us to limit its temperature and therefore its mass. Even if a planet has not been confirmed with the CPM test, it is possible to examine the planet's boundness by comparing an observed magnitude with a magnitude theoretically derived from an atmospheric model, given colors and an assumed distance from Earth.

Another factor which can change hypothetical luminosities of models is elemental abundance. The elemental abundance is typically indicated by [Fe/H], which is defined as

$$[\mathrm{Fe/H}] = \log \left(\frac{N(\mathrm{Fe})}{N(\mathrm{H})} \right)_{\mathrm{Star}} - \log \left(\frac{N(\mathrm{Fe})}{N(\mathrm{H})} \right)_{\mathrm{Sun}}, \qquad (3.6)$$

where $N(\text{Fe})$ and $N(\text{H})$ are the number of iron and hydrogen atoms, or a ratio of the number of carbon atoms to oxygen atoms (C/O). Elemental species compose various kinds of molecules depending on the circumstances, like pressure and temperature, which are decided by stellar or planetary evolution. Some kinds of molecules (e.g. water and methane) dominate opacities of atmospheres at specific wavelengths and, therefore, engrave distinctive features on their spectra. Utilizing it, it is feasible to comprehend what molecular species exist in a planetary atmosphere by employing specific band filter (e.g. Janson et al. 2013) or by investigating planetary spectra obtained with spectroscopy (e.g. Bowler et al. 2010). Moreover, solid particles (so-called "dust") can be made from certain species and aggregate to be cloud and haze in an atmosphere. The cloud and haze, to the contrary, conceal the atmosphere with opacities dependent weakly on wavelength, so that they dim the planetary luminosities in wide wavelength ranges to affect mass estimates. The Dusty model (Chabrier et al., 2000) (applicable to $T_{\text{eff}} \in [1700\,\text{K}, 2700\,\text{K}]$) considers dust opacities. Dust is formed at low temperature and evaporates at high temperature to fade away. However, at extremely low temperature dust grows up into large particles to fall onto planetary surfaces, leading to dust free atmospheres. Although both the NextGen model and the COND model are cloud free models, dust evaporates in the NextGen model and falls out in the COND model. Considering our samples have almost the same metallicity as the Sun, $[\text{Fe/H}] \sim 0$, we assume to adopt the Solar abundance to all our targets when estimating their masses.

The DI method is a very effective technique to know planetary complexions in this way, but also has disadvantages. A mass of a planet is obtained by adopting a magnitude of the planet and an age of the system to an atmospheric model as mentioned above, but the mass is difficult to be exactly estimated since the system's age (i.e. the stellar age) has ambiguity to be determined. Moreover, as for atmospheric models, mainly two models have been proposed (Marley et al., 2007; Fortney et al., 2008). They are called as a hot start model and a cold start model, which differ in initial internally-thermal condition of protoplanets and correspond to the gravitational instability (e.g. Durisen et al. 2007) or direct collapse from molecular clouds, and the core accretion (e.g. Pollack et al. 1996) (The models are described in §1.2.1 in detail). Figure 3.12 (Fortney et al., 2008) shows the difference in luminosities especially in the early stage. Because of the differences, the models lead to different masses inconveniently. Our researches employ one kind of hot-start models due to large separations from target stars, but our samples are hardly affected by the ambiguity because ages of our samples are $\gtrsim 1\,\text{Gyr} = 10^9$ yr.

3.5   Advantages and Disadvantages

The DI method is a unique method compared to the indirect techniques, so there are advantages and disadvantages. The most important strong point is the capability of acquiring its effective temperature. With adopting its magnitudes to an atmospheric model, we can know its mass and radius in addition to the temperature (see §3.4). Moreover, narrow-band imaging and spectroscopy enable us to directly discuss components of its atmosphere. Apart from an atmosphere, DI takes images of planets in wide orbits, which cannot be discovered with the other methods. Since wide-orbit ($a \gtrsim 30$ AU) planets are unlikely formed via the core accretion (CA) model, DI is a device to detect a planet formed through the gravitational instability (GI).

The disadvantages are opposite to the advantages. One is that the dependence on atmospheric models induces uncertainty of planetary mass estimates. A planet detected with DI is young enough to emit infrared flux. However, because a young planet still remembers its formation scenario, different models lead to different masses. In addition, unfortunately the predominance of the CA model to GI model causes the smallness of the number of directly imaged planets, combining with the sensitivity to wide-orbit planets considered to be formed via the GI model. Furthermore, DI instruments are limited due to
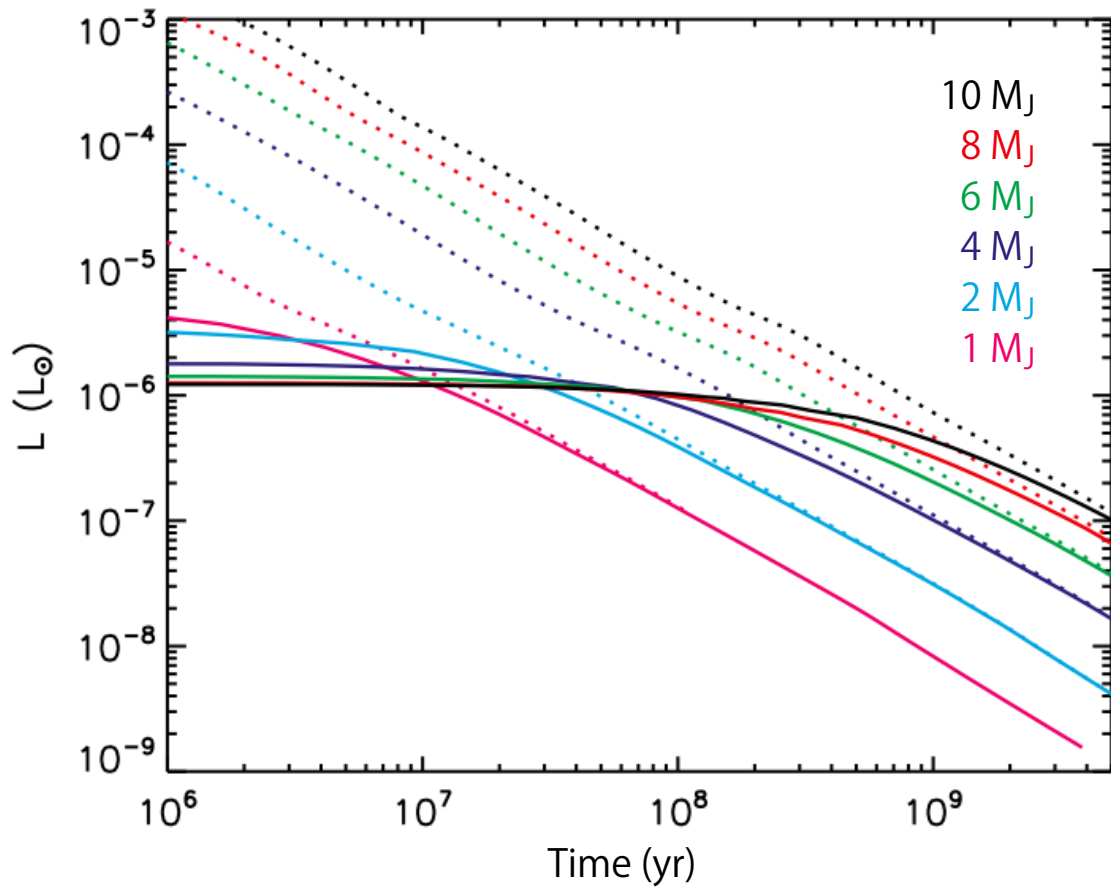
Figure 3.12: Cooling tracks for giant planets illustrating differences in luminosities (Fortney et al., 2008). The horizontal axis and the vertical axis denote the time after planet formation in year and the luminosity in a unit of the Solar luminosity, respectively. The solid and dotted lines represent the cold start model and the hot start model, respectively. The colors reflect planetary masses.

its expensive costs.

Still, it is certain that DI observations are sole ways to investigate wide-orbit planets. Therefore, developments of several new instruments (e.g. GPI on Gemini-South and SPHERE on VLT) are in progress to depress contrast curves and aim to detect fainter and closer objects to bright target stars. Utilizing the power, we employ direct imaging to detect wide-orbit objects around planetary systems in this study (see Chapter 4 and Chapter 5). Our observations are mainly targeting planetary systems to detect companion candidates which can induce Kozai migration. Given a typical example of a planetary system holding one planet whose central star and planet have masses of $1M_\odot$ mass and $1M_J$ and located at 50 pc from Earth, the planet is orbiting at the snow line (2.7 AU) with a period of 4.4 yr. Kozai timescale of $P_{\mathrm{Kozai}} \sim 10 - 100$ Myr, which is adequately shorter than a typical systems's age of $\sim$ Gyr, leads to a necessary companion mass of $M_{\mathrm{B}} \sim 3 \times 10^{(-3)-(-4)} M_\odot$, $\sim 2 \times 10^{(-2)-(-3)} M_\odot$ and $\sim 2 \times 10^{(-1)-(-2)} M_\odot$ at separations of $1'' = 50$ AU, $2'' = 100$ AU and $4'' = 200$ AU, respectively, by substituting such parameters and $e_{\mathrm{B}} = 0$ into Equation 1.15 and Equation 2.4. Meanwhile, our direct imaging could detect a (sub)stellar object around a G-type star with an absolute magnitude at H-band of $M_H \sim 18$ by estimating from its host star's absolute magnitude of $M_H \sim 3$ and a typical HiCIAO's contrast of $\Delta H \sim 10^{-6} = 15$ mag. COND model predicts that a (sub)stellar object with such a magnitude has a mass of $\sim 0.02 M_\odot$ for a 2 Gyr old system, which is comparable to the necessary masses. The estimate clearly shows that DI is required to investigate the presence of possible sources of Kozai migration especially inner regions close to main stars.

Chapter 4

A Common Proper Motion Stellar Companion to HAT-P-7

In this chapter, we actually demonstrate our methodology using a specific case of HAT-P-7, prior to the main observation part. This planetary system have been already known to host one confirmed planet, HAT-P-7b (Pál et al., 2008), which was first reported by (Narita et al., 2009) and (Winn et al., 2009) that HAT-P-7b has a significant obliquity ($\lambda \simeq -130°$ by Narita et al. 2009). Thus, it was required to explain the obliquity using some migration mechanisms. Actually, (Narita et al., 2010b) discovered two companion candidates around HAT-P-7 with separations of $3.''1$ and $3.''9$, but it is unlikely that they had made the obliquity through Kozai oscillation even if bound. We then operated follow-up observations of this system and examine the CPM tests. As a result, we confirm one of the two candidates is really associated with the main star and has a spectral type of M5.5V. Given an additional planet c, newly expected by a RV long-term trend, the sequential Kozai mechanism possibly explicate the obliquity.

4.1 Chapter Abstract

We report that HAT-P-7 has a common proper motion stellar companion. The companion is located at ~ 3.9 arcsec to the east and estimated as an M5.5V dwarf based on its colors. We also confirm the presence of the third companion, which was first reported by Winn et al. (2009), based on long-term radial velocity measurements. We revisit the migration mechanism of HAT-P-7b given the presence of those companions, and propose sequential Kozai migration as a likely scenario in this system. This scenario may explain the reason for an outlier in the discussion of the spin-orbit alignment timescale for HAT-P-7b by Albrecht et al. (2012).

4.2 Chapter Introduction

To uncover formation mechanisms of diverse exoplanetary systems, the (mis)alignment between the planetary orbital axis and the stellar spin axis, which can be measured via the Rossiter-McLaughlin (RM) effect (e.g., Ohta et al. 2005; Hirano et al. 2011) or spot-crossing events (e.g., Sanchis-Ojeda and Winn 2011; Sanchis-Ojeda et al. 2012), has been recognized as an useful clue. Previous observations have revealed that about one third of hot Jupiters have tilted or even retrograde orbits relative to their host star's spin (e.g., Hébrard et al. 2008; Narita et al. 2009; Winn et al. 2009). This indicates that not only disk-planet interaction but also few-body interaction (planet-planet scattering and/or Kozai mechanism)

play an important role in planetary migration processes. Moreover, some studies pointed out the interesting facts that spin-orbit misalignments in planetary orbits are apparently correlated with host star's temperature (Winn et al., 2010a) and age (Triaud, 2011), while these correlations can be explained by the properties and evolution of the internal structure in host stars (Albrecht et al., 2012). Those correlations are important clues to understand the whole picture of planetary migration.

However, previous discussions often overlooked the possible presence of faint distant companions. In most of the RM measurements, except for some obvious cases (e.g., XO-2, HD80606), observers did not check whether the host star has outer companions. Thus any correlation between the spin-orbit misalignment and the existence of binary companions has not been well investigated. To solve this problem, we have started high-contrast direct imaging observations for known transiting planetary systems in the course of the SEEDS (Strategic Explorations of Exoplanets and Disks with Subaru; Tamura (2009)) project.

Narita et al. (2010b) reported two candidate companions around HAT-P-7, which was known to have a retrograde hot Jupiter HAT-P-7b (Narita et al., 2009; Winn et al., 2009; Albrecht et al., 2012). In this letter, we present evidence that one of the two candidate companions is indeed a true companion of HAT-P-7, confirmed by the common proper motion and the distance from Earth inferred from its spectral type and apparent magnitude.
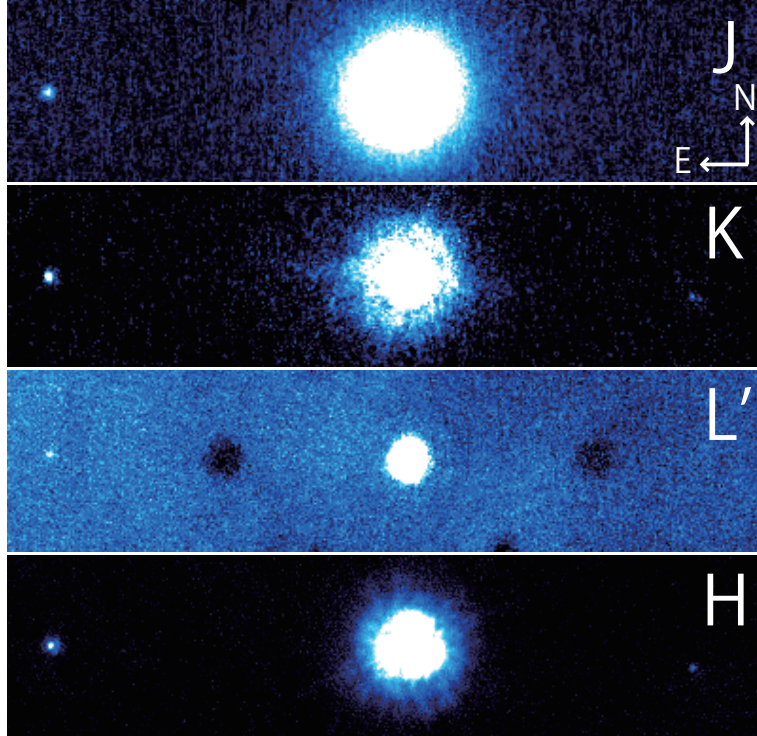
Figure 4.1: High-contrast images around HAT-P-7 taken with the Subaru IRCS (J, K, L') in 2011 and HiCIAO (H) in 2012 (see Table 4.1). The field of view of each panel is 8 arcsec (horizontal) $\times$ 2 arcsec (vertical). Black circle regions in the L' band image are vestiges of dithering pattern. North is up and east is left for all panels. Note that only unsaturated images are used in this figure to highlight the eastern companion. The western companion is not detected in the J and L' band images.
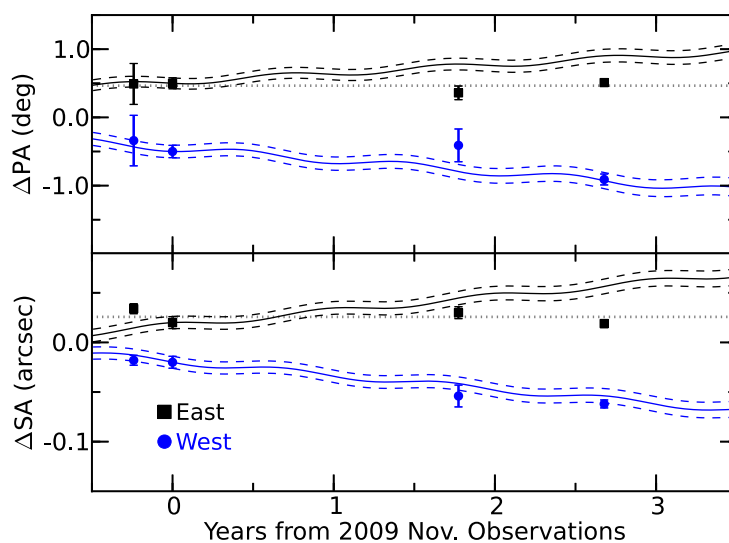
Figure 4.2: The panels illustrate the variations of position angles (top) and separation angles (bottom) of the both candidates over the course of three years. The solid trajectories show the variations expected from an assumption that the candidates are background stars: the dashed lines show the 1σ errors. Note that we add offsets to all the values for clarify. The dotted lines indicate the averages of observed separation angles and position angles for the east candidate. As shown in this figure, the east one is inconsistent with a background source, while the west object is in good agreement with the background hypothesis.

Table 4.1: Observation logs and magnitudes of candidate companions

UT Dates	Inst.	Band	Exp. Time [s]	Mag.(East)	Mag.(West)	Ref.
2009Aug06	HiCIAO	H	585[a]	15.12 ± 0.04	16.64 ± 0.06[b]	this work[b]
2009Oct30	AstraLux	i'	30	18.50 ± 0.21	non-detection	Narita et al. (2010b)
2009Oct30	AstraLux	z'	30	17.43 ± 0.09	non-detection	Narita et al. (2010b)
2009Nov02	HiCIAO	H	100[c]	15.07 ± 0.04	16.56 ± 0.07	this work
2011Aug12	IRCS	J	560.6[d]	15.81 ± 0.19	17.48 ± 0.25	this work
2011Aug12	IRCS	K	560.6[d]	14.81 ± 0.07	16.38 ± 0.09	this work
2011Aug12	IRCS	L'	396[e]	14.45 ± 0.41	non-detection	this work
2012Jul07	HiCIAO	H	1810[f]	15.18 ± 0.07	16.66 ± 0.07	this work

[a] 19.5 s (saturated) × 30 images. [b] The previous value in Narita et al. (2010b) is turned out to be false, and here we present the corrected value. [c] 4.18 s (unsaturated) × 24 images. [d] 180 s (saturated) × 3 images and 4.12 s (unsaturated) × 5 images. [e] 12 s (unsaturated) × 33 images. [f] 20 s (saturated) × 89 images and 1.5 s (unsaturated) × 20 images.

Table 4.2: Separation angles (SA) and position angles (PA) of candidate companions

UT Dates	Inst.	SA(East) ["]	PA(East) [°]	SA(West) ["]	PA(West) [°]	Ref.
2009Aug06	HiCIAO	3.875 ± 0.005	89.81 ± 0.30	3.139 ± 0.005	266.30 ± 0.37	Narita et al. (2010b)
2009Nov02	HiCIAO	3.861 ± 0.006	89.82 ± 0.08	3.137 ± 0.006	266.14 ± 0.09	this work
2011Aug12	IRCS	3.871 ± 0.006	89.68 ± 0.10	3.103 ± 0.011	266.23 ± 0.24	this work
2012Jul07	HiCIAO	3.860 ± 0.004	89.83 ± 0.05	3.095 ± 0.004	265.73 ± 0.08	this work

4.3   Observations and Results

For high-contrast direct imaging, we employed IRCS (for J, K, L' bands) and HiCIAO (for H band) with AO188 (Hayano et al., 2008) on the Subaru 8.2m telescope. Our observation logs (observing dates, instruments, filters, exposure times) and properties of the candidate companions are summarized in Tables 4.1 and 4.2. Magnitudes of the bright companion are derived by relative photometry with the host star using unsaturated images, and then magnitudes of the faint companion are similarly derived by relative photometry with the bright companion using saturated images. Figure 4.1 shows pictures of HAT-P-7 in different epochs and bands. Figure 4.2 plots time changes of positions of the candidate companions. Based on the Tycho-2 Catalogue (Høg et al., 2000), HAT-P-7 has a proper motion of -14.8 ± 1.5 mas/yr in right ascension (RA) and 8.7 ± 1.4 mas/yr in declination (Dec). From Figure 4.2, we find that the motion of the western (fainter) candidate is consistent with a background star ($\chi^2 = 4.3$ for a degree of freedom of 6), while the motion of the eastern (brighter) candidate is different from a background star ($\chi^2 = 83.0$ for a degree of freedom of 6) and consistent with a common proper motion with HAT-P-7.

In addition to the common proper motion, the spectral type of the eastern candidate supports a consistent distance with HAT-P-7, as follows. The distance to HAT-P-7 was estimated as 320^{+50}_{-40} pc by Pál et al. (2008), based on the Yonsei-Yale stellar evolution models (Yi et al., 2001) and SME (Spectroscopy Made Easy: Valenti and Piskunov (1996)) analysis. On the other hand, using the available colors (i', z', J, H, K), we confirm that the eastern companion is an M5.5V dwarf (see Figure 4.3). Based on the absolute magnitude of an M5.5V dwarf in H band (Kraus and Hillenbrand, 2007), we estimate a distance

modulus of ~ 6.15, which corresponds to ~ 300 pc. Thus the spectro-photometric distance to the eastern companion is in good agreement with the distance to HAT-P-7 from Earth.

We thus conclude that HAT-P-7 has a common proper motion stellar (M5.5V) companion at a projected separation of ~ 3.9 arcsec (1240^{+190}_{-160} AU). Note that assuming a random distribution for the companion orbit, the expected unprojected separation is $4/\pi$ times larger than the projected separation (see also table 6 of Dupuy and Liu 2011 for a conversion factor from the projected separation to the semi-major axis). Here we name the eastern companion as "HAT-P-7B" (hereafter, just "B").
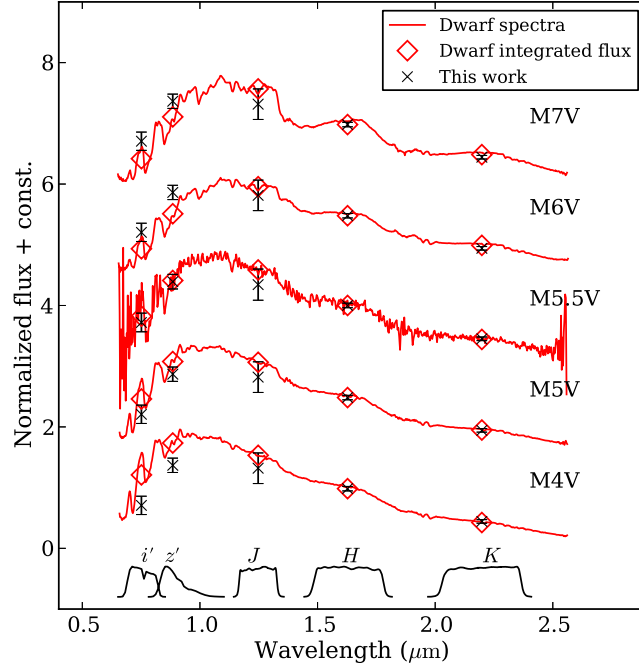
Figure 4.3: Comparisons of the observed colors with template spectra of known M4V-M7V dwarfs (Burgasser et al., 2004, 2008) taken with IRTF/SpeX. We find the M5.5V dwarf template gives a minimum χ^2.

4.4 Discussions

4.4.1 Further Evidence of the Third Companion

Winn et al. (2009) reported the possible existence of a third (different from HAT-P-7b and HAT-P-7B) companion from a long-term radial velocity (RV) trend observed with the Keck HIRES between 2007 and 2009. We confirm the long-term trend based on RVs measured with the Subaru HDS in 2008 and 2010 (the RVs are available upon request). Figure 4.4 shows the RVs taken with the Subaru HDS and residuals from the best-fit one-planet model with and without a long-term linear RV trend $\dot{\gamma}$ (see Narita et al. 2011, for the fitting procedure). We find $\dot{\gamma} = 20.3 \pm 1.8$ m s^{-1} yr^{-1}, which agrees well with Winn et al. (2009) ($\dot{\gamma} = 21.5 \pm 2.6$ m s^{-1} yr^{-1}). Note that "B" cannot explain the observed long-term RV trend.
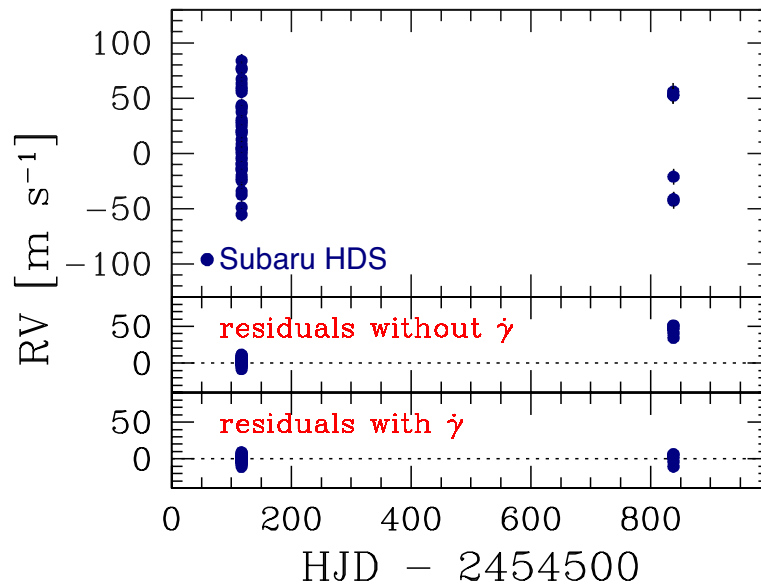
Figure 4.4: The panels illustrate the variations of position angles (top) and separation angles (bottom) of the both candidates over the course of three years. The solid trajectories show the variations expected from an assumption that the candidates are background stars: the dashed lines show the 1σ errors. Note that we add offsets to all the values for clarify. The dotted lines indicate the averages of observed separation angles and position angles for the east candidate. As shown in this figure, the east one is inconsistent with a background source, while the west object is in good agreement with the background hypothesis.

Thus we conclude that there is the third companion in this system. Here we name the long-term RV companion as "HAT-P-7c" (hereafter, just "c").

The trend corresponds to the mass constraint of "c" as,

$$M_c \sin i_c / a_c^2 \sim 0.12 \pm 0.01 \ M_{\text{Jup}} \ \text{AU}^{-2}. \tag{4.1}$$

The orbital period of "c" is presumably longer than 10 yr, since the trend is still approximately linear. Thus "c" is likely to be more massive than Jupiter. We do not detect "c" in high-contrast direct images, because it is too close to the host star.

4.4.2 Migration Mechanism of HAT-P-7b Revisited

Narita et al. (2010b) pointed out that HAT-P-7b (hereafter, just "b") cannot be migrated by Kozai mechanism caused by "B" in the presence of "c" in the system. However, they also pointed out that there is another possibility of "sequential" Kozai migration (see e.g., Takeda et al. 2008; Kita et al. 2010) in this system. Namely, an inclined outer stellar companion "B" causes Kozai mechanism for the outer "c" first, and then the inclined "c" induces Kozai mechanism for the inner "b". Such an initial inclined configuration can be formed by planet-planet scattering of "b" and "c" (and other possible undetected massive planets).

Recently, Albrecht et al. (2012) pointed out the interesting fact that the spin-orbit alignment timescale of HAT-P-7 due to the tidal effect is much shorter than the star's age (see figure 25 of Albrecht et al. 2012). Namely, the retrograde orbit of HAT-P-7b appears to be a strong outlier which should be aligned at the age of HAT-P-7. However, they did not consider the existence of the outer companions "B" and "c". Here we propose an alternative reason of the outlier: if Kozai oscillation of "b" caused by "c" had once happened, the tidal timescale for spin-orbit alignment can be much longer. Based on equation (1) and the timescale of Kozai oscillation as,

$$P_{\text{Kozai}} \sim \frac{M_s}{M_c} \frac{P_c^2}{P_b} (1 - e_c^2)^{3/2}, \tag{4.2}$$

where M_s is the host star's mass, M_c, P_c, and e_c are the mass, orbital period, and eccentricity of "c", and P_b is the orbital period of "b" (Wu et al., 2007), we estimate that the timescale of Kozai oscillation of "b" caused by "c" is comparable to the age of HAT-P-7 (2.14 ± 0.26 Gyr). Thus a possible slowly-changing orbital inclination due to Kozai oscillation might have prevented HAT-P-7b from achieving a spin-orbit alignment. We note that, however, the above discussion may be still optimistic, as Kozai oscillation is easily suppressed by other effects such as general relativity, tides, stellar distortion, or extra bodies (see e.g., Fabrycky and Tremaine 2007). At the current position of "b", the timescale of general relativity is indeed shorter than the timescale of Kozai oscillation of "b" caused by "c". This means Kozai oscillation does not extend the timescale of spin-orbit alignment any more, although it might have once happened. We thus note that we may still overlook other special conditions that inhibit the spin-orbit alignment in this system.

4.4.3 Suggestion to Further Discussions on Planetary Migration

Thus far, the existence of possible faint outer companions around planetary systems has not been checked and is often overlooked, even though Kozai migration models assume the presence of an outer companion. To further discuss planetary migration using the information of the RM effect / spot-crossing events

as well as significant orbital eccentricities, it is important to incorporate information regarding the possible or known existence of binary companions. This is also because a large fraction of the stars in the universe form binary systems (Ghez et al., 1993). Thus it would be important to check the presence of faint binary companions by high-contrast direct imaging. In addition, if any outer binary companion is found, it is also necessary to consider the possibility of sequential Kozai migration in the system, since planet-planet scattering, if it occurs, is likely to form the initial condition of such planetary migration.

4.5 Summary

We present evidence that HAT-P-7 has a common proper motion stellar companion by high-contrast direct imaging with Subaru HiCIAO and IRCS. The companion is located at ~ 3.9 arcsec to the east and estimated as an M5.5V star based on its colors. We also confirm the presence of the third companion HAT-P-7c by RV measurements with the Subaru HDS.

Our finding that HAT-P-7 is a wide binary system increase the potential that the sequential Kozai migration had once occured in this system. This scenario may be favorable to explain the discrepancy between the spin-orbit alignment timescale for HAT-P-7b and the stellar age noted by Albrecht et al. (2012).

In recent years, a number of RM and spot-crossing observations have provided useful information on the spin-orbit (mis)alignment, which is an important clue to understand the variety of planetary migration mechanisms. The same holds for eccentric planetary systems, since the eccentricity is another important clue to discuss planetary migration by few-body interactions. We thus propose that high-contrast direct imaging observations should be made for known planetary systems to check the presence of outer faint companions. Since the dependence of the spin-orbit (mis)alignment or significant eccentricity on the existence of outer companions is still unclear, it is important to conduct such observations to understand the entire picture of planetary migration.

Chapter 5

Observations of Eccentric or Tilted Exoplanet Host Stars

In this chapter, we present main results acquired with high-contrast direct imaging observations. All images are taken with HiCIAO on the Subaru telescope in the ADI mode, and reduced mainly with LOCI and partially with the classical ADI technique (see Chapter 3). Our samples are stars hosting eccentric planets or tilted planets (detection methods are written in §§2.1 and 2.2 in detail), which require planet migration mechanisms (see §1.2.2). Binary rates calculated from results shown in this chapter are discussed in the next chapter.

5.1 Chapter Introduction

Recently relation between planet holders and multiplicity induces strong concern for astronomers and more investigations are in progress. For example, Roell et al. (2012) reported that 57 exoplanet host stars have a stellar companion, corresponding to a rate of 12% of exoplanet host stars. However, it is lower than a multiplicity of Sun-like stars around the Sun of $46 \pm 2\%$ (Raghavan et al., 2010). Though stars in binary systems tend to be averted by planet search surveys because of avoiding contamination of the companions, the discrepancy may suggest difficulty of making planets in multiple systems, whereas some circumbinary planets have been discovered, like NN Ser (Beuermann et al., 2010) by measuring timing variations and Kepler-16 (AB) b (Doyle et al., 2011) by detecting dimmings and measuring their timing variations.

Although to explain how to form planets in multiple systems is an important work, another effect of a companion should also be unforgettable especially in planetary migration regions. So far, more than 800 exoplanets have been discovered, containing about 200 ones with significantly high eccentricity ($e > 0.5$) and more than 10 retrograde or polar orbit planets (e.g. Albrecht et al. 2012). Because such planets are not in consideration of standard planet formation scheme (e.g. core accretion model; Pollack et al. 1996), mainly two new models, named as planet-planet scattering and Kozai mechanism, have been proposed to interpret forming mechanisms (see also §1.2.2).

Planet-planet scattering (e.g. Nagasawa et al. 2008; Chatterjee et al. 2008) occurs in systems hosting more than two gaseous giant planets. Their orbits intersect by gravitational interactions with each other, and therefore, some planets fall onto host stars, while others are ejected from the planetary systems. The remains still orbits their host stars, but can have high eccentricities or high obliquities. The simulations reported the scattering happens at $\sim 10^6$ years from the commencement of the calculations. Kozai mechanisms (e.g. Fabrycky and Tremaine 2007; Wu et al. 2007) are induced by outer objects (e.g. outer

planets in the planetary systems or (sub)stellar companion objects physically related to the planet host stars) in highly mutually-inclined orbits. The outer objects have gravitational influences upon the inner planets and oscillate their inclinations and eccentricities on timescales written in Equation 1.15. Especially, HD 80606 is a surprising and important case for Kozai migration. Namely, it constitutes a binary system with HD 80607 ($M_{HD80606} = 1.0M_\odot$ and $M_{HD80607}/M_{HD80606} \sim 1$) and has a planet HD 80606b with an extremely high eccentricity ($e = 0.9330 \pm 0.0005$) and spin orbit misalignment ($\lambda = 42 \pm 8$ deg) (Hébrard et al., 2010). The system strongly suggests that eccentric and tilted planets can be formed through Kozai migration (Wu and Murray, 2003). Both the scattering and Kozai mechanism make significantly eccentric planets or inclined planets, but if their periastrons fully approach their host stars, tidal dissipation deprives the planets of orbital energy, reducing their semi-major axes (Fabrycky and Tremaine, 2007; Nagasawa et al., 2008). Although eccentric or tilted planets are considered to have experienced Kozai migration or planet-planet scattering, comprehensive and unbiased observations focusing on the migrations have not been carried out so far. Note that in this chapter we basically do not consider the Galactic perturbations proposed by Kaib et al. (2013), especially influencing a wide binary system with $a_* > 1000$ AU (HD 222582AB is relevant in our samples).

5.2 Methodology

The main goal of our researches is to reveal how eccentric planets and tilted planets form (more details of our samples are collected in §5.3 and 5.4; see also §1.3). Because examining planet-planet scattering is difficult due to its chaotic essence, we pay attention to testing Kozai migration, which requires additional objects in a system other than a host star and a planet. Deep observations can clarify the existence of the objects, resulting in the possibility of Kozai migration. In case any objects are discovered, we can calculate a Kozai timescale using Equation 1.15 and examine its possibility. In contrast, if no object are found, planet-planet scattering may have been occurred. In order not to include any biases, our samples were chosen with only two criteria; hosted planets with high eccentricities ($e \geq 0.7$) or tilted orbital axes ($|\lambda| > 0$ deg).

Hence, we operated the direct imaging method using a high-contrast near-infrared camera HiCIAO (Hodapp et al., 2008; Suzuki et al., 2010) and a 188 actuators adaptive optics system AO188 (Minowa et al., 2010) onboard the Subaru Telescope as part of the SEEDS project (Tamura, 2009). The direct imaging method is a powerful and successful technique designed for detecting very faint objects with extremely small separations (typically $\sim$ a few arcsecs) from bright objects. Although the method is employed generally for discovery of wide-separated exoplanets (e.g. Marois et al. 2008; Kuzuhara et al. 2013), we use it for not only undetected planets but also stellar or substellar objects around a star hosting a single eccentric planet or a tilted planet. Actually our team succeeded in detecting a Kozai source candidate around the inclined hot Jupiter system HAT-P-7 (Narita et al., 2010b, 2012) (see Chapter 4). Our observations are capable of depressing detection limits toward planetary mass objects and detecting an undiscovered object.

Detected objects are treated as companion candidates and to be examined with the common proper motion (CPM) test (see §3.3). The CPM test is a way of distinguishing a physically bound companion from a background object. Considering HiCIAO's pixel scale of 9.5 mas/pixel and a typical maximum error size of $\sim 1 - 2$ pixels, we performed follow-up observations after the first observations to satisfy Equation 3.4. We treated all companions which passed the confirmation tests and have shorter Kozai timescales compared to their systems' ages as real sources of Kozai mechanisms without examining whether they exactly satisfy $i > i_{crit} = 39.2°$ (Equation 1.14), where i is the mutual orbital inclination between a planet and a companion. This is because of the following reasons. The fundamental problem

is that we are not able to determine a companion's orbit with time interval of a few years. Secondly, it is plausible that planets in target systems have experienced Kozai migration, considering from the situation that one left planet in each system. Thirdly, if a distribution of the mutual inclination is isotropic, the probability of i satisfying Eq. 1.14 is large:

$$\text{Prob.} = \frac{360° - 2 \times 39.2°}{360°} = 0.78. \tag{5.1}$$

Finally we adopt statistically reduction to the observational results, and then investigate a companion host star rate of eccentric or tilted planetary systems. If the rates are significantly different from the global binary rate or the binary rate of planet host stars, the rates suggest that eccentricity or obliquity of planets and binary systems should have a mutual relation. If the rate is consistent, companions are less effective to planetary systems and therefore the influence of planet-planet scattering is large. The discussions based on our results are presented in the next chapter.

5.3 Eccentric Planets

We chose eight objects from significantly eccentric planetary systems which were discovered by the radial velocity (RV) method (see §2.1) and can be observed from Mauna Kea. Each of our samples has only one planet with high eccentricities ($e \geq 0.7$), which can be explained only by planet-planet scattering or Kozai migration.

Because only an adequate age stabilizes stellar photospheres and, therefore, enables us to detect a planet with the RV method. Consequently, ages of our samples result in $\sim$ Gyr. Although the age also helps tidal forces to afford an eccentric orbit to be circulated on a timescale of

$$\tau_{\text{cir}} = \frac{4Q_p}{63} \left(\frac{a^3}{GM_*} \right)^{1/2} \frac{m_p}{M*} \left(\frac{a}{R_p} \right)^5 (1-e^2)^{13/2} [F(e^2)]^{-1}, \tag{5.2}$$

where Q_p, a, G, M_*, m_p, R_p, e, and F are the tidal quality factor, the planet's orbital semi-major axis, the gravitational constant, the host star's mass, the planet's mass, the planet's radius, the planet's orbital eccentricity and the correction function (Adams and Laughlin, 2006), the timescales for our samples with adequate values are estimated to be larger than their ages, suggesting that tidal circulations would not work. Meanwhile, though planet-planet scattering can explain the high eccentricity, not in single planetary systems but in multiple planetary systems. Because our eccentric samples have not been reported to have secondary planets yet, the scattering could not occur. Moreover, disk interaction with planets cannot excite planetary eccentricity up to 0.2 (D'Angelo et al., 2006). Hence, Kozai mechanism seems to be the best solution to the high eccentricities. While all samples are summarized in Table 5.1 and their planetary properties collected in Table 5.4, each target is explained in detail in this section. Unless otherwise noted, the observed masses $m_p \sin i$ are regarded as true planetary masses m_p, i.e. $i = 90°$, for simpleness.

5.3.1 HD 8673

HD 8673 (HIP 6702) is an F-type main-sequence star located at $01^\text{h}26^\text{m}08\overset{\text{s}}{.}786$, $+34°34'46\overset{''}{.}92$ and has magnitudes of $V = 6.31$, $R = 6.06$ (NOMAD) and $H = 5.22$ (2MASS). Its mass and age have not determined precisely yet; Nordström et al. (2004) estimated its age of 2.5 ± 0.4 Gyr and mass of $1.28^{+0.05}_{-0.04}M_\odot$, while other studies showed different values, for example $1.5^{+0.6}_{-0.9}$ Gyr and $1.36 \pm 0.20M_\odot$

(Valenti and Fischer, 2005), and 2.52 ± 0.24 Gyr and $1.312^{+0.024}_{-0.020} M_\odot$ (Takeda et al., 2007). The metallicity [Fe/H] also varies from -0.12 (Ibukiyama and Arimoto, 2002) to 0.16 (Cayrel de Strobel et al., 2001). The distance from Earth can be derived from the *Hipparcos* parallax (Perryman et al., 1997), 26.14 ± 0.79 mas, converted into $d = 38.3 \pm 1.2$ pc. The distance gives a high proper motion of $(\mu_\alpha \cos \delta, \mu_\delta) = (237.19 \pm 0.33, -84.64 \pm 0.25)$ mas/yr (van Leeuwen, 2007), enabling us to carry out CPM test with a short time interval. The most remarkable characteristics are, if anything, about its planet. Its eccentric ($e = 0.723 \pm 0.016$) and long-periodic ($P = 1634 \pm 17$ days) planet has a mass of $m_p \sin i = 14.2 \pm 1.6 M_J$, possibly exceeding the deuterium burning limit of $\sim 13 M_J$ (Hartmann et al., 2010). The planet on the boundary may be an important clue to reveal difference between a planet and a (sub)stellar object. Mason et al. (2011) reported a bright ($\Delta V = 2.3 \pm 0.5$) companion candidate positioned at $(\rho, \theta) = (0.''087, 257.°3)$ in January 2001 and $(0.''109, 78.°3)$ in August 2007 with speckle observations. If the object is assumed to have its orbital inclination $i = 1.°02$ and its spectral type of K2V, derived from $\Delta V = 2.3$, Mason et al. (2011) discussed that it is possible to explain both and the period of 1634 days and the observed mass of $m_p \sin i = 14.2 M_J$ (Hartmann et al., 2010).

5.3.2   HD 22781

HD 22781 (HIP 17187) is a K0 star with magnitudes of $V = 8.77$ (Tycho-2), $R = 8.45$ (UCAC3), and $H = 6.69$ (2MASS). The star has coordinates of $03^h 40^m 49.^s526$, $+31°49'34.''66$ and a distance of 31.8 ± 1.4 pc from the *Hipparcos* parallax. Its proper motion is moderately high ($(\mu_\alpha \cos \delta, \mu_\delta) = (41.46 \pm 1.28, -91.99 \pm 1.11)$ mas/yr; van Leeuwen 2007), its metallicity is measured to be [Fe/H] $= -0.37 \pm 0.12$, and an age of the star has a wide range (0.6-8.9 Gyr) (Díaz et al., 2012). Its mass is relatively light ($0.75 \pm 0.03 M_\odot$), in contrast to its planet's mass of $m_p \sin i = 13.65 \pm 0.97 M_J$ (Díaz et al., 2012), which is also nearly over the deuterium burning limit. The mass is similar to that of HD 8673b, and additionally, the period of HD 22781b (528.07 ± 0.14 days) is also longer than hot Jupiters. The orbital eccentricity of the planet is over 0.8 (0.8191 ± 0.0023; Díaz et al. 2012), which gives the seventh most eccentric one of all eccentricity-measured exoplanets and the most eccentric planets of our observed targets.

5.3.3   HD 30562

HD 30562 (HIP 22336) is an F8V type star with the nearest to Earth in our observed samples (26.5 ± 0.6 pc; *Hipparcos*), leading its bright magnitudes of $V = 5.77, R = 5.36$ (NOMAD), and $H = 4.57$ (2MASS), and its high proper motion ($(\mu_\alpha \cos \delta, \mu_\delta) = (311.04 \pm 0.33, -249.44 \pm 0.27)$ mas/yr; van Leeuwen 2007). The coordinates are $04^h 48^m 36.^s385$, $-05°40'26.''56$. Its mass, metallicity, and age are estimated to be $1.219 \pm 0.04 M_\odot$, [Fe/H] $= +0.243 \pm 0.04$, and 4.0 Gyr, respectively (Fischer et al., 2009). Because they did not show an error of its age, we independently estimate its age to be 7.7 ± 0.2 Gyr with employing a result of Canto Martins et al. (2011), who measured its chromospheric activity $\log R'_{HK} = -5.06 \pm 0.01$ (consistent with a value Fischer et al. 2009 derived, -5.064), and Equation 3.5. The eccentric ($e = 0.76 \pm 0.05$) planet orbiting HD 30562 has a period of 1157 ± 27 days and a mass of $m_p \sin i = 1.29 \pm 0.08 M_J$ (Fischer et al., 2009).

5.3.4   HD 86264

HD 86264 (HIP 48780) is an F7V star with magnitudes of $V = 7.41$ (Tycho-2), $R = 7.10$ (NOMAD) and $H = 6.34$ (2MASS) located at $09^h 56^m 57.^s839$, $-15°53'42.''43$. The distance from Earth (72.6 ± 4.3 pc; *Hipparcos*) is the second farthest target of our eccentric samples, which provides a not large proper motion, $(\mu_\alpha \cos \delta, \mu_\delta) = (-13.13 \pm 0.51, -65.74 \pm 0.52)$ mas/yr (van Leeuwen, 2007). The star has a

mass of $1.42 \pm 0.05 M_\odot$, a metallicity of $[Fe/H] = +0.202 \pm 0.04$, and an age of 2.24 Gyr (Fischer et al., 2009). In the same way as HD 30562, we obtain an estimated age of 2.3 Gyr with $\log R'_{HK} = -4.73$ (Fischer et al., 2009), which is consistent with a their estimated age. Fischer et al. (2009) reported that the star has a planet with the longest period in our all samples ($P = 1475 \pm 55$ days) and a mass of $m_p \sin i = 7.0 \pm 1.6 M_\odot$. They also mentioned a long term trend in its radial velocity of 0.005 m s^{-1}yr^{-1}.

5.3.5 HD 96167

HD 96167 (HIP 54195) is a star at $11^h05^m15\overset{s}{.}069$, $-10°17'28\overset{''}{.}69$, with magnitudes of $V = 8.08$, $R = 7.63$ (NOMAD), and $H = 6.62$ (2MASS). Addition to its brightness, high metallicity ($[Fe/H] = +0.34 \pm 0.06$; Peek et al. 2009) and the largest *Hipparcos* parallax distance (84 ± 9 pc) of the star reveal the host star's spectral type of G5 subgiant (3.8 ± 1.0 Gyr) with a mass of $1.3 M_\odot$. The discovery of an eccentric (0.71 ± 0.04) planet around the star was reported by Peek et al. (2009) as part of N2K consortium RV observations. They reported that the relatively massive planet ($m_p \sin i = 0.68 \pm 0.18$) moves in an orbit with a semi-major axis of $a_p = 1.3 \pm 0.07$ AU, suggesting an additional planet exists in outer regions of the system. The common proper motion of the system is not so large ($(\mu_\alpha \cos \delta, \mu_\delta) = (-49.69 \pm 0.83, -7.55 \pm 0.80)$ mas/yr; van Leeuwen (2007)) that it takes more than one year to check.

5.3.6 HD 98649

HD 98649 (HIP 55409) is a high proper motion star with a proper motion of $(\mu_\alpha \cos \delta, \mu_\delta) = (-199.28 \pm 0.57, -177.51 \pm 0.48)$ mas/yr, at a location of $11^h20^m51\overset{s}{.}769$, $-23°13'02\overset{''}{.}43$. A planet was discovered by Marmier et al. (2013), though first appeared in Mayor et al. (2011), around the Sun-like ($M_* = 1.00 \pm 0.03 M_\odot$) star with its spectral type of G4V. According to Marmier et al. (2013), the planet is massive ($m_p \sin i = 6.8 \pm 0.5 M_J$) and the most eccentric ($e = 0.85 \pm 0.05$) in our samples. Because the planet orbits the star with a separation of $a_p = 5.6 \pm 0.4$ AU, the period of the planet is so long ($P = 4951^{+607}_{-465}$ days). The star has brightness of $V = 7.99$ (Tycho-2), $R = 7.75$ (UCAC3), $H = 6.49$ (2MASS). Considering the properties, a fact that no other planets have been reported in this system is sufficiently surprising to us.

5.3.7 HD 156279

HD 156279 (HIP 84171) is a G6 (Díaz et al. 2012, K0 in the SIMBAD database) type star at $17^h12^m23\overset{s}{.}204$, $+63°21'07\overset{''}{.}54$. The star has a short distance of 35.4 ± 0.8 pc, leading a high proper motion of $(\mu_\alpha \cos \delta, \mu_\delta) = (-1.21 \pm 0.41, 161.21 \pm 0.58)$ mas/yr (van Leeuwen, 2007) and magnitudes of $V = 8.08$ (Tycho-2), $R = 7.59$ (USNO-B) and $H = 6.35$ (2MASS). The mass, the metallicity and the age of the star are estimated to be $0.93 \pm 0.04 M_\odot$, $[Fe/H] = +0.14 \pm 0.01$ and 0.4-7.7 Gyr (Díaz et al., 2012), respectively. They reported that a planet around the star has the shortest period of our eccentric samples, 131.05 ± 0.54 days, resulting in a semi-major axis of $a_p = 0.495 \pm 0.017$ AU. They also showed that its mass is large, $m_p \sin i = 9.71 \pm 0.66 M_J$, for an inner planet than the speculated snow line position.

5.3.8 HD 222582

HD 222582 (HIP 116906) is a G5V star which was discovered in 2000 as a planet host star (Vogt et al., 2000) with magnitudes of $V = 7.69$ (Tycho-2), $R = 7.29$ (NOMAD) and $H = 6.24$ (2MASS). The star is located at $23^h41^m51\overset{s}{.}530$, $-05°59'08\overset{''}{.}73$ with a proper motion of $(\mu_\alpha \cos \delta, \mu_\delta) = (-144.88 \pm 0.88, -111.93 \pm 0.56)$ mas/yr (van Leeuwen, 2007). The *Hipparcos* distance, the metallicity, the mass

are 41.9 ± 2.0 pc, $[Fe/H] = -0.029 \pm 0.03$ (Valenti and Fischer, 2005), and $M_* = 0.965 \pm 0.02 M_\odot$ (Takeda et al., 2007), respectively. The age of this star has not been determined precisely and Saffe et al. (2005) announced various values: 6.16 Gyr with the Donahue (1993) model, 3.38 Gyr with the Rocha-Pinto and Maciel (1998) model, 11.1 Gyr with an isochrone, and 5.3 Gyr with the [Fe/H] value, whereas Bryden et al. (2009) treated it as 7.2 Gyr. The star is thought to be a member of a double star LDS 5112 and have an M3.5 companion named as HD 222582B separated by $\sim 110''$ (Mason et al., 2001), though Mason et al. (2011) reported it has no additional component in the inner regions based on the speckle observations. The main star also has a planet with a mass of $m_p \sin i = 7.63 \pm 0.35 M_J$ (Butler et al., 2006), a period of 572.38 ± 0.61 days, and an eccentricity of 0.725 ± 0.012. Moreover, the star was observed with *Spitzer* to investigate a debris disk around the star, and Bryden et al. (2009) showed that its observed flux F_ν at 70μm marginally exceeded its expected stellar flux of the star $F_{\nu,*}$ at 70μm, i.e. $(F_{70} - F_{70,*})/\sigma_{70} = 2.6$, while the observed flux at 24μm (F_{24}) was photospheric, i.e. $F_{24}/F_{24,*} = 1.0$. The observational results possibly suggest the existence of cool dust.

5.4 Tilted Planets

We chose fifteen objects from planetary systems with tilted orbital axes against stellar spin axes ($|\lambda| > 0$ deg). The tilted samples have been observed with both the RV method and the transit method. The planets are hot Jupiters with low or zero eccentricities due to the circularization (Equation 5.2) and their planetary masses are well determined. The obliquities of orbital axes were decided by the Rossiter-McLaughlin effect (see §2.2), and the values of their obliquities are collected in Albrecht et al. (2012) except for HAT-P-17b (its λ was measured by Fulton et al. 2013). The orbital axes are thought to have been inclined by planet-planet scattering or Kozai effects as well as the eccentric planets. Because the scattering cannot be ruled out with the present observational techniques similarly to the eccentric samples, the possibilities of Kozai effects were examined with the existence of candidate companions. The companions were not able to be tested with common proper motions because the targets typically have small proper motions except for some systems. Hence, in that case, we discuss their boundship with their colors, for example $H - Ks$, if we obtained magnitudes at both H and other wavelengths.

Recently Winn et al. (2010a) pointed out that the obliquities are related with the stellar effective temperatures. Namely, tilted planets tend to orbit hot stars with $T_{eff} \gtrsim 6250$ K, while cool stars with $T_{eff} \lesssim 6250$ K apt to have aligned planets. Though the reason has not been elucidated, some have been devised, one of which is explained by the stellar masses. Massive stars are more likely to have many massive planets, which may be in unstable states to evoke planet-planet scattering, than cool stars. Another possibility is explained by the convection zones. The zones, which are more developed in cooler stars than in hot stars, are easier to dissipate planetary orbital energy through tides. Therefore, cooler stars are thought to have aligned planets. However, some planets hosted by cool stars have high obliquities, suggesting unknown objects excite their obliquities through Kozai effects. In these cases, causes of the obliquity are not unclear and it is important to survey the tilted planetary systems. If binary rates for stars hosting tilted planets are different from global binary rates for all stars with planets, i.e. Kozai mechanisms are likely to occur, it may be able to constrain the mystery of the relationship between the temperature and the obliquity.

We do not show the results of HAT-P-7 in this chapter because shown in the previous chapter, but we include the system in discussion in the next chapter.

Table 5.1: Stellar Properties of Targets with Eccentric Planets

Name	HD 8673	HD 22781	HD 30562	HD 86264	Ref.
α (J2000.0)	01 26 08.786	03 40 49.526	04 48 36.385	09 56 57.839	
δ (J2000.0)	+34 34 46.92	+31 49 34.66	−05 40 26.56	−15 53 42.43	
SpT	F7	K0	F8	F7	
Dist. (pc)	38.3 ± 1.2	31.8 ± 1.4	26.5 ± 0.6	72.6 ± 4.3	1
$\mu_\alpha \cos\delta$ (mas/yr)	237.19 ± 0.33	41.46 ± 1.28	311.04 ± 0.33	-13.13 ± 0.51	2
μ_δ (mas/yr)	-84.64 ± 0.25	-91.99 ± 1.11	-249.44 ± 0.27	-65.74 ± 0.52	2
V (mag)	6.31	8.77	5.77	7.41	3
R (mag)	6.06	8.45	5.36	7.10	4
J (mag)	5.44	7.15	4.98	6.51	5
H (mag)	5.22	6.69	4.57	6.34	5
Ks (mag)	5.17	6.61	4.31	6.22	5
M_* ($M_\odot$)	$1.28^{+0.05}_{-0.04}$	0.75 ± 0.03	1.219 ± 0.04	1.42 ± 0.05	6,7,8
[Fe/H] (dex)	$+0.02 \pm 0.14$	-0.37 ± 0.12	$+0.243 \pm 0.04$	$+0.202 \pm 0.04$	7,8,9
$\log g$ (cm s^{-2})	4.35 ± 0.15	4.60 ± 0.02	4.09 ± 0.10	4.02 ± 0.10	7,8,9
T_{eff} (K)	6361 ± 45	5027 ± 50	5861 ± 44	6210 ± 44	7,8,9
Age (Gyr)	2.5 ± 0.4	[0.6-8.9]	4.0	2.24	6,7,8

Name	HD 96167	HD 98649	HD 156279	HD 222582	Ref.
α (J2000.0)	11 05 15.069	11 20 51.769	17 12 23.204	23 41 51.530	
δ (J2000.0)	−10 17 28.69	−23 13 02.43	+63 21 07.54	−05 59 08.73	
SpT	G5	G4	G6/K0	G5	
Dist. (pc)	84 ± 9	41.5 ± 1.4	35.4 ± 0.8	41.9 ± 2.0	1
$\mu_\alpha \cos\delta$ (mas/yr)	-49.69 ± 0.83	-199.28 ± 0.57	-1.21 ± 0.41	-144.88 ± 0.88	2
μ_δ (mas/yr)	-7.55 ± 0.80	-177.51 ± 0.48	161.21 ± 0.58	-111.93 ± 0.56	2
V (mag)	8.08	7.99	8.08	7.69	3
R (mag)	7.63	7.75	7.59	7.29	4
J (mag)	6.93	6.81	6.68	6.52	5
H (mag)	6.62	6.49	6.35	6.24	5
Ks (mag)	6.55	6.42	6.27	6.17	5
M_* ($M_\odot$)	1.31 ± 0.09	1.0 ± 0.03	0.93 ± 0.04	0.965 ± 0.02	7,10,11,12
[Fe/H] (dex)	$+0.34 \pm 0.06$	$+0.02 \pm 0.03$	$+0.14 \pm 0.01$	-0.029 ± 0.03	7,8,10,11
$\log g$ (cm s^{-2})	4.0 ± 0.2	4.38 ± 0.08	4.46 ± 0.03	4.342 ± 0.06	7,8,10,11
T_{eff} (K)	5770 ± 70	5759 ± 35	5453 ± 40	5727 ± 44	7,8,10,11
Age (Gyr)	3.8 ± 1.0	2.3 ± 2.0	[0.4-7.7]	[3.4-11.1]	7,10,11,13

References: (1) *Hipparcos* (Perryman et al., 1997), (2) van Leeuwen (2007), (3) Tycho-2 (Høg et al., 2000), (4) NOMAD (Zacharias et al., 2004), (5) 2MASS (Skrutskie et al., 2006), (6) Nordström et al. (2004), (7) Díaz et al. (2012), (8) Fischer et al. (2009), (9) Hartmann et al. (2010), (10) Peek et al. (2009), (11) Marmier et al. (2013), (12) Takeda et al. (2007), (13) Saffe et al. (2005)

Table 5.2: Properties of Eccentric Planets

Name	HD 8673b[1]	HD 22781b[2]	HD 30562b[3]	HD 86264b[3]
$m_p \sin i$ (M_J)	14.2 ± 1.6	13.65 ± 0.97	1.29 ± 0.08	7.0 ± 1.6
P (days)	1634 ± 17	528.07 ± 0.14	1157 ± 27	1475 ± 55
a (AU)	3.02 ± 0.15	1.167 ± 0.039	2.3 ± 0.02	2.86 ± 0.07
e	0.723 ± 0.016	0.8191 ± 0.0023	0.76 ± 0.05	0.7 ± 0.2
ω (deg)	323.4 ± 3.5	315.92 ± 0.56	81 ± 10	306 ± 10
T_{peri} (JD-2450000)	4420.5 ± 7.9	$4881.40 \pm 0.12^*$	131.5 ± 14	5172 ± 114

Name	HD 96167b[4]	HD 98649b[5]	HD 156279b[2]	HD 222582b[6]
$m_p \sin i$ (M_J)	0.68 ± 0.18	7.63 ± 0.35	9.71 ± 0.66	7.63 ± 0.35
P (days)	498.9 ± 1.0	4951^{+607}_{-465}	131.05 ± 0.54	572.38 ± 0.61
a (AU)	1.3 ± 0.07	5.6 ± 0.4	0.495 ± 0.017	1.337 ± 0.022
e	0.71 ± 0.04	0.85 ± 0.05	0.708 ± 0.018	0.725 ± 0.012
ω (deg)	285 ± 7	248 ± 9	264.2 ± 1.7	319.0
T_{peri} (JD-2450000)	3057 ± 5	271 ± 22	$5525.59 \pm 0.18^*$	706.7 ± 3

References: *: Days in BJD, not in JD. (1) Hartmann et al. (2010), (2) Díaz et al. (2012), (3) Fischer et al. (2009), (4) Peek et al. (2009), (5) Marmier et al. (2013), (6) Butler et al. (2006)

5.4.1   HAT-P-6

HAT-P-6b is a retrograde ($\lambda = 165 \pm 6$ deg; Albrecht et al. 2012) planet, discovered by Noyes et al. (2008) as part of the HATNet project (Bakos et al., 2002, 2004). The host star is located at $23^h39^m05\overset{s}{.}806$, $+42°27'57\overset{''}{.}51$ (J2000, for all coordinates in this section) and a late F-type star with an effective temperature of 6570 ± 80 K. The planet is a typical but inflated hot Jupiter with a density of 0.558 ± 0.047 g cm^{-3} and likely to have no or small thermal inversion (Todorov et al., 2012). Adams et al. (2013) operated direct imaging at *Ks* band and exclude any objects within $4''$ from the target star.

5.4.2   HAT-P-11

HAT-P-11 has a unique target with a high proper motion of $(\mu_\alpha \cos \delta, \mu_\delta) = (127.20 \pm 0.83, 231.23 \pm 0.80)$ mas/yr (van Leeuwen, 2007) in the tilted targets, enabling us to examine the common proper motion (CPM) test easily. The host star is mapped at $19^h50^m50\overset{s}{.}248$, $+48°04'51\overset{''}{.}09$ and is a K4-type star with an effective temperature of 4780 ± 50 K (Bakos et al., 2010). However, in spite of the low temperature, the projected obliquity of the planetary orbital axis is $\lambda = 103^{+26}_{-10}$ deg (Winn et al., 2010b). It leads to be an evident outlier in Figure 20 of Albrecht et al. (2012). Moreover, Sanchis-Ojeda and Winn (2011) showed results of sunspot crossing events and presented a true obliquity $\psi = 97$ or 106 deg. The planet has a high eccentricity of $e = 0.198 \pm 0.0046$ (Bakos et al., 2010) regardless of its orbital period of 4.887 days, suggesting some gravitational effects affect the planet.

5.4.3   HAT-P-14

HAT-P-14b is a retrograde ($\lambda = -170.9 \pm 5.1$ deg; Winn et al. 2011) planet, announced by Torres et al. (2010). The host star is laid at $17^h20^m27\overset{s}{.}874$, $+38°14'31\overset{''}{.}94$ and has a spectral type of F. The planet

has a significant eccentricity of 0.107 ± 0.013 (Torres et al., 2010), suggesting a gravitational effect has been affected. Since the effective temperature of the star is 6600 ± 90 K, the system agrees with the temperature-projected obliquity trend.

5.4.4 HAT-P-17

HAT-P-17b is a planet orbiting a K dwarf, discovered by Howard et al. (2012) in addition to an additional planet HAT-P-17c. The system has coordinates of $21^{\mathrm{h}}38^{\mathrm{m}}08\overset{\mathrm{s}}{.}732$, $+30°29'19\overset{''}{.}42$ and considerably large proper motion of $(\mu_\alpha \cos\delta, \mu_\delta) = (-76.8 \pm 1.6, -124.8 \pm 1.5)$ mas/yr (Høg et al., 2000). The planet b has a quiet projected obliquity of $\lambda = 19^{+14}_{-16}$ deg (Fulton et al., 2013), which possibly indicates an aligned planet. However, b has a significantly high eccentricity of 0.342 ± 0.006. In contrast with b's orbital period of 10.34 days, c has an extremely long period of 1610 ± 20 days (Howard et al., 2012) or 5584^{+7770}_{-2100} days (Fulton et al., 2013). Based on the arrangement of the two planets, it is likely to support planet-planet scattering for a cause of the obliquity and the eccentricity. Adams et al. (2013) ruled out any companion candidates around HAT-P-17.

5.4.5 HAT-P-30

HAT-P-30b/WASP-51b (hereafter HAT-P-30b) was independently discovered by HAT (Johnson et al., 2011) and WASP (Enoch et al., 2011), and is located at $08^{\mathrm{h}}15^{\mathrm{m}}47\overset{\mathrm{s}}{.}976$, $+05°50'12\overset{''}{.}39$. It has a planet with a projected obliquity of $\lambda = 73.5 \pm 9.0$ deg and orbiting an F-type star with an effective temperature of 6304 ± 88 K (Johnson et al., 2011) or 6250 ± 100 K (Enoch et al., 2011), on the 6250 K transition border. Adams et al. (2013) reported a companion candidate with a separation of $3\overset{''}{.}74$ and a relative magnitude of $\Delta Ks = 2.92$, though their survey was operated only at *Ks* band. They also mentioned that a companion which was announced by Enoch et al. (2011) and had a separation of $1\overset{''}{.}5$ was not detected at *Ks* band.

5.4.6 HAT-P-32

HAT-P-32b was discovered by Hartman et al. (2011), and is an extremely inflated hot Jupiter with a density of 0.14 g cm^{-3}. HAT-P-32 is an F- or G-type star at $02^{\mathrm{h}}04^{\mathrm{m}}10\overset{\mathrm{s}}{.}278$, $+46°41'16\overset{''}{.}21$. HAT-P-32b has a nearly polar orbit of $\lambda = 85 \pm 1.5$ deg (Albrecht et al., 2012) in spite of the stellar effective temperature of 6001 ± 88 K, suggesting an additional object. Recently Gibson et al. (2013) reported the planet has a featureless atmosphere with optical transmission spectroscopy, possibly caused by clouds. Adams et al. (2013) discovered a faint object separated by $2\overset{''}{.}87$ with a magnitude difference of $\Delta Ks = 3.38$.

5.4.7 TrES-4

TrES-4 is an F-type star with a long distance of 479 ± 26 pc (Chan et al., 2011) from Earth and located at $17^{\mathrm{h}}53^{\mathrm{m}}13\overset{\mathrm{s}}{.}058$, $+37°12'42\overset{''}{.}36$, which hosts a planet TrES-4b. The planet b was first announced by Mandushev et al. (2007), and the detailed characteristics were determined and updated by Sozzetti et al. (2009) and Chan et al. (2011), respectively. It has a small obliquity of $\lambda = 6.3 \pm 4.7$ deg (Narita et al., 2010c) and the host star has a temperature on the border (6200 ± 75 K; Chan et al. 2011). Bergfors et al. (2013) confirmed that the star has a physical companion, originally discovered by Daemgen et al.

(2009), separated by $1''55$ with an estimated spectral type of from K4.5V to M1.5V. Though the spin-orbit obliquity, λ, is small, the stellar spin axis is significantly inclined toward a line of sight (Schlaufman, 2010).

5.4.8   WASP-8

WASP-8b is a retrograde ($\lambda = -123^{+3.4}_{-4.4}$ deg) and eccentric ($e = 0.31$) planet, discovered by Queloz et al. (2010). The system has an adequate proper motion of $(\mu_\alpha \cos\delta, \mu_\delta) = (110.2 \pm 1.4, 7.7 \pm 1.4)$ mas/yr (Høg et al., 2000) with its coordinates of $23^h59^m36\overset{s}{.}068$, $-35°01'52''86$. The planet orbits a G8-type star with an effective temperature of 5600 ± 80 K, and therefore, the planet is an outlier in Figure 20 of Albrecht et al. (2012). Queloz et al. (2010) also reported a companion candidate B separated by $4''$ and decided that it is physically associated comparing with the Washington Visual Double Star Catalog (Mason et al., 2001). It is likely that B has caused Kozai effects on the planet b.

5.4.9   WASP-12

WASP-12b is a bloated (0.340 ± 0.0039 g cm^{-3}) hot Jupiter with a mass of $1.403 \pm 0.099 M_J$ at $06^h30^m32\overset{s}{.}794$, $+29°40'20''29$. The discovery was curried out by Hebb et al. (2009) and its parameters were updated by Chan et al. (2011). The stellar effective temperature of 6300 ± 150 K is on the 6250 K transition border. The planet has an extremely high equilibrium temperature of $T_{eq} = 2516 \pm 36$ K (Hebb et al., 2009) due to its short period of 1.091 days. An additional planet may be present in this system possibly detected by TTVs (Maciejewski et al., 2013), being a counterpart of planet-planet scattering. Some molecules in b's atmosphere have been discussed with data by transmission spectroscopy (e.g. Stevenson et al. 2013) and secondary eclipses were detected by Croll et al. (2011). Bergfors et al. (2013) pointed out an elongated companion candidate separated by $1''04$, and Bechter et al. (2013) confirmed that the object is a close double star with estimated spectral types of M3V.

5.4.10   WASP-14

WASP-14b, orbiting WASP-14 at $14^h33^m06\overset{s}{.}355$, $+21°53'40''98$, is significantly massive ($m_p = 7.341^{+0.508}_{-0.496} M_J$) hot Jupiter with a period of 2.244 days, leading to an extremely high density of $3.501^{+0.636}_{-0.495}$ g cm^{-3}, discovered by Joshi et al. (2009). It also has a tilted ($\lambda = -33.1 \pm 7.4$ deg; Johnson et al. 2009) orbit, and an effective temperature of the host star is 6475 ± 100 K, supporting the T_{eff}-λ relationship. The eccentricity is finite (0.091 ± 0.003), not zero, also suggesting planetary migration.

5.4.11   WASP-15

WASP-15b is a bloated planet ($\rho_p = 0.247 \pm 0.035$ g cm^{-3}) hosted by an F7-type star WASP-15, located at $13^h55^m42\overset{s}{.}705$, $-32°09'34''66$ and was originally reported by West et al. (2009). After the discovery, Triaud et al. (2010) and recently Southworth et al. (2013) updated the stellar and the planetary parameters. Triaud et al. (2010) also measured the Rossiter-McLaughlin effect of WASP-15b and decided it as a retrograde planet ($\lambda = -139.6^{+4.3}_{-5.2}$ deg). Considering that the main star is beyond the 6250 K border ($T_{eff} = 6405 \pm 80$; Doyle et al. 2013), it agrees with the T_{eff}-λ trend. Bergfors et al. (2013) observed this system with the lucky imaging method, but failed to detect any objects around the system.

5.4.12 WASP-17

WASP-17b, discovered by Anderson et al. (2010), is an extremely low density planet ($\rho_p = 0.0819 \pm 0.0106$ g cm^{-3}) orbiting an F4-type star WASP-17 at $15^h59^m50^s947$, $-28°03'42''33$. The low density tempts people into investigating the planetary atmosphere, and thus it became known that the planet b has sodium in its air (e.g. Wood et al. 2011; Bento et al. 2013). Additionally, Anderson et al. (2011) were able to detect thermal emission from the planet using the *Spitzer* telescope. The projected obliquity of the planet of $\lambda = -148.7^{+7.7}_{-6.7}$ deg indicates the planet as a retrograde one and the host star has a high temperature of 6650 ± 80 K (Anderson et al., 2011).

5.4.13 WASP-33

WASP-33b was discovered by Christian et al. (2006) with the transit method and confirmed by Collier Cameron et al. (2010) with the RV method. The system has a retrograde orbit of $\lambda = -107.7 \pm 1.6$ deg (Collier Cameron et al., 2010) and is mapped at $02^h26^m51^s058$, $+37°33'01''73$. Because the host star is an A5-type star, a planetary mass is only constrained by an upper limit of $< 4.59M_J$ (Smith et al., 2011) and the planet has a significantly high effective temperature of 3290^{+66}_{-67} K (de Mooij et al., 2013) to be bright by its heat. The age of the system has not been determined yet. Moya et al. (2011) detected a companion candidate separated by $1''961$ in the near-infrared region. Its colors indicated a dwarf star or a brown dwarf, depending on the age of the system, if bound. Adams et al. (2013) also detected the object at *Ks* band.

5.4.14 XO-4

XO-4b was first reported in McCullough et al. (2008) discovered by the XO project (McCullough et al., 2005) and is orbiting an F5V star. XO-4 is located at $07^h21^m33^s166$, $+58°16'05''00$. The planet is a typical hot Jupiter with a mass of $1.72 \pm 0.20M_J$ and an orbital period with 4.125 days. The star's effective temperature is estimated to be 5700 K, under 6250 K, but the planet has a projected obliquity of $\lambda = -46.7^{+8.1}_{-6.1}$ deg (Narita et al., 2010a). Both Bergfors et al. (2013) and Adams et al. (2013) observed this planetary system in order to detect additional objects in the system, but they could not find any objects. No molecules have been reported in the planetary atmosphere, but a thermal inversion is likely to be present (Todorov et al., 2012).

5.5 Observations & Reduction

Our observations were carried out with HiCIAO/AO188 on the Subaru telescope. The observation logs are summarized in Table 5.5. All nights were clear and photometric. The observations were performed at first in the ADI mode Marois et al. (2006) at *H* band, but some targets were taken at different wavelengths to obtain colors in case that a target has any possible or known companion candidates. In this mode, HiCIAO has a 2048×2048 pixels plate with a field of view (FOV) of $20'' \times 20''$, resulting in a pixel scale of 9.5 mas/pixel. Observational schedules were determined to enlarge a rotation angle of the parallactic angle ($\Delta\pi$) during the observations. AO reference stars were the target stars themselves, because the targets are sufficiently bright at *R* band ($R \lesssim 13$ mag needed to perform). The coronagraphic mask (Lyot stop; Lyot 1939) was employed, but an occultation mask was not used since the mask occults completely within the mask's radius and it makes difficult to find the precise positions of the target stars. Instead of the usage of the mask, we adopted long exposures and made very close regions to the targets ($r \lesssim 0''1$) saturated to obtain more photons for finding faint objects at the outer regions. Apart from scientific

Table 5.3: Stellar Properties of Targets with Tilted Planets

Name	HAT-P-6	HAT-P-7	HAT-P-11	HAT-P-14	Ref.
α (J2000.0)	23 39 05.806	19 28 59.362	19 50 50.248	17 20 27.874	
δ (J2000.0)	+42 27 57.51	+47 58 10.26	+48 04 51.09	+38 14 31.94	
SpT	F	F6	K4	F	
Dist. (pc)	260 ± 20	320^{+50}_{-40}	38.0 ± 1.3	205 ± 11	1,2,3,4
$\mu_\alpha \cos\delta$ (mas/yr)	-19.5 ± 1.3	-14.8 ± 1.5	127.20 ± 0.83	-3.10 ± 1.70	5,6,7
μ_δ (mas/yr)	3.0 ± 1.2	8.7 ± 1.4	231.23 ± 0.80	-3.80 ± 1.60	5,6,7
V (mag)	10.52	8.77	9.47	9.99	5
R (mag)	10.23	8.45	8.76	9.75	8
J (mag)	9.56	9.56	7.61	9.09	9
H (mag)	9.44	9.34	7.13	8.93	9
Ks (mag)	9.31	9.33	7.01	8.85	9
M_* ($M_\odot$)	1.29 ± 0.06	$1.47^{+0.08}_{-0.05}$	$0.81^{+0.02}_{-0.03}$	1.386 ± 0.045	1,2,3,4
R_* ($R_\odot$)	1.46 ± 0.06	$1.84^{+0.23}_{-0.11}$	0.75 ± 0.02	1.468 ± 0.054	1,2,3,4
[Fe/H] (dex)	-0.13 ± 0.08	$+0.26 \pm 0.08$	$+0.31 \pm 0.05$	$+0.11 \pm 0.08$	1,2,3,4
$\log g$ (cm s^{-2})	4.22 ± 0.03	$4.07^{+0.04}_{-0.08}$	4.59 ± 0.03	4.25 ± 0.03	1,2,3,4
T_{eff} (K)	6570 ± 80	6350 ± 80	4780 ± 50	6600 ± 90	1,2,3,4
Age (Gyr)	$2.3^{+0.5}_{-0.7}$	2.2 ± 1.0	$6.5^{+5.9}_{-4.1}$	1.3 ± 0.4	1,2,3,4

Name	HAT-P-17	HAT-P-30	HAT-P-32	TrES-4	Ref.
α (J2000.0)	21 38 08.732	08 15 47.976	02 04 10.278	17 53 13.058	
δ (J2000.0)	+30 29 19.42	+05 50 12.39	+46 41 16.21	+37 12 42.36	
SpT	K	F	F/G	F8	
Dist. (pc)	90 ± 3	193 ± 8	320 ± 16	479 ± 26	10,11,12,13
$\mu_\alpha \cos\delta$ (mas/yr)	-76.8 ± 1.6	-15.2 ± 1.8	-12.3 ± 1.3	-8.1 ± 4.8	5,14
μ_δ (mas/yr)	-124.8 ± 1.5	23.4 ± 1.7	4.6 ± 2.4	-33.0 ± 4.4	5,14
V (mag)	10.38	10.35	11.44	11.59	5,15
R (mag)	7.63	9.98	11.24	11.69	8
J (mag)	9.02	9.44	10.25	10.58	9
H (mag)	8.62	9.22	10.02	10.35	9
Ks (mag)	8.54	9.15	9.99	10.33	9
M_* ($M_\odot$)	0.857 ± 0.039	1.242 ± 0.041	$1.176^{+0.043}_{-0.070}$	1.388 ± 0.042	10,11,12,13
R_* ($R_\odot$)	0.838 ± 0.021	1.215 ± 0.051	1.387 ± 0.067	1.798 ± 0.052	10,11,12,13
[Fe/H] (dex)	0.00 ± 0.08	$+0.13 \pm 0.08$	-0.16 ± 0.08	$+0.14 \pm 0.09$	10,11,12,13
$\log g$ (cm s^{-2})	4.52 ± 0.02	4.36 ± 0.03	4.22 ± 0.04	4.071 ± 0.024	10,11,12,13
T_{eff} (K)	5246 ± 80	6304 ± 88	6001 ± 88	6200 ± 75	10,11,12,13
Age (Gyr)	7.8 ± 3.3	$1.0^{+0.8}_{-0.5}$	$3.8^{+1.5}_{-0.5}$	2.9 ± 0.3	10,11,12,13

Table 5.3: Stellar Properties of Targets with Tilted Planets — *Continued.*

Name	WASP-8	WASP-12	WASP-14	WASP-15	Ref.
α (J2000.0)	23 59 36.068	06 30 32.794	14 33 06.355	13 55 42.705	
δ (J2000.0)	-35 01 52.86	$+29$ 40 20.29	$+21$ 53 40.98	-32 09 34.66	
SpT	G8	G0	F5	F7	
Dist. (pc)	87 ± 7	427 ± 90	160 ± 20	308	13,16,17,18
$\mu_\alpha \cos\delta$ (mas/yr)	110.2 ± 1.4	-0.7 ± 1.3	29.1 ± 0.9	5.5 ± 2.6	5,14
μ_δ (mas/yr)	7.7 ± 1.4	-7.8 ± 1.0	-5.3 ± 0.9	-23.2 ± 2.4	5,14
V (mag)	9.79	11.57	9.75	10.97	5
R (mag)	9.34	11.22	9.48	10.76	8
J (mag)	8.50	10.48	8.87	9.96	9
H (mag)	8.22	10.23	8.65	9.71	9
Ks (mag)	8.09	10.19	8.62	9.69	9
M_* $(M_\odot)$	1.04 ± 0.08	1.36 ± 0.14	$1.211^{+0.127}_{-0.122}$	1.23 ± 0.09	13,17,20
R_* $(R_\odot)$	1.05 ± 0.12	1.599 ± 0.071	$1.306^{+0.066}_{-0.073}$	1.15 ± 0.16	13,17,20
[Fe/H] (dex)	$+0.17 \pm 0.07$	0.30 ± 0.10	0.0 ± 0.2	-0.17 ± 0.11	13,16,17,19
$\log g$ (cm s^{-2})	4.5 ± 0.1	4.164 ± 0.029	$4.287^{+0.043}_{-0.038}$	4.169 ± 0.033	13,16,17,19
T_{eff} (K)	5560 ± 90	6300 ± 150	6475 ± 100	6405 ± 80	13,17,20
Age (Gyr)	[3-5]	1.7 ± 0.8	[0.5-1.0]	$3.9^{+2.8}_{-1.3}$	13,16,17,19

Name	WASP-17	WASP-33	XO-4		Ref.
α (J2000.0)	15 59 50.947	02 26 51.058	07 21 33.166		
δ (J2000.0)	-28 03 42.33	$+37$ 33 01.73	$+58$ 16 05.00		
SpT	F4	A5	F5		
Dist. (pc)	400 ± 60	116 ± 16	293 ± 19		21,22,23
$\mu_\alpha \cos\delta$ (mas/yr)	-7.9 ± 1.5	-1.26 ± 0.91	-15.30 ± 3.10		14
μ_δ (mas/yr)	-11.0 ± 1.5	-9.22 ± 0.61	-4.00 ± 1.80		14
V (mag)	11.59	8.14	10.81		5
R (mag)	11.47	8.15	10.62		8
J (mag)	10.51	7.58	9.67		9
H (mag)	10.32	7.52	9.48		9
Ks (mag)	10.22	7.47	9.41		9
M_* $(M_\odot)$	1.306 ± 0.026	1.512 ± 0.040	1.32 ± 0.02		21,22,23
R_* $(R_\odot)$	1.572 ± 0.056	$1.512^{+0.060}_{-0.054}$	1.56 ± 0.05		21,22,23
[Fe/H] (dex)	-0.19 ± 0.09	0.1 ± 0.2	-0.04 ± 0.03		21,22,23
$\log g$ (cm s^{-2})	4.161 ± 0.026	$4.258^{+0.027}_{-0.029}$	4.18 ± 0.07		21,22,23
T_{eff} (K)	6650 ± 80	7430 ± 100	6397 ± 70		21,22,23
Age (Gyr)	[1.4-2.9]	—	2.1 ± 0.6		23,24

References: (1) Noyes et al. (2008), (2) Pál et al. (2008), (3) Bakos et al. (2010) (4) Torres et al. (2010) (5) Tycho-2 (Høg et al., 2000), (6) van Leeuwen (2007), (7) Tycho (Høg et al., 1998), (8) NOMAD (Zacharias et al., 2004), (9) 2MASS (Skrutskie et al., 2006), (10) Howard et al. (2012), (11) Johnson et al. (2011), (12) Hartman et al. (2011), (13) Chan et al. (2011), (14) UCAC2 (Zacharias et al., 2003), (15) Mandushev et al. (2007), (16) Queloz et al. (2010), (17) Joshi et al. (2009), (18) exoplanet.eu (Schneider et al., 2011), (19) West et al. (2009), (20) Doyle et al. (2013), (21) Anderson et al. (2011), (22) Smith et al. (2011), (23) McCullough et al. (2008), (24) Collier Cameron et al. (2010)

Table 5.4: Properties of Tilted Planets

Name	HAT-P-6b[1]	HAT-P-7b[2]	HAT-P-11b[3]	HAT-P-14b[4]
m_p (M_J)	1.057 ± 0.119	$1.776^{+0.077}_{-0.049}$	0.081 ± 0.009	2.232 ± 0.059
R_p (R_J)	1.330 ± 0.061	$1.363^{+0.195}_{-0.087}$	0.422 ± 0.014	1.150 ± 0.052
ρ_p (g cm^{-3})	0.558 ± 0.047	$0.876^{+0.17}_{-0.24}$	1.33 ± 0.20	1.82 ± 0.24
P (days)	3.853	2.205	4.887	4.627
a (AU)	0.05235 ± 0.00087	0.0377 ± 0.0005	$0.0530^{+0.0002}_{-0.0008}$	0.0606 ± 0.0007
e	0	0	0.198 ± 0.046	0.107 ± 0.013
i (deg)	85.51 ± 0.35	$85.7^{+3.5}_{-3.1}$	88.5 ± 0.6	83.5 ± 0.3
ω (deg)	—	—	355.2 ± 17.3	94 ± 4
T_c (BJD-2450000)	4035.68[†]	3790.26	4605.89	4875.28
λ (deg)	165 ± 6	155 ± 37	103^{+26}_{-10}	-170.9 ± 5.1

Name	HAT-P-17b[5]	HAT-P-30b[7]	HAT-P-32b[8]	TrES-4b[9]
m_p (M_J)	0.534 ± 0.0018	0.711 ± 0.028	0.941 ± 0.166	0.917 ± 0.070
R_p (R_J)	1.010 ± 0.029	1.340 ± 0.065	2.037 ± 0.099	0.827 ± 0.055
ρ_p (g cm^{-3})	0.64 ± 0.05	0.37 ± 0.05	$0.14^{+0.03}_{-.02}$	1.29 ± 0.25
P (days)	10.34	2.811	2.150	3.554
a (AU)	0.0882 ± 0.0014	0.0419 ± 0.0005	$0.0344^{+0.0004}_{-0.0007}$	0.05084 ± 0.00050
e	0.342 ± 0.006	0.035 ± 0.024	0.163 ± 0.061	0
i (deg)	$89.2^{+0.2}_{-0.1}$	83.6 ± 0.4	88.7 ± 0.6	82.81 ± 0.37
ω (deg)	201 ± 1	252 ± 84	52 ± 29	—
T_c (BJD-2450000)	4801.17	5456.47	4416.15	4230.91[†]
λ (deg)	$19^{+14(6)}_{-16}$	73.5 ± 9.0	85 ± 1.5	6.3 ± 4.7

Table 5.4: Properties of Tilted Planets — *Continued.*

Name	WASP-8b[10]	WASP-12b[9]	WASP-14b[11]	WASP-15b[12]
m_p (M_J)	$2.244^{+0.079}_{-0.093}$	1.403 ± 0.099	$7.341^{+0.508}_{-0.496}$	0.592 ± 0.019
R_p (R_J)	$1.038^{+.007}_{-.047}$	1.732 ± 0.092	$1.281^{+0.075}_{-0.082}$	1.408 ± 0.046
ρ_p (g cm^{-3})	2.53 ± 0.22	0.340 ± 0.039	$3.501^{+0.636}_{-0.495}$	0.263 ± 0.024
P (days)	8.159	1.091	2.244	3.752
a (AU)	$0.0801^{+0.0014}_{-0.0016}$	0.02293 ± 0.00078	0.036 ± 0.001	0.05165 ± 0.00067
e	$0.3100^{+0.0029}_{-.0024}$	0	0.091 ± 0.003	0
i (deg)	$88.55^{+0.15}_{-0.17}$	86.2 ± 3.0	$84.32^{+0.67}_{-0.57}$	85.74 ± 0.38
ω (deg)	$274.27^{+0.17}_{-0.18}$	—	$253.37^{+0.69}_{-0.68}$	—
T_c (BJD-2450000)	4679.33	4508.98[†]	4463.58	4584.70
λ (deg)	$-123^{+3.4}_{-4.4}$	59^{+15}_{-20}	-33.1 ± 7.4	$-139.6^{+4.3}_{-5.2}$

Name	WASP-17b[13]	WASP-33b[14]	XO-4b[15]
m_p (M_J)	0.486 ± 0.032	< 4.59	1.78 ± 0.08
R_p (R_J)	1.991 ± 0.081	$1.501^{+0.073}_{-0.064}$	1.33 ± 0.05
ρ_p (g cm^{-3})	0.0819 ± 0.0106	—	0.90 ± 0.11
P (days)	3.735	1.220	4.125
a (AU)	0.05150 ± 0.00034	0.02565 ± 0.00023	0.0554 ± 0.002
e	$0.028^{+0.015}_{-0.018}$	0	0
i (deg)	$86.83^{+0.68}_{-0.56}$	$84.9^{+2.1}_{-1.7}$	88.8 ± 0.6
ω (deg)	$277.4^{+14.6}_{-2.6}$	—	—
T_c (BJD-2450000)	4577.86[†]	4590.18[†]	4485.93
λ (deg)	$-148.7^{+7.7}_{-6.7}$	-107.7 ± 1.6	$-46.7^{+8.1}_{-6.1}$

References: Data and references of λ are summarized in Albrecht et al. (2012) except for HAT-P-17 (or written in the main text). [†]: Dates in HJD, not in BJD. (1) Noyes et al. (2008), (2) Pál et al. (2008), (3) Bakos et al. (2010), (4) Torres et al. (2010), (5) Howard et al. (2012), (6) Fulton et al. (2013), (7) Johnson et al. (2011), (8) Hartman et al. (2011), (9) Chan et al. (2011), (10) Queloz et al. (2010), (11) Joshi et al. (2009), (12) Southworth et al. (2013), (13) Anderson et al. (2011), (14) Smith et al. (2011), (15) Narita et al. (2010a)

frames for finding the companion, we obtained reference frames with unsaturated target stars using short exposures and/or ND filters in order to measure full widths at half-maximum (FWHMs) and photometry for the target stars. The values of the FWHMs and the photometry were used for the LOCI reduction and relative photometry for detected companion candidates.

After flat fielding, we corrected distortions of the frames, which were precisely calibrated with stars in globular clusters. Next, we registered stars at the center of the frames and subtracted halos of the stars. After that, data sets were reduced with the LOCI pipeline (Lafrenière et al., 2007) for targets with a large field rotation (i.e. $\Delta\pi \gtrsim 10°$) to efficiently suppress speckle noises and spider noises or the classical ADI analysis (Marois et al., 2006) for targets with a small field rotation ($\Delta\pi \lesssim 10°$) to investigate inner regions, though we also combined deroted (i.e. parallactic angles corrected) frames into a frame in order to escape from the self-subtraction effects. The self-subtraction effects were corrected in the following procedure; 1) embed artificial signals into scientific frames in a radial pattern for each target, 2) operate LOCI or the classical analysis in the same manner as the scientific analysis, 3) measure photometry for each artificial signal, 4) obtain photometric ratios of the signals in the reduced frame to the raw artificial signals as a function of a separation (typically the ratios are less than 1.0), and 5) divide a value of photometry for a companion candidate by the ratio to correct the subtraction. Astrometric measurements and photometry were executed with IRAF `imexam` and `phot` and a magnitude of a companion candidate was derived from relative photometry to its host star. Targets taken in more than two epochs or with a published companion candidate were examined with the common proper motion (CPM) test to confirm whether it is a physical companion or a background star.

5.6   Results & Discussions of Individual Targets with Companion Candidates

We introduce our observational results. For targets with some companion candidates, we also discuss the possibility of Kozai migration of the planet. The targets without companions are shown in the following section. Each error in tables collecting their properties includes both a random error and a systematic error of 0.1% in a separation (Sep., ρ) and 0°03 in a position angle (PA, θ), induced mainly by distortion.

We summarize our results of detected companion candidates in Table 5.6 (around eccentric planet systems) and Table 5.7 (around tilted planet systems).

5.6.1   HD 8673

We discover one faint object (named as HD 8673 B) separated by only 0.″3 from the main star HD 8673. Although the object cannot easily be found in the LOCI image (Figure 5.1), the S/N map (Figure 5.2) clearly shows it surrounded by speckle noises. Our three observations (summarized in Table 5.8) have satisfactory time intervals to execute common proper motion (CPM) tests. The results, represented in Figure 5.5, sharply suggest that the companion candidate is co-moving. Hence, we assume that this object has the same distance as HD 8673 and estimate its projected separation to the main star to be $a_B = 11.07 \pm 0.05$ AU. Because the distance significantly exceeds the planet's semi-major axis of $a_b = 3.02 \pm 0.15$ AU (Hartmann et al., 2010), the companion B cannot be the planet b.

Next we compare B with the object reported by Mason et al. (2011). They discovered a faint companion around HD 8673 at $(\rho, \theta) = (0.″087, 257°3)$ (i.e. $(\Delta\alpha, \Delta\delta) = (-0.″085, -0.″019)$) on 2001.0193 and $(0.″109, 78°3)$ (i.e. $(0.″107, 0.″022)$) on 2007.6049. If the companion has a linear motion, they estimated positions of $(\rho, \theta) = (0.″266, 78°06)$ (i.e. $(\Delta\alpha, \Delta\delta) = (0.″260, 0.″055)$) on 6th November 2012 (2012.8474). In that case, the expected position is thoroughly different from our measurements. Thus we

Table 5.5: Observation Logs

Target	Date (UT)	Filter	FWHM ($''$)	ET (s)	Frames	Total ET (min)	$\Delta\pi$ (deg)
HD 8673	2011-09-04	*H*	0.083	1.5×3	57	4.28	17.9
	2012-09-13	*H*	0.070	1.5×2	175	8.75	31.0
	2012-11-06	*Ks*	0.079	1.5×2	209	10.5	14.8
HD 22781	2013-01-04	*H*	0.063	10×3	51	25.5	39.4
HD 30562	2013-01-03	*H*	0.070	10×3	69	34.5	29.3
HD 86264	2013-02-27	*H*	0.074	20×3	32	32.0	13.3
HD 96167	2011-03-15	*H*	0.059	20×1	52	17.3	17.1
	2012-02-28	*H*	0.063	20×1	107	35.7	16.6
HD 98649	2011-12-30	*H*	0.082	10×2	120	40.0	18.7
HD 156279	2012-07-09	*H*	0.077	5×2	122	20.3	13.2
	2013-05-20	*J*	0.058	10×1	34	5.67	3.15
	2013-05-20	*Ks*	0.072	5×1	35	2.92	3.73
HD 222582	2012-11-07	*H*	0.069	20×1	100	33.3	19.0
HAT-P-6	2011-08-02	*H*	0.056	20×1	34	11.3	10.2
HAT-P-11	2011-05-23	*H*	0.068	30×1	27	13.5	8.89
	2011-09-06	*H*	0.058	20×1	56	18.7	10.8
HAT-P-14	2011-05-21	*H*	0.060	10×1	14	2.33	3.38
	2011-05-21	*Ks*	0.072	20×1	6	2.0	2.39
HAT-P-17	2012-09-14	*H*	0.085	10×2	70	23.3	25.3
HAT-P-30	2012-01-02	*H*	0.067	10×1	28	4.67	1.71
HAT-P-32	2012-09-12	*H*	0.089	10×3	51	25.5	20.1
TrES-4	2011-05-21	*H*	0.068	5×1	20	1.67	4.75
	2011-05-21	*Ks*	0.077	10×1	20	3.33	4.78
WASP-8	2011-09-03	*H*	0.103	15×1	60	15.0	7.09
	2011-09-03	*Ks*	0.103	25×1	5	2.08	0.741
WASP-12	2012-11-07	*H*	0.077	15×1	79	19.8	35.6
	2012-11-07	*J*	0.107	7.5×1	10	1.25	1.75
	2012-11-07	*Ks*	0.078	5×1	10	0.833	1.28
WASP-14	2011-01-25	*H*	0.060	10×1	48	8.0	9.00
WASP-15	2011-05-25	*H*	0.073	60×1	23	23.0	7.64
WASP-17	2011-05-24	*H*	0.065	60×1	28	28.0	9.24
WASP-33	2010-12-01	*H*	0.092	20×1	33	11.0	18.9
XO-4	2011-11-16	*H*	0.074	20×1	59	19.7	10.8

Note: "ET" and "Total ET" stand for exposure time of each exposure times the number of coadd (i.e. exposure time of each frame), and total exposure time, respectively. $\Delta\pi$ is a parallactic angle rotation during each observation.

Table 5.6: Summary of Detected Companion Candidates around Eccentric Planet Systems

Name	Date (UT)	Filter	Sep. ($''$)	PA (deg)	Δm
HD 8673 B	2011-09-04*	*H*	0.2781±0.0011	337.89±0.94	4.39±0.12
	2012-09-13	*H*	0.2874±0.0121	342.02±0.66	4.46±0.14
	2012-11-06*	*H*	0.3165±0.0017	336.10±0.57	4.48±0.09
HD 96167 B	2011-03-15	*H*	5.885±0.012	297.01±0.04	6.24±0.34
	2012-02-28	*H*	5.888±0.008	296.85±0.03	6.40±0.08
HD 96167 C	2011-03-15	*H*	3.592±0.007	306.27±0.03	11.92±0.34
	2012-02-28	*H*	3.565±0.005	306.53±0.04	12.01±0.08
HD 96167 D	2011-03-15	*H*	6.562±0.007	41.07±0.09	13.06±0.35
	2012-02-28	*H*	6.593±0.009	41.28±0.07	13.09±0.09
HD 96167 E	2011-03-15*	*H*	6.953(±0.007)	61.57(±0.03)	(13.89±0.36)
	2012-02-28	*H*	6.997±0.007	61.79±0.08	14.20±0.12
HD 156279 B	2012-07-09	*H*	9.466±0.009	191.95±0.04	10.36±0.17
	2013-05-20	*J*	9.600±0.011	191.88±0.04	10.86±0.14
	2013-05-20	*Ks*	9.695±0.011	191.92±0.04	9.79±0.10

Stars in italic are confirmed to be unbound. Data sets of rows with the mark * are reduced with the classical ADI (Marois et al., 2006).

exclude that this companion candidate does not have a linear motion if the candidate has a magnitude difference of $\Delta H \lesssim 12$. The candidate B has infrared magnitudes of $H = 9.65 \pm 0.09$ and $Ks = 9.65 \pm 0.09$, leading to a color of $H - Ks = -0.01 \pm 0.13$. Based on an age of 2.5 ± 0.4 Gyr, our color and absolute magnitudes of $M_H = 6.73 \pm 0.11$ and $M_{Ks} = 6.73 \pm 0.11$ are slightly inconsistent with magnitudes of a $\sim 0.4 M_\odot$ star predicted by the NextGen model (Hauschildt et al., 1999a,b), but agree with the PARSEC model (Bressan et al., 2012) to yield a theoretical mass of $M_B \sim 0.35 M_\odot$ (an M-type star). According to both the model, a star with the mass produces a V magnitude of $V \sim 13 - 14$ mag, in discord with the magnitude of the object Mason et al. (2011) reported ($V = 8.6 \pm 0.5$). Therefore, we conclude that the object should be distinguished from our object HD 8673 B and be under the detection limit (see Figure 5.3 and 5.4), if exists. More high-resolved observations are necessary to investigate the system. Here, we ignore the Mason's object due to its absence from our images.

If the object B orbits HD 8673 A with a semi-major axis of $a_B = 11$ AU, its orbital period is estimated to be ~ 28 yr. Note that this assumption is guaranteed by a conversion factor from projected separations to true semi-major axes of roughly equal to 1 (Dupuy and Liu, 2011). Assuming the orbit to be circular ($e_B = 0$), a Kozai timescale P_{Kozai} for the planet b is calculated to be $P_{\text{Kozai}} \sim 640$ yr with Equation 1.15. It suggests that Kozai migration has been able to occur in the system. However, because the apocenter of the planet has a distance of 5.2 AU, the gravitational effect of B may be able to destroy the planetary system if B is separated only by 11 AU. Presuming other possibilities of B with a semi-major axis of $a_B = 20, 30, 50$ or 100 AU, the orbital periods are $\sim 70, 130, 280$ or 780 yr to obtain Kozai timescales of $\sim 4, 14, 64,$ or 500 kyr, respectively. The timescales are significantly shorter than relativistic effect ($P_{\text{GR}} \sim 400$ Myr for $e_{p,0} = 0$). Hence, it is robust that B induces the effect on the planet b. Additionally it is possible that the object reported by Mason et al. (2011) and HD 8673 B cause the sequential Kozai effect (Takeda et al., 2008) to oscillate b's orbit.

Table 5.7: Summary of Detected Companion Candidates around Tilted Planet Systems

Name	Date (UT)	Filter	Sep. ($''$)	PA (deg)	Δm
HAT-P-6 B	2011-08-02	H	1.189 ± 0.003	13.15 ± 0.30	11.46 ± 0.11
HAT-P-6 C	2011-08-02	H	4.128 ± 0.008	348.62 ± 0.09	10.31 ± 0.08
HAT-P-6 D	2011-08-02	H	6.485 ± 0.006	39.67 ± 0.06	8.24 ± 0.06
HAT-P-6 E	2011-08-02	H	8.540 ± 0.011	300.22 ± 0.04	9.11 ± 0.07
HAT-P-11 B	2011-05-23	H	7.827 ± 0.010	121.13 ± 0.04	11.64 ± 0.15
	2011-09-06	H	7.864 ± 0.010	121.38 ± 0.03	12.29 ± 0.09
HAT-P-11 C	2011-05-23	H	8.240 ± 0.011	7.44 ± 0.05	6.56 ± 0.15
	2011-09-06	H	8.191 ± 0.009	7.61 ± 0.05	7.31 ± 0.07
HAT-P-11 D	2011-05-23	H	8.386 ± 0.011	304.94 ± 0.03	11.04 ± 0.15
	2011-09-06	H	8.337 ± 0.010	304.71 ± 0.03	11.84 ± 0.08
HAT-P-11 E	2011-05-23	H	8.971 ± 0.009	60.60 ± 0.06	11.53 ± 0.15
HAT-P-11 F	2011-05-23	H	9.133 ± 0.009	240.70 ± 0.10	13.88 ± 0.17
	2011-09-06*	H	9.129 ± 0.009	240.46 ± 0.03	14.90 ± 0.18
HAT-P-11 G	2011-05-23	H	9.304 ± 0.009	54.52 ± 0.06	13.38 ± 0.16
HAT-P-11 H	2011-05-23	H	10.17 ± 0.01	223.79 ± 0.05	13.29 ± 0.16
	2011-09-06*	H	10.21 ± 0.01	223.45 ± 0.03	14.19 ± 0.14
HAT-P-14 B	2011-05-21	H	0.858 ± 0.003	264.03 ± 0.15	6.21 ± 0.20
		Ks	0.861 ± 0.004	264.09 ± 0.20	5.75 ± 0.06
HAT-P-17 B	2012-09-14	H	3.192 ± 0.004	110.32 ± 0.03	11.56 ± 0.20
HAT-P-17 C	2012-09-14	H	8.124 ± 0.011	69.50 ± 0.06	11.39 ± 0.19
HAT-P-17 D	2012-09-14	H	11.95 ± 0.02	268.83 ± 0.03	10.06 ± 0.18
HAT-P-30 B	2012-01-02	H	3.827 ± 0.004	4.21 ± 0.04	3.40 ± 0.06
HAT-P-30 C	2012-01-02	H	10.48 ± 0.01	52.35 ± 0.04	7.70 ± 0.14
HAT-P-32 B	2012-09-12	H	2.769 ± 0.003	110.62 ± 0.03	3.85 ± 0.03
TrES-4 B	2011-05-21	H	1.560 ± 0.002	0.20 ± 0.05	3.49 ± 0.11
		Ks	1.566 ± 0.002	0.22 ± 0.07	3.49 ± 0.12
TrES-4 C	2011-05-21	H	8.125 ± 0.008	249.01 ± 0.03	4.42 ± 0.17
		Ks	8.161 ± 0.009	249.02 ± 0.04	4.56 ± 0.24
WASP-8 B	2011-09-03	H	4.500 ± 0.007	170.89 ± 0.07	2.58 ± 0.12
		Ks	4.523 ± 0.005	170.89 ± 0.05	2.41 ± 0.07
WASP-12 B	2012-11-07	H	1.061 ± 0.001	251.42 ± 0.07	2.80 ± 0.10
		Ks	1.067 ± 0.002	251.61 ± 0.09	2.81 ± 0.04
WASP-12 C	2012-11-07	H	1.068 ± 0.001	247.13 ± 0.10	3.17 ± 0.05
		Ks	1.072 ± 0.002	246.94 ± 0.11	3.00 ± 0.03
WASP-12 B/C	2012-11-07	J	1.059 ± 0.002	250.76 ± 0.10	3.33 ± 0.08
WASP-14 B	2011-01-25	H	1.446 ± 0.002	101.87 ± 0.06	5.17 ± 0.15
WASP-17 B	2011-05-24	H	3.121 ± 0.003	203.23 ± 0.03	9.21 ± 0.05
WASP-17 C	2011-05-24	H	7.539 ± 0.008	257.28 ± 0.03	8.95 ± 0.05
WASP-17 D	2011-05-24	H	11.19 ± 0.01	200.12 ± 0.03	7.94 ± 0.05
WASP-33 B	2010-12-01	H	1.925 ± 0.020	275.66 ± 0.33	7.31 ± 0.52

Stars in italic are confirmed to be unbound. Data sets of rows with the mark * are reduced with the classical ADI (Marois et al., 2006).

Table 5.8: A Detected Companion Candidate in the HD 8673 system

Name	Date (UT)	Filter	Sep. ($''$)	PA (deg)	Δm (mag)
HD 8673 B	2011-09-04*	H	0.2781 ± 0.0011	337.89 ± 0.94	4.39 ± 0.12
	2012-09-13	H	0.2874 ± 0.0121	342.02 ± 0.66	4.46 ± 0.14
	2012-11-06*	Ks	0.3165 ± 0.0017	336.10 ± 0.57	4.48 ± 0.09

The rows marked with * are results of data sets reduced with the classical ADI.
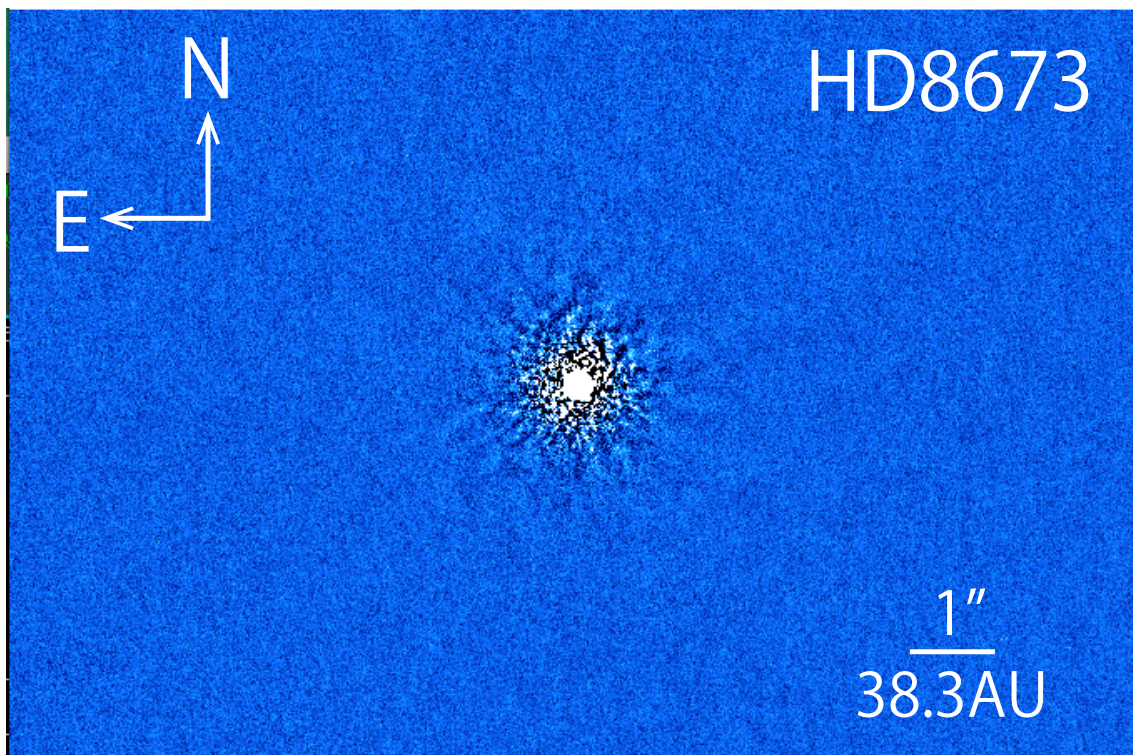
Figure 5.1: A final image of HD 8673 at H band obtained on 13th September 2012. North is up and east is to the left. A faint object at $0.''3$ from the star cannot be distinguished from the noises.
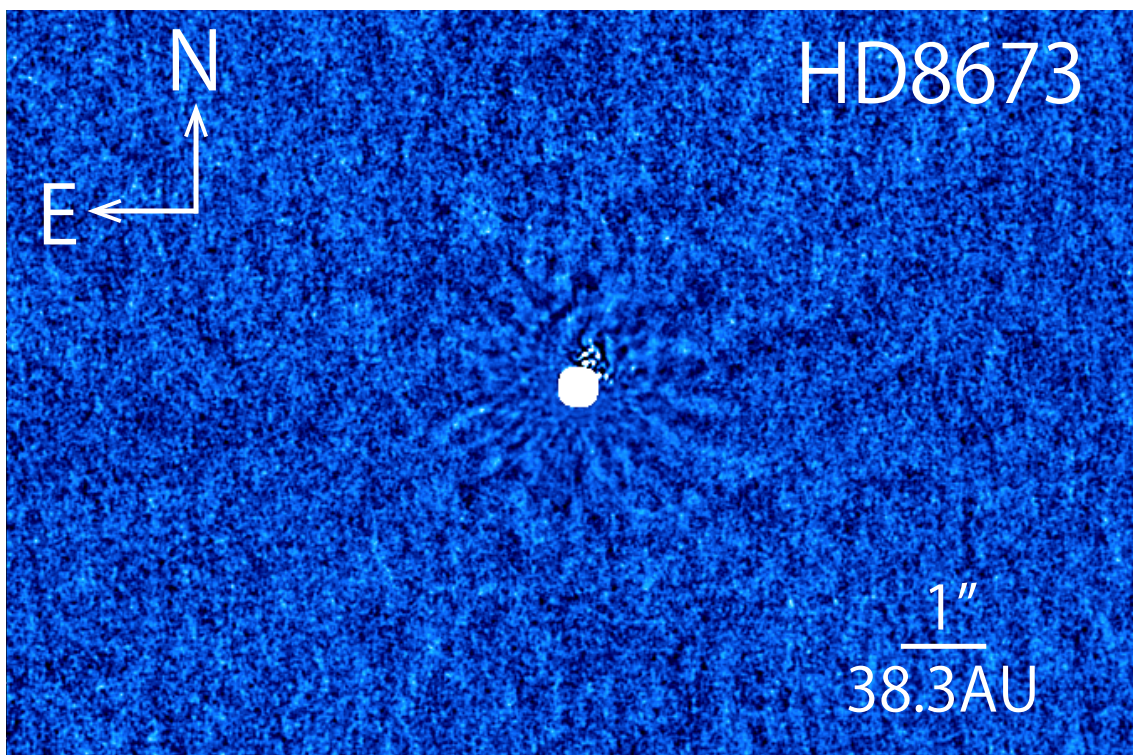
Figure 5.2: An S/N map of HD 8673 at *H* band obtained on 13th September 2012. North is up and east is to the left. A faint object at $0.''3$ from the star can be distinguished from the noises.
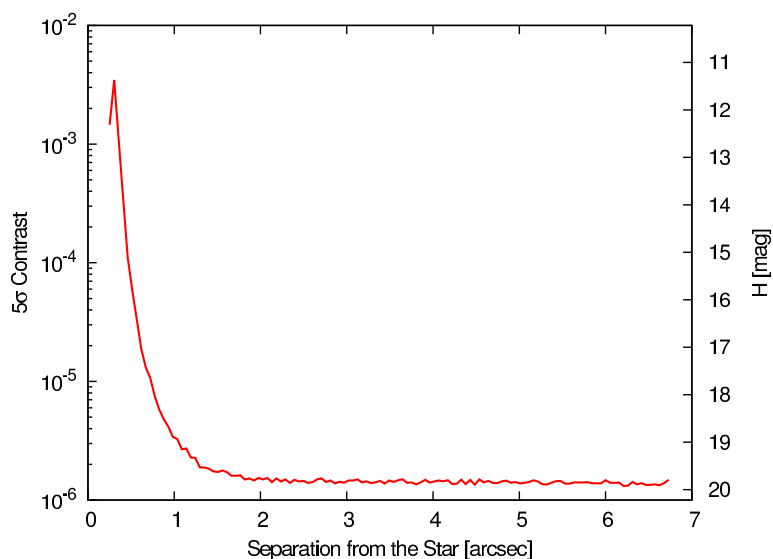
Figure 5.3: A 5σ contrast curve for HD 8673 obtained on 13th September 2012. The vertical axes show the contrast in the log scale (left) and the apparent magnitude *H* (right). The horizontal axis shows the separation from HD 8673.
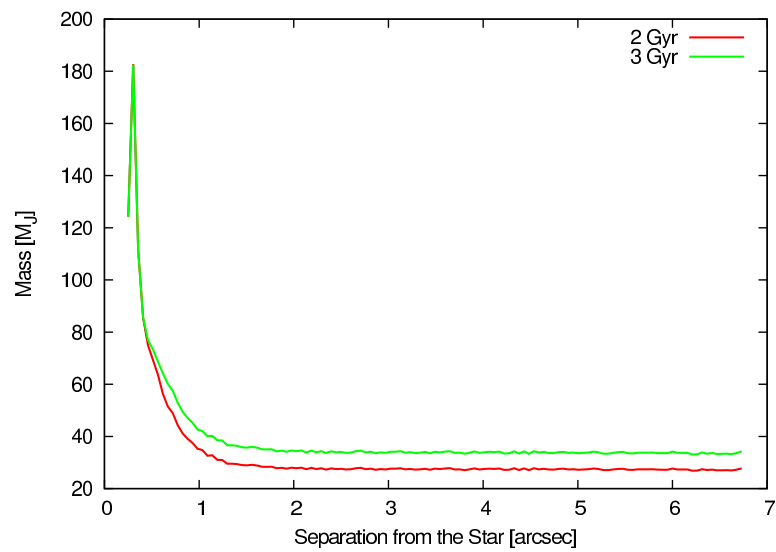
Figure 5.4: Five-σ contrast curves for HD 8673 in mass in a unit of the Jupiter mass converted with the COND model. The horizontal axis shows the separation from HD 8673. The colors represent ages. The data obtained on 13th September 2012.
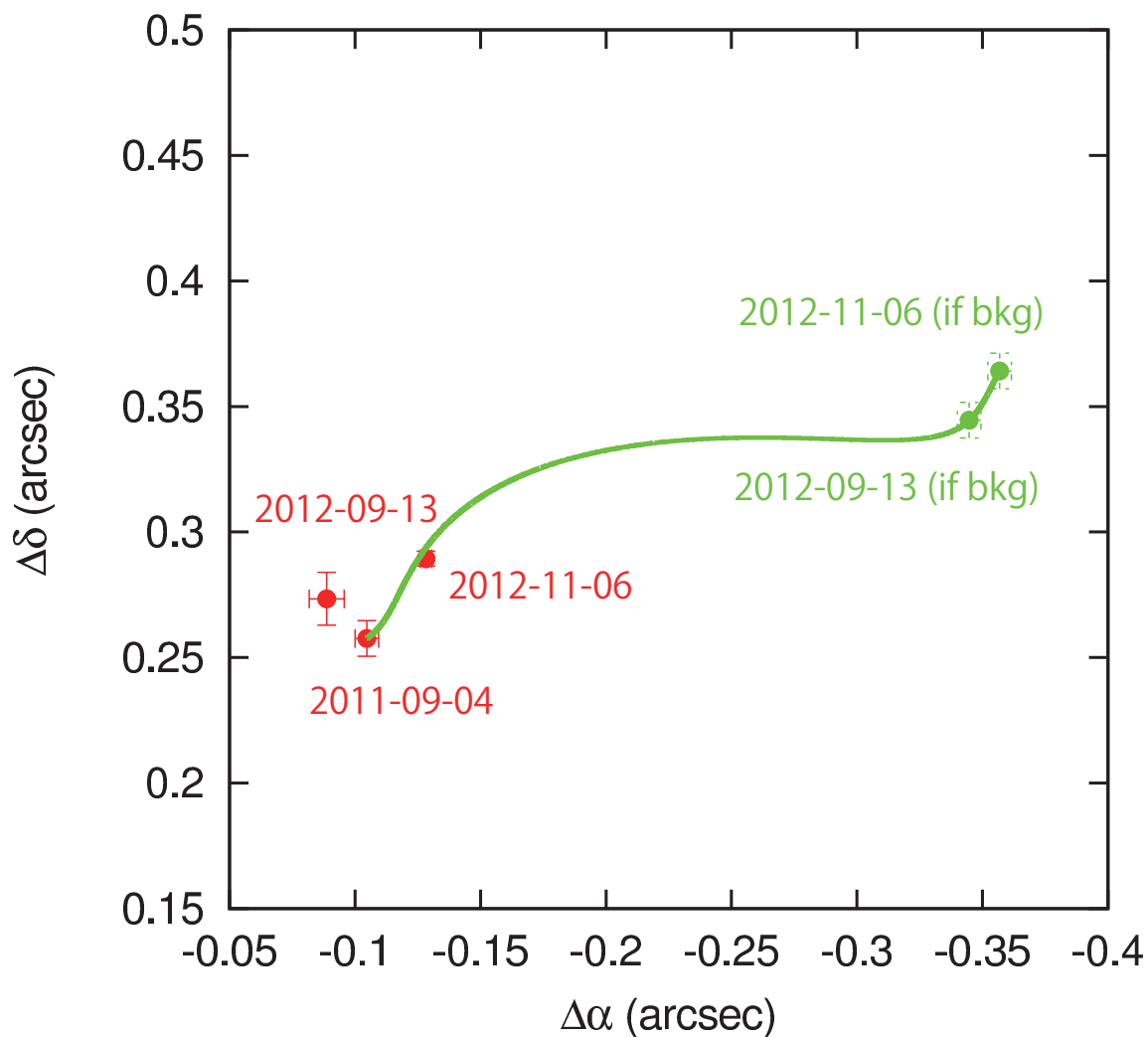
Figure 5.5: A track of a proper motion. The horizontal axis and the vertical axis are relative distances to the main star. The red crosses represent the observational points with error bars. The green crosses indicate the positions on the observational dates if the companion candidate is a background star. The green line is a track driven by the proper motion and the parallax of HD 8673. The result supports that HD 8673 B is physically associated with the main star.

Table 5.9: Detected Companion Candidates in the HD 96167 system

Name	Date (UT)	Filter	Sep. ($''$)	PA (deg)	Δm (mag)
HD 96167 B	2011-03-15	H	5.885 ± 0.012	297.01 ± 0.04	6.24 ± 0.34
	2012-02-28	H	5.888 ± 0.008	296.85 ± 0.03	6.40 ± 0.08
HD 96167 C	2011-03-15	H	3.592 ± 0.007	306.27 ± 0.03	11.92 ± 0.34
	2012-02-28	H	3.565 ± 0.005	306.53 ± 0.04	12.01 ± 0.08
HD 96167 D	2011-03-15	H	6.562 ± 0.007	41.07 ± 0.09	13.06 ± 0.35
	2012-02-28	H	6.593 ± 0.009	41.28 ± 0.07	13.09 ± 0.09
HD 96167 E	2011-03-15*	H	$6.953(\pm 0.007)$	$61.57(\pm 0.03)$	(13.89 ± 0.36)
	2012-02-28	H	6.997 ± 0.007	61.79 ± 0.08	14.20 ± 0.12

Due to shallow observation, data in the row marked with * are obtained and estimated with the S/N map. The objects in italic are concluded to be unrelated objects.

5.6.2　HD 96167

We discovered four companion candidates and obtained data in two epochs separated by about one year, enabling us to examine the CPM. Figure 5.6 clearly displays the final image reduced with LOCI, showing the companions with their labels as B, C, D, and E. Contrast curves are represented in Figures 5.7 and 5.8. Comparing our results, collected in Table 5.9, our photometry measurements are well consistent and authentic. With the proper motion of HD 96167 of $(\mu_\alpha \cos \delta, \mu_\delta) = (-49.69 \pm 0.83, -7.55 \pm 0.80)$ (van Leeuwen, 2007), we conclude that HD 96167 B has a CPM with the main star and others are assumed to be unrelated objects (see Figure 5.9). Considering B's apparent magnitude of $H = 13.01 \pm 0.10$, its absolute magnitude at H band is estimated to be $M_H = 8.39 \pm 0.25$ and leads to its spectral type of M with a mass of $\sim 0.17 M_\odot$ and an effective temperature of ~ 3200 K adopting the age of HD 96167 and the NextGen model. If B has the same distance of a semi-major axis as its projected separation, 84 pc $\times 5.''9 = 500$ AU, its orbital period is calculated to be ~ 9 kyr.

　　Given B's period and mass, a timescale of Kozai effects of HD 96167 B on the planet HD 96167b at the current position is estimated to be $P_{\text{Kozai}} \sim 500$ Myr. In the orbit, the relativistic effect timescale of $P_{\text{GR}} \sim 40$ Myr (for a circular orbit) is shorter than Kozai mechanism, suggesting that it has perturbed Kozai effects. On the other hand, an assumptive circular planet at 4.6 AU (the position of the snow line) can be affected on the timescale of $P_{\text{Kozai}} \sim 70$ Myr, which is much shorter than P_{GR} of ~ 1 Gyr for the position. Hence, we suppose that the planet has been under the gravitational influence of the companion B beyond the snow line.
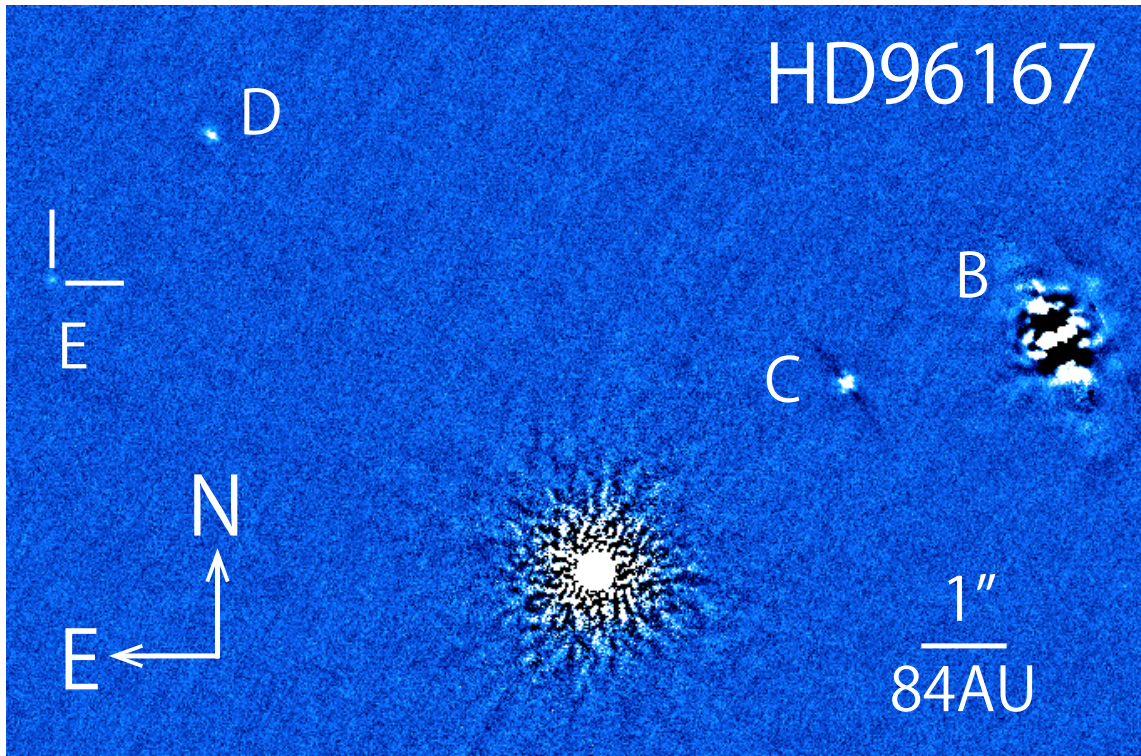
Figure 5.6: A final image of HD 96167 at *H* band taken on 28th February 2012. North is up and east is to the left. Four objects other than HD 96167 main star are labeled and can be seen in the figure. The brightest object is significantly affected by the self-subtraction.
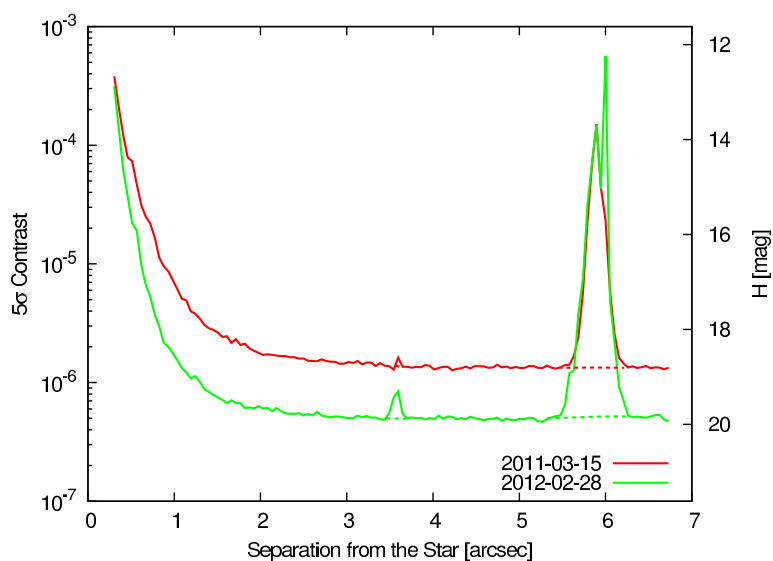
Figure 5.7: Five-σ contrast curves for HD 96167. The vertical axes show the contrast in the log scale (left) and the apparent magnitude H (right). The horizontal axis shows the separation from HD 96167. The colors represent the observational dates. The dotted lines correct the anomalies at $3{.}''6$ and $\sim 6''$ induced by the bright companion candidates with interpolations.
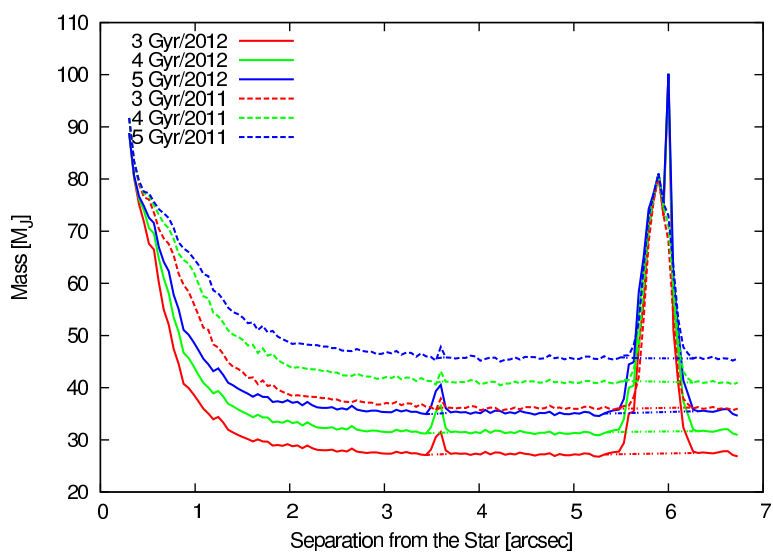
Figure 5.8: Five-σ contrast curves for HD 96167 in mass in a unit of the Jupiter mass converted with the COND model. The horizontal axis shows the separation from HD 96167. The colors represent ages. The dotted lines correct the anomalies at $\sim 6''$ induced by the bright companion candidates with interpolations.
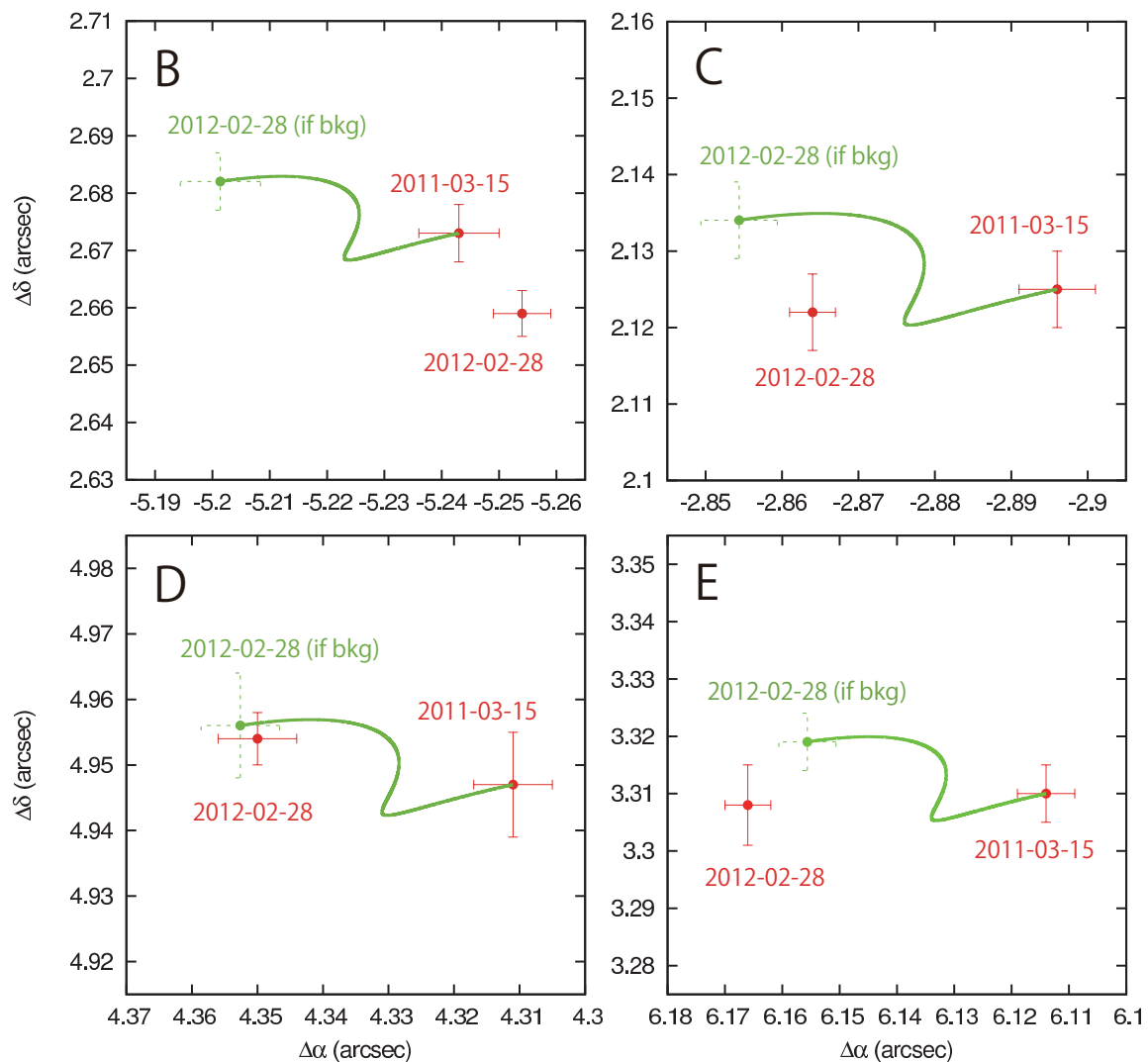
Figure 5.9: Tracks of a proper motion. The horizontal axes and the vertical axes are relative distances to the main star. The red crosses represent the observational points with error bars. The green crosses indicate the positions on 28th February 2012 if the companion candidates are background stars. The green lines are tracks driven by the proper motion and the parallax of HD 96167. The results support that only B is physically bound to the main star, while C, D and E are unrelated.

Table 5.10: A Detected Companion Candidate in the HD 156279 system

Name	Date (UT)	Filter	Sep. ($''$)	PA (deg)	Δm (mag)
HD 156279 B	2012-07-09	*H*	9.466 ± 0.009	191.95 ± 0.04	10.36 ± 0.17
	2013-05-20	*J*	9.600 ± 0.011	191.88 ± 0.04	10.86 ± 0.14
	2013-05-20	*Ks*	9.695 ± 0.011	191.92 ± 0.04	9.79 ± 0.10

5.6.3   HD 156279

We found a faint object which is $9.''5$ distant from HD 156279 in Figure 5.10, thanks to our high-contrast observations (see Figures 5.11 and 5.12). Our data are taken in two epochs to carry out the CPM test. The result is shown in Figure 5.13 and the observational positions are consistent with a theoretical position given by a background star hypothesis, though the positions measured at *J* and *Ks* stand apart from each other. A cause of the difference of the observational positions has not been revealed. Infrared colors derived from magnitudes of $J = 17.54 \pm 0.14$, $H = 16.71 \pm 0.17$ and $Ks = 16.06 \pm 0.10$ lead to a late type star, but disagree with our magnitudes. Therefore we rule out the object as a real companion star. The origin of the eccentric orbit of the planet HD 156279b is likely explained by planet-planet scattering.
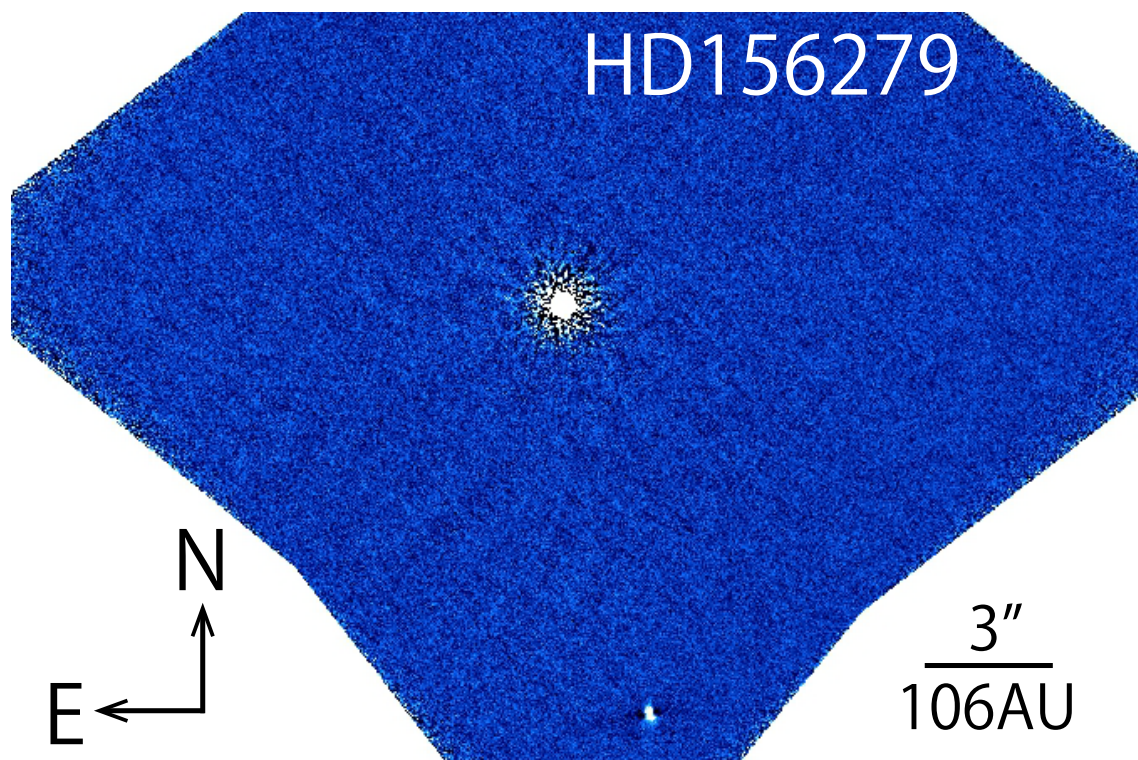
Figure 5.10: A final image of HD 156279 at *H* band obtained on 9th July 2012. North is up and east is to the left. One bright object is at far from HD 156279.
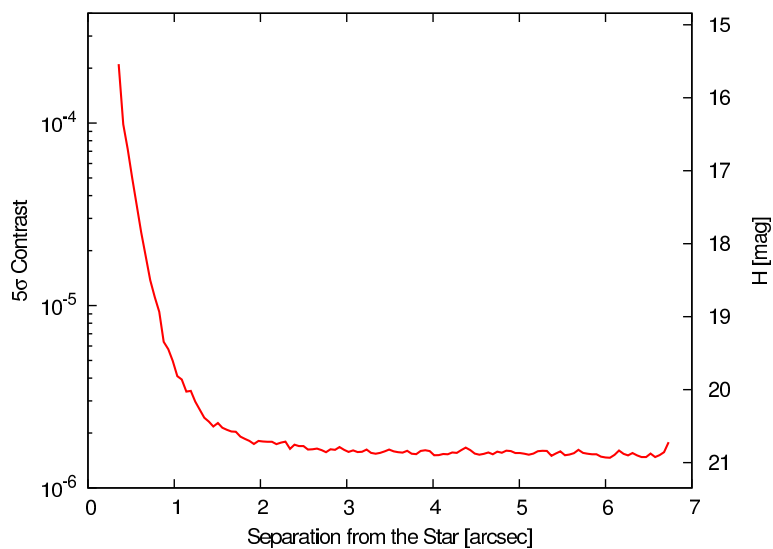
Figure 5.11: A 5σ contrast curves for HD 156279 obtained on 9th July 2012 at H band. The vertical axes show the contrast in the log scale (left) and the apparent magnitude H (right). The horizontal axis shows the separation from HD 156279.
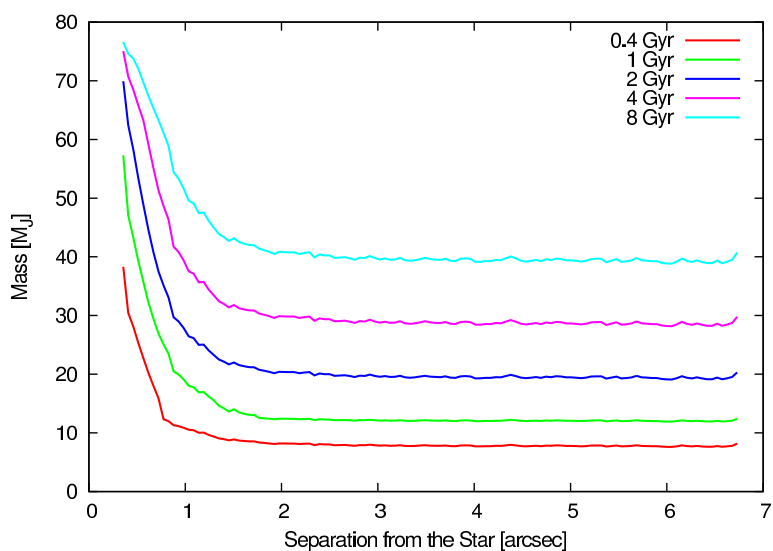

Figure 5.12: Five-σ contrast curves for HD 156279 in mass in a unit of the Jupiter mass converted with the COND model. The horizontal axis shows the separation from HD 156279. The colors represent ages. Obtained on 9th July 2012 at H band.
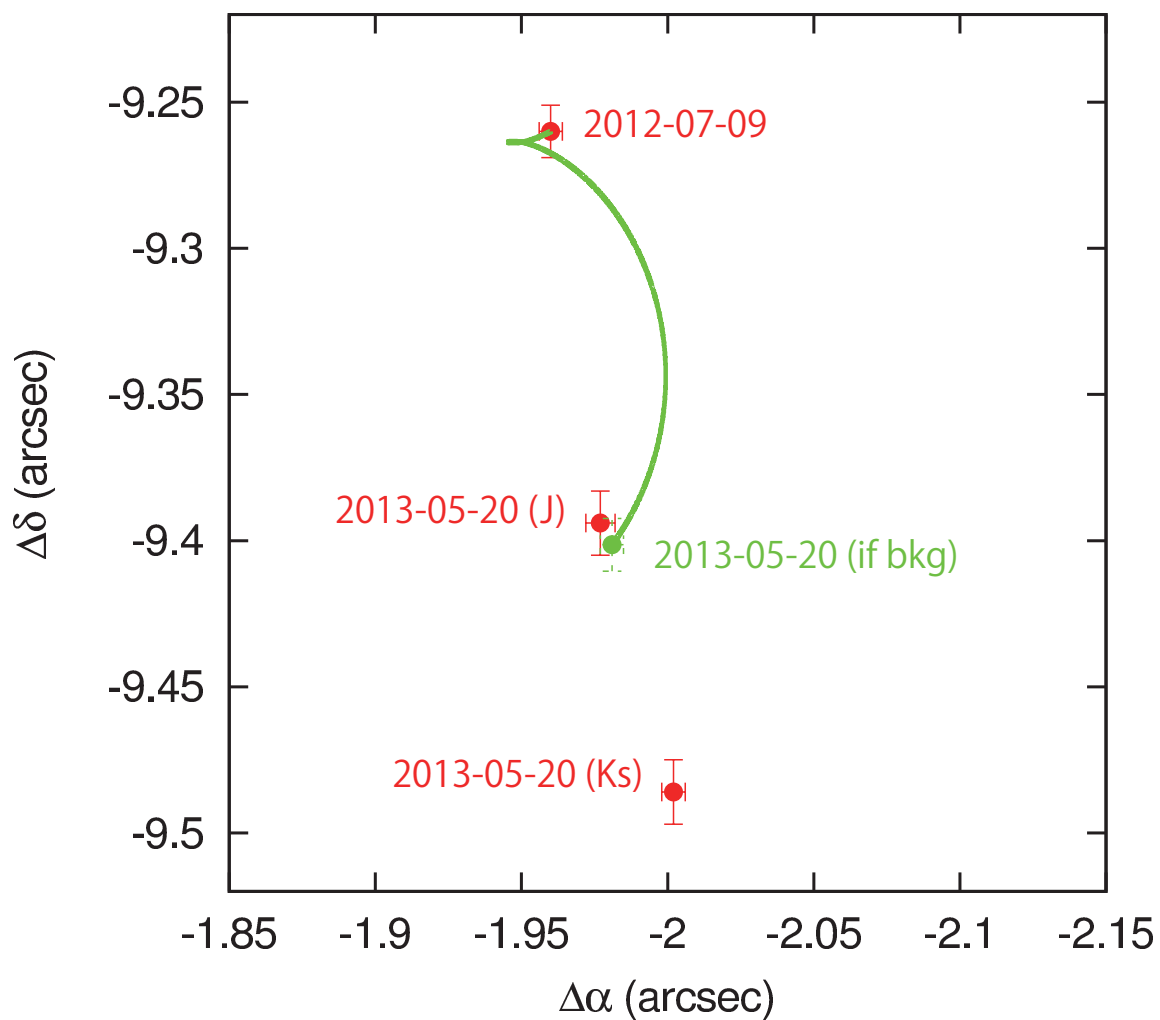
Figure 5.13: A track of a proper motion. The red crosses represent the observational points with error bars. The green cross indicates the position on 20th May 2013 if the companion candidate is a background star. The green line is a track driven by the proper motion and the parallax of HD 156279. Our results are consistent with the background star hypothesis.

Table 5.11: A Detected Companion Candidate in the HAT-P-6 system

Name	Date (UT)	Filter	Sep. ($''$)	PA (deg)	Δm (mag)
HAT-P-6 B	2011-08-02	H	1.189 ± 0.003	13.15 ± 0.30	11.46 ± 0.11
HAT-P-6 C	2011-08-02	H	4.128 ± 0.008	348.62 ± 0.09	10.31 ± 0.08
HAT-P-6 D	2011-08-02	H	6.485 ± 0.006	39.67 ± 0.06	8.24 ± 0.06
HAT-P-6 E	2011-08-02	H	8.540 ± 0.011	300.22 ± 0.04	9.11 ± 0.07

5.6.4 HAT-P-6

We discovered four companion candidates (named as B, C, D and E) around HAT-P-6 with separations of $1''.2$, $4''.1$, $6''.5$ and $8''.5$, respectively, in the final image (Figure 5.14) with high contrast observations (see Figures 5.15 and 5.16). If they have the same age and distances from Earth as those of HAT-P-6, we estimate their absolute magnitudes of $M_H = 13.83 \pm 0.20$, 12.68 ± 0.19, 10.61 ± 0.18 and 11.48 ± 0.18, leading to an L-type star with its mass of $\sim 0.06 M_\odot$ and its temperature of ~ 1500 K, an L-type star with $\sim 0.07 M_\odot$ and ~ 1700 K, an M-to-L-type star with $\sim 0.08 M_\odot$ and ~ 2500 K, and an L-type star with $\sim 0.08 M_\odot$ and ~ 2000 K, for B, C, D and E, respectively, using the Dusty model (Chabrier et al., 2000).

Next we estimate Kozai timescales affected by the candidate companions. The orbital periods of the companions can be calculated to be $P_B \sim 5$ kyr, $P_C \sim 30$ kyr, $P_D \sim 60$ kyr, and $P_E \sim 90$ kyr, if their orbital semi-major axes are the same as the projected separations. The timescales P_{Kozai} for the planet HAT-P-6b at the current position is ~ 50 Gyr, ~ 2 Tyr, ~ 5 Tyr, and ~ 120 Tyr for B, C, D and E, respectively. The timescales indicate that the candidate companions cannot affect the planet now. Then we assume a hypothetical planet at the snow line (4.5 AU for HAT-P-6) in a circular orbit. The timescales P_{Kozai} for the planet are estimated to be ~ 60 Myr, ~ 2 Gyr, ~ 6 Gyr and ~ 20 Gyr, while the timescale of the relativistic effect is calculated to be $P_{\text{GR}} \sim 1$ Gyr. The results suggest that HAT-P-6 B, if bound, were able to affect HAT-P-6b through Kozai effects in the past, while C, D and E were not, in contrast. A Galactic model, the TRILEGAL model (ver 1.6; e.g. Girardi et al. 2005), estimates the number of background stars within $\sim 8''.5$ from HAT-P-6 to be two with a limiting magnitude of $H \sim 22.2$ mag, a binary rate of 0.5 (e.g. Raghavan et al. (2010)) and setting a binary mass fraction to from 0.1 to 1.0, suggesting that the companion candidates may be in background. The boundship of the companions, especially HAT-P-6 B, will be an important key to investigate migration scenarios in the HAT-P-6 system.
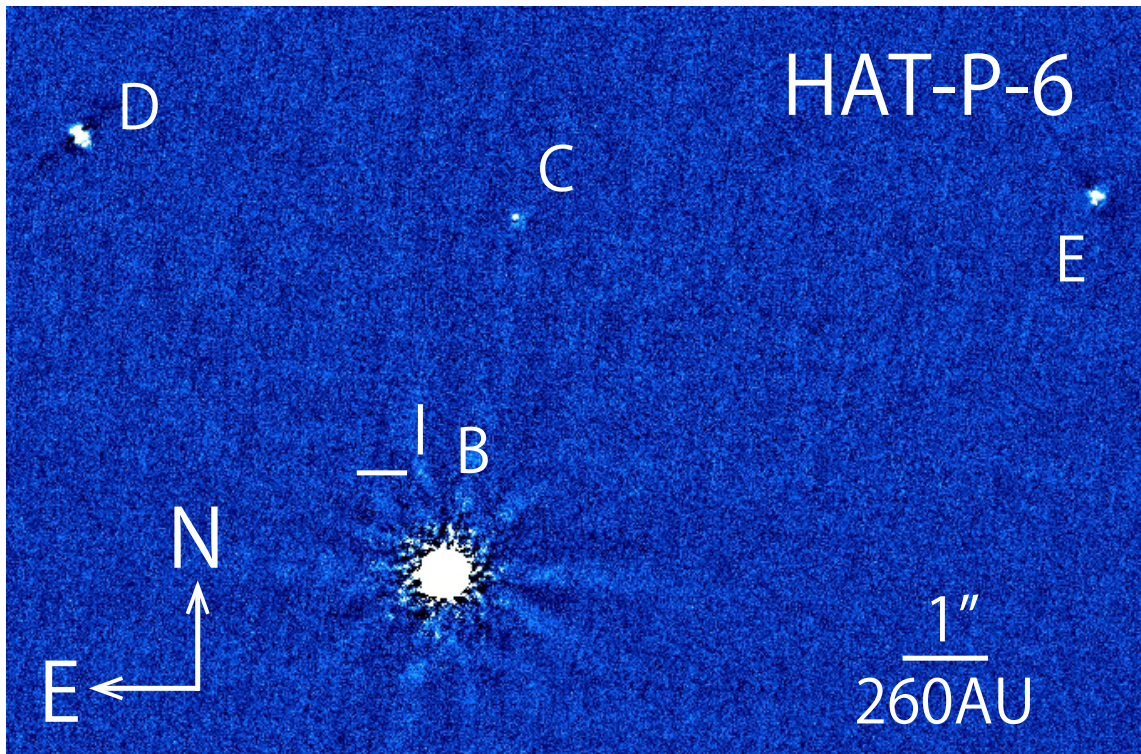
Figure 5.14: A final image of HAT-P-6 at *H* band. North is up and east is to the left. Four objects can be seen and denoted by the crosses in the figure. The two bright objects have the dark tails induced by the self-subtraction.
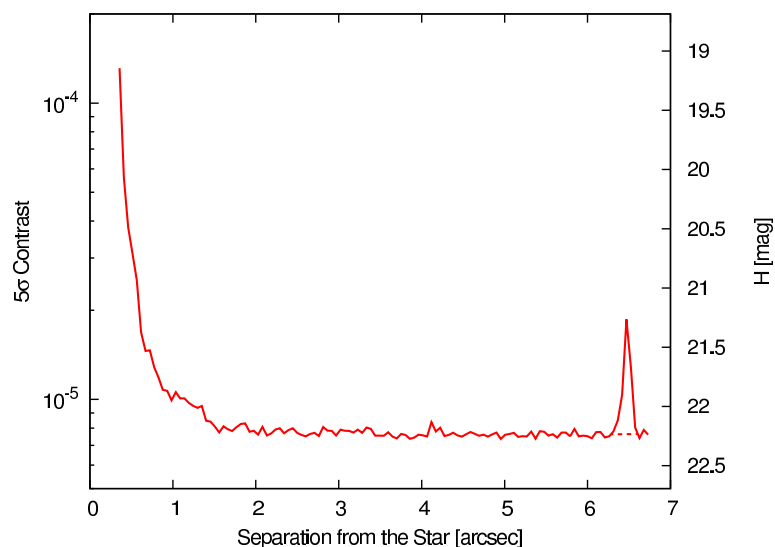
Figure 5.15: A 5σ contrast curve for HAT-P-6. The vertical axes show the contrast in the log scale (left) and the apparent magnitude H (right). The horizontal axis shows the separation from HAT-P-6. The dotted line corrects the anomaly at $\sim 6\rlap{.}''5$ induced by the bright companion candidate with an interpolation.
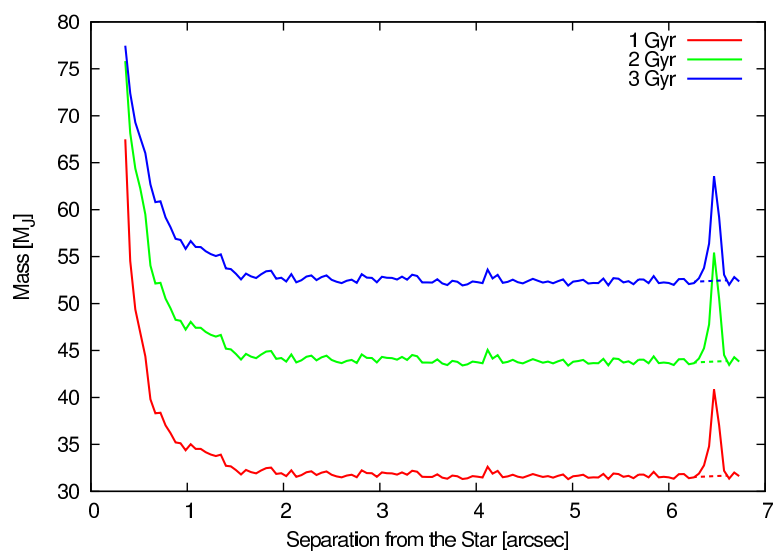
Figure 5.16: Five-σ contrast curves for HAT-P-6 in mass in a unit of the Jupiter mass converted with the COND model. The horizontal axis shows the separation from HAT-P-6. The colors represent ages. The dotted lines correct the anomalies at $\sim 6\rlap{.}''5$ induced by the bright companion candidate with interpolations.

Table 5.12: A Detected Companion Candidate in the HAT-P-11 system

Name	Date (UT)	Filter	Sep. ($''$)	PA (deg)	Δm (mag)
HAT-P-11 B	2011-05-23	*H*	7.827 ± 0.010	121.13 ± 0.04	11.64 ± 0.15
	2011-09-06	*H*	7.864 ± 0.010	121.38 ± 0.03	12.29 ± 0.09
HAT-P-11 C	2011-05-23	*H*	8.240 ± 0.011	7.44 ± 0.05	6.56 ± 0.15
	2011-09-06	*H*	8.191 ± 0.009	7.61 ± 0.05	7.31 ± 0.07
HAT-P-11 D	2011-05-23	*H*	8.386 ± 0.011	304.94 ± 0.03	11.04 ± 0.15
	2011-09-06	*H*	8.337 ± 0.010	304.71 ± 0.03	11.84 ± 0.08
HAT-P-11 E	2011-05-23	*H*	8.971 ± 0.009	60.60 ± 0.06	11.53 ± 0.15
HAT-P-11 F	2011-05-23	*H*	9.133 ± 0.009	240.70 ± 0.10	13.88 ± 0.17
	2011-09-06*	*H*	9.129 ± 0.009	240.46 ± 0.03	14.90 ± 0.18
HAT-P-11 G	2011-05-23	*H*	9.304 ± 0.009	54.52 ± 0.06	13.38 ± 0.16
HAT-P-11 H	2011-05-23	*H*	10.17 ± 0.01	223.79 ± 0.05	13.29 ± 0.16
	2011-09-06*	*H*	10.21 ± 0.01	223.45 ± 0.03	14.19 ± 0.14

The rows marked with * are estimated from the S/N map. The objects with names in italic are concluded to be background objects.

5.6.5   HAT-P-11

We discovered 7 companion candidates and observed them in two epochs to examine the CPMs, though two of them were out of FOV in one epoch. Figure 5.17 represents and names them in close order. Contrasts are shown in Figure 5.18 and 5.19. Table 5.12 summarizes our results. The photometric magnitudes are systematically shifted, and a cause may be induced by cirrus or cloud passage. Meanwhile, we found a star on the 2MASS catalog at $19^h50^m50^s.496$, $+48°05'01''.78$ with an *H* magnitude of 13.19 ± 0.07. The star has a relative position of $(\Delta\alpha, \Delta\delta) = (+2''.49, +10''.69)$ on JD $= 2450990.9521$ (26th June 1998). The relative position is similar to one of the candidates, C, $(\Delta\alpha, \Delta\delta) = (+1''.07, +8''.17)$ on JD $= 2455705.1229$ (23rd May 2011). The difference can be explained by the proper motion of HAT-P-11 $(\mu_\alpha \cos\delta, \mu_\delta) = (127.20, 231.23)$ mas/yr (van Leeuwen, 2007). Thus we conclude that C is a known background star and magnitudes taken in May are more reliable, compared to our *H* magnitudes of $H = 13.71 \pm 0.15$ in May and $H = 14.36 \pm 0.07$ in September.

We next perform the CPM tests for the companion candidates B, C, D, F and H, and consequently rule out them as bound objects (results in Figure 5.20). The remains, E and G, are discussed in the following sentences. If E and G are physically bound to HAT-P-11, absolute magnitudes are $M_H = 8.63 \pm 0.17$ and 10.48 ± 0.18, and estimated masses are $M_E \sim 0.15 M_\odot$ and $M_G \sim 0.08 M_\odot$ for E and G, respectively, with the NextGen and the Dusty model. Assuming semi-major axes as the same distances as the projected separations, $a_E = 340$ AU and $a_G = 350$ AU, their orbital periods are predicted to be ~ 6400 yr and ~ 6900 yr, respectively. Kozai timescales for HAT-P-11b are ~ 17 Gyr and ~ 36 Gyr for E and G, respectively, and therefore it is difficult for Kozai effects to illustrate the tilted axis. For a planet at the snow line (1.8 AU) with a period of ~ 2.6 yr, the timescales P_{Kozai} are calculated to be ~ 85 Myr and ~ 190 Myr, while P_{GR} is estimated to be ~ 200 Myr. Hence, the possibility of E or G being real companions and causing Kozai effects remains, though P_{Kozai} and P_{GR} are comparable. We note that the TRILEGAL model calculates the number of background stars in the FOV to be 5, being consistent with our candidates being background stars.
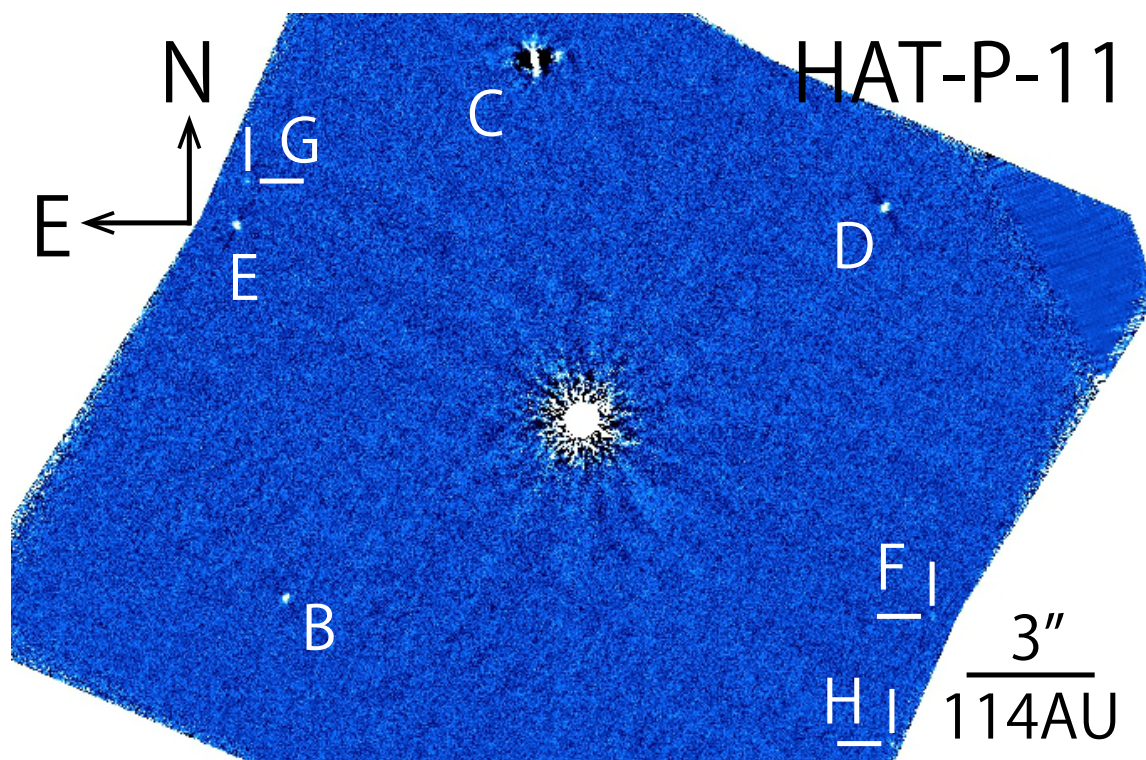
Figure 5.17: A final image of HAT-P-11 at *H* band taken on 23rd May 2011. North is up and east is to the left. Seven objects, labeled with the crosses and the names, can be seen in the field.
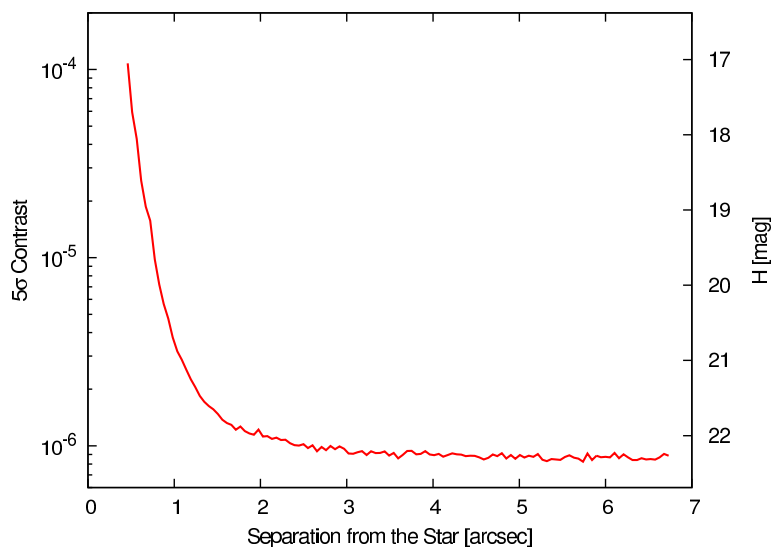

Figure 5.18: A 5σ contrast curve for HAT-P-11 taken on 23rd May 2011. The vertical axes show the contrast in the log scale (left) and the apparent magnitude *H* (right). The horizontal axis shows the separation from HAT-P-11.
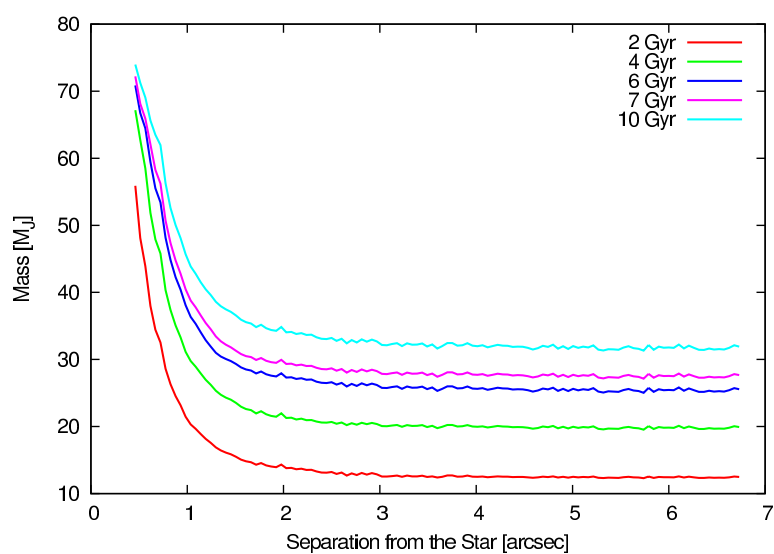
Figure 5.19: Five-σ contrast curves for HAT-P-11 in mass in a unit of the Jupiter mass converted with the COND model. The curves represent data observed on 23rd May 2011. The horizontal axis shows the separation from HAT-P-11. The colors represent ages.
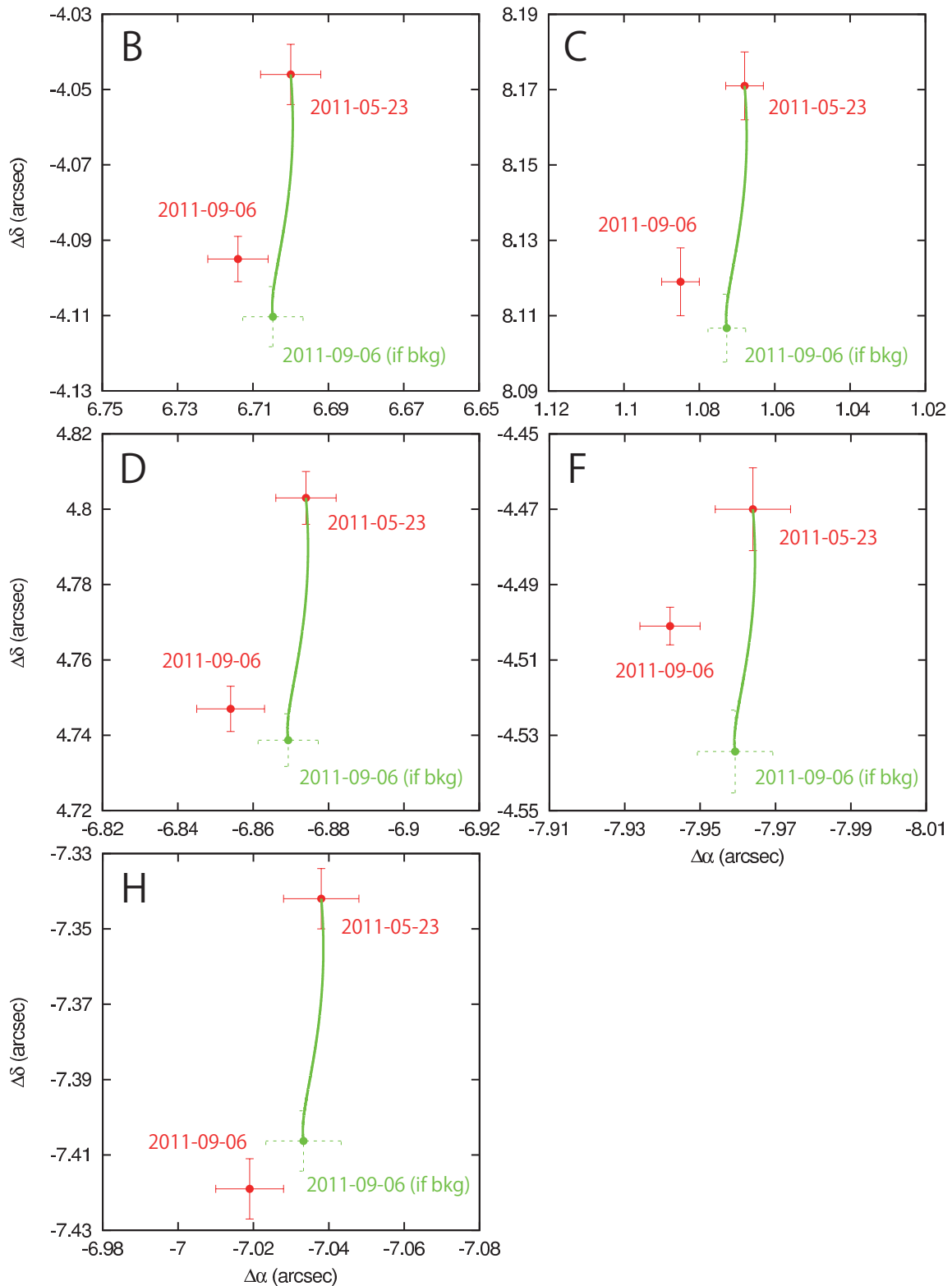
Figure 5.20: Tracks of a proper motion. The red crosses represent the observational points with error bars. The green crosses indicate the position on 6th September 2011 if the companion candidates are background stars. The green lines are tracks driven by the proper motion and the parallax of HAT-P-11.

Table 5.13: A Detected Companion Candidate in the HAT-P-14 system

Name	Date (UT)	Filter	Sep. ($''$)	PA (deg)	Δm (mag)
HAT-P-14 B	2011-05-21	H	0.858 ± 0.003	264.03 ± 0.15	6.21 ± 0.20
		Ks	0.861 ± 0.004	264.09 ± 0.20	5.75 ± 0.06

5.6.6 HAT-P-14

After the reduction, we discovered an unknown companion candidate (named as "HAT-P-14 B") around the HAT-P-14 main star with a separation of $\rho = 0.''86$ and a position angle of $\theta = 264°$ (see Table 5.13 in detail) in Figure 5.21, though it is hard to find it in Figure 5.22. The contrasts of our observations are shown in Figure 5.23 and 5.24. By using the companion candidate's color of $H - Ks = 0.54 \pm 0.21$ and its absolute magnitude of $M_H = 8.58 \pm 0.23$, the object is likely to be a physically-bound M-type star with an estimated effective temperature of $T_{\mathrm{eff}} \sim 3000$ K and a mass of $\sim 0.15 M_\odot$ with adopting the NextGen model. It is difficult to confirm the CPM, because the proper motion of the main star is quite small (~ 4.9 mas/yr). Considering that the TRILEGAL model estimates only one background star in our FOV and zero within $\sim 0.''86$, it is likely that HAT-P-14 B is physically bound to HAT-P-14, though more observations at various wavelengths are necessary to investigate HAT-P-14 B's character.

If B's semi-major axis is the same as its projected distance, i.e. $a_{\mathrm{B}} = a_{\mathrm{B,proj}} = 205$ pc $\times 0.''86 = 180$ AU, the orbital period is estimated to be ~ 2 kyr. Therefore, the timescale of Kozai migration is calculated to be $P_{\mathrm{Kozai}} \sim 3$ Gyr for the planet HAT-P-14b at the current position, or $P_{\mathrm{Kozai}} \sim 3$ Myr for a circular planet at the position of the snow line (5.2 AU). Combining with $P_{\mathrm{GR}} \sim 10$ kyr for the current semi-major axis and ~ 1 Gyr for the snow line, these values suggest that HAT-P-14b formed in the outer regions and migrated inward with tilting its orbital axis by the gravitational influence of HAT-P-14 B.
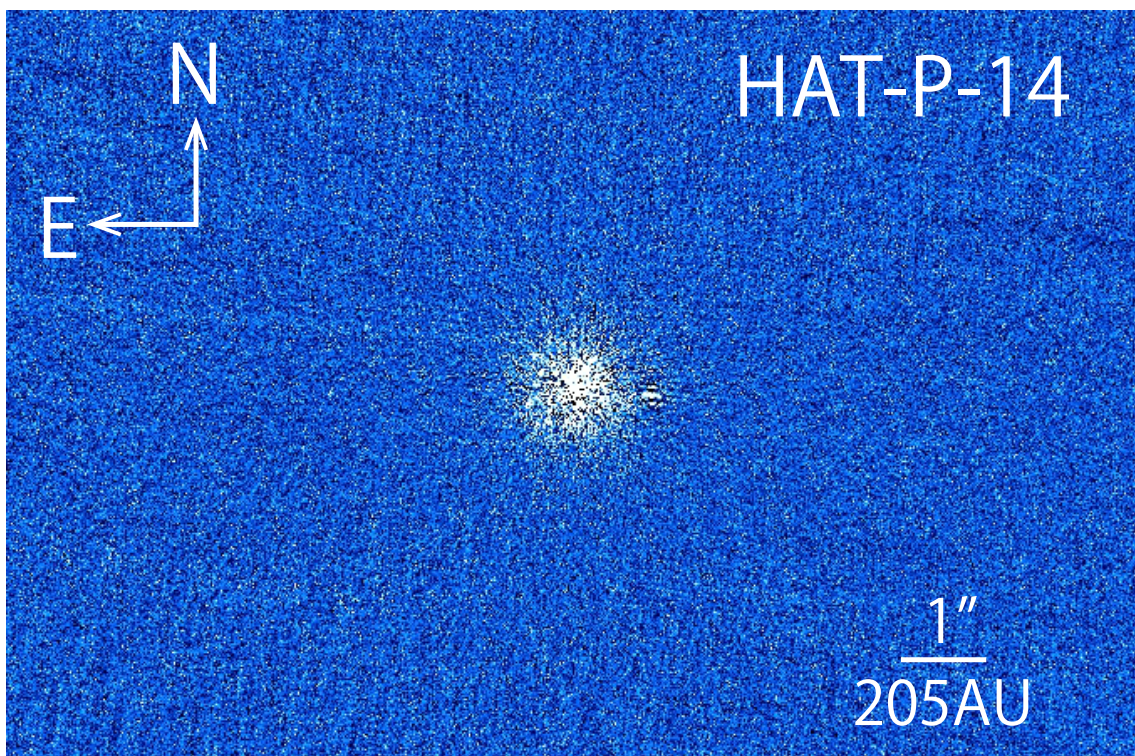
Figure 5.21: A final image of HAT-P-14 at H band reduced with the classical ADI method. North is up and east is to the left. One object with a small separation can be found.
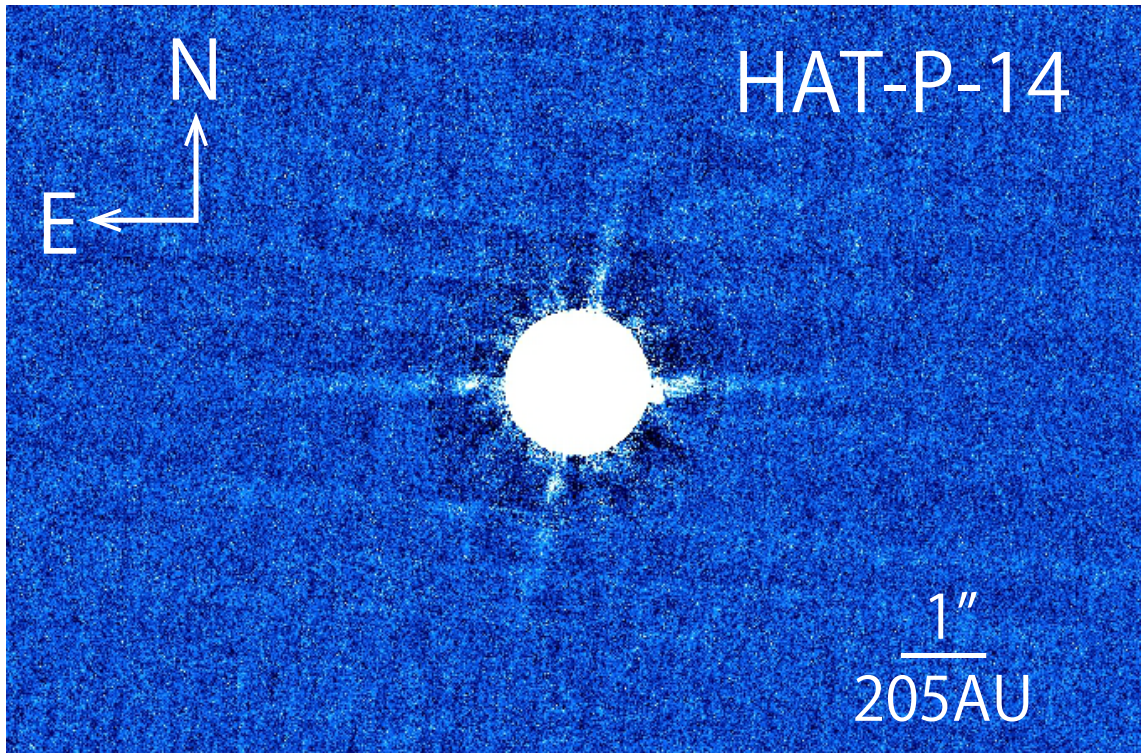
Figure 5.22: A final image of HAT-P-14 at H band reduced with LOCI. North is up and east is to the left. One object to the west can be found with difficulty. A small rotation angle prevents us investigating closer regions to the central star.
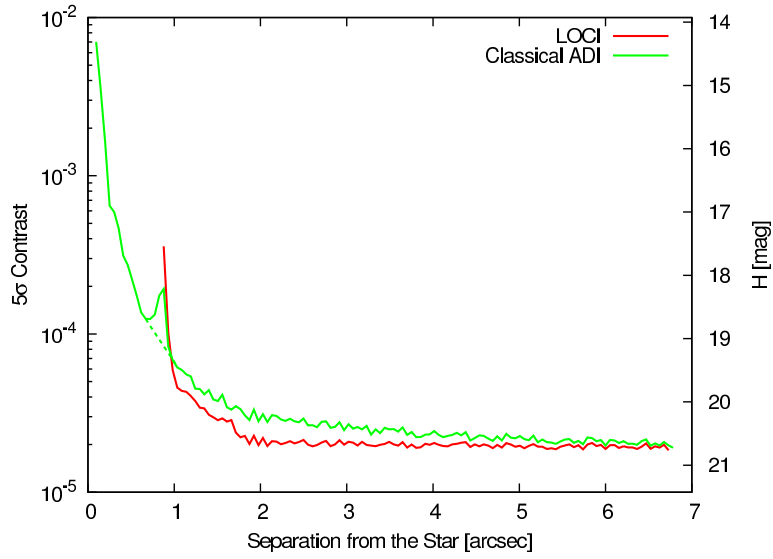
Figure 5.23: Five-σ contrast curves for HAT-P-14. The vertical axes show the contrast in the log scale (left) and the apparent magnitude H (right). The horizontal axis shows the separation from HAT-P-14. The red and green lines represent data reduced with LOCI and the classical ADI method, respectively. The dotted line corrects the anomaly at $\sim 0\rlap{.}''8$ induced by the bright companion candidate with an interpolation.
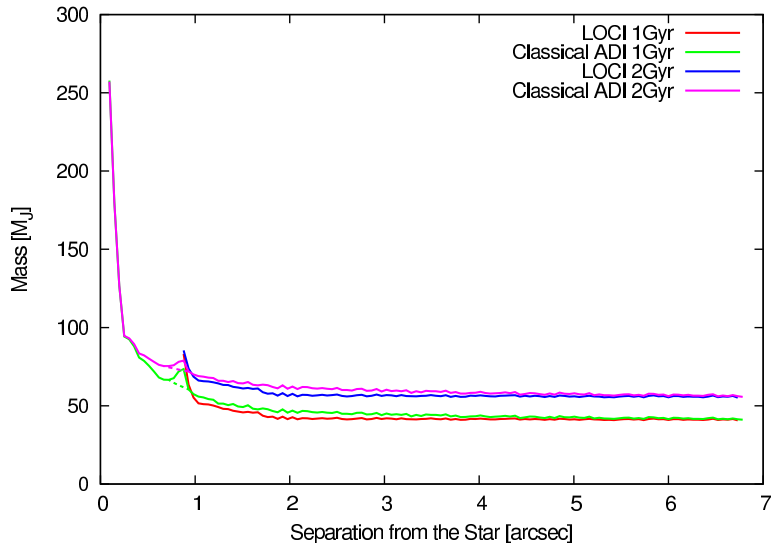
Figure 5.24: Five-σ contrast curves for HAT-P-14 in mass in a unit of the Jupiter mass converted with the COND model. The horizontal axis shows the separation from HAT-P-14. The colors represent reduction methods and ages. The dotted lines correct the anomalies at $\sim 0\rlap{.}''8$ induced by the bright companion candidate with interpolations.

Table 5.14: Detected Companion Candidates in the HAT-P-17 system

Name	Date (UT)	Filter	Sep. ($''$)	PA (deg)	Δm (mag)
HAT-P-17 B	2012-09-14	H	3.192 ± 0.004	110.32 ± 0.03	11.56 ± 0.20
HAT-P-17 C	2012-09-14	H	8.124 ± 0.011	69.50 ± 0.06	11.39 ± 0.19
HAT-P-17 D	2012-09-14	H	11.95 ± 0.02	268.83 ± 0.03	10.06 ± 0.18

5.6.7   HAT-P-17

We discovered three faint objects with S/N > 5 (see Figure 5.25 for a final image and Figure 5.26 for its S/N map) thanks to high-contrast observations (see Figure 5.27 and 5.28). Moreover, an object candidate near D was discovered with relative coordinates of $(\rho, \theta) = (12.''22, 186.°9)$, but we do not treat it as a companion detection because of its low S/N= 3.7. If the candidates have the same distances of 90 pc from Earth as HAT-P-17, the absolute magnitudes are estimated to be $M_H = 15.41 \pm 0.21$, 15.24 ± 0.21, 13.91 ± 0.20. Assuming the age of HAT-P-17 of 7.8 ± 3.3 Gyr (Howard et al., 2012) and based on the COND model, the companion candidates have $\sim 0.06 M_{\odot}$, $\sim 0.06 M_{\odot}$, and $\sim 0.07 M_{\odot}$, for B, C, and D, respectively. Orbital periods can be calculated to be 5 kyr, 20 kyr and 40 kyr for B, C and D, respectively, on the assumption that they orbits HAT-P-17 and their semi-major axes are the same distances as their projected separations.

Kozai timescales for the planet HAT-P-17b at the current position are 13 Gyr, 200 Gyr and 800 Gyr for B, C, and D, respectively. Therefore, we rule out the direct Kozai effects from B, C or D upon b. However, HAT-P-17 has another planet, HAT-P-17c, whose orbital period, semi-major axis and mass are estimated to be $P_c = 1610 \pm 20$ days, $a_c = 2.555 \pm 0.041$ AU and $m_c \sin i_c = 1.31^{+0.18}_{-0.15} M_J$ (Howard et al., 2012), or $P_c = 5584^{+7770}_{-2100}$ days, $a_c = 5.6^{+3.5}_{-1.4}$ AU, and $m_c \sin i_c = 3.4^{+1.1}_{-0.7} M_J$ (Fulton et al., 2013), respectively. Note that the both semi-major axes are larger than the snow line for HAT-P-17 of 2.0 AU. If the planet c is affected on a Kozai timescale of ~ 80 Myr, ~ 1 Gyr, and ~ 5 Gyr for the Howard parameters, or ~ 20 Myr, ~ 400 Myr, and ~ 1 Gyr for the Fulton parameters, for B, C and D, respectively, it is possible for the companion candidate B (both the Howard and Fulton parameters) and the companion candidate C (only the Fulton parameters) to effectively have a power to oscillate c's orbit. In these cases, according to Takeda et al. (2008), the "sequential" Kozai migration may be effective. Namely, Kozai effects are induced to both the inner planet b and the outer planet c, and then c affects b additionally on a timescale written as

$$P_{SK} \sim \frac{P_c^2}{P_b} \frac{M_*}{m_c} \tag{5.3}$$

(Takeda et al., 2008). Because the additional Kozai timescale for b at the current position is calculated to be ~ 500 kyr for the Howard parameters or ~ 2 Myr for the Fulton parameters supposing $i_c = 90°$, it is possible that the companion B or C, if bound, has oscillated the outer planet c, and then the planet has sequentially oscillated the inner planet b and tilted its orbital axis, though depends on the c's parameters. Although the relativistic effect for the current b is estimated to be shorter ($P_{GR} \sim 100$ kyr) than P_{SK}, it also strongly depends on a previous position of the planet b.

Meanwhile, the TRILEGAL model estimates the number of background star in the FOV to be two. Based on the calculation, the companion candidates may be background stars.
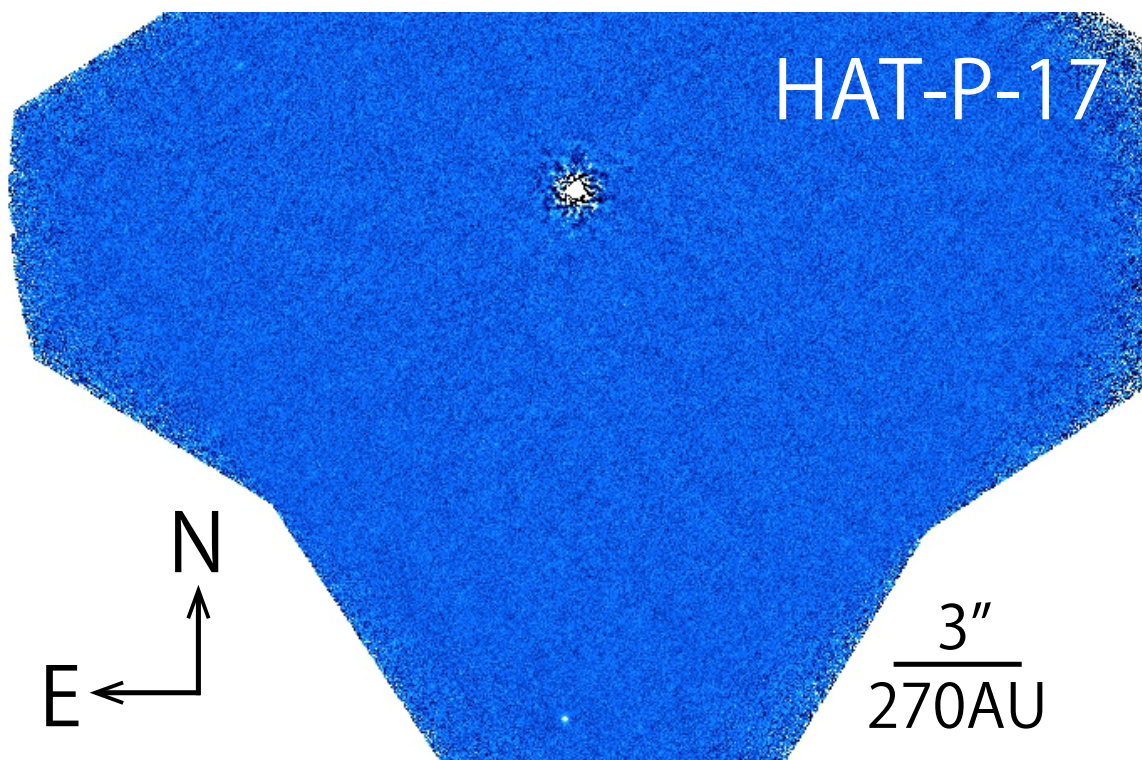
Figure 5.25: A final image of HAT-P-17 at *H* band. North is up and east is to the left. One object can be clearly found to the south in addition to two faint objects in the field.
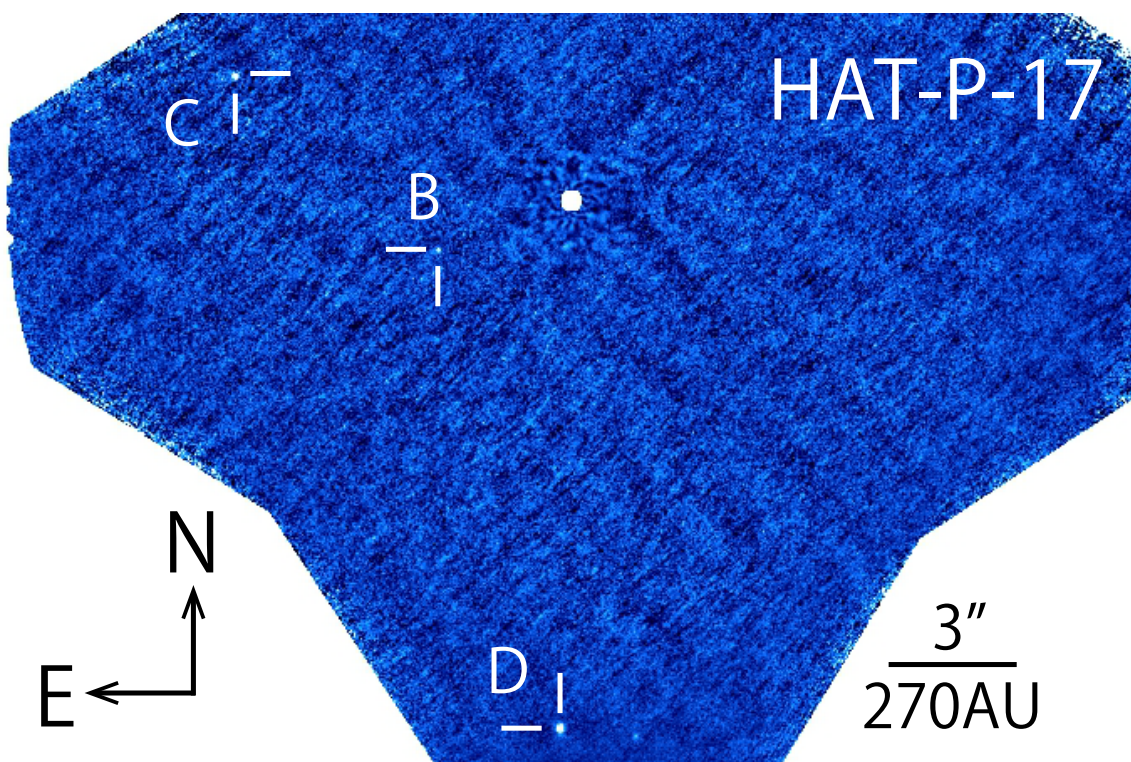
Figure 5.26: An S/N map of HAT-P-17 at *H* band. North is up and east is to the left. Three Objects are indicated by the crosses and labeled. The marginally detected object can be seen near D.
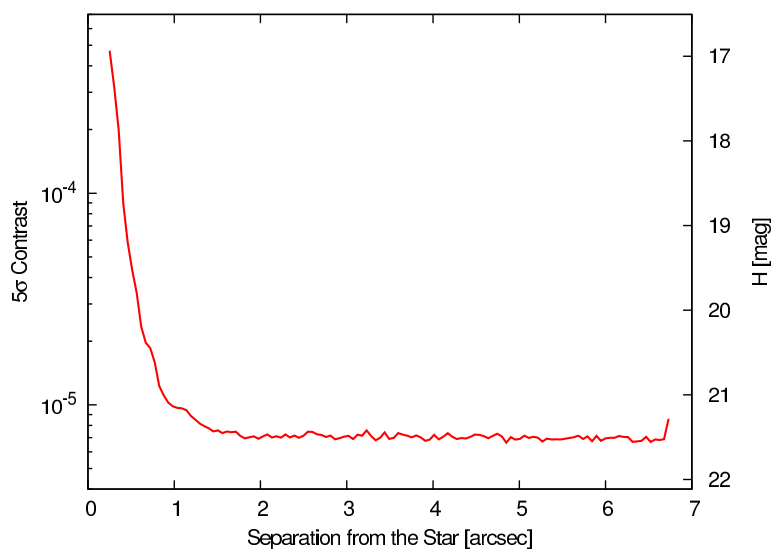
Figure 5.27: A 5σ contrast curve for HAT-P-17. The vertical axes show the contrast in the log scale (left) and the apparent magnitude *H* (right). The horizontal axis shows the separation from HAT-P-17.
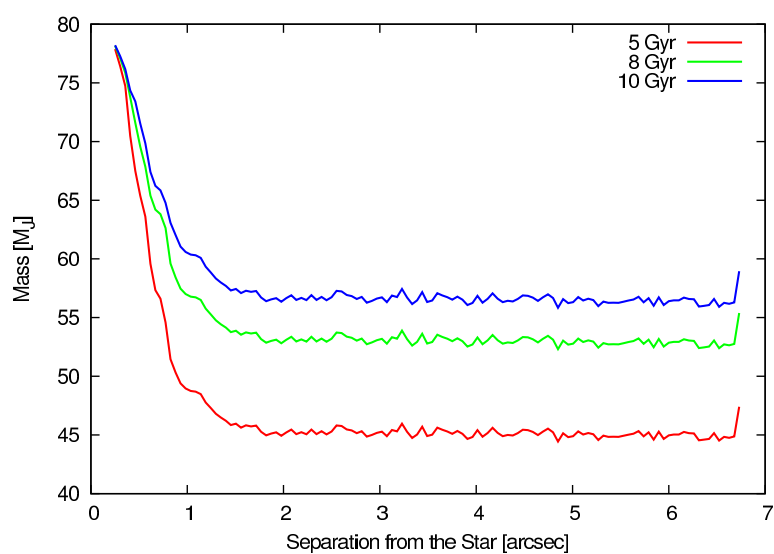
Figure 5.28: Five-σ contrast curves for HAT-P-17 in mass in a unit of the Jupiter mass converted with the COND model. The horizontal axis shows the separation from HAT-P-17. The colors represent ages.

Table 5.15: Detected Companion Candidates in the HAT-P-30 system

Name	Date (UT)	Filter	Sep. ($''$)	PA (deg)	Δm (mag)
HAT-P-30 B	2012-01-02	H	3.827 ± 0.004	4.21 ± 0.04	3.40 ± 0.06
HAT-P-30 C	2012-01-02	H	10.48 ± 0.01	52.35 ± 0.04	7.70 ± 0.14

The object written in italic is estimated to be an unrelated object.

5.6.8   HAT-P-30/WASP-51

We detected two companion candidates and obtained their properties at H band. A final image and contrasts are shown in Figure 5.29 and Figures 5.30 and 5.31, respectively. While one of the companions was reported by Adams et al. (2013), the other was not reported. According to Adams et al. (2013), the companion B, separated by $3.''8$, has a contrast of $\Delta Ks = 2.92$, resulting in an apparent magnitude of $Ks = 12.07$. On the other hand, our results of B represent a magnitude difference of $\Delta H = 3.40$ and, therefore, an apparent magnitude of $H = 12.62 \pm 0.07$. A resultative color of $H - Ks = 0.55$ is, however, slightly different from $H - Ks = 0.2$-0.3, derived from a mass estimate of $\sim 0.5 M_\odot$ using the NextGen model, and a given age of ~ 1 Gyr (Johnson et al., 2011) and an obtained absolute magnitude of $M_H = 6.19 \pm 0.11$ on the assumption that B has the same distance as HAT-P-30. Although the marginal disagreement may suggest that B is a background/foreground star, we here assume HAT-P-30 B is a candidate companion orbiting HAT-P-30 based on a calculation by the TRILEGAL model (zero within $\sim 3.''8$).

If B is a physical companion, B has an orbital period of ~ 15 kyr. For a planet at the current position of HAT-P-30b, a Kozai timescale is estimated to be ~ 70 Gyr. Similarly, we calculate the timescale to be ~ 70 Myr for a planet at the snow line (4.2 AU for HAT-P-30), while the relativistic timescale is presumed to be $P_{GR} \sim 900$ Myr for a circular orbit. The timescales are consistent with a possible scenario that HAT-P-30b formed and was affected by B in the outer regions, and then migrated into the current position, if B is really bound. It is necessary to confirm B's character to discuss the migration scenario for HAT-P-30b.

The other companion candidate C, separated by $10.''5$, has a $\Delta H = 7.7$, leading to an apparent magnitude of $H = 16.92 \pm 0.14$. According to the 2MASS catalog (Skrutskie et al., 2006), an object located at $08^h 15^m 48.^s 518$, $+05°50'18.''77$ has an H magnitude of $H = 16.280 \pm 0.296$, which agrees with our companion candidate C. Because of the long interval between our observations and 2MASS observations (2000-01-28), we can examine the CPM. The relative coordinates to the main star varied from $(\Delta\alpha, \Delta\delta) = (+8.''10, +6.''58)$ to $(+8.''30, +6.''40)$ with the interval of 12 years. If C is a background star and fixed at the constant position, the relative relation varies by HAT-P-30's proper motion of $(\mu_\alpha \cos\delta, \mu_\delta) = (-15.2 \pm 1.8, 23.4 \pm 1.7)$ mas/yr (van Leeuwen, 2007). Based on the 2MASS position, the relative coordinates are estimated to be $(\Delta\alpha, \Delta\delta) = (+8.''28 \pm 0.''02, +6.''30 \pm 0.''02)$ on our observational date (only the PM errors considered). They are congruous with our measurements considering the position errors. Hence, we conclude that HAT-P-30 C is a background star.

Table 5.15 summarizes the properties of the companion candidates, and no other objects (especially an object reported by Enoch et al. 2011) were not detected.
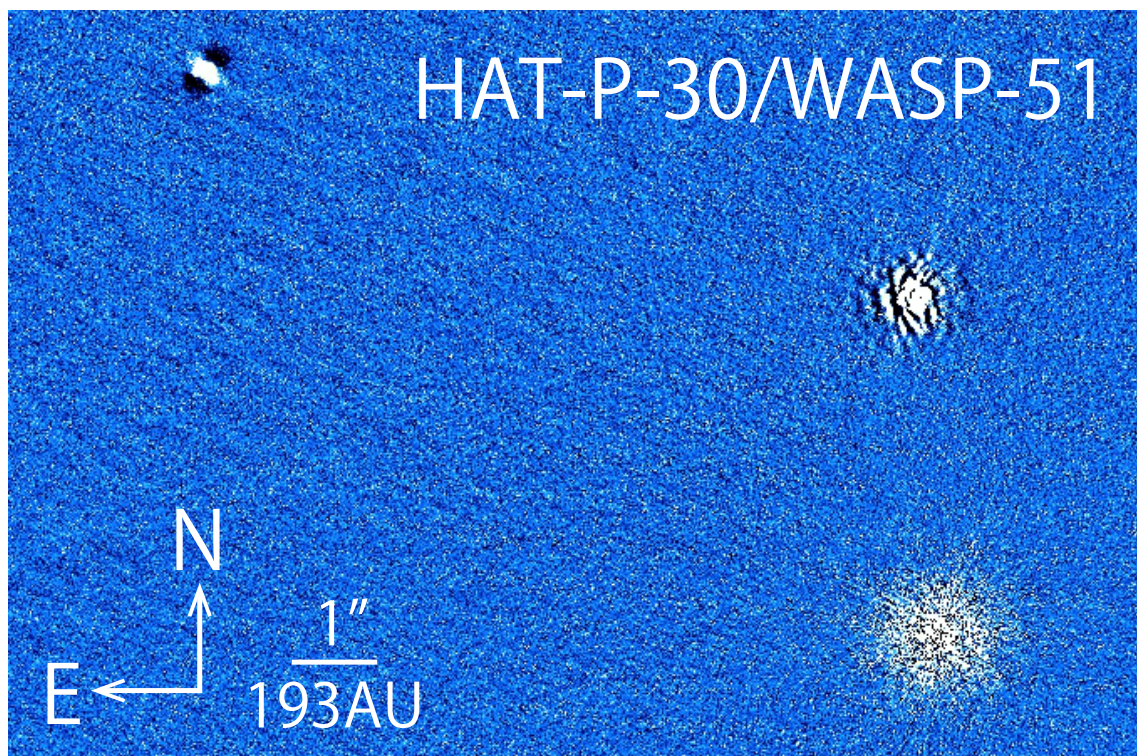
Figure 5.29: A final image of HAT-P-30 at *H* band reduced with the classical ADI. North is up and east is to the left. The main star suppressed by the reduction is located at west-southern side. A brighter companion candidate (HAT-P-30 B) is located at northern side from the main star, and a fainter object (HAT-P-30 C) with the dark tails is mapped at northeastern side.
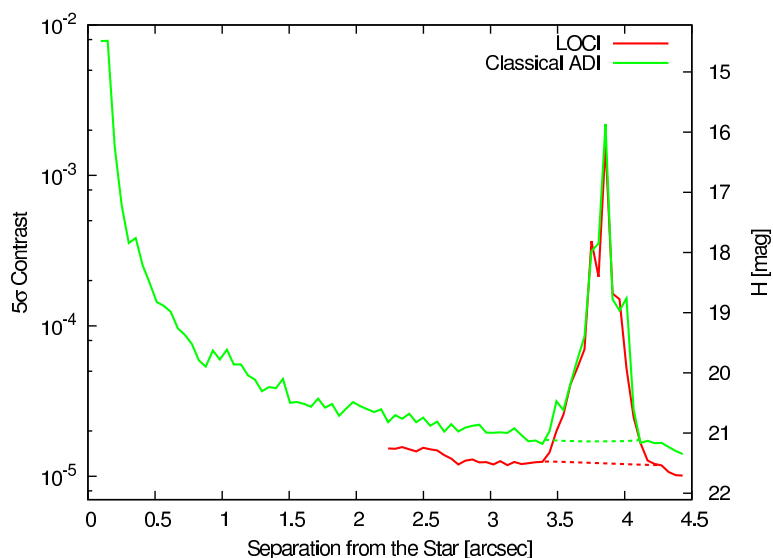
Figure 5.30: Five-σ contrast curves for HAT-P-30. The vertical axes show the contrast in the log scale (left) and the apparent magnitude H (right). The horizontal axis shows the separation from HAT-P-30. The dotted lines correct the anomalies at $\sim 3\rlap{.}''8$ induced by the bright companion candidate with interpolations.
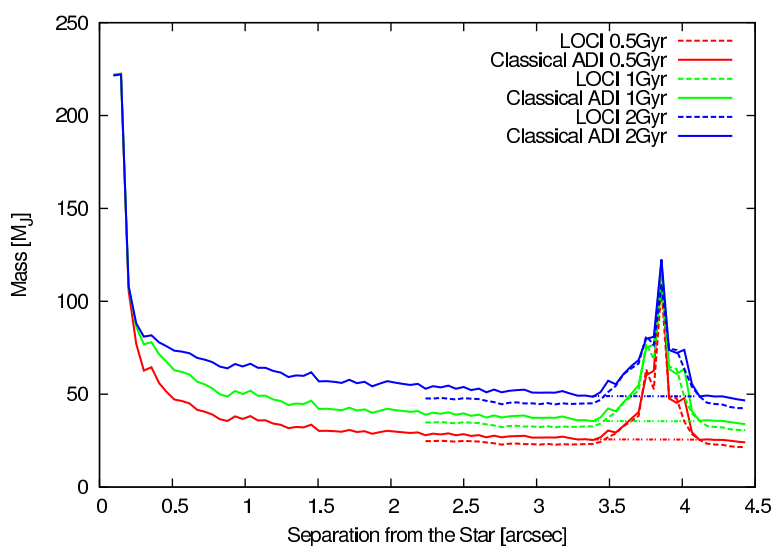
Figure 5.31: Five-σ contrast curves for HAT-P-30 in mass in a unit of the Jupiter mass converted with the COND model. The horizontal axis shows the separation from HAT-P-30. The solid and dotted lines show the data reduced with the classical ADI method and LOCI, respectively. The colors represent ages. The dash-dotted lines correct the anomalies at $\sim 3\rlap{.}''8$ induced by the bright companion candidate with interpolations.

Table 5.16: A Detected Companion Candidate in the HAT-P-32 system

Name	Date (UT)	Filter	Sep. ($''$)	PA (deg)	Δm (mag)
HAT-P-32 B	2012-09-12	H	2.769 ± 0.003	110.62 ± 0.03	3.85 ± 0.03

5.6.9 HAT-P-32

Our observations with high contrasts (see Figures 5.33 and 5.34) revealed that HAT-P-32 has a known companion candidate (Adams et al., 2013) separated by $2''8$ (see Figure 5.32). The results are summarized in Table 5.16. The object (hereafter HAT-P-32 B) has a relative magnitude of $\Delta H = 3.9$ to the main star HAT-P-32, resulting in an apparent magnitude of $H = 13.87 \pm 0.04$ and an absolute magnitude of $M_H = 6.34 \pm 0.11$. Here, we assume it to be a physical companion without respect of a magnitude of Adams et al. (2013). Given its absolute magnitude and the system's age of 3.8 Gyr (Hartman et al., 2011) and based on the NextGen model, it would be an M-type star with a mass of $\sim 0.45 M_\odot$ with an effective temperature of $T_{\mathrm{eff}} \sim 3500$ K. With a magnitude difference of $\Delta Ks = 3.4$ (Adams et al., 2013), a color of $H - Ks = 0.5$ shows a little of inconsistency with our estimate of $H - Ks = 0.25$, but not so serious. The CPM test is not executable due to a short time interval of eleven months. Although the color difference may support B being an unbound star, precise astrometry and precise photometry at other wavelengths are needed to confirm, considering with the TRILEGAL calculation of zero within $\sim 2''8$.

Assuming the candidate object being a physical companion to HAT-P-32 with a semi-major axis of the same value as its projected distance, its orbital period is calculated to be ~ 20 kyr. In case of a circular orbit, we estimate a Kozai timescale to be ~ 200 Gyr, suggesting that it is difficult to explain. For a hypothetical planet at the snow line (3.7 AU for HAT-P-32), the timescales get to be $P_{\mathrm{Kozai}} \sim 200$ Myr and $P_{\mathrm{GR}} \sim 700$ Myr, possibly enabling us to interpret Kozai mechanism as a source of the migration of HAT-P-32b.
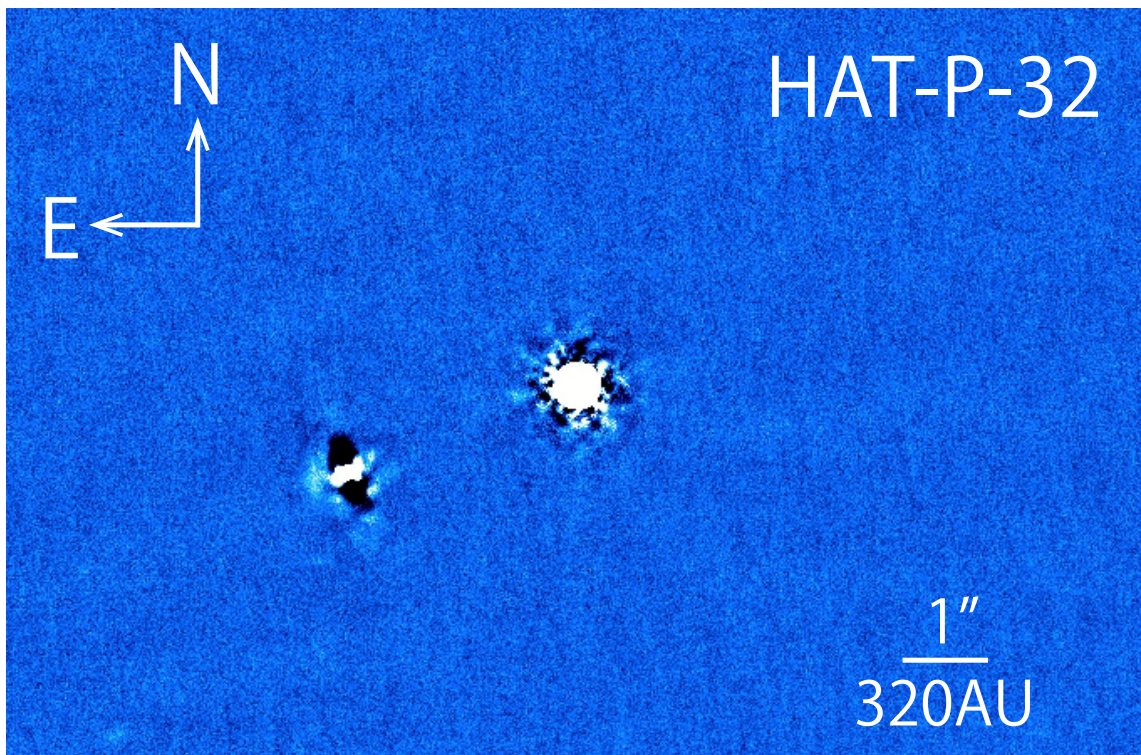
Figure 5.32: A final image of HAT-P-32 at H band. North is up and east is to the left. A companion candidate with the dark tails can be seen.
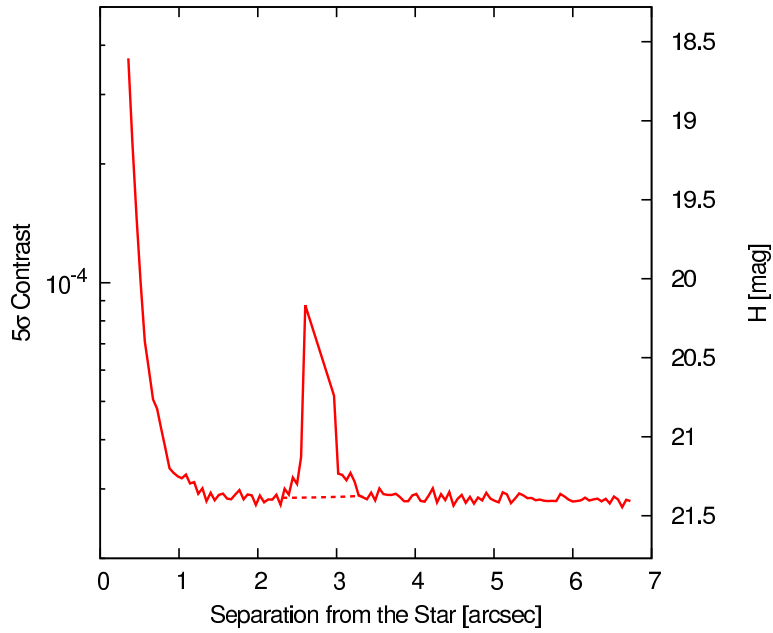
Figure 5.33: A 5σ contrast curve for HAT-P-32. The vertical axes show the contrast in the log scale (left) and the apparent magnitude H (right). The horizontal axis shows the separation from HAT-P-32. The dotted line corrects the anomaly at $\sim 2''\!8$ induced by the bright companion candidate with an interpolation.
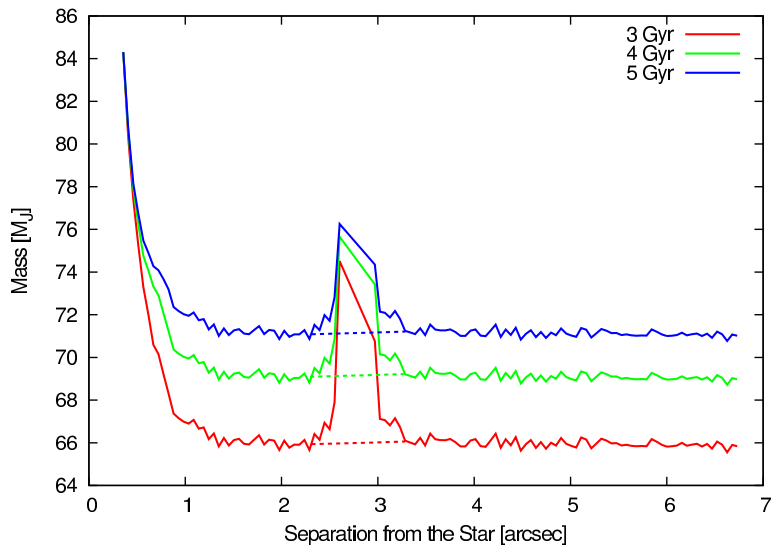

Figure 5.34: Five-σ contrast curves for HAT-P-32 in mass in a unit of the Jupiter mass converted with the COND model. The horizontal axis shows the separation from HAT-P-32. The colors represent ages. The dotted lines correct the anomalies at $\sim 2''\!8$ induced by the bright companion candidate with an interpolation.

Table 5.17: Detected Companion Candidates in the TrES-4 system

Name	Date (UT)	Filter	Sep. ($''$)	PA (deg)	Δm (mag)
TrES-4 B	2011-05-21	H	1.560 ± 0.002	0.20 ± 0.05	3.49 ± 0.11
		Ks	1.566 ± 0.002	0.22 ± 0.07	3.49 ± 0.12
TrES-4 C	2011-05-21	H	8.125 ± 0.008	249.01 ± 0.03	4.42 ± 0.17
		Ks	8.161 ± 0.009	249.02 ± 0.04	4.56 ± 0.24

The object written in italic is estimated to be an unrelated object.

5.6.10   TrES-4

We discovered two bright objects and name them as "TrES-4 B" and "C" (clearly detected in 5.35). The results are summarized in Table 5.17. Our observations reached $\Delta H \simeq 20$ (see Figure 5.36) and $M_{\text{limit}} \simeq 80 M_{\text{J}}$ (see Figure 5.37) based on the COND model (Baraffe et al., 1998) for outer regions. TrES-4 B was reported and measured by Daemgen et al. (2009) and Bergfors et al. (2013), but they observed in the optical regions. Consequently we can compute the mass of TrES-4 B combining with our results in the infrared wavelengths, though the CPM test cannot be examined due to its small proper motion. Given the age of 2.9 ± 0.3 Gyr and the distance of 479 ± 26 pc (Chan et al., 2011), a derived absolute H magnitude of $M_H = 5.01 \pm 0.16$ and an infrared color of $H - Ks = 0.02 \pm 0.16$ lead to a late K type star with an estimated mass of $\sim 0.65 M_\odot$ and an effective temperature of ~ 4000 K (the NextGen model). Our estimates are consistent with the SDSS magnitudes of $i = 15.44 \pm 0.1$ and $z = 15.20 \pm 0.1$, and a color of $i - z = 0.36 \pm 0.14$ (Bergfors et al., 2013), suggesting that this companion candidate has the same age and distance as the main star. Hence, we conclude that TrES-B is a physical companion star.

If the companion has a circular ($e_B = 0$) orbit with a semi-major axis, $a_B = a_{B,\text{proj}} = 747 \pm 41$ AU, the orbital period is estimated to be 1.4×10^4 yr. On the other hand, the timescale of Kozai migration is calculated to be 43 Gyr on the assumption that the planet TrES-4b stays at the current position, which is longer than the system's age. It means that Kozai mechanism was not able to affect the planet at the current position. In contrast, $P_{\text{Kozai}} \sim 40$ Myr for a hypothesis planet at 5.2 AU, the position of the snow line for TrES-4, suggesting Kozai mechanism was fully able to have a power to carry the planet, comparing with $P_{\text{GR}} \sim 1$ Gyr. The values are consistent with a possible migration scenario that TrES-4b formed at outer regions, and migrated inward with tilting its orbital axis, affected by TrES-4 B.

Meanwhile, TrES-4 C has not been reported so far. The object is estimated to have a significantly blue color of $H - Ks = -0.14 \pm 0.29$, which indicates a B type star, though its error is large, though its error is large. If the B-type star is physically bound to TrES-4, it is considerably brighter than the main star. However, the star is fainter at H and Ks than the main star, TrES-4. This result suggests that C be a background star, not a real companion. Even if C is bound to TrES-4, it is unlikely that C causes Kozai mechanism because of the large distance of 3900 AU.
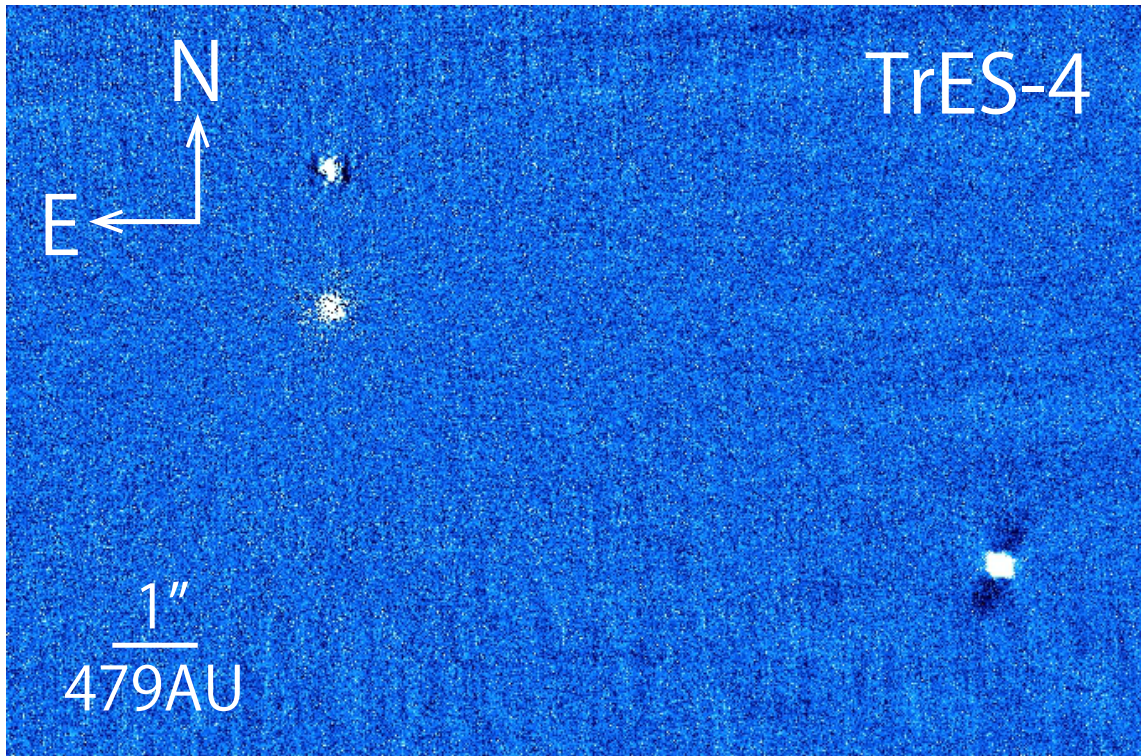
Figure 5.35: A final image of TrES-4 at *H* band reduced with the classical ADI method. North is up and east is to the left. Two companion candidates can be found; one is located to the north from the main star (named as TrES-4 B), and the other lies to the southwestern (named as TrES-4 C).
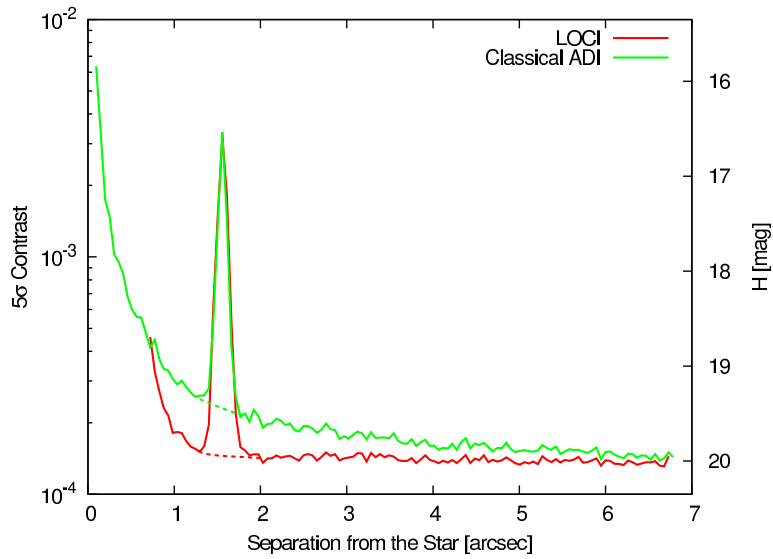
Figure 5.36: Five-σ contrast curves for TrES-4. The vertical axes show the contrast in the log scale (left) and the apparent magnitude *H* (right). The horizontal axis shows the separation from TrES-4. The red and green lines represent data reduced with LOCI and the classical ADI method, respectively. The dotted lines correct the anomalies at ∼ 1″6 induced by the bright companion candidate with interpolations.
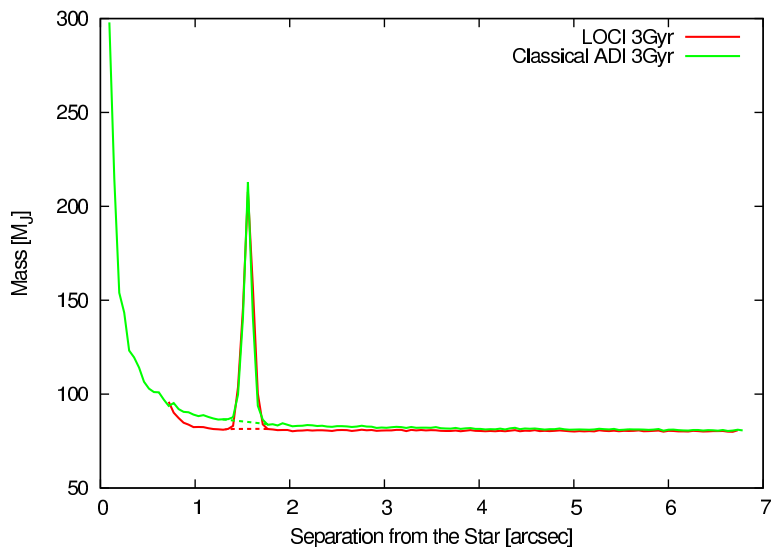
Figure 5.37: Five-σ contrast curves for TrES-4 in mass in a unit of the Jupiter mass converted with the COND model. The horizontal axis shows the separation from TrES-4. The colors represent ages. The dotted lines correct the anomalies at ∼ 1″6 induced by the bright companion candidate with an interpolation.

Table 5.18: A Detected Companion Candidate in the WASP-8 system

Name	Date (UT)	Filter	Sep. ($''$)	PA (deg)	Δm (mag)
WASP-8 B	2011-09-03	H	4.500 ± 0.007	170.89 ± 0.07	2.58 ± 0.12
		Ks	4.523 ± 0.005	170.89 ± 0.05	2.41 ± 0.07

5.6.11 WASP-8

We detected a reported companion with a spectral type of M (Queloz et al., 2010), but no additional objects in the system (see Figure 5.38) in spite of our high-contrast observations (the contrasts are shown in Figures 5.39 and 5.40). Our results are summarized in Table 5.18. The color of $H - Ks = 0.30 \pm 0.15$ is consistent with their measurements of $H - Ks = 0.2$ derived from 2MASS images, though our contrasts to the main star is slightly larger than their measurements. The infrared color leads to an early M to a late K type with $M_* \sim 0.5 M_\odot$ and $T_{\text{eff}} \sim 3600$ K using the NextGen model. Comparing the relative position on the 2MASS catalog, $(\Delta\alpha, \Delta\delta) = (+0''69, -3''97)$ obtained on JD $= 2451401.7563$, to our H-band positions of $(+0''71, -4''44)$ on JD $= 2455807.9493$, a proper motion of WASP-8 of $(\mu_\alpha \cos\delta, \mu_\delta) = (110.2, 7.7)$ mas/yr (Høg et al., 2000) cannot explain the relative motion. We thus confirm WASP-8 B is physically associated with WASP-8.

Considering that the companion's orbit is circular with a semi-major axis of $a_{\text{B}} = a_{\text{B,proj}} = 87\text{pc} \times 4''5 = 390$ AU and a resultant period of 6 kyr, a Kozai timescale for the planet WASP-8b is estimated to be $P_{\text{Kozai}} \sim 3$ Gyr for the current position and $P_{\text{Kozai}} \sim 6$ Myr for a planet at a position of the snow line (2.9 AU). Comparing with the system's age of 4 ± 1 Gyr (Queloz et al., 2010) and the timescale of the relativistic effect of $P_{\text{GR}} \sim 500$ Myr for a circular planet at the snow line, it is likely that Kozai mechanism affected a planet at outer regions and inclined the planet's orbital axis.
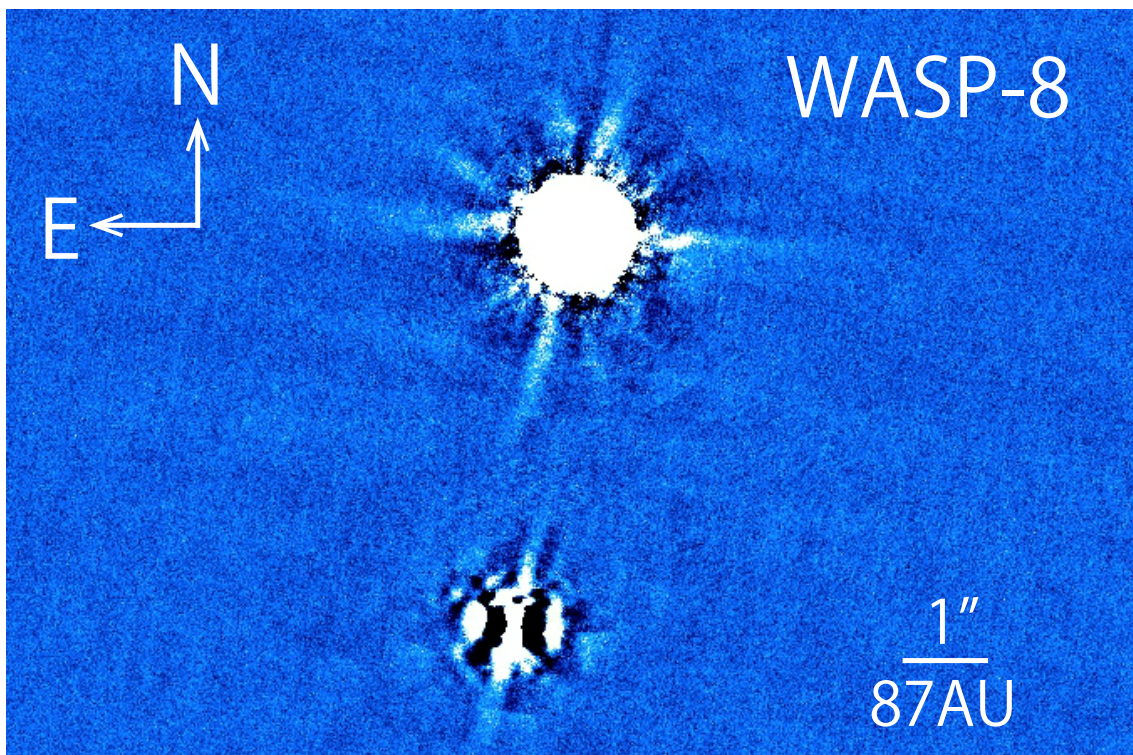
Figure 5.38: A final image of WASP-8 at *H* band. North is up and east is to the left. The known companion is clearly found in the figure.
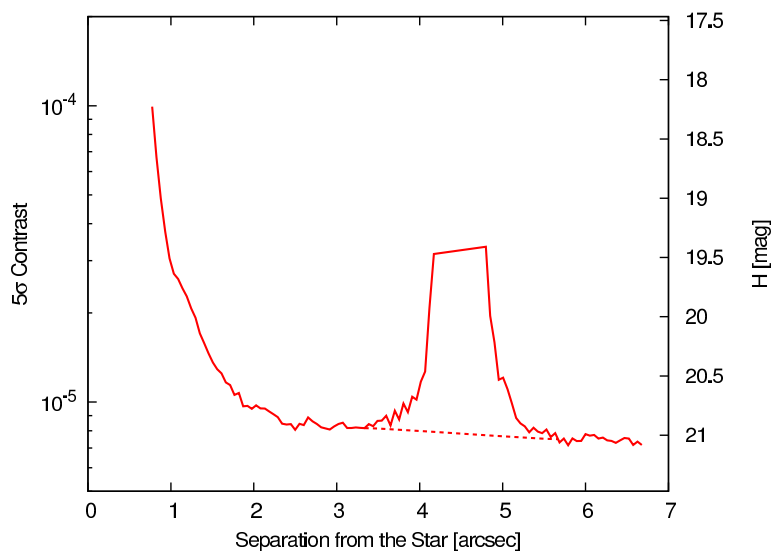

Figure 5.39: A 5σ contrast curve for WASP-8. The vertical axes show the contrast in the log scale (left) and the apparent magnitude *H* (right). The horizontal axis shows the separation from WASP-8. The dotted line corrects the anomaly at $\sim 4\rlap{.}''5$ induced by the bright companion candidate with an interpolation.
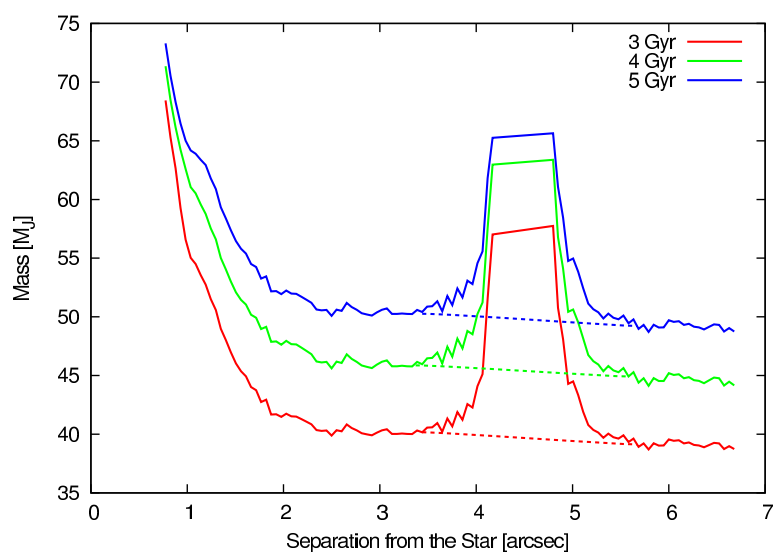
Figure 5.40: Five-σ contrast curves for WASP-8 in mass in a unit of the Jupiter mass converted with the COND model. The horizontal axis shows the separation from WASP-8. The colors represent ages. The dotted lines correct the anomalies at $\sim 4\rlap{.}''5$ induced by the bright companion candidate with interpolations.

Table 5.19: Detected Companion Candidates in the WASP-12 system

Name	Date (UT)	Filter	Sep. ($''$)	PA (deg)	Δm (mag)
WASP-12 B	2012-11-07	*H*	1.061 ± 0.001	251.42 ± 0.07	2.80 ± 0.10
		Ks	1.067 ± 0.002	251.61 ± 0.09	2.81 ± 0.04
WASP-12 C	2012-11-07	*H*	1.068 ± 0.001	247.13 ± 0.10	3.17 ± 0.05
		Ks	1.072 ± 0.002	246.94 ± 0.11	3.00 ± 0.03
WASP-12 B/C	2012-11-07	*J*	1.059 ± 0.002	250.76 ± 0.10	3.33 ± 0.08

5.6.12   WASP-12

We confirmed two known companion candidates suggested by Bergfors et al. (2013) and angularly re-solved by Bechter et al. (2013) into "B" ($\Delta J = 3.81 \pm 0.05$ and $\Delta Ks = 3.25 \pm 0.04$) and "C" ($\Delta J = 3.92 \pm 0.05$ and $\Delta Ks = 3.28 \pm 0.04$). Our observations had a power of high angular resolution to dis-tinguish B and C at both *H* and *Ks* bands in Figure 5.42, but unfortunately failed at *J* band (Details in Table 5.19. The contrasts are shown in Figure 5.43 and 5.44). Measurements of astrometry result in consistent values with those in Bechter et al. (2013), though a proper motion of WASP-12 is so small that we cannot examine the CPM test. However, our photometry differs from theirs by about 0.3 mag, leading to different estimates of mass of $\sim 0.65 M_\odot$ (~ 4000 K) for B and $\sim 0.61 M_\odot$ (~ 3900 K) for C using absolute magnitudes M_H and colors $H - Ks$ with the NextGen model. The difference may be responsible to speckle noises or Airy rings in our images. No additional object was discovered in the LOCI-processed image (see Figure 5.41).

A period of the orbit of WASP-12 B/C around WASP-12 A is calculated to be $\sim 6 - 7$kyr for both mass estimates. Kozai timescales for a planet at the current position of WASP-12b is estimated to be ~ 10 Gyr for our results and ~ 30 Gyr for the results in Bechter et al. (2013), if the B/C binary orbits A circularly. In these cases, the planet could not be affected via Kozai effects. On the other hand, a Kozai timescale for a planet at the snow line for WASP-12 ($\simeq 5.0$ AU) with a planetary period of 6.9 yr is valued at $P_{\mathrm{Kozai}} \sim 6$ Myr for our estimates and $P_{\mathrm{Kozai}} \sim 13$ Myr for Bechter et al. (2013). Based on these calculations and the timescale of the relativistic effect of $P_{\mathrm{GR}} \sim 1$ Gyr for the position, the obliquity of the orbital axis of WASP-12b can be explained by Kozai effects of the WASP-12 B/C binary, regardless of the uncertainty of masses for B and C. If an additional and possible planet WASP-12c really exists (Maciejewski et al., 2013), the mechanism may be more complicated.
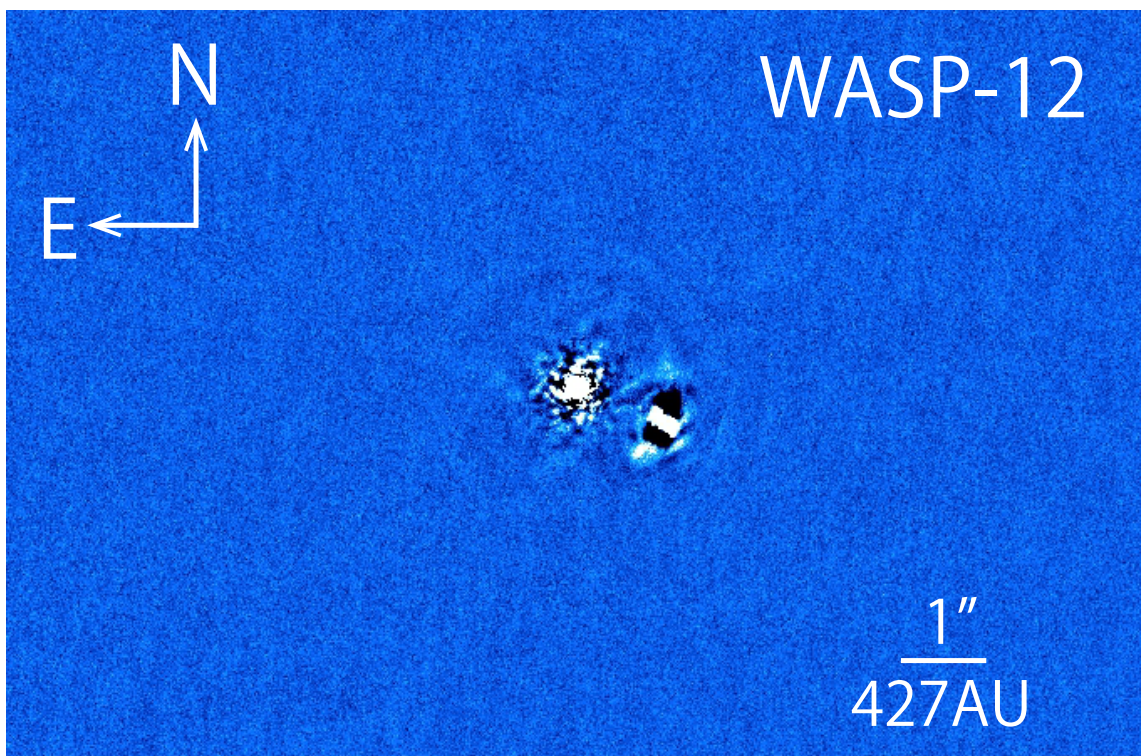
Figure 5.41: A final image of WASP-12 at *H* band reduced with LOCI. North is up and east is to the left. Two companion candidates can be seen to the west from the main star, but not resolved.
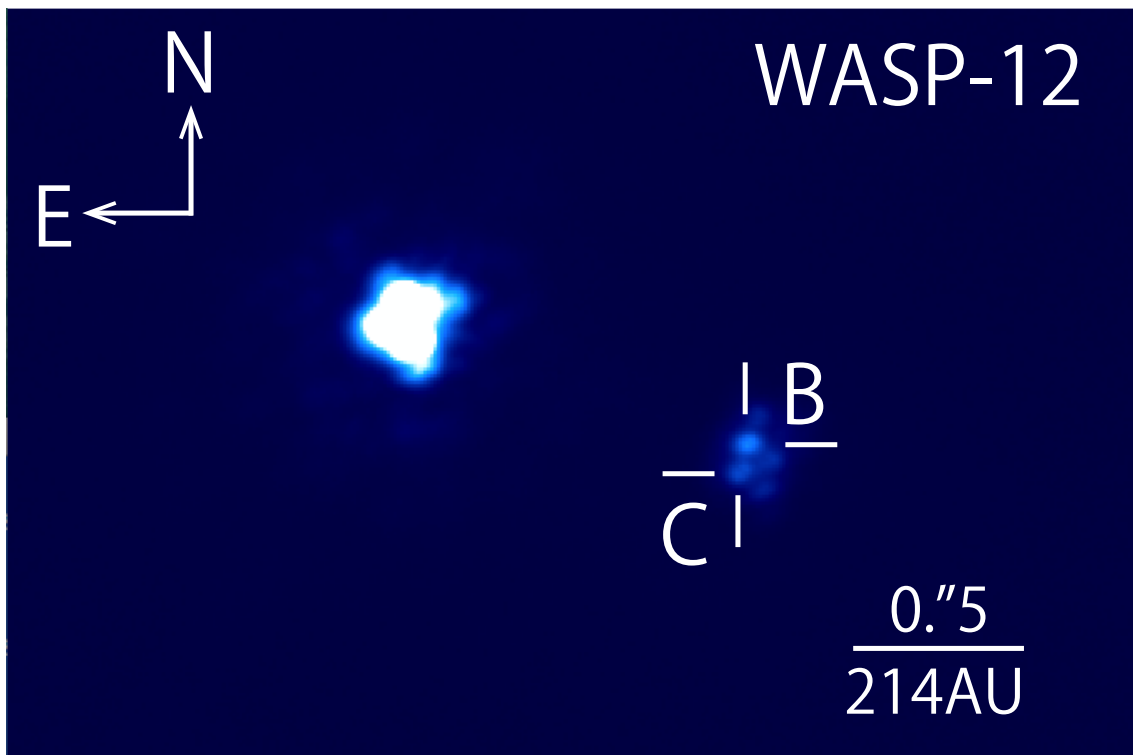
Figure 5.42: A combined WASP-12 image at *H* band. Companions are resolved into two faint stars with speckles. WASP-12 B and C are denoted by the crosses.
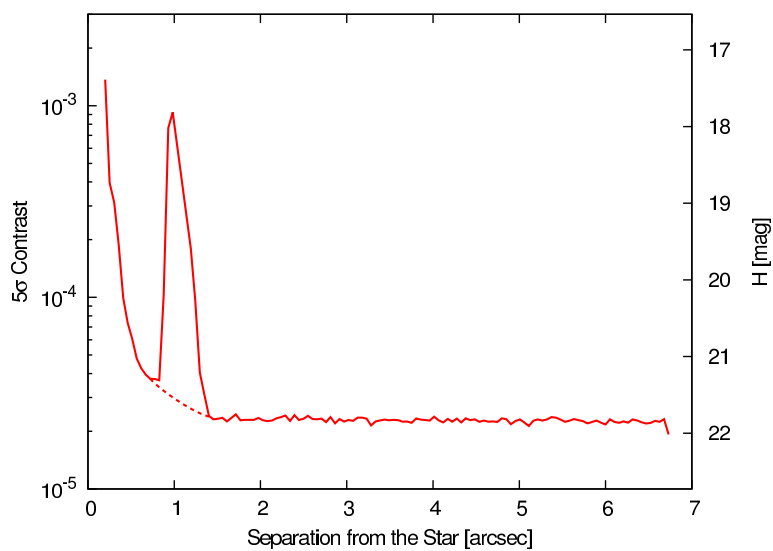

Figure 5.43: A 5σ contrast curve for WASP-12. The vertical axes show the contrast in the log scale (left) and the apparent magnitude *H* (right). The horizontal axis shows the separation from WASP-12. The dotted line corrects the anomaly at $\sim 1''1$ induced by the bright companion candidate with an interpolation.
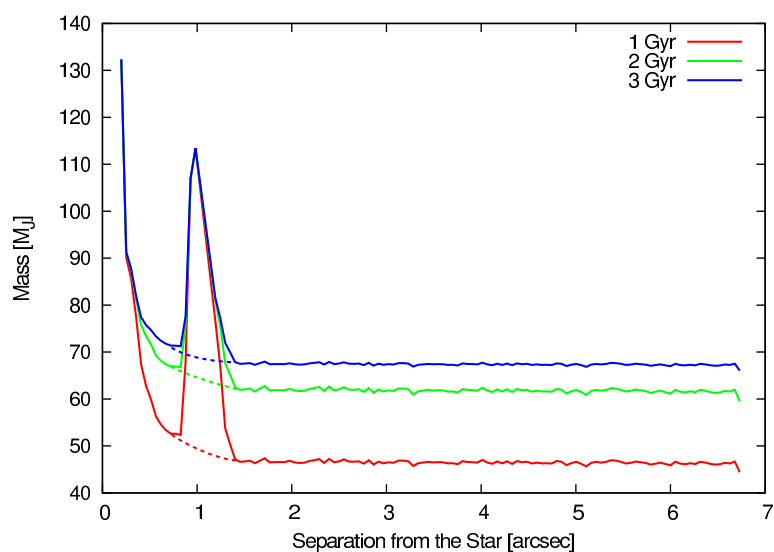
Figure 5.44: Five-σ contrast curves for WASP-12 in mass in a unit of the Jupiter mass converted with the COND model. The horizontal axis shows the separation from WASP-12. The colors represent ages. The dotted lines correct the anomalies at $\sim 1.\!''1$ induced by the bright companion candidate with interpolations.

Table 5.20: A Detected Companion Candidate in the WASP-14 system

Name	Date (UT)	Filter	Sep. ($''$)	PA (deg)	Δm (mag)
WASP-14 B	2011-01-25	H	1.446 ± 0.002	101.87 ± 0.06	5.17 ± 0.15

5.6.13   WASP-14

We first discovered an unknown companion candidate around WASP-14 in the final image (Figure 5.45). The object, named as "WASP-14 B," is located at $(\rho, \theta) = (1.''45, 102°)$ (see Table 5.20), converted into a projected distance of 230 AU. Contrasts of our observations are presented in Figures 5.46 and 5.47. Although we cannot conclude the object as a physical companion because of no additional reliable information except for an apparent magnitude of $H = 13.82 \pm 0.15$, an assumptive absolute magnitude of $M_H = 7.79 \pm 0.31$ can be translated into an M-type star with an effective temperature of $T_{\text{eff}} \simeq 3300$ K and a mass of $\sim 0.2 M_\odot$ based on the NextGen model if B has the same distance as WASP-14. Since the speed of its proper motion is ~ 30 mas/yr, the confirmation by the CPM test will be executable in some years. The TRILEGAL model calculates the number of background stars within $1.''45$ to be zero, supporting that B is a real companion.

If WASP-14 B is really bound to the main star WASP-14 A and its orbital semi-major axis is the same as its projected distance, it orbits A with a period of ~ 3 kyr. With B in a circular orbit, a Kozai timescale is estimated to be $P_{\text{Kozai}} \sim 8$ Gyr for WASP-14b at the current position, or $P_{\text{Kozai}} \sim 3$ Myr for a planet at the snow line with a distance of 3.9 AU. Compared to WASP-14's age (0.5-1.0 Gyr, Joshi et al. 2009) and $P_{\text{GR}} \sim 800$ Myr for a planet at the snow line, Kozai effects on the planet in the outer regions could be effective. The results are consistent with a scenario that WASP-14b migrated into the inner regions due to Kozai effects.
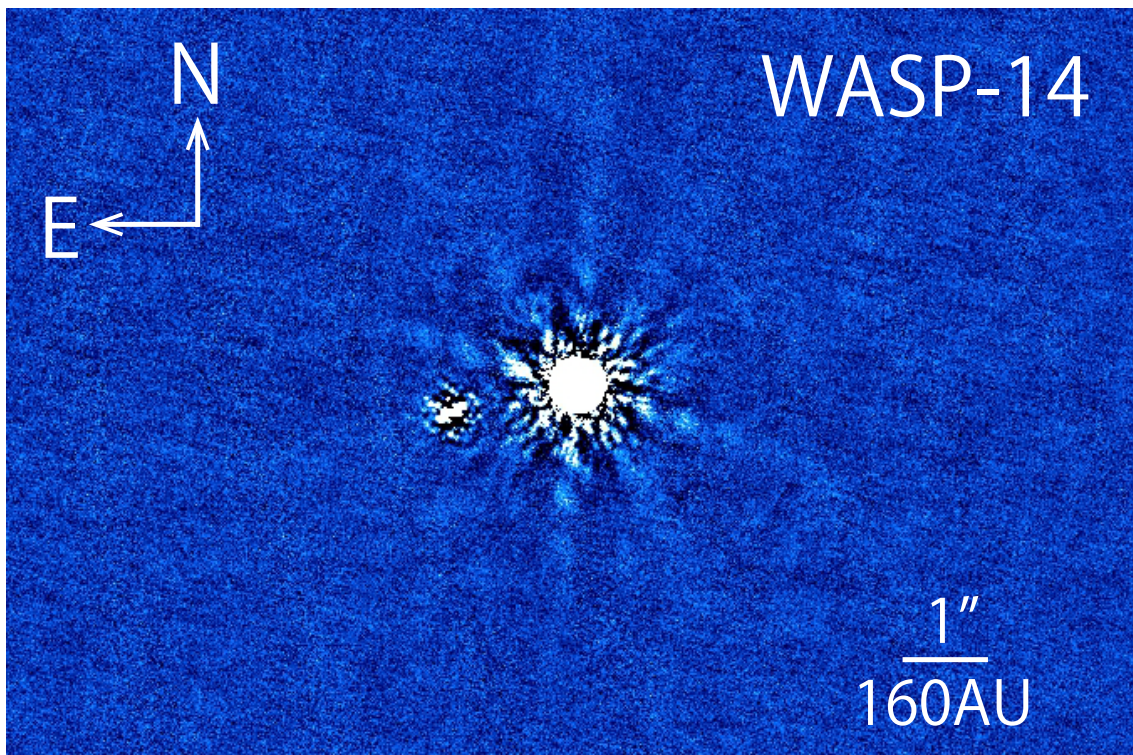
Figure 5.45: A final image of WASP-14 at H band. North is up and east is to the left. A companion candidate is located to the east.
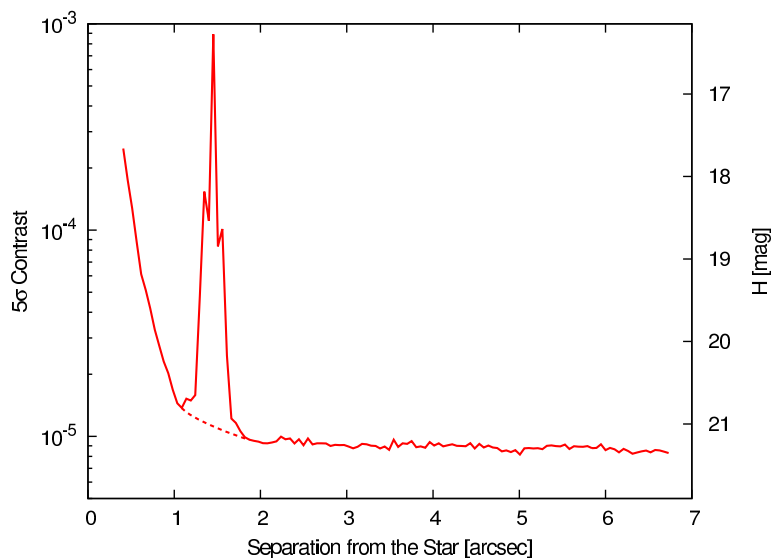

Figure 5.46: A 5σ contrast curve for WASP-14. The vertical axes show the contrast in the log scale (left) and the apparent magnitude H (right). The horizontal axis shows the separation from WASP-14. The dotted line corrects the anomaly at $\sim 1\rlap{.}''4$ induced by the bright companion candidate with an interpolation.
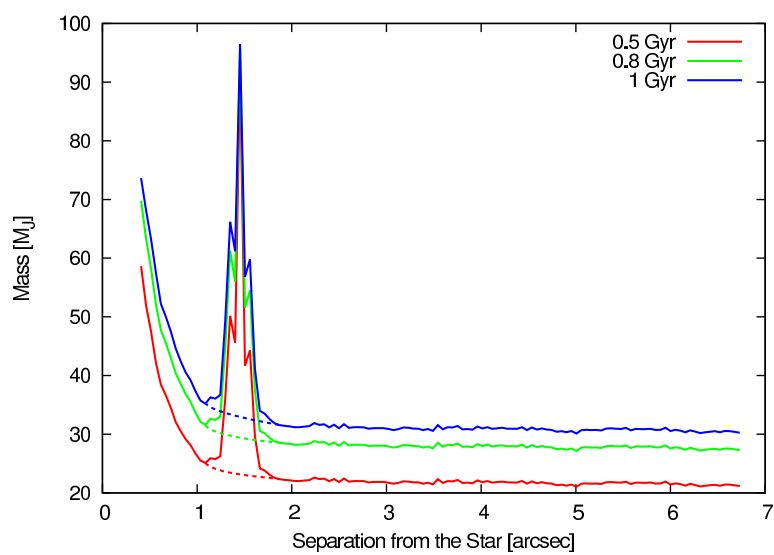
Figure 5.47: Five-σ contrast curves for WASP-14 in mass in a unit of the Jupiter mass converted with the COND model. The horizontal axis shows the separation from WASP-14. The colors represent ages. The dotted lines correct the anomalies at $\sim 1.''4$ induced by the bright companion candidate with interpolations.

Table 5.21: Detected Companion Candidates in the WASP-17 system

Name	Date (UT)	Filter	Sep. ($''$)	PA (deg)	Δm (mag)
WASP-17 B	2011-05-24	*H*	3.121 ± 0.003	203.23 ± 0.03	9.21 ± 0.05
WASP-17 C	2011-05-24	*H*	7.539 ± 0.008	257.28 ± 0.03	8.95 ± 0.05
WASP-17 D	2011-05-24	*H*	11.19 ± 0.01	200.12 ± 0.03	7.94 ± 0.05

5.6.14 WASP-17

We detected three companion candidates around WASP-17, named as WASP-17 B, C and D in close order, thanks to a high contrast (see Figures 5.49 and 5.50). Figure 5.48 presents their positions and properties are summarized in Table 5.21. Their relative magnitudes at *H* band are $\Delta H = 9.2$, 9.0 and 7.9, and can be converted into apparent magnitudes of $H = 19.53$, 19.23, and 18.26. In case these candidates are located at the same distance as WASP-17, their absolute magnitudes of $M_H = 11.5 \pm 0.3$, 11.3 ± 0.3 and 10.3 ± 0.3 indicate theoretical masses of $\sim 0.08 M_\odot$, $\sim 0.08 M_\odot$, and $\sim 0.09 M_\odot$ for B, C, and D, respectively, given WASP-17's age of ~ 2 Gyr and based on the Dusty model.

If the companion candidates have semi-major axes of 1200 AU, 3000 AU, and 4500 AU, which are the same value as their projected distances, their orbital periods are estimated to be 35 kyr, 140 kyr, and 260 kyr for B, C, and D, respectively. Kozai timescales derived from the periods for a planet at the current position of WASP-17b considerably exceed the system's age. Thus, Kozai effects of the companions are not effective for the present WASP-17b. On the other hand, we assume a planet at the snow line (4.6 AU for WASP-17) orbiting WASP-17 with a period of 8.6 yr. Kozai timescales for the planet are ~ 3 Gyr, 40 Gyr, and 100 Gyr for B, C, and D, respectively. Because the age of the system is estimated to be younger than 3 Gyr, Kozai effects were not efficient, suggesting planet-planet scattering occurred in the system and inclined b's orbital axis. The TRILEGAL model estimates 9 objects in the FOV, suggesting that the companions are background stars.
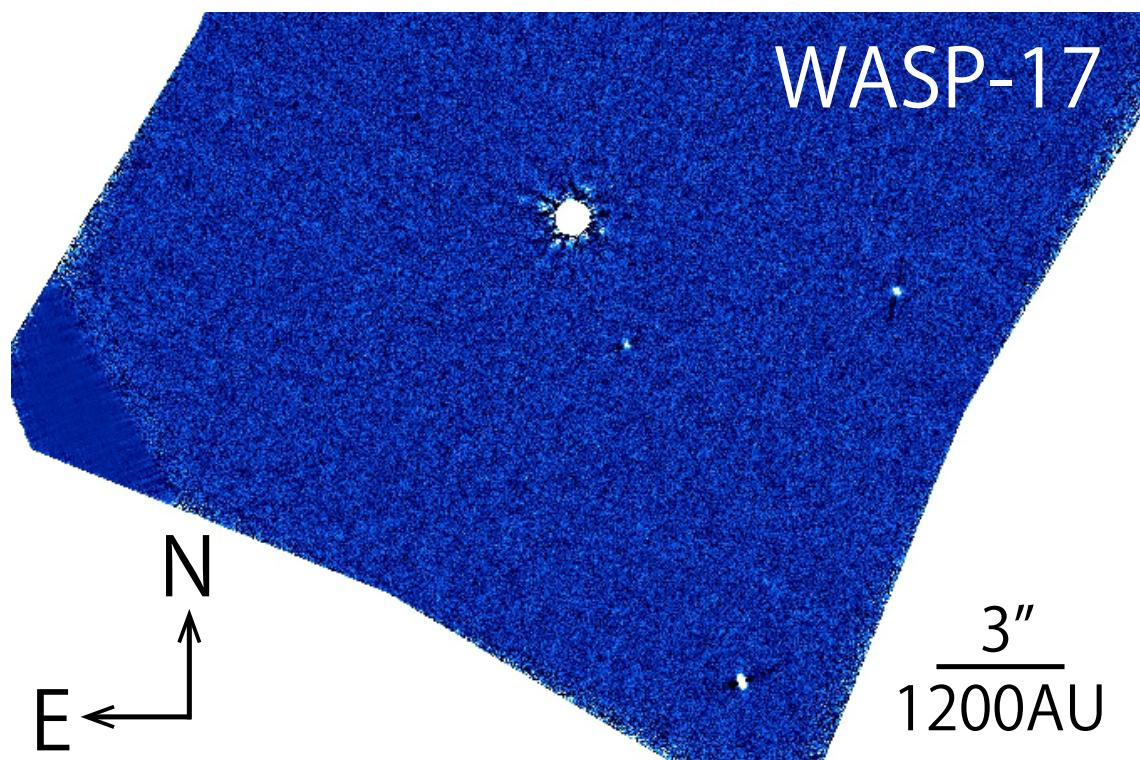
Figure 5.48: A final image of WASP-17 at *H* band. North is up and east is to the left. Three objects, named as WASP-17 B, C, and D in close order, can be seen in the field.
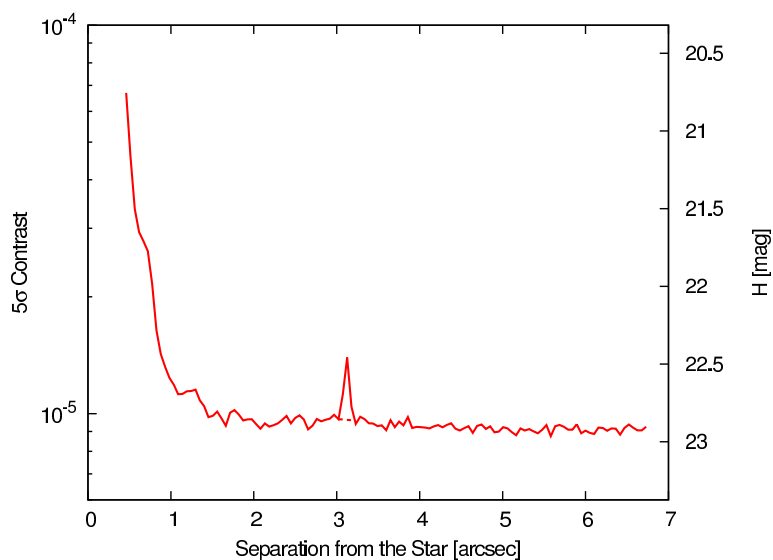
Figure 5.49: A 5σ contrast curve for WASP-17. The vertical axes show the contrast in the log scale (left) and the apparent magnitude *H* (right). The horizontal axis shows the separation from WASP-17. The dotted line corrects the anomaly at $\sim 3\farcs1$ induced by the bright companion candidate with an interpolation.
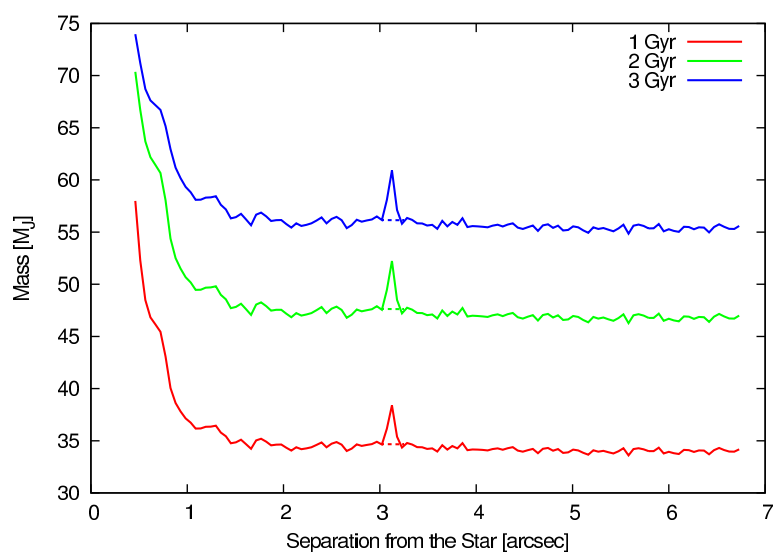
Figure 5.50: Five-σ contrast curves for WASP-17 in mass in a unit of the Jupiter mass converted with the COND model. The horizontal axis shows the separation from WASP-17. The colors represent ages. The dotted lines correct the anomalies at $\sim 3\rlap{.}''1$ induced by the bright companion candidate with interpolations.

Table 5.22: A Detected Companion Candidate in the WASP-33 system

Name	Date (UT)	Filter	Sep. ($''$)	PA (deg)	Δm (mag)
WASP-33 B	2010-12-01	H	1.925 ± 0.020	275.66 ± 0.33	7.31 ± 0.52

5.6.15   WASP-33

We detected a faint object WASP-33 B around WASP-33 (see Figure 5.51), reported by Moya et al. (2011). Our results showed a consistent values with theirs, $(\rho, \theta) = (1''9, 276°)$ and a slightly different magnitude of $\Delta H = 7.3$, and no additional object similarly in spite of high contrast imaging observations (see Figures 5.52 and 5.53). The properties of the object are collected in Table 5.22, whose errors, especially for the magnitude, are relatively large due to variable sky. The contrast at H band can be converted into $M_H = 13.81 \pm 0.56$, leading to a mass of $\sim 0.004 M_\odot$ with an effective temperature of ~ 1000 K for 10 Myr, $\sim 0.01 M_\odot$ with ~ 1200 K for 100 Myr, and $\sim 0.04 M_\odot$ with ~ 1300 K for 1 Gyr using the COND model, if bound. The TRILEGAL model also supports the boundship by its calculation of zero within $\sim 1''9$.

If B has an orbit hosted by WASP-33 with a semi-major axis of $a_B = a_{B,proj} = 116$ pc $\times 1''93 = 224$ AU, its orbital period is estimated to be ~ 3 kyr. Assuming its orbital eccentricity of 0, a Kozai timescale can be calculated to be ~ 800 Gyr for 10 Myr, ~ 300 Gyr for 100 Myr, ~ 80 Gyr for 1 Gyr. The values reveal that Kozai mechanism is inefficient for a planet at the current position. If a planet were at the snow line (6 AU for WASP-33) with a period of 12 yr, the timescale would be ~ 300 Myr for 10 Myr, ~ 100 Myr for 100 Myr, and ~ 30 Myr for 1 Gyr. Comparing with the system's ages and $P_{GR} \sim 2$ Gyr for a position of the snow line, ages of $\gtrsim 100$ Myr can explain Kozai mechanism for the WASP-33 system. For more investigation into the migration mechanism, it is important to decide the age.
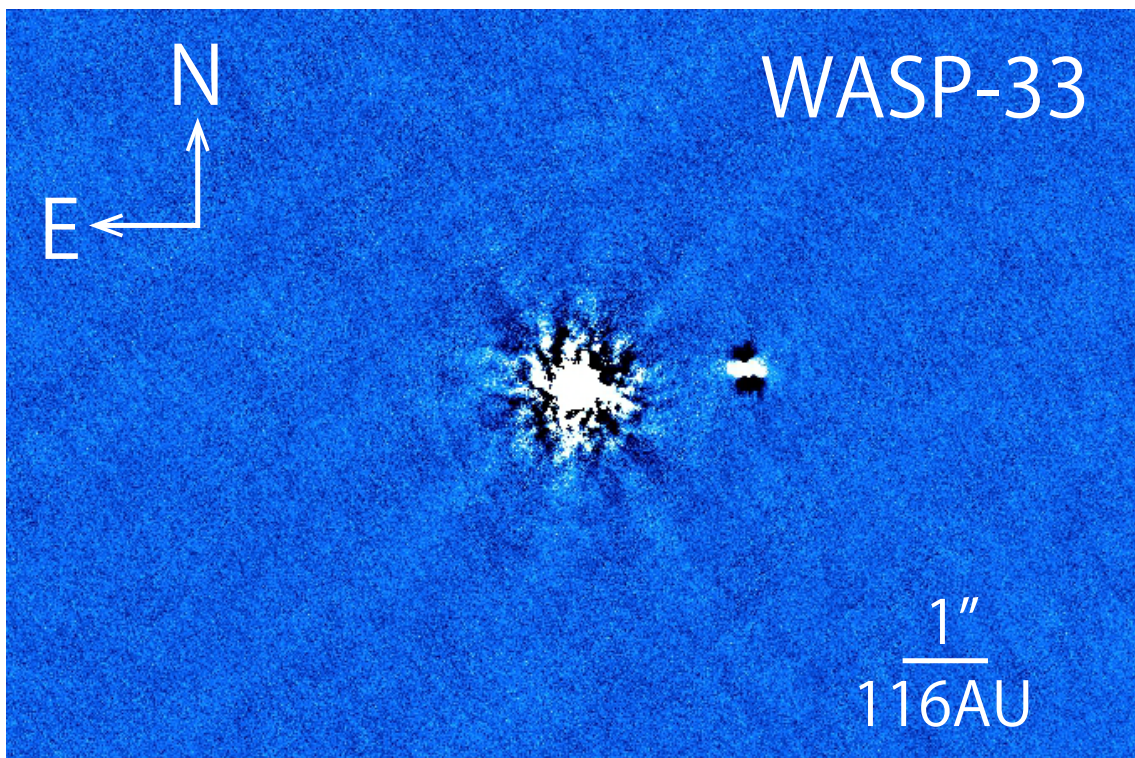
Figure 5.51: A final image of WASP-33 at H band. North is up and east is to the left. The known companion can be seen in the western side.
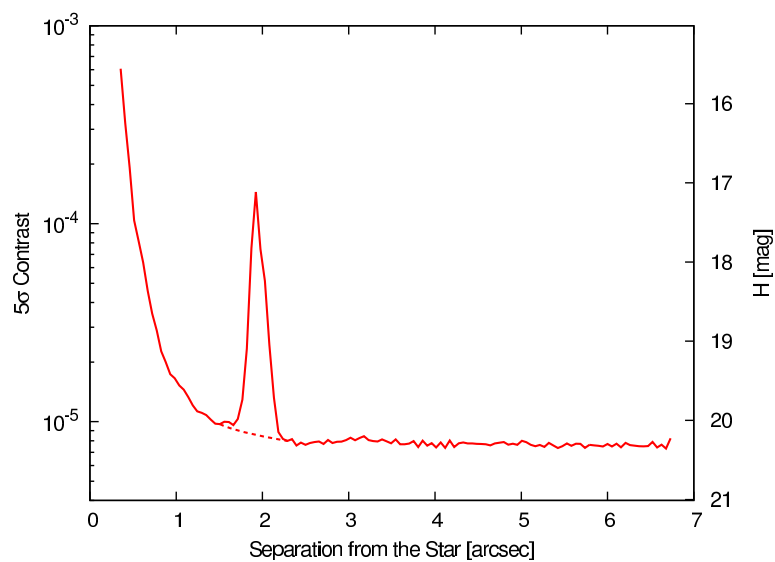
Figure 5.52: A 5σ contrast curve for WASP-33. The vertical axes show the contrast in the log scale (left) and the apparent magnitude H (right). The horizontal axis shows the separation from WASP-33. The dotted line corrects the anomaly at $\sim 1''9$ induced by the bright companion candidate with an interpolation.
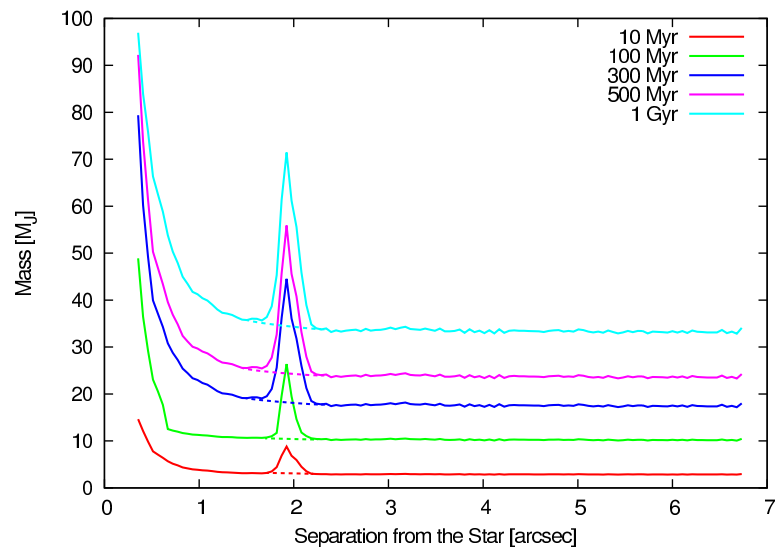
Figure 5.53: Five-σ contrast curves for WASP-33 in mass in a unit of the Jupiter mass converted with the COND model. The horizontal axis shows the separation from WASP-33. The contrast curves are dependent on ages, represented in colors, but its age has not been disclosed. The dotted lines correct the anomalies at $\sim 1.\!\!''9$ induced by the bright companion candidate with interpolations.

Table 5.23: Detection limits for Targets without Any Companion Candidates

Name	Date (UT)	5σ Limits (ΔH)				5σ Limits ($M_{\rm J}$)				Age
		0$\!''$5	1$\!''$0	2$\!''$0	4$\!''$0	0$\!''$5	1$\!''$0	2$\!''$0	4$\!''$0	
HD 22781	2013-01-04	11.4	13.7	14.8	15.1	46	25	18	17	3 Gyr
HD 30562	2013-01-03	11.1	13.2	14.1	14.3	68	50	41	39	4 Gyr
HD 86264	2013-02-27	8.4	10.7	12.1	12.6	89	68	53	48	2 Gyr
HD 98649	2011-12-30	9.9	12.4	14.2	14.5	62	35	22	19	2 Gyr
HD 222582	2012-11-07	11.2	14.2	15.5	15.8	68	43	32	29	7 Gyr
WASP-15	2011-05-25	—	12.2	12.7	12.7	—	62	58	57	4 Gyr
XO-4	2011-11-16	9.5	11.5	11.9	12.0	76	60	54	54	2 Gyr

The values correspond to 5σ detection limits. The limits in mass are estimated with COND model based on the rough age estimates. Limits at other separations or based on other ages are shown in figures in the following subsections.

5.7 Results of Targets without Companion Candidates

We could not find any companion candidates around HD 22781, HD 30562, HD 86264, HD 98649, HD 222582, WASP-15 or XO-4. Our observations reached so high contrasts, shown in figures in the following subsections, that we sufficiently exclude additional (sub)stellar objects ($\gtrsim$ tens $M_{\rm J}$) around the stars. Although the contrasts are not enough to completely rule out the Kozai migration scenario, our observations are the deepest observations of the targets so far to confirm the absence of (sub)stellar mass objects.

One possibility of how to make single eccentric or tilted planets is the planet-planet scattering. In this case it is likely that necessary counterparts have not been detected by RV surveys due to its large period and unfortunately by our observations due to its low masses. The case of additional objects having tilted inclinations of $i \sim 0$ deg also disable us to discover them. Perhaps there may be another common way to leave only one planet through the planet-planet scattering.

Another possibility of a cause of single-eccentric planets is marginally gravitationally unstable (Boss, 2013), which may leave only one Jovian planet with a high eccentricity due to interactions with a gravitationally unstable disk, but it is necessary to be investigated more, especially for the inner regions.

5.7.1 HD 22781

We could not find any objects around HD 22781. Figure 5.54 clearly shows the fact and Figure 5.55 represents that any objects with $\Delta H \lesssim 18.1, 20.4, 21.5$, and 21.8 are absent at 0$\!''$5, 1$\!''$0, 2$\!''$0, and 4$\!''$0, respectively. Figure 5.56 denotes the 5σ detection limit converted with COND model (the colors correspond to the age of the main star). Depending on the age estimates, an object with a mass of $\gtrsim 40M_{\rm J}$ is fully ruled out by our observations, except for a region within 1$''$. Kozai timescales for a planet at the current position induced by an object with $40M_{\rm J}$ (i.e. $\sim 0.04M_\odot$) at 1$''$, 2$''$ and 4$''$ (and the same semi-major axes as the projected distances) in circular orbits are estimated to be ~ 600 kyr, ~ 4 Myr, and ~ 40 Myr, while the timescales for a planet at the snow line (1.5 AU) are ~ 400 kyr, ~ 3 Myr, and ~ 20 Myr, respectively. Combining the estimates and our detection limits, we exclude an object at a separation of 1$''$, 2$''$ and 4$''$ being able to induce Kozai migration with a timescale of shorter than $\sim$ a few

hundreds kyr, $\sim$ Myr, and $\sim$ tens Myr, respectively. Though the possibility of Kozai migration remains, we can put limits on the migration. The fact that no objects are found around the star is consistent with no significant RV trend (Díaz et al., 2012) which may be induced by a companion. For investigating a planet formation scenario, it is necessary to execute more precise RV measurements to detect a faint object which could not be detected with our observations.
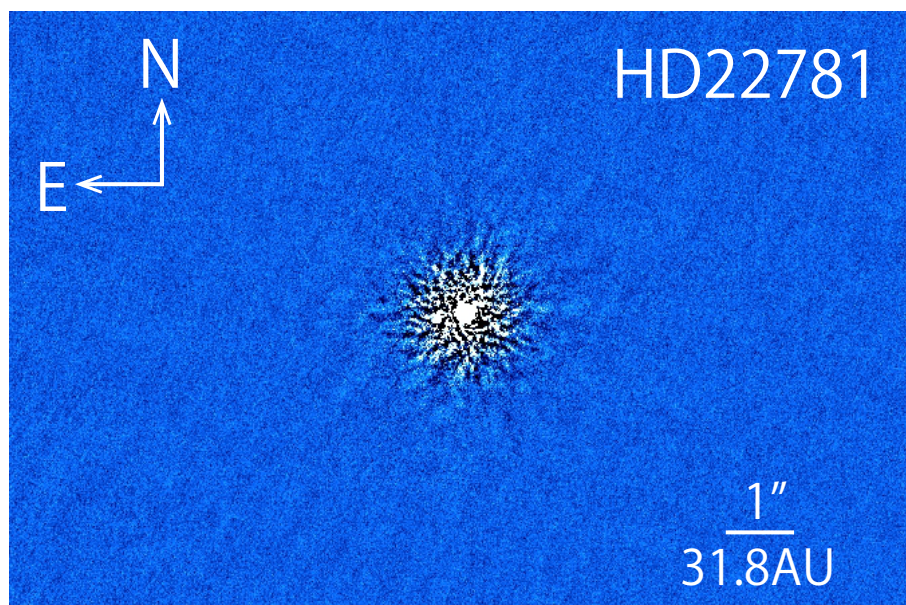
Figure 5.54: A final image of HD 22781 at *H* band. North is up and east is to the left. No other object than HD 22781 appears in the figure.
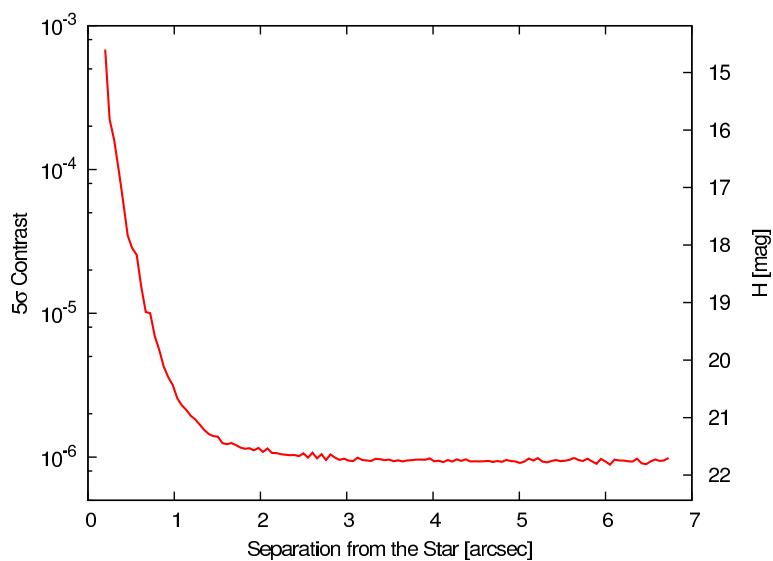
Figure 5.55: A 5σ contrast curve for HD 22781. The vertical axes show the contrast in the log scale (left) and the apparent magnitude H (right). The horizontal axis shows the separation from HD 22781.
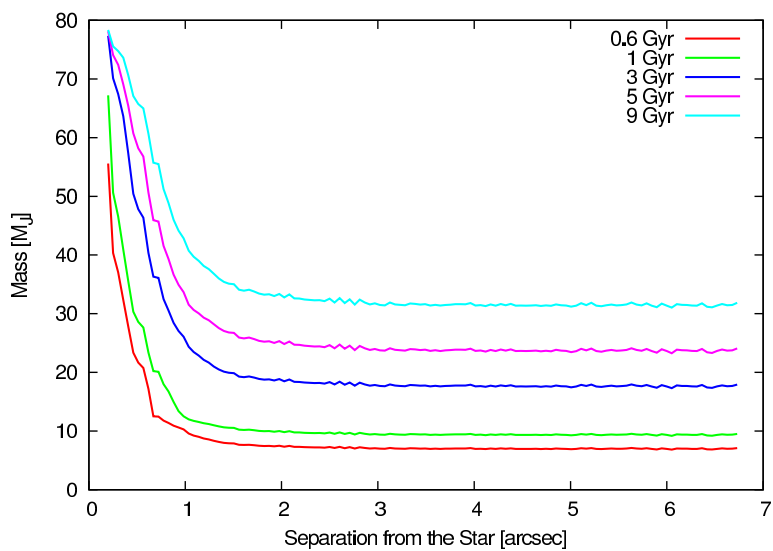
Figure 5.56: Five-σ contrast curves for HD 22781 in mass in a unit of the Jupiter mass converted with the COND model. The horizontal axis shows the separation from HD 22781. The colors represent ages.

5.7.2   HD 30562

We could not detect any objects around HD 30562 (see Figure 5.57) notwithstanding our high-contrast observations (see Figure 5.58). Based on the COND model, we can exclude an object with $\gtrsim 50M_{\rm J}$ for its age of 5 Gyr, or $\gtrsim 40M_{\rm J}$ for 3 Gyr in a region beyond $1''$ (see Figure 5.59). Because the corresponding mass objects ($50M_{\rm J}$) at $1''$, $2''$ and $4''$ (the same as its semi-major axes) in assumptive circular orbits induce Kozai migration for a planet at the current position on timescales of ~ 100 kyr, ~ 900 kyr, and ~ 8 Myr, respectively, and for a planet at the snow line (4.0 AU) Kozai timescales are calculated to be ~ 50 kyr, ~ 400 kyr, and ~ 3 Myr, respectively, we conclude that no objects which can cause Kozai effect with timescales of shorter than such scales. Though the limits are imperfect to fully exclude the possibility of Kozai migration, we can put strong limits on Kozai migration scenario. With no RV trend observed (Fischer et al., 2009), it is possible that another adequately small and wide-orbit planet exists and have caused planet-planet scattering or Kozai migration on the known planet, HD 30562b.
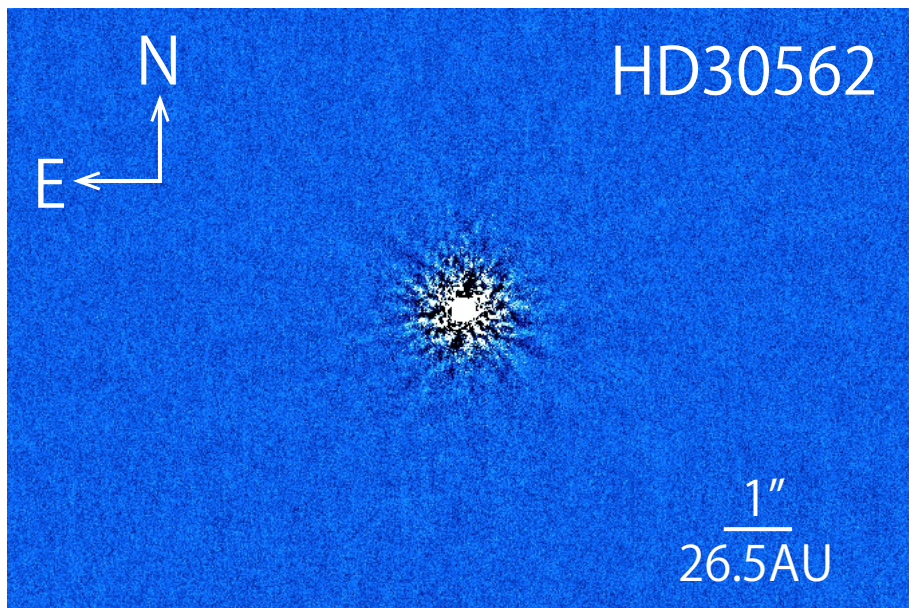
Figure 5.57: A final image of HD 30562 at *H* band. North is up and east is to the left. No other object than HD 30562 appears in the figure.
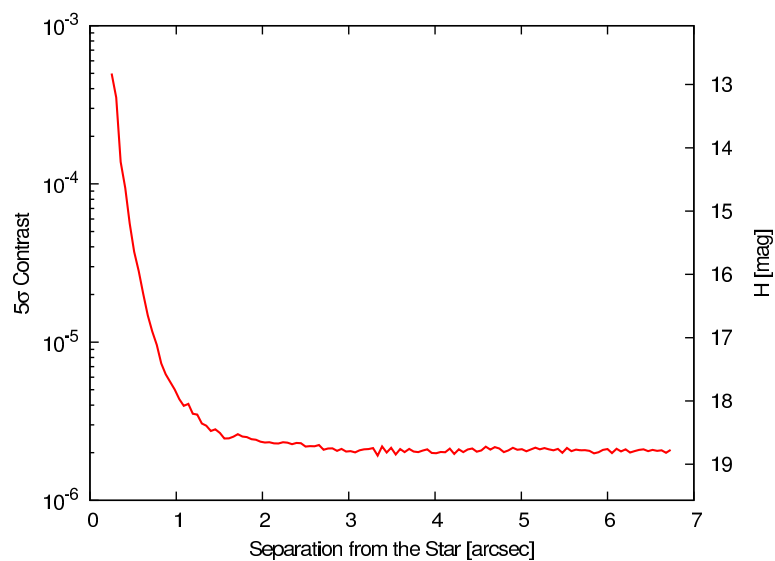
Figure 5.58: A 5σ contrast curve for HD 30562. The vertical axes show the contrast in the log scale (left) and the apparent magnitude H (right). The horizontal axis shows the separation from HD 30562.
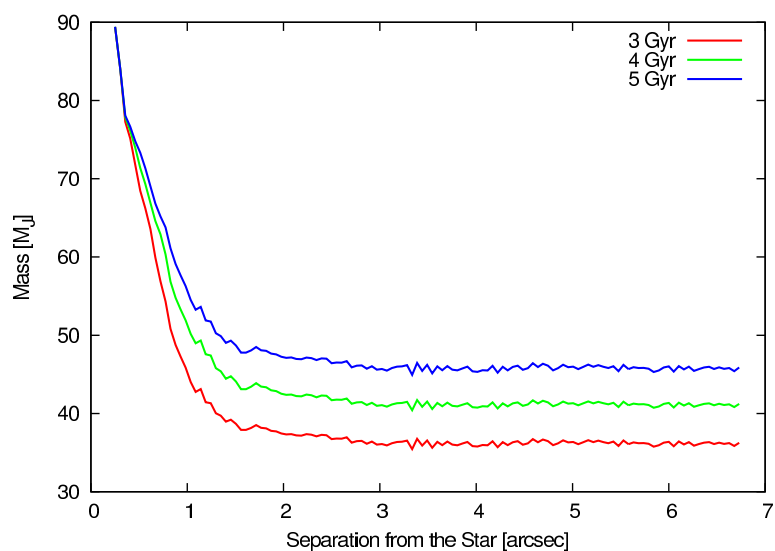
Figure 5.59: Five-σ contrast curves for HD 30562 in mass in a unit of the Jupiter mass converted with the COND model. The horizontal axis shows the separation from HD 30562. The colors represent ages.

5.7.3   HD 86264

Although it is known that the main star, HD 86264, has a long RV trend of 0.005 m s^{-1} yr^{-1} (Fischer et al., 2009), we could not find any objects around the star (see Figure 5.60). Our observations reach high-contrasts of $\Delta H = 10.7$, 12.1, and 12.6 (5σ detection limits) at $1''$, $2''$ and $4''$, respectively, which can be converted into $\sim 80 M_{\rm J}$, $\sim 60 M_{\rm J}$, and $\sim 60 M_{\rm J}$ for the oldest age estimate of ~ 3 Gyr (see Figure 5.62). An object just on the detection limits with separations of $1''$, $2''$ and $4''$ (i.e. $a = 73$ AU, 150 AU, and 290 AU in circular orbits) can induce Kozai migration on a planet in the current orbit on timescales of ~ 1 Myr, ~ 10 Myr, ~ 100 Myr, while Kozai timescales for a planet at the snow line (5.4 AU) are ~ 400 kyr, ~ 5 Myr, and ~ 40 Myr, respectively. Our observations rule out the presence of an object inducing Kozai timescales shorter than such scales, but the possibility of Kozai migration remains especially in an inner region.

If the reported RV trend of 0.005 m s^{-1} yr^{-1} (Fischer et al., 2009) is caused by an unknown object "c", the trend can be converted into the following equation:

$$\frac{m_{\rm c} \sin i_{\rm c}}{a_{\rm c}^2} \sim 4 \times 10^{-5} \ M_{\rm J} \ {\rm AU}^{-2}, \tag{5.4}$$

where $m_{\rm c}$, $i_{\rm c}$ and $a_{\rm c}$ are c's mass, inclination, and semi-major axis. If we assume $i_{\rm c} \sim 90$ deg and combine our detection limits, it is possible that "c" has a semi-major axis of $\lesssim 1000$ AU (i.e. $\lesssim 14''$). Combining our observations and the long term trend, it is reasonable that HD 86264b experienced a scattering and its counterpart "HD 86264c" did not detected with our observations due to its small mass.
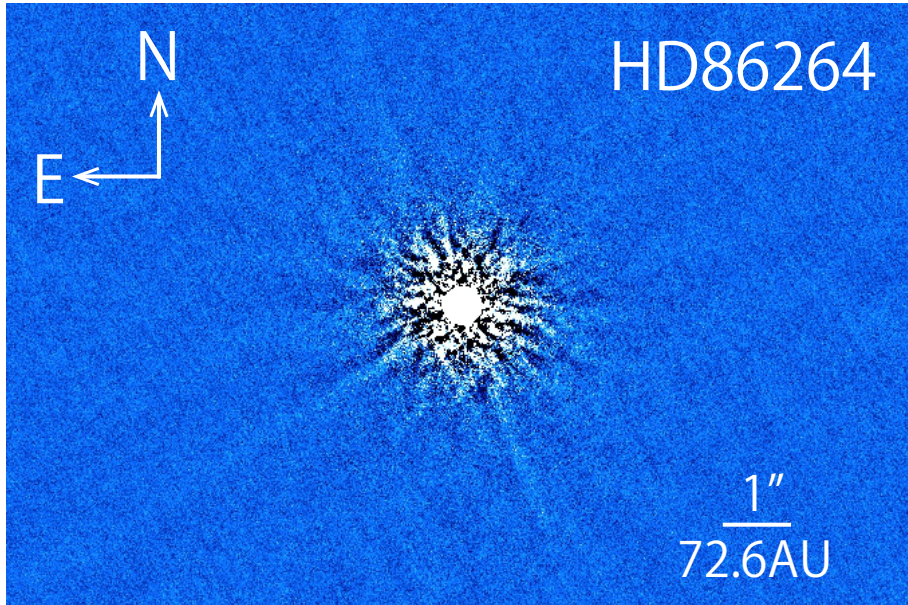

Figure 5.60: A final image of HD 86264 at *H* band. North is up and east is to the left. No other object than HD 86264 appears in the figure.
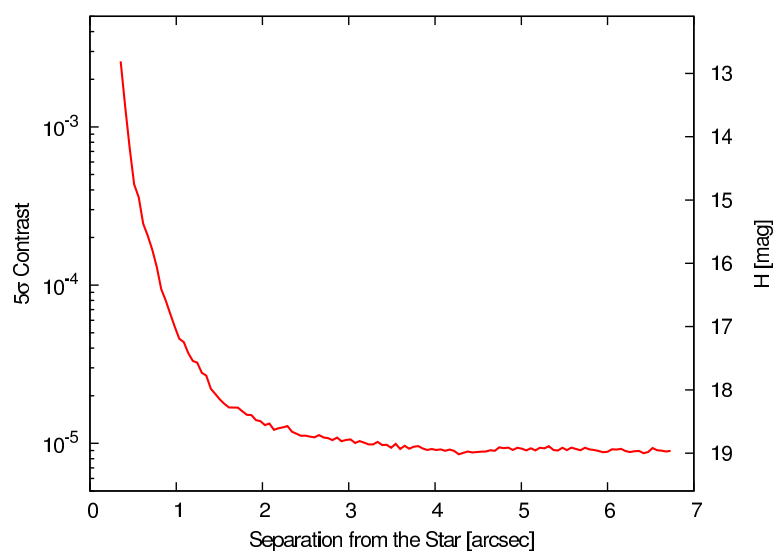
Figure 5.61: A 5σ contrast curve for HD 86264. The vertical axes show the contrast in the log scale (left) and the apparent magnitude H (right). The horizontal axis shows the separation from HD 86264.
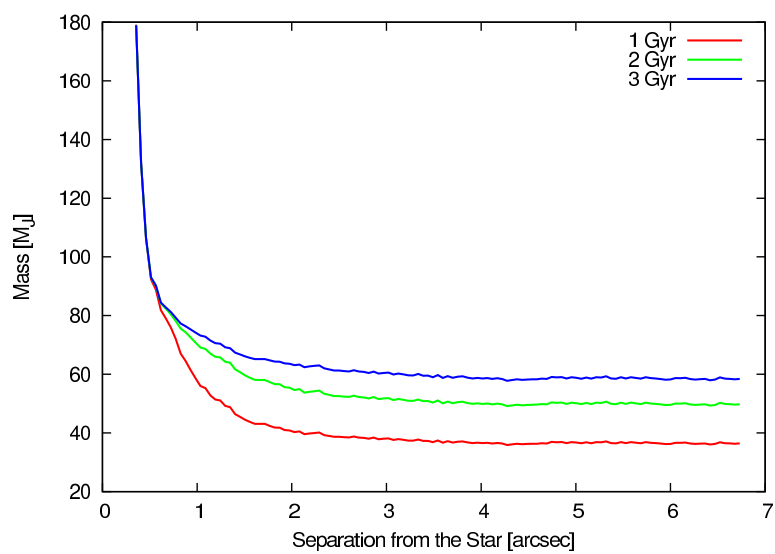

Figure 5.62: Five-σ contrast curves for HD 86264 in mass in a unit of the Jupiter mass converted with the COND model. The horizontal axis shows the separation from HD 86264. The colors represent ages.

5.7.4   HD 98649

We did not find any objects around HD 98649 (see Figure 5.63). Our observations reach high-contrasts of $\Delta H = 12.4$, 14.2 and 14.5 mag at $1''$, $2''$ and $4''$, respectively (5σ detection limits, see Figure 5.64), leading to exclusion of an object with a mass of $\gtrsim 50M_J$ at $1''$, $\gtrsim 30M_J$ at $2''$ and $4''$ in the oldest case (~ 4 Gyr; other cases are presented in Figure 5.65). A hypothetical object with the same mass as the detection limit and in a circular orbit with the same semi-major axis as the projected separation can induce Kozai mechanism on a planet at the current position on timescales of ~ 100 kyr at $1''$, ~ 1 Myr at $2''$, and ~ 10 Myr at $4''$. Note that Kozai timescales for a planet at the snow line (2.7 AU) are longer than the scales in the current orbit due to the planet b orbits in outer regions. The detection limits are not enough to fully rule out the possibility of Kozai mechanism, but we can constrain the existence of a Kozai source around HD 98649.

The results of our observations are consistent with no RV trend (Marmier et al., 2013), suggesting that no additional (sub)stellar objects are absent from this systems. It is possible that there is an additional planetary mass object around HD 98649 which cannot be detected with the DI method due to its low mass and it was a counterpart of planet-planet scattering. High precision RV measurements are necessary to confirm the migration scenario.
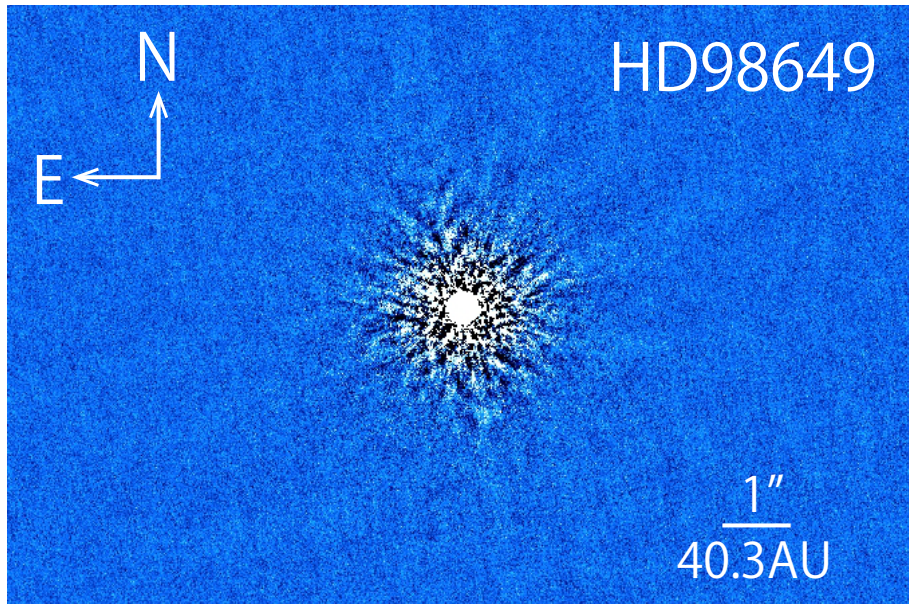

Figure 5.63: A final image of HD 98649 at H band. North is up and east is to the left. No other object than HD 98649 appears in the figure.
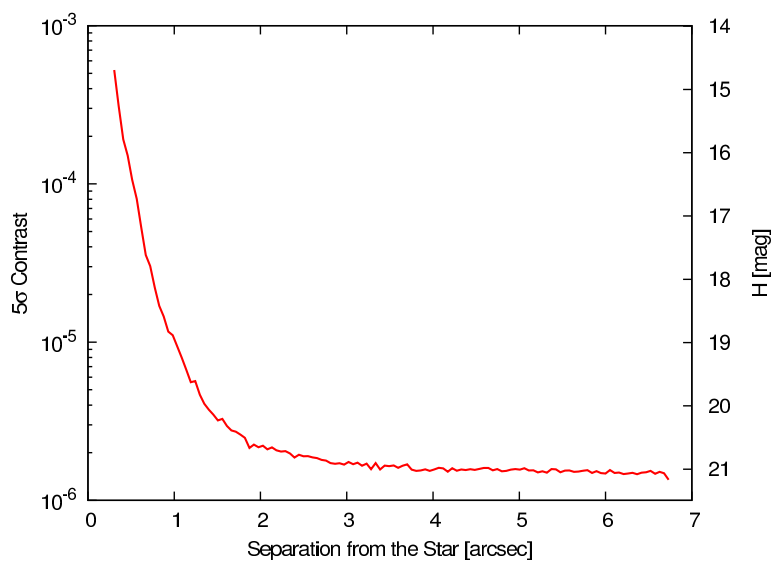
Figure 5.64: A 5σ contrast curve for HD 98649. The vertical axes show the contrast in the log scale (left) and the apparent magnitude H (right). The horizontal axis shows the separation from HD 98649.
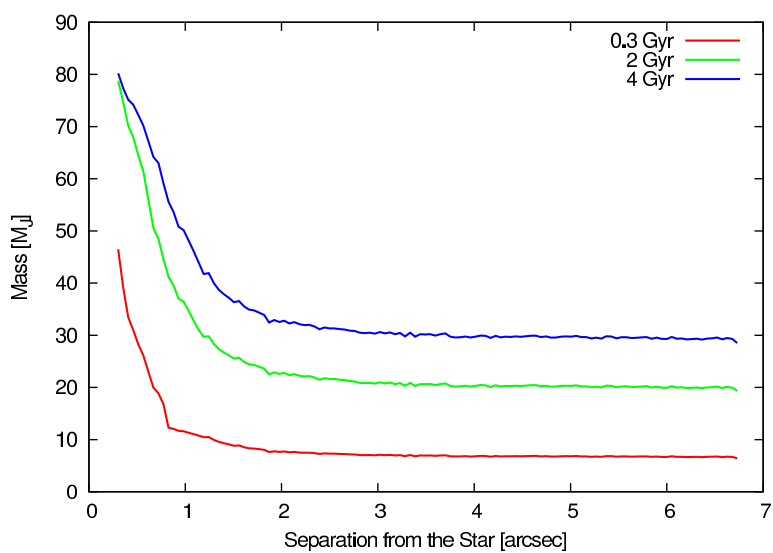

Figure 5.65: Five-σ contrast curves for HD 98649 in mass in a unit of the Jupiter mass converted with the COND model. The horizontal axis shows the separation from HD 98649. The colors represent ages.

5.7.5   HD 222582

As Figure 5.66 shows, we find no objects around HD 222582, though our observations reach high-contrasts (see Figure 5.67). The 5σ contrasts are converted into Figure 5.68 with the COND model, revealing that objects with masses of $\gtrsim 50M_J$, $\gtrsim 40M_J$ and $\gtrsim 40M_J$ are excluded in cases of their separations of $1''$, $2''$ and $4''$, respectively. Because such objects induce Kozai migration on timescales of ~ 900 kyr, ~ 9 Myr, and ~ 80 Myr for a planet at the current position or ~ 400 kyr, ~ 4 Myr, and ~ 30 Myr for a planet at the snow line (2.5 AU), which are shorter than its age, we cannot completely rule out the possibility of Kozai migration.

For HD 222582, no long term trend was reported by Vogt et al. (2000), but it has an M-type companion star HD 222582 B (Mason et al., 2001) separated by $\sim 110''$ with a common proper motion (Gould and Chanamé, 2004). Hence, we can discuss a Kozai timescale for the planet HD 222582b affected by the companion HD 222582 B. Because its estimated spectral type of M3.5 leads to a typical mass of $\sim 0.3M_\odot$ (Kaltenegger and Traub, 2009), its orbital period is calculated to be $P_B \sim 300$ kyr on the assumption that the projected separation is the same as its semi-major axis (~ 4600 AU) and its orbit is circular. With the period, a Kozai timescale for a planet at the present position is $P_{Kozai} \sim 160$ Gyr, while the timescale for a planet at the snow line for HD 222582 (2.5 AU) is estimated as $P_{Kozai} \sim 60$ Gyr. Compared to the system's age of 3.4-11.1 Gyr (Saffe et al., 2005), Kozai mechanism could not occur in the system, also supporting planet-planet scattering for the HD 222582 system on the assumption that the Galactic perturbations (Kaib et al., 2013) can be ignored. If the perturbations are valid, a separation of the binary could decrease, leading to HD 222582 B being a source of Kozai effects.
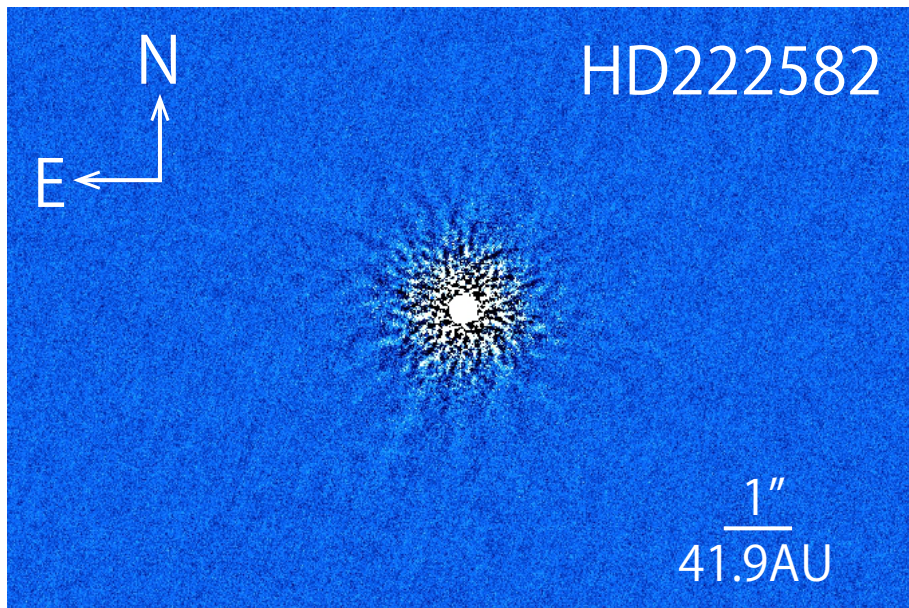

Figure 5.66: A final image of HD 222582 at H band. North is up and east is to the left. No other object than HD 222582 appears in the figure, because the known companion is out of the HiCIAO FOV.
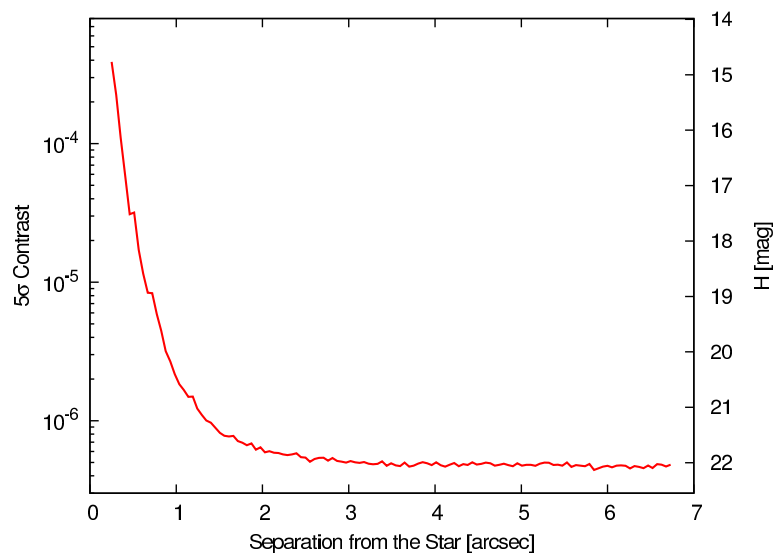
Figure 5.67: A 5σ contrast curve for HD 222582. The vertical axes show the contrast in the log scale (left) and the apparent magnitude H (right). The horizontal axis shows the separation from HD 222582.
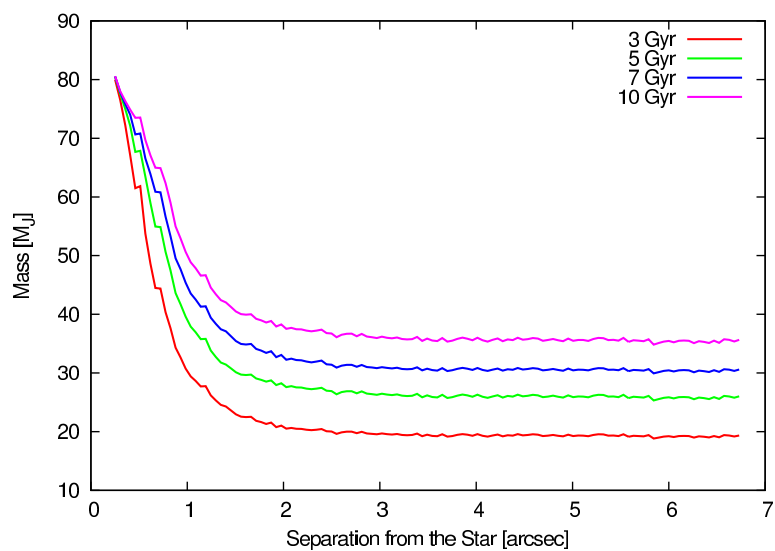

Figure 5.68: Five-σ contrast curves for HD 222582 in mass in a unit of the Jupiter mass converted with the COND model. The horizontal axis shows the separation from HD 222582. The colors represent ages.

5.7.6   WASP-15

We could not find any objects around WASP-15 (see Figure 5.69), though some noise could not be removed due to small filed rotation ($\Delta \pi = 7.6$ deg). However, our observations approached $\Delta H \sim 10^{-5}$ beyond $\sim 2''$ as Figure 5.70 shows, leading to detection limits of $\sim 70 M_{\mathrm{J}}$ for its age estimate of 7 Gyr (see Figure 5.71). If we assume objects with separations of $1''$, $2''$ and $4''$ and masses of $70 M_{\mathrm{J}}$, and presume that they have circular orbits with semi-major axes whose values are the same as the projected distances, they can cause Kozai migration on a planet at the current position on timescales of ~ 40 Gyr, ~ 300 Gyr, and ~ 3 Tyr, respectively. Because the values are too long to explain WASP-15b's orbit compared to the system's age of ~ 4 Gyr, we conclude that our observations rule out the possibility of Kozai migration in this case. Meanwhile, the hypothetical objects at $1''$, $2''$ and $4''$ cause Kozai mechanisms on a planet at the snow line (4.1 AU) on timescales of ~ 60 Myr, ~ 400 Myr, ~ 4 Gyr. In this case, we exclude the possibility of Kozai migration only in regions beyond $\sim 2''$, but the possibility remains in regions within $\sim 2''$. Although no significant long-term trend has been reported, Triaud et al. (2010) reported maximum limit as $|\dot{\gamma}| < 30$ m s^{-1} yr^{-1}, which can be converted into the following:

$$\frac{m_{\mathrm{c}} \sin i_{\mathrm{c}}}{a_{\mathrm{c}}} < 0.3 \ M_{\mathrm{J}} \ \mathrm{AU}^{-2}, \tag{5.5}$$

where m_{c}, i_{c} and a_{c} are a mass, an inclination, and a semi-major axis, under assumption that an RV trend is caused by a hypothetical planet "c." Combining the detection limits and the long-term trend limit, it is consistent that we could not detect any candidates which may cause RV trend. Though there is a possibility that an unknown additional object may cause Kozai migration, it is likely that there is no (sub)stellar object.
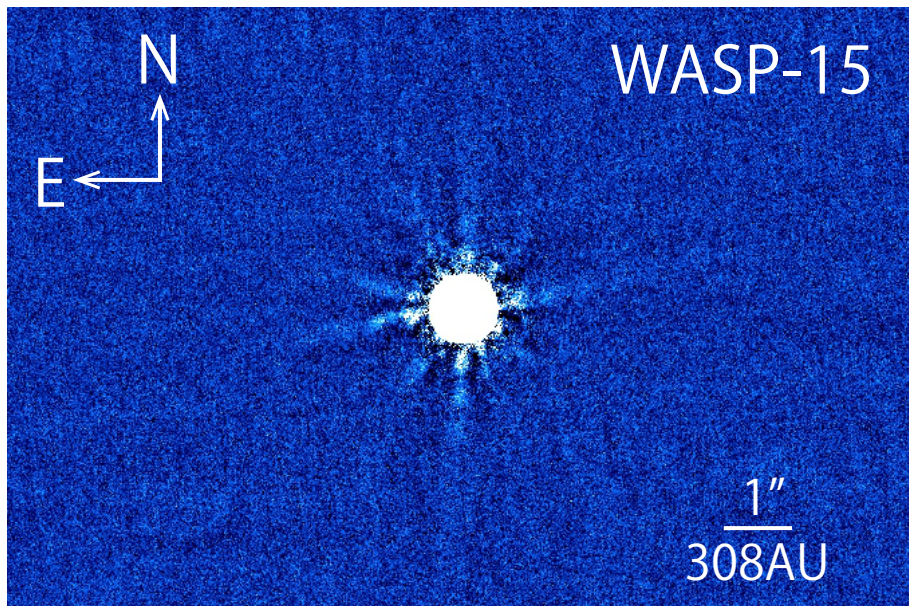

Figure 5.69: A final image of WASP-15 at H band. North is up and east is to the left. No other object than WASP-15 appears in the figure.
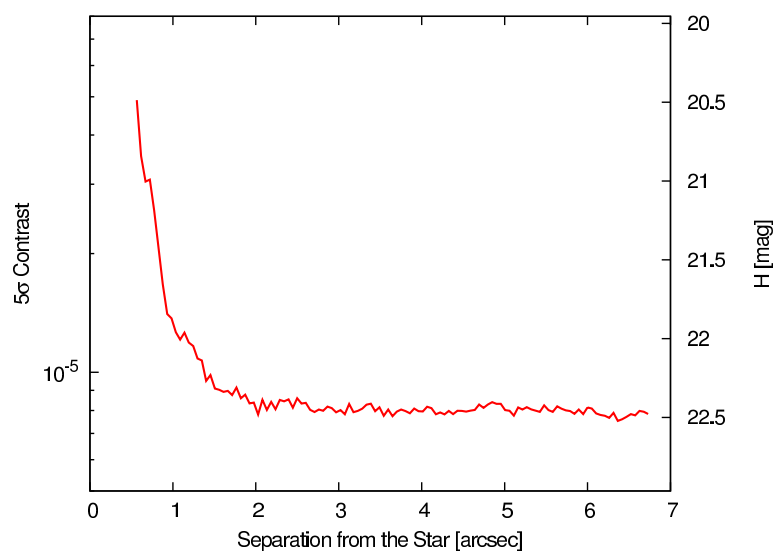
Figure 5.70: A 5σ contrast curve for WASP-15. The vertical axes show the contrast in the log scale (left) and the apparent magnitude *H* (right). The horizontal axis shows the separation from WASP-15.
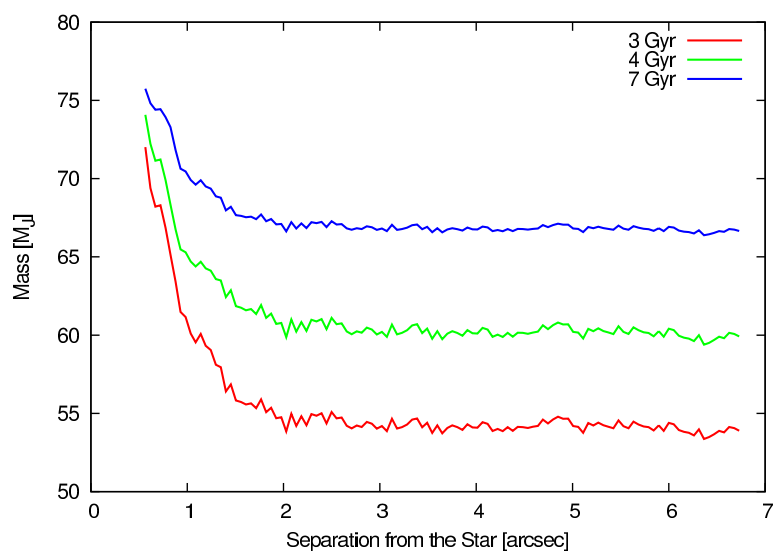

Figure 5.71: Five-σ contrast curves for WASP-15 in mass in a unit of the Jupiter mass converted with the COND model. The horizontal axis shows the separation from WASP-15. The colors represent ages.

5.7.7   XO-4

We could not find an additional object around XO-4 though spider noise remains in Figure 5.72 due to small field rotation of $\Delta\pi = 10.8$ deg. Contrast ratios of detection limits of our observations are shown in Figure 5.73, reaching $\Delta H \sim 2 \times 10^{-5}$, and the ratios correspond to $\sim 65 M_J$ by calculating with the COND model based on the age estimate of 3 Gyr (see Figure 5.74). Objects with a mass of $\sim 65 M_J$ in circular orbits with semi-major axes of 290 AU, 590 AU and 1200 AU (i.e. corresponding to $1''$, $2''$ and $4''$, respectively) can cause Kozai effect on a planet at the current position on timescales of ~ 30 Gyr, ~ 300 Gyr and ~ 2 Tyr, respectively. Because lighter objects cause longer Kozai timescales and XO-4's age is ~ 2 Gyr, our detection limits fully exclude the possibility of Kozai migration scenario in the case of the planet being in the current orbit. Meanwhile, a planet at the snow line (4.7 AU) can be affected by Kozai mechanism on timescales of ~ 40 Myr, ~ 300 Myr, and ~ 3 Gyr. Compared to the system's age of ~ 2 Gyr, we can rule out the possibility of Kozai migration which is caused by an object only beyond $2''$. The results of our observations are consistent with no RV trend (Narita et al., 2010a), supporting that additional massive objects are absent from XO-4 planetary system.
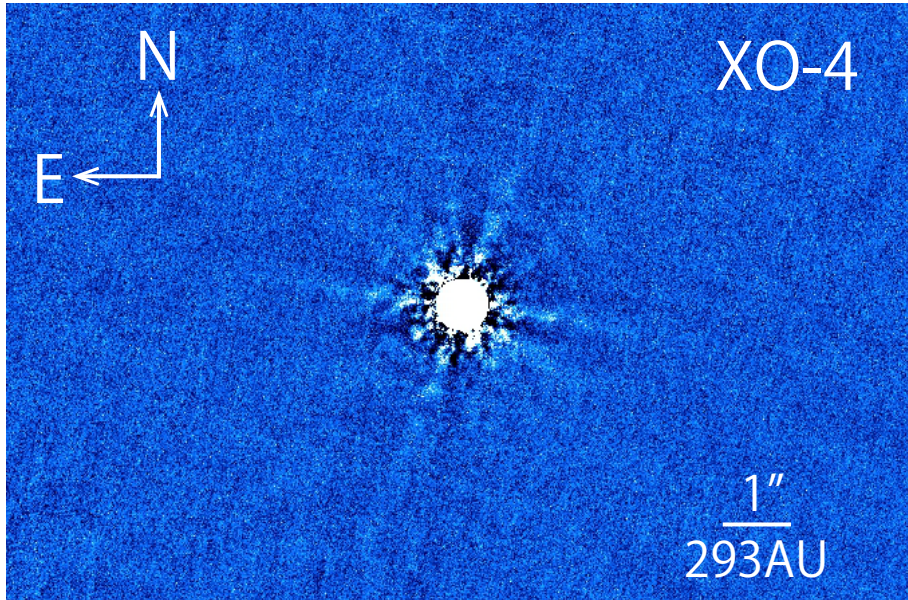

Figure 5.72: A final image of XO-4 at H band. North is up and east is to the left. No other object than XO-4 appears in the figure.
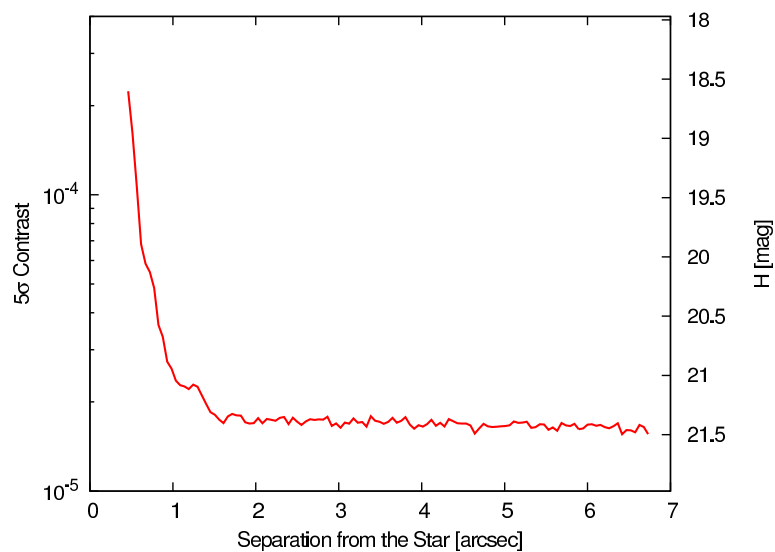
Figure 5.73: A 5σ contrast curve for XO-4. The vertical axes show the contrast in the log scale (left) and the apparent magnitude H (right). The horizontal axis shows the separation from XO-4.
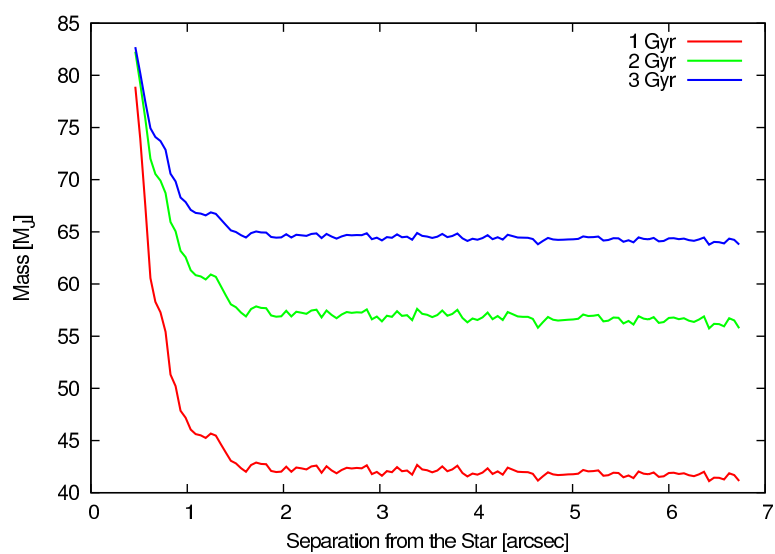

Figure 5.74: Five-σ contrast curves for XO-4 in mass in a unit of the Jupiter mass converted with the COND model. The horizontal axis shows the separation from XO-4. The colors represent ages.

Chapter 6

Statistical Discussion of Our Binary Rates

With our results shown above, let us make a discussion of statistical influences of the companions to approach migration mechanisms. Here, we compare our binary rates with previous works by Raghavan et al. (2010) and Roell et al. (2012). Raghavan et al. (2010) estimated multiplicity of Solar-type ($0.5 \leq B - V \leq 1.0$; corresponding to $\sim$F6-K3) stars around the Sun (parallaxes of $\pi > 40$ mas) to be 46%$\pm$2% (hereafter SN). The result is consistent with the values reported by Duquennoy and Mayor (1991). Roell et al. (2012) reported a multiplicity of 11.95% for exoplanet host stars (hereafter PH). The difference are thought to arise due to a sample bias (RV surveys tend to avoid binary systems in order to escape from high amplitudes caused by companions) and/or gravitational influence from the companions (Kozai migration and perturbations to protoplanetary disks preventing from forming planets). Although our tilted samples exactly include early type stars ($<$ F6), we do not distinguish between the Solar-type stars (F6-K3) and the early type stars ($<$ F6). This is because the number of the early type stars is limited and some targets have uncertainty of their spectral types. Apropos, Raghavan et al. (2010) pointed out that B- to A-type stars have a multiplicity of more than 70%.

   Again, we note that our sample sizes are limited due to the first attempt with high-contrast direct imaging aiming to uncover the mysteries of planetary migration mechanisms. However, even if we cannot definitely conclude statistical suggestions because of the small sample sizes, it will not belittle the value of this study. It is now important to calculate binary rates for stars hosting eccentric planets or tilted planets to be compared with other rates.

6.1   Binomial Tests for Our Binary Rates

Here, in order to confirm whether our multiplicities agree with the previous works or not, we adopt the binomial test to our sample targets, which is based on the binomial distribution defined as

$$P[x = k] = \binom{n}{k} p^k (1-p)^{n-k}, \tag{6.1}$$

where x, n and p denote the probability variable and the parameters. For the eccentric systems, we discovered and confirmed companions in two systems, HD 8673 and HD 96167. Although HD 222582 has a companion, it cannot cause Kozai effects directly and we therefore divide them into two cases; assumed HD 222582 as a single or a binary. Based on the test, our samples resulting in a rate of 2/8 can be statistically identified with the SN samples ($p = 0.46$) with the probability of 0.30 and PH samples ($p = 0.1195$) with the probability of 0.25 on a 95% confidence level, in case that HD 222582 is a single. On the other side, the rate of 3/8, including HD 222582 in binaries, the probabilities are calculated to be

Table 6.1: Probability of Agreement with Binary Rate for Eccentric Targets

Samples	Binary Rate	Solar Neighbors	Planet Hosts
Confirmed	2/8	0.30	0.25
With HD 222582	3/8	0.73	0.060
With HD 80606	4/9	1	0.016

0.73 and 0.060 for SN and PH, respectively. The low probability for PH implies that an eccentric planet may have a binary companion in the higher ratio than that of the all planet host stars, while identical with SN. Incidentally, if we add HD 80606, which has an eccentric and tilted planet and constitutes a binary system, to our samples, the ratio of 4/9 shows statistical significance with the probability of 0.016 with comparing to PH. Although more samples are necessary to consolidate the trend, our results possibly show that the high binary rate is statistically valid for highly-eccentric ($e \geq 0.7$) planets. The results are summarized in Table 6.1.

For the tilted samples, we define binaries as stars hosting a companion being a candidate source of Kozai effects. Objects which cannot induce Kozai effects are not regarded as companions. In addition, we separate the companions into four categories based on their confirmation possibilities; (I) only companions confirmed with the CPM tests or rigid colors (the most strict), (II) (I)+companions confirmed with colors (likely but the CPM tests needed), (III) (II)+companions to be confirmed and no background stars estimated by the TRILEGAL model (possible but not confirmed yet), (IV) (III)+companions to be confirmed and some background stars estimated by the TRILEGAL model (possible but unreliable). The category (I) includes HAT-P-7, TrES-4, WASP-8 and WASP-12 (four systems), and the category (II) contains HAT-P-14, HAT-P-30, HAT-P-32 and WASP-33 in addition to (I) (eight systems in total). The category (III) adds WASP-14 to (II) (nine in total), and the category (IV) has HAT-P-6, HAT-P-11, HAT-P-17 plus the stars in (III) (twelve systems in total). The binary rates for the categories (I), (II), (III), and (IV) result in 4/15, 8/15, 9/15, and 12/15, respectively. The probabilities of the two-sided tests for SN are 0.19, 0.61, 0.31, 0.0092 for the categories (I), (II), (III) and (IV), respectively. Moreover, for PH the probabilities of 0.095, 1.2×10^{-4}, 1.3×10^{-5} and 1.7×10^{-9} of the one-sided test for the categories (I), (II), (III) and (IV), respectively, likely indicate that tilted-planet host stars are prone to have more companions than the global binary rate of PH, though statistically unreliable for only the CPM-confirmed systems. If we add HD 80606 to our category (I), the probabilities for PH change into 0.034, 2.6×10^{-5}, 2.4×10^{-6} and 4.0×10^{-10}. We conclude that the trend to PH binary rate is robust in spite of our small samples. Table 6.2 summarizes our results for the tilted planetary systems.

First, we focus on the possibility of the sample bias. Because a target star of the transit method is defocused not to make it saturated, it is frequent that a companion candidate separated by only a few arcsec is not discovered during a planet survey and follow-up observations. In addition, it is possible only for a companion candidate with a separation of a few arcsec to explain Kozai mechanism, since a transiting system is located with a typical distance from Earth of ~ 100 pc. Therefore, the ongoing transit surveys certainly detect exoplanets without distinguishing between a single star and a binary whose companion possibly induces Kozai mechanism. These facts agree with the consistent binary rate for the tilted samples with SN, in case that the transiting stars have the same binary rate as SN. We note that the binary rate for the tilted systems could be lower than the rate for SN because the multiplicity for SN contains eclipsing binaries and spectroscopic binaries, where planet formation around such binaries are likely unsuccessful, but it should be discussed together with the rate for PH. As for the eccentric

Table 6.2: Probability of Agreement with Binary Rate for Tilted Targets

Category	Binary Rate	Solar Neighbors	Planet Hosts
I	4/15	0.19	0.095
II	8/15	0.61	1.2×10^{-4}
III	9/15	0.31	1.3×10^{-5}
IV	12/15	0.0092	1.7×10^{-9}
I+HD 80606	5/16	0.32	0.034
II+HD 80606	9/16	0.46	2.6×10^{-5}
III+HD 80606	10/16	0.22	2.4×10^{-6}
IV+HD 80606	13/16	5.2×10^{-3}	4.0×10^{-10}

systems, they have the possibility of the sample bias to make the rate lower than those of SN due to the RV surveys' escape form binary systems, as mentioned at the beginning of this chapter. Additionally, the sample of Roell et al. (2012) mostly consists of planets discovered by the RV surveys, but contains few systems discovered with the *Kepler* satellite. Thus, we should compare the eccentric samples' rate with PH. However, we beware that the influence of the bias is not certain. The most important thing is that the binary rate for the planetary host stars has been specifically unclear. Prior to Roell et al. (2012), Raghavan et al. (2006) and Mugrauer and Neuhäuser (2009) estimated the rate for planet hosts to be 22.9% and 17.2%, respectively. We adopt the value in Roell et al. (2012), the most recent result, but note that our discussions could be changeable when the rate varies.

Next, we discuss the probabilities of the agreement of the eccentric samples and the tilted samples with SN. Immediately, we can find that our rates are statistically consistent with the SN except for the extreme case of the tilted samples, in other words; the case that the all potential sources of Kozai mechanism around the target stars are really bound and cause the mechanism. To begin with, we mention the influences of the companions upon planet formation. With the observational limitations of direct imaging, companions have separations of a few hundreds AU from the central stars. On the other hand, it is certain that protoplanetary disks have radii of several tens AU based on the observational facts that planets in wide orbits of $\lesssim$ several tens AU have been discovered. Thus, we can consider that companions are so distant that they cannot affect planet formation, and easily explain the existence of planets in (wide-separated) binary system.

However, only the extreme case of the tilted systems has a significantly higher binary rate than that of SN. It possibly suggests that the influence of the companions cannot be ignored for the tilted planet formation, if reliable. With more conservative assumptions that the binary rate for the category (III)+HD 80606 keeps constant and we multiply the sample size by 2.5, the probability decreases to 0.040 (for two-sided test. 0.027 for the one-sided test) and rules out the hypothesis of the same binary rates on a 95% confidence level (see also Figure 6.3). That is, it is necessary to increase the sample size nearly threefold in order to compare the rates for the tilted samples and SN with a statistical significance. Anyhow, the number of tilted planets itself is necessary to in the future.

We then compare our rates with PH. Although the probability of only the two-confirmed-planet case of 0.25 indicates a statistical agreement with PH, statistical significance for the samples involving HD 222582 and/or HD 80606 slightly arises. Though the robustness is weak due to its variability depending on one sample, the higher binary rate for the eccentric samples suggests a non-negligible frequency of eccentric planets which migrate via Kozai mechanism. If we conservatively fix the rate at 3/8 and

multiply the sample size threefold, the robustness is improved and a probability decreases to 0.0012 (see also Figure 6.2). If we believe our rate is reliable and the companions always cause some influences, we can expect that one or two out of eight single-eccentric planets have been caused by the companions (e.g. Kozai mechanism) due to the number of additional companions of $2 - 8 \times 11.95\% = 1.04$ based on the PH rate, but a Poisson noise ($\sqrt{8 \times 11.95\%} = 0.98$) is comparable to the expected number. Hence, our rate for the eccentric sample does not directly favor Kozai mechanism. Meanwhile, it is likely that the other of more than six eccentric planetary systems have been formed through planet-planet scattering, with the proviso that counterparts of the scattering are necessary to be discovered. The fact that the influence of Kozai mechanism may not be statistically negligible is possibly helpful to explain an occurrence difference of eccentric planets between derived from observations and from hypotheses (see Figure 6.1). On the other side, the tilted system sufficiently shows the statistical significance at present. These minuscule probabilities strongly suggest that more than 15% of tilted systems should be illustrated with the influence of the companions (e.g. Kozai mechanism), since typically $15 \times 11.95\% = 1.8$ (with an error of ± 1.3) systems have a companion star based on the PH rate. Moreover, because of the tilted samples consisting of single-planetary systems except for HAT-P-7 and HAT-P-17 and of observational fact that planetary systems hosting hot Jupiters are statistically indicated to have few additional outer planets, planet-planet scattering, which needs counterparts, is hard to explain. Also, apart from the scattering, some hypotheses have been proposed; one is a possibility that a stellar spin axis is inclined by inner gravity wave regardless of the presence of planets (Rogers et al., 2012), and another is that a rotation axis of a protoplanetary disk is *ab initio* tilted due to an influence of a magnetic field (Lai et al., 2011). Hence, more than half of tilted planets should be explained by Kozai mechanism, and the others be illustrated by the spontaneous spin leaning or the inclined disks. The influence of the scattering is expected to be small, if additional planets are really absent from planetary systems.

Meanwhile, Morton and Johnson (2011a) pointed out that the λ distribution composed with the measured λs could be explained not with Kozai migration (with the tidal effects) plus an aligned model which produces $\lambda = 0$ deg but with planet-planet scattering (with the tidal effects) plus the aligned model, based on discussion with the Bayes factor. Their results seems to conflict with our high binary rate for our tilted samples. Moreover, the low binary rate for our eccentric samples cannot explain the high eccentricities with Kozai migration. Although there exactly are possibility of presence of unknown additional planets and possibility of a high binary rate due to their early spectral types, we do not have any more information to help to work out this puzzle. We propose these problems as questions to be solved.

6.2   Discussion of Relation between Binary Rate and Stellar Temperature

Furthermore, we investigate a relationship proposed by Winn et al. (2010a) between stellar effective temperature and the obliquity (see §5.4). Based on some studies of binary rate (Raghavan et al., 2010), it is possible that the hotter stars have more companion stars and thus their obliquities are higher than the cool stars with Kozai effects. Then we divide our tilted samples between hot stars ($T_{\text{eff}} > T_{\text{crit}} = 6250$ K) and cool stars ($T_{\text{eff}} < T_{\text{crit}}$) and compare binary rates. The hot star sample consists of HAT-P-6, HAT-P-7, HAT-P-14, HAT-P-30, WASP-12, WASP-14, WASP-15, WASP-17, WASP-33 and XO-4, while the cool star sample includes HAT-P-11, HAT-P-17, HAT-P-32, TrES-4 and WASP-8 (errors of the temperatures are not considered). Table 6.3 summarizes results of Fisher's exact test for the each category. As you see, no significant correlation arises (all probabilities $\lesssim 0.05$). Therefore, the results suggest that the proposition by Winn et al. (2010a) is not related with a binary rate. A possible explanation is that a companion star increases $|\lambda|$ but $|\lambda|$ of a planet orbiting a cool star bumps into zero because of developed
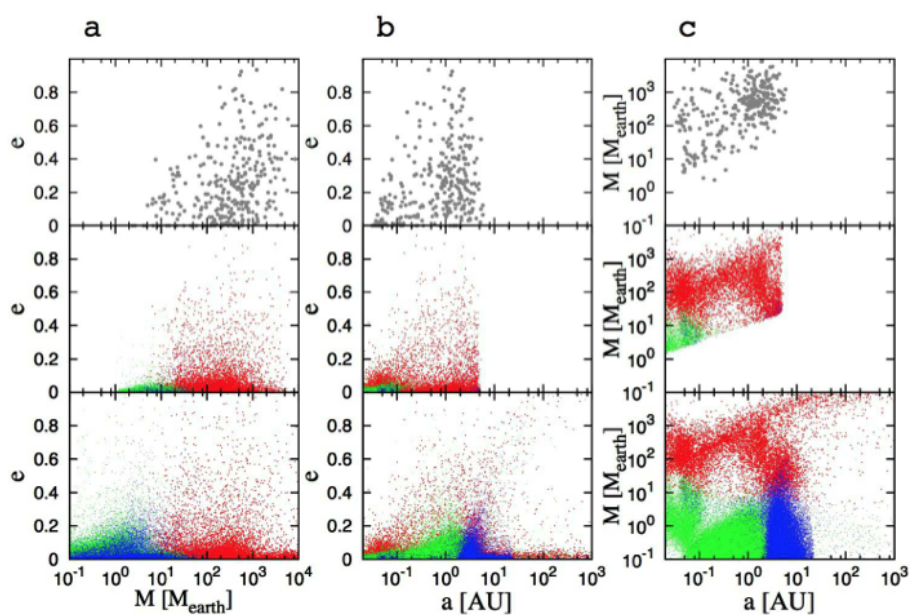
Figure 6.1: Distributions of eccentricity as results of population synthesis based on the core accretion model (Ida et al., 2013). The top row, the middle row and the bottom row show the observed planets (discovered only with RV method), theoretical observable planets and all 10^4 planets formed in theory. Colors represent planets' main component (rocky in green, gaseous in red and icy in blue). Eccentric planets appear to be more discovered than predicted of the theory.

Table 6.3: Relationship of Binary Rate between Hot Stars and Cool Stars

Category	Rate for Hot Stars	Rate for Cool Stars	Probability
I	2/10	2/5	0.56
II	5/10	3/5	1
III	6/10	3/5	1
IV	7/10	5/5	0.51
I+HD 80606	2/10	3/6	0.30
II+HD 80606	5/10	4/6	0.63
III+HD 80606	6/10	4/6	1
IV+HD 80606	7/10	6/6	0.25

stellar convection zone and its tidal friction with the planet, while $|\lambda|$ of a planet around a hot star keeps large due to the lack of stellar convection zone, supporting Albrecht et al. (2012). It is, of course, necessary to observe aligned hot Jupiter systems with $|\lambda| \simeq 0$ deg for more robust discussion. If a binary rate for aligned planetary systems is significantly lower than our results, we can confirm that Kozai mechanism is responsible for the high obliquity. Conversely, no difference of binary rates leads to no correlation with λ but a close relationship between hot Jupiters and binaries.

6.3   Future Works

As for future studies, it is most important that the eccentric samples increase its size. Figure 6.2 and Figure 6.3 indicate probabilities of agreement for the known binary rates (i.e. SN or PH) using the fixed binary rates as functions of sample size based on the binomial test. At present, there are 26 systems that have planets with extreme eccentricity of $e \geq 0.7$, including 20 systems with only single planet each in total. The number of all eccentric ($e \geq 0.7$) systems will adequately enable us to discuss the agreement with a 2/8 rate for SN or PH at a 5% level (see Figure 6.2). Our sample size will be doubled by observing the stars in the southern sky, which cannot be observed from Hawaii. To involve samples with $e \geq 0.6$ significantly contributes to increasing the sample size as well. The large sample size will also allow us to discuss a relationship between eccentricity and a binary rate. Meanwhile, the number of the tilted samples with companion candidates are necessary to be confirmed at first for a robustness of the statistic significance, because the probabilities of agreement strongly depend on the binary rate (see Figure 6.3). Although the stars in the tilted sample can be validated with a mass estimate using colors due to their small proper motions, discussions about common proper motions will be in progress in adequate time. From another point of view, the enormous planetary candidates discovered by *Kepler* are useful to consolidate a certainty of our statistics.

Furthermore, observing systems with non-eccentric or aligned planets allows us to more directly compare differences of binary rates and improves the rates of planet host stars. We expect that future observations will more concretely quantify planetary migration theories based on discussion about binary rates.
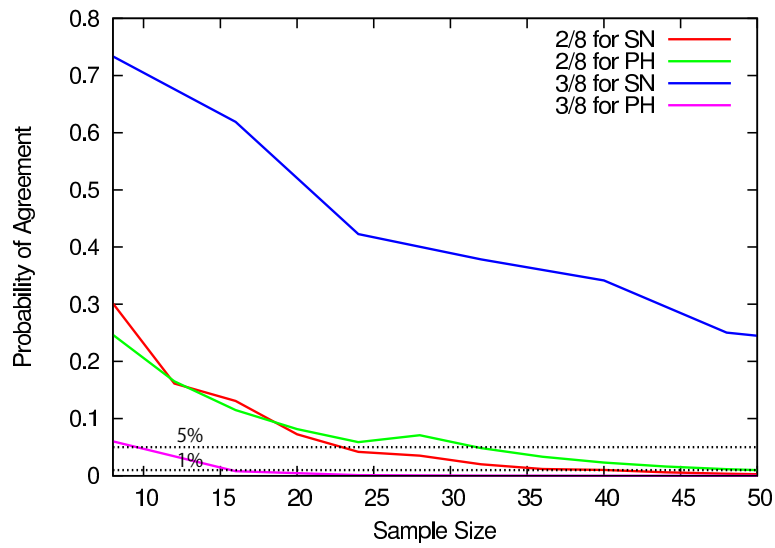
Figure 6.2: Tracks of probability of agreement with the fixed binary rates for the eccentric targets as functions of sample size. Lines are written for each our binary rate and each binary rate model (SN or PH).
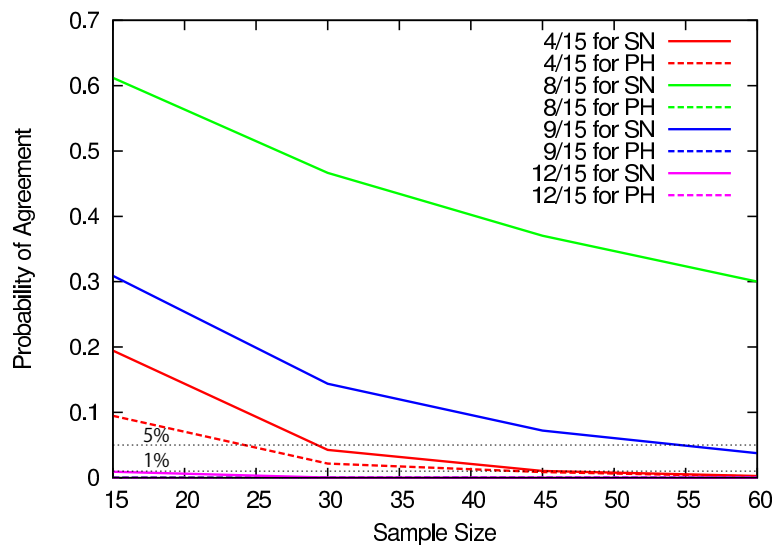
Figure 6.3: Same as Figure 6.2, but for the tilted samples. Lines which are not able to be seen are below a 1% level.

Chapter 7

Summary

We conducted high-contrast direct imaging observations in near-infrared regions with HiCIAO+AO188 on the Subaru telescope in order to detect binary companions which can cause Kozai effects on planets orbiting the central stars. With the intension to eliminate a possibility of interactions with protoplanetary disks (e.g. type II migration), we observed eight targets with highly-eccentric ($e \geq 0.7$) planets, and fifteen targets with tilted ($|\lambda| > 0$ deg) planets including HAT-P-7. This is the first high-contrast direct imaging survey for approaching exoplanet migration mechanisms, although the number of targets is still limited.

Of the eccentric samples, we newly discovered two co-moving M-type companions in the HD 8673 and the HD 96167 systems at $\rho = 0.''3$ and $\rho = 5.''9$, respectively. They can cause Kozai migration of the planets. Though HD 156279 has a companion candidate at $\rho = 9.''6$, it is not in association. HD 222582 is a known binary component, but we did not detect any objects within $\lesssim 10''$ from the star. Other stars, HD 22781, HD 30562, HD 86264, HD 98649, or HD 156279, do not host any companions in our FOVs. The binary rate of 2/8 is statistically identical with the multiplicity of the Solar-type stars in the Solar neighborhood (Raghavan et al., 2010) and of the planet host stars (Roell et al., 2012) on a 95% confidence level, if HD 222582 is assumed to be a single star due to a large separation from its central star. If HD 222582 is treated as a binary, the rate 3/8 shows marginal disagreement with the rate of the planet host stars. It is possible that stars with eccentric planets tend to have more binary companions than global planet host stars, but our sample size is inadequate for determining the relation between an eccentricity and a binary.

As for the tilted samples, we detected companion candidates around all target stars except for WASP-15 and XO-4. Among the companion host stars, we discovered unknown companion candidates around HAT-P-6, HAT-P-11, HAT-P-14, HAT-P-17, WASP-14 and WASP-17, in addition to known companion candidates around HAT-P-30, HAT-P-32, TrES-4, WASP-8, WASP-12 and WASP-33. However, because the companions around WASP-17 are distant from the main star and many background stars are predicted by using the Galactic model, we assume that the companions around WASP-17 are unassociated. Based on our detections, the binary rates of the tilted planetary systems result in at least 4/15 and at most 12/15. The rates are statistically identical with the rate of the solar neighbors except for the highest rate case, but statistically distinguishable from the planet host stars except for the lowest rate case on a 95% confidence level. Therefore we conclude that tilted stars have a tendency to host companion stars compared to typical planet host stars. Furthermore, we investigate binary rates for hot stars and cool stars to examine a T_{eff}-λ relation proposed by Winn et al. (2010a), but no statistical significance is acquired. It is compatible with a scenario that a companion raises an obliquity through Kozai mechanism and only a cool main star decreases the obliquity due to the convection zones.

We also discuss a relevance between distributions of e and λ and our binary rates. Morton and Johnson (2011a) pointed out that the measured λ distribution favored planet-planet scattering for explaining tilted planets compared to Kozai migration. However, our binary rate for the tilted samples is higher than planet host stars. Our observations reveal that the eccentric samples have not enough companions to elucidate a formation scenario for the single eccentric planets with Kozai migration. These inconsistencies for our samples between the high binary rate and the low explanation capability of Kozai mechanism will be explained by future observations and theories.

For future works, we need to establish the associations of the systems with companion candidates. Stars with tilted planets often have small proper motions and therefore it is difficult to examine the common proper motion tests. Hence, future observations at various wavelengths will play an important role to constrain its mass and consequently establish the relationship. Moreover, our samples are too small to conclude the binary rate difference. Future observations are necessary to enlarge the number of the samples with eccentric planets and tilted planets, and to exclude the statistical ambiguity. Then we can strongly put an observational limit on the planet migration mechanisms, for example an occurrence rate of Kozai mechanism. Combining with the future rates for stars with eccentric planets or tilted planets, a binary rate for exoplanet host stars and a ratio of eccentric or tilted planets, we can investigate a frequency of planet-planet scattering and, therefore, give a restriction on the number of Jovian planets in planetary systems before migration. The limit will be possibly allow us to quantitatively discuss how many Earth-like planets on stable conditions and, eventually, how many intelligent lives are present in the Galaxy in the future.

Appendix A

Discussion of Binary Rates Based on Bayesian Statistics

We adopt the Bayes factor to our data in the same manner as described in Morton and Johnson (2011a). In the simple case of comparing Kozai mechanism and planet-planet scattering with no free parameters, a likelihood ratio (i.e. the Bayes factor) is written as

$$\mathscr{R}_{\mathscr{P}} = \log_{10}\left(\frac{\mathscr{L}_{\mathrm{Koz}}(\{\mathscr{P}\})}{\mathscr{L}_{\mathrm{scat}}(\{\mathscr{P}\})}\right), \tag{A.1}$$

where $\mathscr{L}_{\mathrm{Koz}}(\{\mathscr{P}\})$ and $\mathscr{L}_{\mathrm{scat}}(\{\mathscr{P}\})$ are likelihoods of the observed data $\{\mathscr{P}\}$ under the two models ($\mathscr{P} = \{e, \lambda\}$). $\mathscr{R} > 0$ supports Kozai mechanism (plus tidal dissipation), while $\mathscr{R} < 0$ the scattering (plus the dissipation). The likelihoods are calculated as

$$\mathscr{L}_{\mathscr{M}}(\{\mathscr{P}\}) = \prod_{i=1}^{N} P_{\mathscr{M}}(\mathscr{P}_i), \tag{A.2}$$

where

$$P_{\mathscr{M}}(\mathscr{P}_i) = \int p_i(\mathscr{P}) p_{\mathscr{M},\mathscr{P}}(\mathscr{P}) d\mathscr{P}, \tag{A.3}$$

with $p_i(\mathscr{P})$ being the probability distribution function (PDF) of the i-th $\mathscr{P}$ and $p_{\mathscr{M},\mathscr{P}}(\mathscr{P})$ being the $\mathscr{P}$ PDF for the model. Here, we assume the $p_i(\mathscr{P})$ as a Gaussian centered at the published value with width as the published error bar. Figure A.1 shows the $p_{\mathscr{M},e}(e)$ (the red and green solid lines; original data in Nagasawa and Ida 2011) and $p_i(e)$ (the black thin lines), which are suitably scaled, while Figure A.2 represents $p_{\mathscr{M},\lambda}(\lambda)$ (the red and green solid lines; original data in Fabrycky and Tremaine 2007 and Nagasawa and Ida 2011) and scaled $p_i(\lambda)$ (the black thin lines). Results of $\mathscr{R}_e = -1.035$ and $\mathscr{R}_\lambda = -2.045$ support the those of Morton and Johnson (2011a), who pointed out that λ distribution favored planet-planet scattering (plus an aligning model) compared to Kozai migration. A reason that our samples support the scattering model even without using the aligning models (e.g. type II migration) can be reasonably explained by our sample selections, which were designed to exclude a chance of the type II migration (see §1.3).

Here, we replace Kozai PDF by linearly mixed Kozai mechanism with the scattering in the various ratios (hereafter "mixed" models). Namely, a PDF for the mixed model is defined as

$$p_{\mathrm{mix},\mathscr{P}}(\mathscr{P}) = f p_{\mathrm{Koz},\mathscr{P}}(\mathscr{P}) + (1-f) p_{\mathrm{scat},\mathscr{P}}(\mathscr{P}), \tag{A.4}$$

where f is the mixing ratio. Thus, new Bayes factor is rewritten as

$$\mathscr{R}_{\mathscr{P}} = \log_{10}\left(\frac{\mathscr{L}_{\text{mix}}(\{\mathscr{P}\})}{\mathscr{L}_{\text{scat}}(\{\mathscr{P}\})}\right), \tag{A.5}$$

where

$$P_{\text{mix}}(\mathscr{P}_i) = \int p_i(\mathscr{P})p_{\text{mix},\mathscr{P}}(\mathscr{P})d\mathscr{P} \tag{A.6}$$

and

$$\mathscr{L}_{\text{mix}}(\{\mathscr{P}\}) = \prod_{i=1}^{N} P_{\text{mix}}(\mathscr{P}_i), \tag{A.7}$$

resulting in Figure A.3. The $\mathscr{R}_{\mathscr{P}}$ values decrease as the mixing ratios increase, possibly supporting the pure scattering model in these cases.
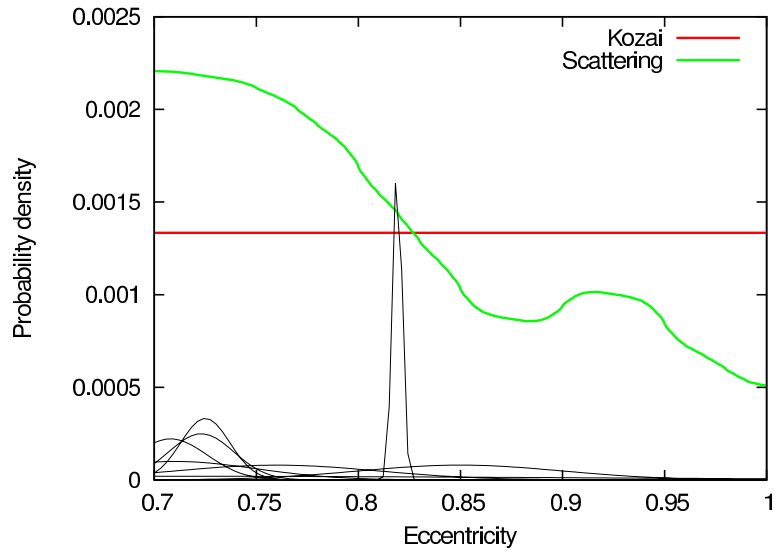
Figure A.1: Probability distributions for the eccentricity. The distribution for Kozai mechanism (the red line) is assumed as a flat with reference to Takeda and Rasio (2005), and for planet-planet scattering (the green line) is calculated from Gaussian filtered data in Nagasawa and Ida (2011). Scaled probability distributions for each data set are shown in the bottom.

Then, we adopt the Bayes factor to our binary rates. The number of single stars in our eccentric planet sample is 6 or 5, while the number of double stars is revealed as 2 or 3, for the "Confirmed" samples or for the "With HD 222582" samples, respectively. Because the values of published binary rates are 46% for the Solar neighbors (Raghavan et al., 2010) and 11.95% for all planet host stars (Roell et al., 2012), the likelihood $\mathscr{L}_{\text{SN}}(\{e\})$ is calculated as

$$\mathscr{L}_{\text{SN}}(\{e\}) = (1 \times 54\%)^6 \times (1 \times 46\%)^2 \tag{A.8}$$

for the "Confirmed" samples or

$$\mathscr{L}_{\text{SN}}(\{e\}) = (1 \times 54\%)^5 \times (1 \times 46\%)^3 \tag{A.9}$$
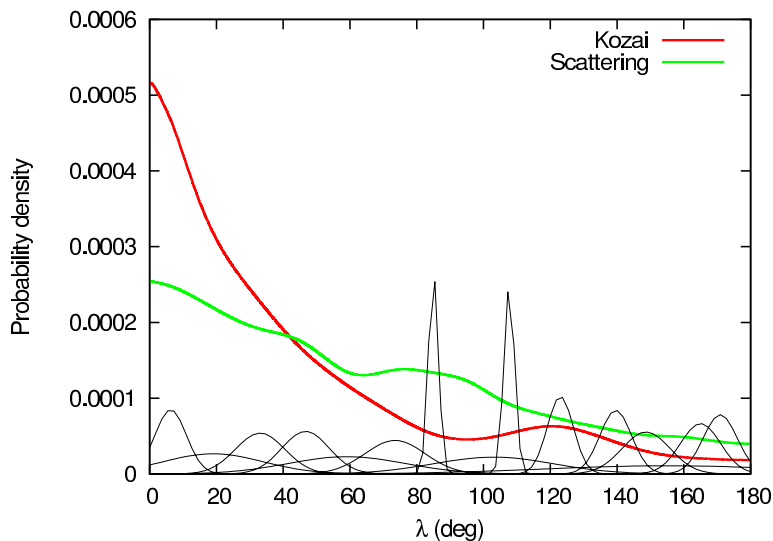
Figure A.2: Probability distributions for λ (absolute values). The distribution for Kozai mechanism (the red line) and for planet-planet scattering (the green line) is calculated from Gaussian filtered and projected data in Fabrycky and Tremaine (2007) and Nagasawa and Ida (2011). Scaled probability distributions for each data set are shown in the bottom.
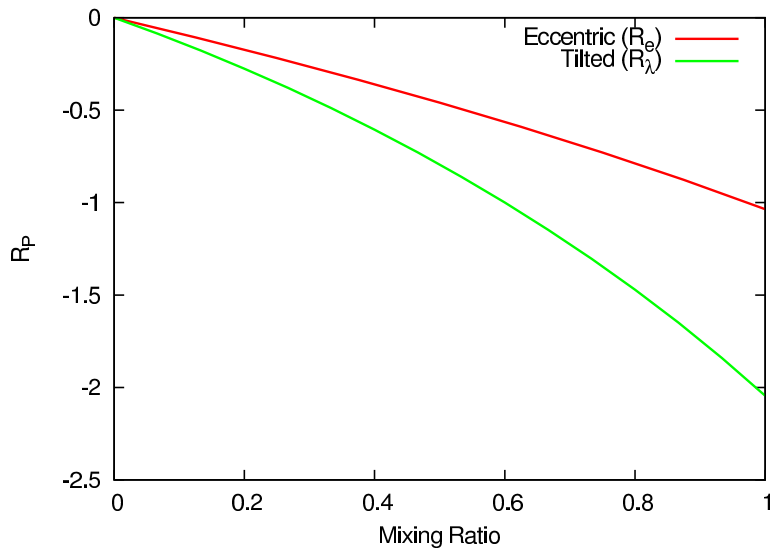
Figure A.3: Lines showing $\mathscr{R}_{\mathscr{P}}$ profiles as functions of the mixing ratio (f; defined in Equation A.4). $\mathscr{R}_{\mathscr{P}}$ is defined by Equation A.5. The mixing ratios of 0 and 1 denote the pure scattering model and the pure Kozai mechanism, respectively.

for the "With HD 222582" samples. In the same manner, $\mathscr{L}_{PH}(\{e\})$ is written as

$$\mathscr{L}_{PH}(\{e\}) = (1 \times 88.05\%)^6 \times (1 \times 11.95\%)^2 \tag{A.10}$$

for the "Confirmed" samples or

$$\mathscr{L}_{PH}(\{e\}) = (1 \times 54\%)^5 \times (1 \times 11.95\%)^3 \tag{A.11}$$

for the "With HD 222582" samples. Hence, the $\mathscr{R}_e$ values are calculated as

$$\mathscr{R}_e = \log_{10}\left(\frac{\mathscr{L}_{SN}(\{e\})}{\mathscr{L}_{PH}(\{e\})}\right) = \begin{cases} -0.103 & \text{for "Confirmed" samples} \\ 0.694 & \text{for "With HD 222582" samples} \end{cases} . \tag{A.12}$$

The $\mathscr{R}_e$ for "Confirmed" samples indicates a neutral result and, conversely the value for "With HD 222582" samples relatively favors the SN binary rate, with good agreement with the binomial probability in Table 6.1. To estimate robustness of the $\mathscr{R}_e$ values, we randomly create 5000 sets of 8 target stars for each binary rate and then, by combining the all samples, we build a cumulative $\mathscr{R}_e$ distribution (see Figure A.4), which indicates the both $\mathscr{R}_e$ values are not significant in the model selection.
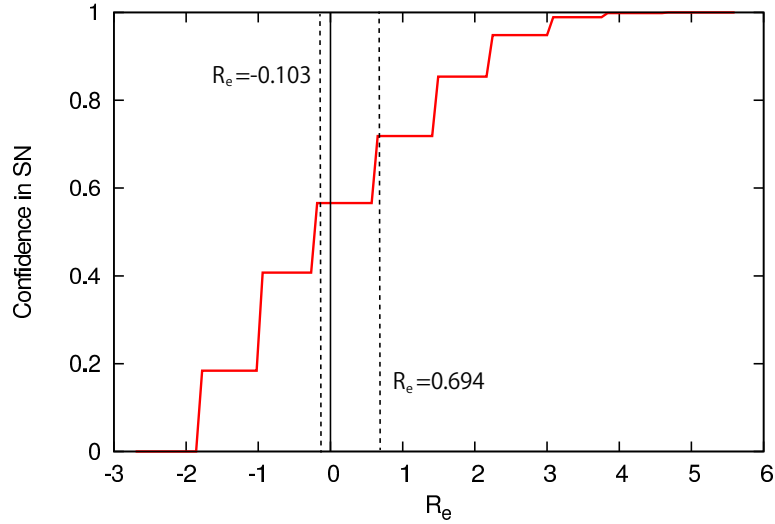
Figure A.4: Relationship between our model selection statistic $\mathscr{R}_e$ and a model selection confidence. We randomly create 5000 sets of eccentric samples with a sample size of 8 for each model to build the cumulative $\mathscr{R}_e$ distribution. The current data are not significant in the model selection.

Similarly, likelihoods for the tilted samples can be written as

$$\mathscr{L}_{SN}(\{\lambda\}) = \begin{cases} (1 \times 54\%)^{11} \times (1 \times 46\%)^4 & \text{for Category (I)} \\ (1 \times 54\%)^7 \times (1 \times 46\%)^8 & \text{for Category (II)} \\ (1 \times 54\%)^6 \times (1 \times 46\%)^9 & \text{for Category (III)} \\ (1 \times 54\%)^3 \times (1 \times 46\%)^{12} & \text{for Category (IV)} \end{cases} \tag{A.13}$$

and

$$\mathscr{L}_{PH}(\{\lambda\}) = \begin{cases} (1 \times 88.05\%)^{11} \times (1 \times 11.95\%)^4 & \text{for Category (I)} \\ (1 \times 88.05\%)^7 \times (1 \times 11.95\%)^8 & \text{for Category (II)} \\ (1 \times 88.05\%)^6 \times (1 \times 11.95\%)^9 & \text{for Category (III)} \\ (1 \times 88.05\%)^3 \times (1 \times 11.95\%)^{12} & \text{for Category (IV)} \end{cases} . \tag{A.14}$$

Therefore the $\mathscr{R}_\lambda$ values are

$$\mathscr{R}_\lambda = \log_{10}\left(\frac{\mathscr{L}_{SN}(\{\lambda\})}{\mathscr{L}_{PH}(\{\lambda\})}\right) = \begin{cases} 5.868 \times 10^{-3} & \text{for Category (I)} \\ 3.197 & \text{for Category (II)} \\ 3.994 & \text{for Category (III)} \\ 6.388 & \text{for Category (IV)} \end{cases}, \tag{A.15}$$

which also support the binomial probabilities (see Table 6.2). The confidence levels for Category (III), and (IV) are 0.9568, and 0.9996, respectively, indicating high significance of $> 95\%$ (see Figure A.5). Thus, the binary rates for Category (III) and (IV) of the tilted samples can be explained by the SN binary rate. However, because the rate especially for Category (IV) significantly exceeds the SN binary rate of 46%, it is unreasonable to believe such a confidence level.
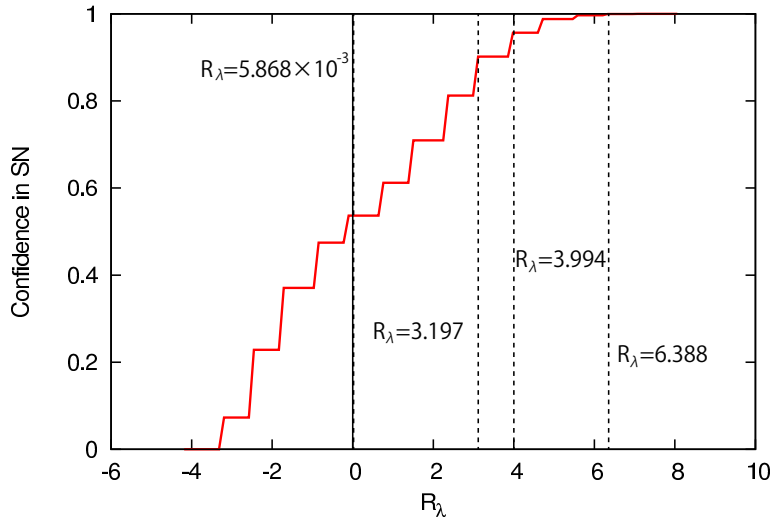
Figure A.5: Relationship between our model selection statistic $\mathscr{R}_\lambda$ and a model selection confidence (SN vs PH). We randomly create 5000 sets of tilted samples with a sample size of 15 for each model to build the cumulative $\mathscr{R}_\lambda$ distribution. The current data for Category (III) and (IV) are significant of the model selection.

Hence, we assume another model that all the tilted planets in our samples have been formed via Kozai mechanism. Although the model should consequently lead to a 100% binary rate, we suppose its binary rate of 99.69%, assuming that a companion in a region within $0.''28$, the smallest separation of the detected objects in this study, cannot be detected, while ones out of the region (within $< 5''$) can. Under the models, the comparisons between the model (represented as "All" in the following equation) and SN for the tilted targets result in

$$\mathscr{R}_\lambda = \log_{10}\left(\frac{\mathscr{L}_{SN}(\{\lambda\})}{\mathscr{L}_{All}(\{\lambda\})}\right) = \begin{cases} 23.31 & \text{for Category (I)} \\ 13.00 & \text{for Category (II)} \\ 10.42 & \text{for Category (III)} \\ 2.692 & \text{for Category (IV)} \end{cases}. \tag{A.16}$$

The results appear to strongly support that not all planets have been formed via Kozai mechanism even for the highest binary rate for Category (IV), but only the value of $\mathscr{R}_\lambda$ for Category (I), which has an

apparently lower rate than the SN rate, favors the SN binary rate (see Figure A.6). The confidence levels for Category (III) and (IV), which significantly favors the SN model in the previous calculation, indicate low significances in this case (see Figure A.6).
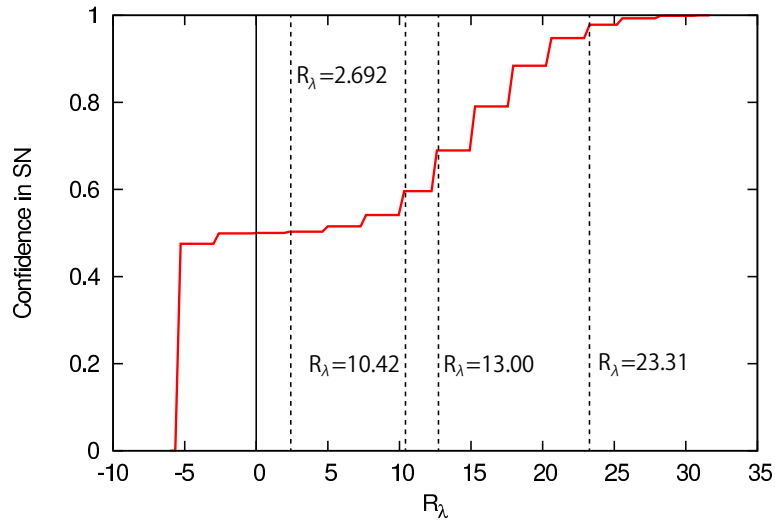
Figure A.6: Relationship between our model selection statistic $\mathscr{R}_\lambda$ and a model selection confidence (SN vs All). We randomly create 5000 sets of tilted samples with a sample size of 15 for each model to build the cumulative $\mathscr{R}_\lambda$ distribution. The current data are not significant of the model selection except for Category (I).

Summarizing the Bayes factor discussions, at first, we verify that our sample selections effectively exclude an influence of type II migration. Thanks to the selection, both our eccentric and tilted planet host samples also support the results of Morton and Johnson (2011a) without employing an additional model. According to the discussion of binary rates, we can conclude that only Category (III) of the tilted sample favors the SN rate compared to the PH rate, while the other Bayes factors do not support any binary rates of SN, PH, or All on significant confidence levels. The fact, conversely, can lead to an explanation that even the "All" model has a little capability of explaining the binary rates especially for the tilted samples. However, the explanation is likely inconsistent with our result based on $\mathscr{P}_{\mathscr{M},\lambda}(\lambda)$ PDFs. A likely solution to the conflict is that mutual inclinations between a planetary orbit and a companion's orbit, i, do not exceed the critical inclination i_{crit} (i.e. $i < i_{\mathrm{crit}}$), but in this case, we cannot give an appropriate answer to the question of why tilted planet host stars have more companion candidates than the global binary rate for planet host stars (see Table 6.2). Anyway, we require to confirm the binary rate for the tilted samples by determining the boundness of the companion candidates. Meanwhile, it is likely that the eccentric planets have been formed via the scattering, considering our Bayes factor discussion both based on $\mathscr{P}_{\mathscr{M},e}(e)$ PDFs and of the binary rates.

Appendix B

A Discovery of a Candidate Companion to a Transiting System KOI-94: A Direct Imaging Study for a Possibility of a False Positive

Observations are carried out not only with employing one method, but also with combining plural methods in order to supplement disadvantages of each technique. As mentioned in §2.2, since some events or objects other than a planet can induce transit-like dimmings in light curves, it is necessary to confirm whether transits are exactly caused by a real planet or not. Namely, based on the transit method, defocusing frequently forces us to employ aperture photometry with large apertures, and therefore contamination by background objects possibly occurs. If a hidden object is variable in magnitude, the photometry consequently produces a variable light curve. Hence, we cannot distinguish periodical dimmings caused by a real planet from actually by a mixed object, named as "a false positive," only with the light curve analysis. On the other hand, direct imaging has a strong power in detecting a faint object close to a bright target star, and thus can play an important role in examining the presence of a possible mixed object. Here, we focus on the transiting system KOI-94 and report the result of direct imaging observations and a transit light curve analysis.

B.1   Chapter Abstract

We report a discovery of a companion candidate around one of *Kepler* Objects of Interest (KOIs), KOI-94, and results of our quantitative investigation of the possibility that planetary candidates around KOI-94 are false positives. KOI-94 has a planetary system in which four planetary detections have been reported by *Kepler*, suggesting that this system is intriguing to study the dynamical evolutions of planets. However, while two of those detections (KOI-94.01 and 03) have been made robust by previous observations, the others (KOI-94.02 and 04) are marginal detections, for which future confirmations with various techniques are necessary. We have conducted high-contrast direct imaging observations with Subaru/HiCIAO in H band and detected a faint object located at a separation of $\sim 0.6''$ from KOI-94. The object has a contrast of $\sim 1 \times 10^{-3}$ in H band, and corresponds to an M type star on the assumption that the object is at the same distance of KOI-94. Based on our analysis, KOI-94.02 is likely to be a real planet because of its transit depth, while KOI-94.04 can be a false positive due to the companion candidate. The success in

detecting the companion candidate suggests that high-contrast direct imaging observations are important keys to examine false positives of KOIs. On the other hand, our transit light curve reanalyses lead to a better period estimate of KOI-94.04 than that on the KOI catalogue and show that the planetary candidate has the same limb darkening parameter value as the other planetary candidates in the KOI-94 system, suggesting that KOI-94.04 is also a real planet in the system. It is unlikely that the companion candidate, even if bound, has caused the Kozai effect on the planets at their current positions.

B.2 Chapter Introduction

One of the best ways to determine orbital parameters of extrasolar planets (exoplanets) is the transit method. Particularly the *Kepler* satellite, launched in 2009, has executed successful transit observations, resulting in discovery of more than 3,600 planet candidates[1]. It drastically increases the number of exoplanets we know and has found many multi-transiting planetary systems.

The principal problem related to the transit method is a possibility of a false positive. A false positive in transit surveys means misidentifying a signal caused by an object other than a planet orbiting the target star as its true planetary companion. In transit surveys, false positives are induced by some objects, for example eclipsing binaries, background transiting planetary systems or companions with transiting planets (Fressin et al., 2013) within photometric apertures of target stars. Such objects reduce their brightness periodically, and total flux containing both from the target stars and from the mimicking objects consequently decreases periodically. Since the presence of the false positive sources cannot be verified only with the transit method, the depressions in light curves cannot be translated directly into planets orbiting the targets, and follow-up observations are necessary to confirm that the depressions are really caused by planets.

Although most of *Kepler* planetary candidates are waiting to be confirmed, false positive rates reported by spectroscopic follow-up observations (Santerne et al. 2012; $\sim 35\%$) and other planet surveys (e.g. HAT-Net; Latham et al. 2009) are significantly higher than the rates for *Kepler* candidates theoretically expected by Morton and Johnson (2011b) (less than 5% for over half targets) and Santerne et al. (2013) ($11.3 \pm 1.1\%$ for whole targets) based on Galactic models. The inconsistency has not been elucidated yet, and therefore, suggests that *Kepler* candidates are necessary to be confirmed with other manners, including the radial velocity method, TTVs (Agol et al., 2005), the centroid analysis (Batalha et al., 2010), BLENDER analysis (Torres et al., 2004), and the direct imaging observations.

Many follow-up observations with the direct imaging method have been executed so far, but most observations were too shallow to confirm candidates efficiently. For example, let us assume that there is a false positive source within the target star's photometric aperture with the magnitude of $\Delta m = 10$ mag compared to the target. A full occultation of the source induces a depression with the depth of 100 ppm, which is a typical value caused by an Earth-like planet transiting a Sun-like star. A false positive source with a smaller contrast ($\Delta m < 10$) can cause the 100 ppm depression by its partial occultation, while a source with a larger contrast ($\Delta m > 10$) can induce a shallower depression. Thus, if a depression with the depth of 100 ppm is detected, direct imaging observations with a contrast of $\Delta m = 10$ mag can fully and efficiently put a constraint on the possibility of a false positive. However, some studies employ direct imaging with a detection limit of $\Delta m < 10$ mag for confirming a transit detection with the depth of < 100 ppm (e.g. Barclay et al. 2013). Such shallow observations cannot fully reject false positive sources. Moreover, if a companion candidate is found around the target by the direct imaging, we can evaluate gravitational influences upon the orbital migrations of the planetary system by the companion.

---

[1]http://kepler.nasa.gov/

We focus on KOI-94, which was listed on the earliest *Kepler* Object of Interest (KOI) list (Borucki et al., 2011; Batalha et al., 2013). KOI-94 is a relatively faint — $Kp = 12.2$ (Borucki et al., 2011), $H = 11.0$ (2MASS; Skrutskie et al. 2006) — late F-type star with the age of $3.9^{+0.3}_{-0.2}$ Gyr (Hirano et al., 2012) or 3.16 ± 0.39 Gyr (Weiss et al., 2013). This system has four planet candidates named as KOI-94.01, 02, 03 and 04, which are also known as KOI-94 d, c, e and b, respectively (properties listed on Table **??**). Hirano et al. (2012) discovered the "planet-planet eclipse" phenomenon in the light curves, where the term means that a planet occults another planet transiting their host star at that time. Combining the event with measurements of the Rossiter-McLaughlin effect (Ohta et al., 2005) of KOI-94.01, they confirmed that KOI-94.01 and 03, at least, are real planets and showed that orbital axes of KOI-94.01 and 03 and the spin axis of the main star KOI-94 are well aligned. The fact suggests that the planets have not experienced the planet-planet scattering (e.g. Chatterjee et al. 2008; Nagasawa and Ida 2011) or the Kozai migration (e.g. Kozai 1962; Wu et al. 2007; Fabrycky and Tremaine 2007). In contrast, a boundness of KOI-94.02 and 04 remains unclear; radial velocities observed by Weiss et al. (2013) represented so low amplitudes that they could detect 04 only at a 2σ significance and 02 at the same level of non-detection, and their direct imaging observations had shallow depths ($\Delta K_S = 3.4$ at $0.''5$, 5.9 at $1.''0$) in spite of the depth of KOI-94.04 (131 ppm). Hence, deeper direct imaging observations for KOI-94 are necessary to confirm detections of the candidates.

In this paper, we present results of high-contrast direct imaging observations for KOI-94 and elucidate the presence of a faint object around the star. Details of the direct imaging observations and discussion based on the observations are described in Section B.3 and B.4, respectively. We then show our results and discussion of reduced light curves of planetary candidates KOI-94.04 in Section B.5. Section B.7 summarizes the paper.

B.3 Deep direct imaging observations for KOI-94 and analyses

In employing the direct imaging observations, we first estimate the distance of KOI-94 from the Earth. Given KOI-94's magnitudes of $g = 12.551, i = 12.057$ (*Kepler* Input Catalog) and metallicity of $[Fe/H] = +0.0228 \pm 0.0020$ (Weiss et al., 2013) for KOI-94, we can infer its r-band absolute magnitude $M_r \sim 4.0$ according to Equation 1 in Ivezić et al. (2008), who developed the Galactic model. A comparison between the M_r and an observed magnitude of $r = 12.186$ (*Kepler* Input Catalog) for KOI-94 enables us to estimate its distance to be ~ 440 pc. On the other hand, by applying an KOI-94's estimated mass of $1.25^{+0.03}_{-0.04} M_\odot$ (Hirano et al., 2012) to Yonsei-Yale isochrone model (Demarque et al., 2004), we calculate $M_V \sim 3.9$, which can be compared with V-band magnitude of KOI-94 $V = 12.6$ (NOMAD catalogue; Zacharias et al. 2004) to infer the distance of ~ 550 pc. The accurate distance does not matter for our following discussions, and we therefore adopt the average of both estimations, ~ 500 pc, in this study.

In order to check the presence of possible false positive sources, we observed the star as a part of the SEEDS project (Tamura, 2009). The SEEDS has directly imaged stellar companions that are the important clue to the origin of close-in exoplanets (Narita et al., 2010b, 2012), as well as substellar or planetary companions (e.g. Thalmann et al. 2009; Carson et al. 2013; Kuzuhara et al. 2013). We obtained H band images using a high-contrast near-infrared camera HiCIAO (Hodapp et al., 2008; Suzuki et al., 2010) with a 188 actuators adaptive optics system (AO188; Minowa et al. 2010). The detector of HiCIAO consists of 2048×2048 pixels with the plate scale of 9.5 mas/pixel, and has the field of view (FOV) of about $20'' \times 20''$. The observations were performed on 2012 July 10[2], where we employed angular

---

[2]On the observation night, the eclipse of KOI-94.02 or 04 did not occur based on their transit information on the KOI catalogue.
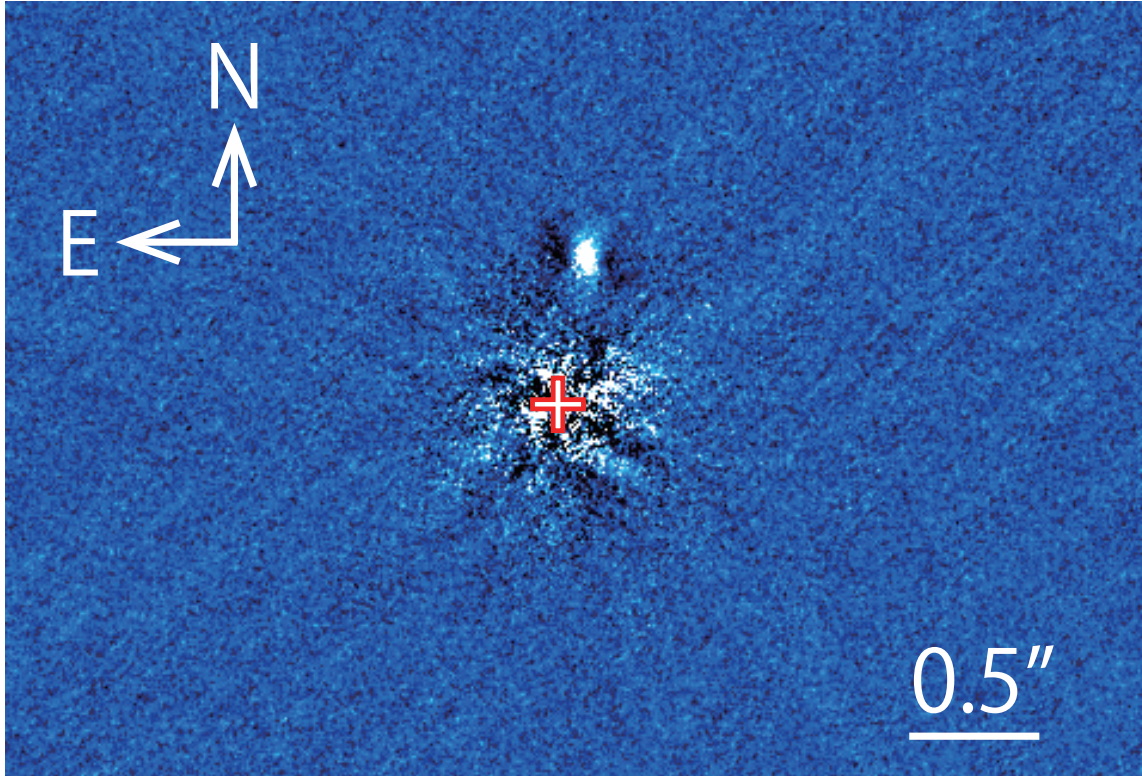
Figure B.1: An *H* band image of KOI-94 reduced by the classical ADI analysis. The position of the central star is shown as a cross. A faint companion candidate appears at a separation of $\sim 0\rlap{.}''6$ from the star. Artificial dark tails extending east-west are induced by the ADI analysis.

differential imaging (ADI; Marois et al. 2006) to remove the starlight and the stellar speckles. The sky was photometric, and the typical full width at half maximum (FWHM) of our observed PSFs was $\sim$15.4 pixels ($0\rlap{.}''146$) after AO corrections. We obtained 35 images, of which all frames were adequate for high-contrast science. Individual integration times were 15 seconds and 3 coadds per image were taken (i.e. each image has an integration time of 45 seconds). Thus our observations allow for the cumulative integration time of 26 minutes, where the field rotation through ADI observations was 13.9 degrees in total. We note that the observations were performed without an occulting mask and array saturation, which allow us to carefully calibrate the acquired data sets.

For the first attempt in data reductions, we plainly combined all frames after derotating them and subtracting halos from them, but spider noises and speckle noises prevented us from discussing the presence of faint objects around the target star. We then employed the locally optimized combination of images (LOCI) algorithm (Lafrenière et al., 2007) in order to remove the noises. As a result, we detect a faint object (hereafter KOI-94 B, or B for short) at a separation of $\sim 0\rlap{.}''6$ from KOI-94 (see Figure B.1), regardless of the fact that Weiss et al. (2013) did not find the object with AO direct imaging observations using MMT/ARIES and the speckle imaging observations using DSSI camera on the WIYN 3.5m telescope. This is the first discovery of a false positive source candidate around KOI-94. The LOCI processing is powerful method for high-contrast data reductions, but it may not be efficient in the case
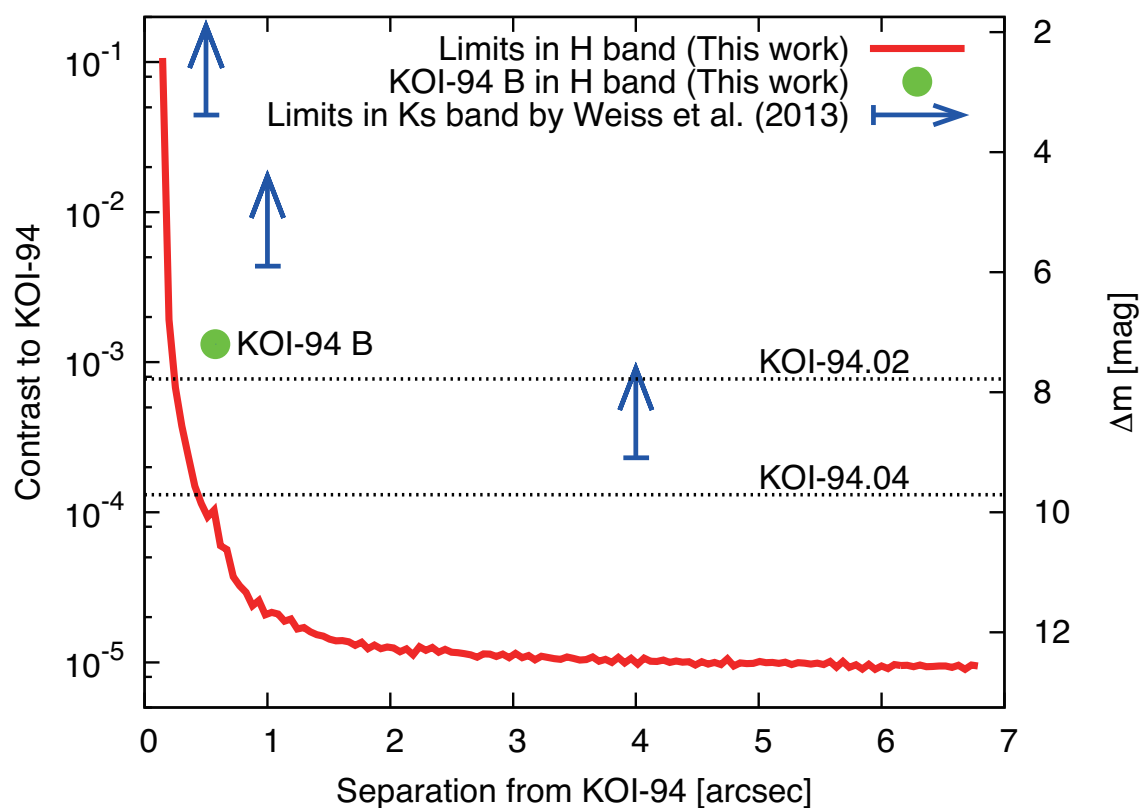
Figure B.2: A comparison between detection limits for our observations and the contrast of the companion candidate B, with the depths of KOI-94.02 and 04. The solid line shows a 5σ contrast curve in *H* band with Subaru/HiCIAO for KOI-94 overlaid with a position of KOI-94 B. The size of the circle is larger than its errors. The two dotted lines depict each depth of planetary candidates in *Kp* band. The arrows represent limits by Weiss et al. (2013) in K_S band with MMT/ARIES for reference.

of small field rotations as our observations for KOI-94 because of the serious self-subtraction problem[3], though some new techniques have been developed for avoiding the self-subtraction (e.g. Currie et al. 2012). Hence, we simply attempted to apply the classical ADI (Marois et al., 2006) data processing to the images, after subtracting the halos of KOI-94 PSFs on each frame. Indeed, this additional attempt improved the signal-to-noise ratio (SNR) of KOI-94 B. A final image made by combining all frames reduced with the classical ADI analysis and its 5σ contrast curve are shown in Figure B.1 and B.2, respectively. We can easily find the faint star in Figure B.1 at the position with a separation of $0\rlap{.}''6$ to the north (PA$= 350°$) from the central star. Figure B.2 shows that our deep high contrast imaging (the red line) reaches 1.1×10^{-4} at $0\rlap{.}''5$ and 2.1×10^{-5} at $1\rlap{.}''0$, enabling us to detect B (shown by the green circle), in contrast to the shallow detection limits by Weiss et al. (2013) (the blue arrows). The brightness of B was obtained from the aperture photometry relative to the central star ($H = 11.0$), and compensated for the self-subtraction induced by the ADI analysis with estimates from measuring fluxes of artificial signals embedded in the science frames. Its photometric error is attributed mainly to the uncertainties of the estimates. Although the arrows are based on their brief descriptions of the detection limits in K_S band, the difference of wavelengths does not affect the discussion as long as B has a moderate color of $H - K_S \lesssim 3$. The depths of KOI-94.02 and 04 in Kp band are also represented in Figure B.2 as the dotted lines, because we can directly compare them with B's contrast in H band under condition that the transit depths are constant in various wavelengths. Properties of KOI-94 B are summarized in Table **??** in detail.

Under an assumption that KOI-94 B is a single star with the same distance as that of KOI-94 (~ 500 pc), our measured magnitude, $H = 18.2$, for KOI-94 can be converted into an absolute magnitude of $M_H = 9.7$, which can be compared with 3-4 Gyr isochrones in NextGen model (Baraffe et al., 1998) to infer a mass of $\sim 0.1 M_\odot$ for B. The measured projected separation of B ($\sim 0\rlap{.}''6$) corresponds to ~ 300 AU at the assumed distance.

B.4 Interpretation of the results of the direct imaging observations

B.4.1 Photometric Influences of the new companion upon the KOI-94 system

In this section, we examine influences from the companion candidate B found with the direct imaging. First of all, we note that B does not correspond to any of the reported four planets orbiting KOI-94. This is because it is unrealistic that a planet with the separation of ~ 300 AU (see Section 2) orbits the Sun-like star with the period of less than 54 days, the longest value in the KOI-94 system. Since the most important fact is that the candidate B is within the *Kepler* photometric aperture (typically a few arcsecs), we discuss influences for all hypotheses upon the light curves of KOI-94 in this section. Among the depressions of KOI-94, because we know that KOI-94.01 and 03 are real planets transiting KOI-94 (Hirano et al., 2012; Weiss et al., 2013), only KOI-94.02 and 04 are to be discussed.

The following cases can cause depressions in the light curves of KOI-94.02 or 04; (1) a real planet transiting the central star KOI-94, (2) a real planet transiting the companion B, and (3) B being an eclipsing binary. In case of (1), B cannot affect estimates of stellar and planetary parameters from the light curves seriously, because B is much fainter than the central star. In cases of (2) and (3), whether B is bound or not to the central star KOI-94 does not become a serious issue. If (2) or (3) is true, planet candidates of KOI-94.02 or 04 may not be a real planet orbiting KOI-94. These hypotheses

---

[3]The self-subtraction is an inherent problem in the ADI analysis and means a diminution of a signal's flux together with various noises, induced by subtraction of the signal itself. In case that the signal is sufficiently bright and scarcely rotated, like KOI-94 B, LOCI tends to regard the signal as a noise and, consequently, LOCI attempts to decide coefficients too hard for the sake of removing the signal. As a result, the self-subtraction of LOCI can be larger than that of the classical ADI analysis.

about KOI-94.02 are examined and concluded in the following paragraphs based on the direct imaging observations. The hypotheses (2) and (3) about KOI-94.04 are precisely discussed in §A.3.2 in addition to this subsection, while the hypothesis (1) about it is argued in §A.4.2 grounded on our light curve reanalyses (§A.4.1).

Considering an extreme case that the companion candidate is completely occulted, the brightness of B can be translated into upper limit for the depth of depression induced by B. Then if the upper limit is shallower than the transit depth of KOI-94.02 or 04, it is impossible that KOI-94.02 or 04 is orbiting the companion candidate, i.e., it is a real planet transiting the central star. In order to estimate B's *Kepler* magnitude from our *H* band magnitude and directly compare it with the depths of the depressions of the planetary candidates in *Kp* band on the KOI catalogue, we adopt the following analyses.

First, if B is physically bound to KOI-94 and a single star, B's mass should be $\sim 0.1 M_\odot$ (see Section 2) and we can then calculate its apparent brightness in *Kp* band to be $Kp = 24.0$ using estimated absolute magnitudes of $M_g = 16.9$ and $M_r = 15.4$ (Baraffe et al., 1998) from the observed magnitude in *H* band and the equation[4]

$$Kp = \begin{cases} 0.2g + 0.8r & \text{for } g - r \leq 0.8 \\ 0.1g + 0.9r & \text{for } g - r > 0.8 \end{cases}, \tag{B.1}$$

where *g* and *r* are apparent magnitudes for an apparent *Kp* magnitude. Consequently we obtain $\Delta Kp = 11.8$, corresponding to a contrast of 1.9×10^{-5} in *Kp* band. The contrast, which means an upper limit, is too small to explain the depths of KOI-94.02 (7.6×10^{-4}) or 04 (1.3×10^{-4}). Therefore, in this case, hypothesis (2) is ruled out.

Simultaneously, the hypothesis (3) that B is an eclipsing binary bound to KOI-94 can be discussed. Because each component of the binary would be fainter than the single M star, the binary would consist of later type stars than the above estimate. The later stars can produce shallower depressions in the light curves, and thus the hypothesis (3) is also excluded.

Next we investigate the situation that B is not bound to KOI-94. In this case, the B's color cannot be constrained from our measured *H*-band magnitude and the theoretical evolutionary trucks, since it is sufficiently possible that B has the distance and age different from those of KOI-94. Thus we are not able to directly estimate the *Kp* magnitude. We employ statistical discussions to estimate it based on Howell et al. (2012), who compared *Kepler* Input Catalogue with 2MASS catalogue and derived empirical relationships between infrared magnitudes and *Kp* magnitudes of stars in the *Kepler* field. Since they did not indicate *Kp-H* relationship, we substitute our *H* magnitude into *J* and K_S magnitudes in their equations in order to obtain a rough estimate of B's *Kp* magnitude. Then we acquire $Kp = 19.9$ and $Kp = 21.5$ with *Kp-J* and *Kp-K_S* relationships, respectively. Since the magnitude of KOI-94 central star is $Kp = 12.2$, the contrasts are $\Delta Kp = 7.7$ or 9.3. These contrasts correspond to flux ratios of 8.3×10^{-4} and 1.9×10^{-4}, respectively. Comparing them with the depth of KOI-94.02 (7.8×10^{-4}), we suggest that it is difficult to regard KOI-94.02 as a planet transiting B or a false positive induced by B; in other words, an extreme case that B is completely occulted can explain the depth of KOI-94.02. On the other hand, the possibility that KOI-94.04 (1.3×10^{-4}) is a false positive cannot be excluded by comparing B's magnitude and its depth. Hence we conclude that KOI-94.02 is a real planet orbiting KOI-94, assuming the typical color of stars in the field, and discuss KOI-94.04's nature in the following sections.

B.4.2 Is KOI-94.04 a False Positive?

In this subsection, we assume KOI-94.04 as a false positive.

---

[4]http://keplergo.arc.nasa.gov/CalibrationZeropoint.shtml

First we examine the hypothesis (2) that the planetary candidate orbits B. Because the assumption that the companion B is physically bound to the central star is rejected in §B.4.1, we here assume the companion candidate to be a background star.

Comparing the depth of planetary candidate KOI-94.04 of 1.3×10^{-4} with the contrast of B of $(1.9 - 8.3) \times 10^{-4}$ in Kp band (see §A.3.1), a ratio of their radii is $R_{\text{KOI}-94.04}/R_{\text{B}} = 0.4 - 0.8$, if any light from KOI-94.04 is neglected. The estimation of $R_{\text{KOI}-94.04}/R_{\text{B}}$ can constrain the radius of KOI-94.04. If B has a radius larger than $0.5R_{\odot}$, the ratio leads to $R_{\text{KOI}-94.04} > 2.0R_{\text{J}}$; an exoplanet with a radius larger than $2.1\ R_{\text{J}}$ has not been discovered so far (Weiss et al. 2013, see also exoplanets.org). Considering the estimate of $R_{\text{KOI}-94.04}/R_{\text{B}}$ and the observational knowledge cumulative for exoplanet properties, we can suggest that a star with a radius of $> 0.5R_{\odot}$ can hardly explain the depressions for KOI-94.04. Note, however, an object with $R_{\text{B}} < 0.5R_{\odot}$ can account for our estimated $R_{\text{KOI}-94.04}/R_{\text{B}}$. Obtaining a spectral type of B and determining its radius by future observations are important for investigating the possibility of the hypothesis (2).

Secondly we investigate the hypothesis (3) that the companion candidate B is a binary. B's contrast in Kp band and the depth of KOI-94.04 are the same as those in the above situation. If the amount of B's fluxes decreases by 20-70% via the eclipse in the system, the depth can be explained, and thus the possibility of B being a binary is not rejected. Moreover, Fressin et al. (2013) and Santerne et al. (2013) calculated the probability of false positive with a given *Kepler* transit depth, leading to the estimated false positive rate of $8.9 \pm 2.0\%$ for KOI-94.04 in combination of their calculations. Consequently, the possibility of a false positive remains for KOI-94.04. If the secondary eclipses of KOI-94.04 is detected, it becomes strong evidence supporting KOI-94.04 as an eclipsing binary. However, we did not find a significant secondary eclipse in the following light curve analyses. Thus the possibility that KOI-94.04 is a planet (i.e. the hypothesis (1)) remains, which is discussed in the next section.

B.5 Constraints by KOI-94 light curves

Because we cannot fully exclude the possibility that KOI-94.04 is a false positive even with the new direct imaging observations, we investigate the possibility of KOI-94.04 being a real planet by revisiting the KOI-94.04 transit light curves. §A.4.1 shows our reductions and results, and we discuss the possibility in §A.4.2 based on §A.4.1.

B.5.1 Reanalysis and results of light curves

We here employ *Kepler*'s public data sets (Borucki et al., 2011; Batalha et al., 2013) of Quarter 1 through Quarter 13. In order to detect §KOI-94.04 in the light curves, we first remove trends on the curves by fitting polynomial functions with masking transit depressions. Second we fold the curves by KOI-94.04's period on the KOI catalogue (3.743245 days in Borucki et al. 2011). Third we bin the folded light curves into thousand data points. Errors of the binned points are based on the scatter of the data points in each bin. As a result, we see a depression of KOI-94.04.

The shape of phase-folded transit light curve looks asymmetric, suggesting that the fiducial period may be incorrect. Therefore, we systematically changed its period from the catalogued value with shifts in unit of its error (0.000031 days) to find a symmetric transit light curve, because a folded transit light curve with an exact period would give a symmetric curve. Figure B.3 shows three light curves with various periods and their best fit model curves. The -1.9σ light curve (i.e. $P = 3.743245 - 1.9 \times 0.000031 = 3.743186$ days) gives the most symmetric light curve. We adopt transit model by Ohta et al.
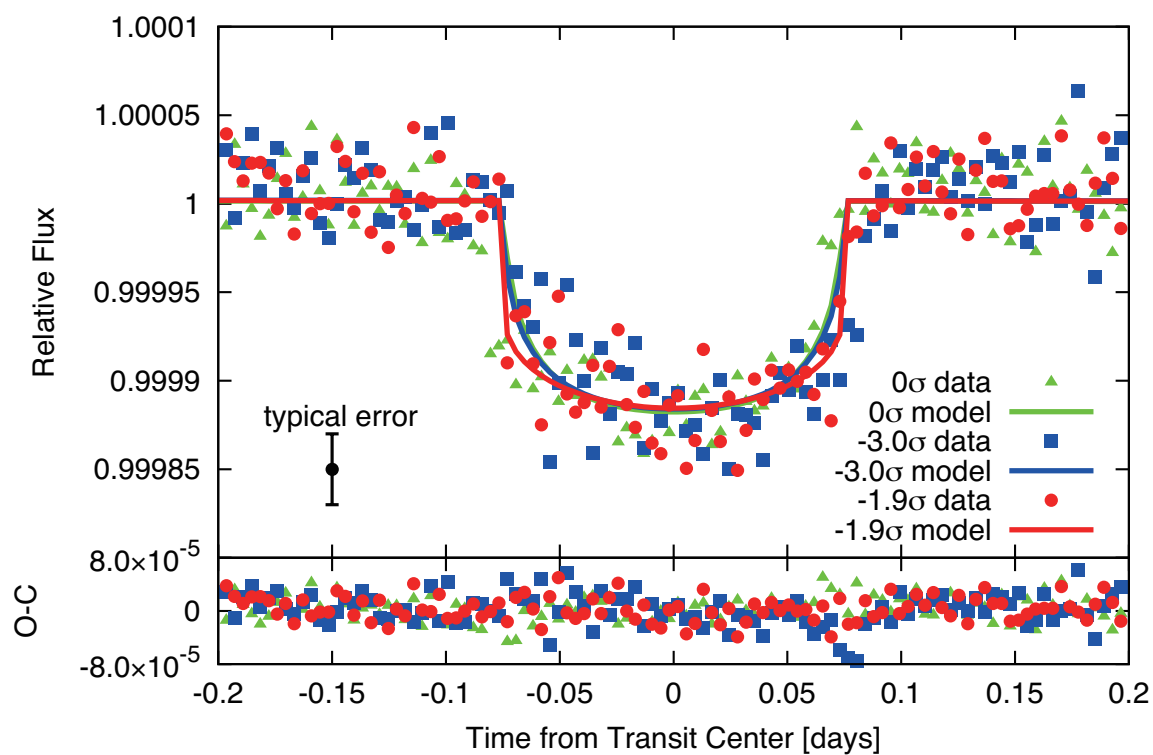
Figure B.3: Three KOI-94.04 light curves phase-folded by three periods as a function of time from the transit centers. The dots and lines in the upper panel represent observational and modeled relative flux data. Typical error size for each dot is shown at the lower left. The colors reflect differences of KOI-94.04's period; 0σ (i.e. not shifted), -3.0σ and -1.9σ (the lowest χ^2) shifted from the KOI-catalogued period are green, blue and red, respectively. Lower panel shows residuals.
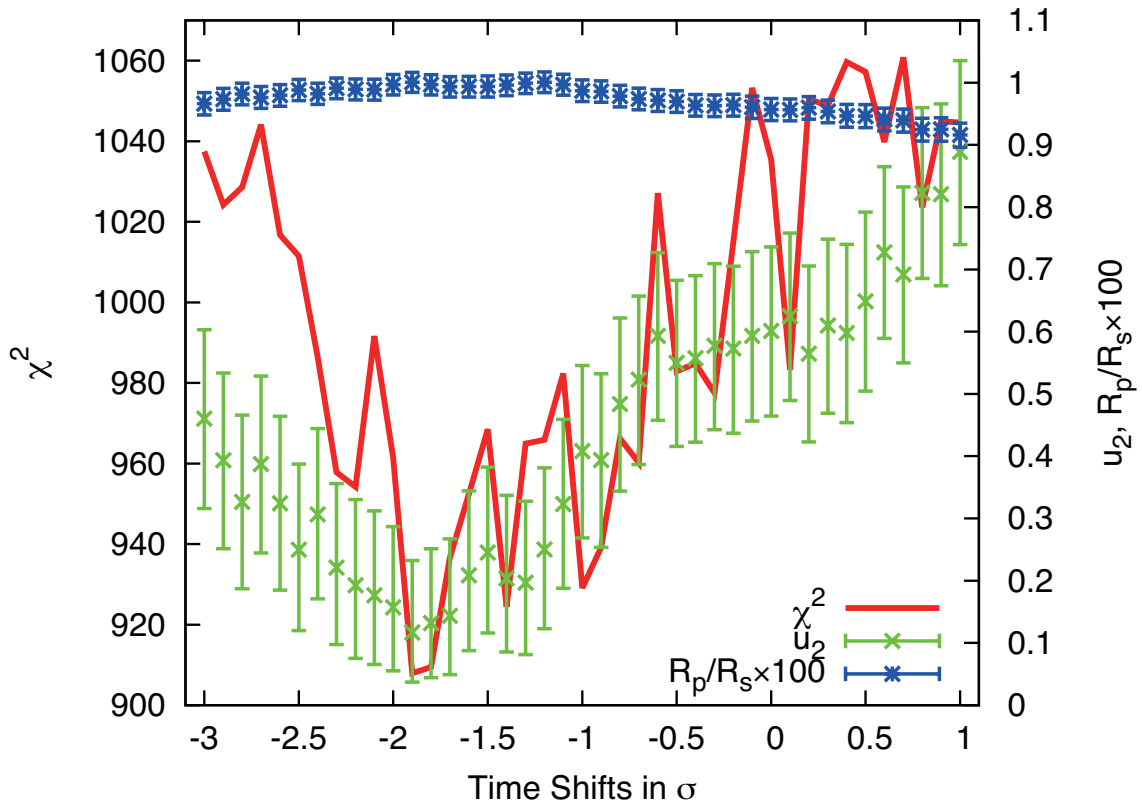
Figure B.4: Variations of parameters for KOI-94.04 as a function of its period. The red line indicates variation of the χ^2 values. The green and blue dots with error bars represent the limb-darkening u_2 parameter and the radial ratio between the planet (KOI-94.04) and the star (KOI-94) multiplied by 100. The horizontal axis shows period shifts from the KOI-catalogued period in a unit of its error.

(2009), which uses the quadratic limb-darkening law, defined as

$$I(\mu) = 1 - u_1(1 - \mu) - u_2(1 - \mu)^2, \tag{B.2}$$

where I is the intensity and μ is the cosine of the angle between the line of sight and the line from the stellar center to the position of the stellar surface. In order to quantify their symmetricities, we measured a χ^2 parameter obtained by fitting a transit model function to the curves. Here, the χ^2 parameter is expressed as

$$\chi^2 = \sum_i \frac{(F_{\text{model},i} - F_{\text{obs},i})^2}{\sigma_i^2}, \tag{B.3}$$

where $F_{\text{model},i}$ and $F_{\text{obs},i}$ are the i-th modeled and observed relative flux data, and σ_i is its error. The curves other than -1.9σ shifted data sets resulted in the higher χ^2 parameters. In addition to χ^2, limb-darkening parameter u_2 and their radial ratio between the planet candidate KOI-94.04 and its host star KOI-94, R_p/R_s, are depicted in Figure B.4 as a function of time shift. In the reduction, we fixed the other limb-darkening parameter u_1 at 0.40 (Masuda et al., 2013) and see the variation of the best-fit u_2 value. The light curve shifted by -1.9σ (the red dots and line in Figure B.3) indicates the smallest χ^2 value in our grid survey (cf. Figure B.4), which means 3.743186 days gives the best for its period. The corresponding u_2 and R_p/R_s are $0.12^{+0.12}_{-0.08}$ and 0.01001 ± 0.00016, respectively. This estimate of u_2 is especially used for the confirmation of planetary candidate KOI94.04 in the following section.

B.5.2 Is KOI-94.04 a Planet?

In contrast to §B.4.2, we investigate the possibility of KOI-94.04 as a real planet orbiting KOI-94 — the hypothesis (1). Weiss et al. (2013) conducted spectroscopic observations with Keck/HIRES, putting limits on the masses of KOI-94.02 and 04. They showed KOI-94.04's period of 3.74 days, scaled semi-major axis of $a/R_* = 7.25 \pm 0.59$, eccentricity of 0.25 ± 0.17, radius of $1.71 \pm 0.16 R_\oplus$, and mass of $10.5 \pm 4.6 M_\oplus$. Surprisingly, the radius and the mass lead to an extraordinarily high density of 10.1 ± 5.5 g cm^{-3}. Also, they determined that KOI-94.02 has a period of 10.42 days and eccentricity of 0.43 ± 0.23. Meanwhile, according to their orbital stability analysis, 80% of the random simulations with eccentric orbits reached close encounters between KOI-94.04 and KOI-94.02. Namely eccentric orbits typically become dynamically unstable in the KOI-94 system in their analysis, and they therefore suggested that the planets should have circular orbits to keep the system dynamically stable. Nevertheless their radial velocity data support the eccentric orbits for KOI-94.02 and 04. This inconsistency allows us to consider the mass or eccentricity estimate for KOI94.02 or 04 possibly inaccurate. Furthermore, though Weiss et al. (2013) also showed TTVs in the KOI-94 system, the TTV of KOI-94.04 was not discussed in their TTV analysis. Hence, the possibility that KOI94.04 is a false positive cannot be ruled out by the discussions of Weiss et al. (2013).

Our limb-darkening analyses also enable us to discuss whether the planetary candidates orbiting the same host star or not by comparing them. Our analyses show that the limb darkening parameter u_2 for the -1.9σ shifted data (i.e. the lowest χ^2) is $u_2 = 0.12^{+0.12}_{-0.08}$, under the condition that the u_1 parameter is fixed at 0.40. Our values of u_1 and u_2 are consistent with those of KOI-94.01, 02 and 03 reported by Masuda et al. (2013) ($u_1 \sim 0.40$ and $u_2 \sim 0.14$), who analyzed u_1 and u_2 simultaneously as free parameters. The consistency supports that KOI-94.04 is orbiting the same host star. In contrast, the u_2 parameter of the data sets phase-folded with the catalogued period (i.e. 0σ) is $u_2 = 0.60^{+0.13}_{-0.14}$, which is inconsistent with those of the other planets. The discrepancy implies KOI-94.04 does not transit KOI-94, but its χ^2 parameter is worse than that of -1.9σ data sets. The χ^2 parameter suggests that true KOI-94.04's period may not be the value on the catalogue but slightly shifted (our result $P = 3.743186$ days is

compatible with that of Weiss et al. (2013), $P = 3.743208 \pm 0.000015$ days), and KOI-94.04 is a possible planet orbiting KOI-94 based on the limb-darkening parameters. Although the results are still imperfect for the confirmation, the discussions in this section contribute to improving the limits on the possibility of a false positive of KOI-94.04.

B.6 Gravitational Influences from the Companion Candidate

Apart from the problem of false positives for KOI-94, B may induce gravitational interaction with the planets in the system under the assumption that B is physically bound to KOI-94. The interaction can make the planets migrate and intersect their orbits, leading the system unstable. The Kozai migration, one of the considerable gravitational interactions, has a timescale, P_{Kozai}, approximated as (Holman et al., 1997)

$$P_{\text{Kozai}} \sim \frac{M_A}{M_B} \frac{P_B^2}{P_{p,0}} (1 - e_B^2)^{3/2}, \tag{B.4}$$

where M_A and M_B are the masses of the main star KOI-94 A and the companion candidate KOI-94 B, respectively, and P_B and $P_{p,0}$ are the orbital periods of KOI-94 B and an orbital period of a planet in the KOI-94 system at an initial position. We estimate $P_{p,0}$ to be 3.7 or 54.3 days, the shortest or longest periods of all planets in the system, or ~ 8 years, where we presume a hypothetical planet initially formed at the snow line of the KOI-94 A system, having an initial semi-major axis of $a_{p,0} = 2.7(M_A/M_\odot)^2 \sim 4$ AU. Adopting $M_B = 0.1M_\odot$ (see Section 2), and assuming that the orbital eccentricity of B is equal to 0 ($e_B = 0$) and the B's orbital semi-major axis is the same distance as the projected separation from the main star (i.e. $a_B \sim 300$ AU; see Section 2), we obtain $P_{\text{Kozai}} \sim 20$ Gyr, 2 Gyr, or 30 Myr for $P_{p,0} = 3.7$ days, 54.3 days, or 8 years, respectively. Considering the estimates of the age ($\sim 3 - 4$ Gyr; Hirano et al. 2012; Weiss et al. 2013), P_{Kozai} for $P_{p,0} = 8$ years suggests the Kozai effect from B on a planet at the snow line to oscillate its orbit and destabilize the planetary system, while P_{Kozai} for $P_{p,0} = 3.7$ or 54.3 days (i.e. the present positions of the planets) cannot explain the Kozai effect on the planets sufficiently.

In addition, the timescale of general relativity is approximated as (Wu and Murray, 2003)

$$P_{\text{GR}} \sim \frac{2\pi c^2 (1 - e_{p,0}^2) a_{p,0}^{5/2}}{3(GM_A)^{3/2}}, \tag{B.5}$$

where c, G and $e_{p,0}$ are the speed of light, the gravitational constant, and an initial eccentricity of a planet, respectively. Given $a_{p,0} = 0.052$, 0.30 or 4 AU for the shortest or longest semi-major axis of all planets in the system, or the position of the snow line of the system, and assuming $e_{p,0} = 0$, P_{GR} is estimated to be ~ 20 kyr, ~ 1 Myr, or ~ 800 Myr, respectively. These results show that the general relativistic effect dominates and disturbs the Kozai effect in the present positions of the planets, though they are competitive at the position of the snow line. Note that because the general relativistic effect does not have a strong force to excite a planetary orbit's eccentricity significantly, the planetary orbits would keep stable at the present positions of the planets.

On the other hand, Hirano et al. (2012) showed the orbital axes of KOI-94.01 and KOI-94.03 to be aligned with the spin axis of KOI-94 A. Their observational fact suggests that the system has not experienced such orbital instabilities. Combining with their results, we support a formation scenario for the KOI-94 system that the planets in the compact system formed in outer regions of a protoplanetary disk and migrated into the present positions before the disk dissipated (Cossou et al., 2013). In this scenario, protoplanets were able to escape from the Kozai effect due to the interactions with the disk, and the protoplanets' masses were able to grow up to a few tens times as large as Earth's mass in the outer

regions. Moreover, the migration scenario can explain the distribution of rates of extrasolar planets in the mean motion resonances (Rein 2012; KOI-94.01 and 02 orbit in nearly 2:1 MMR.). This scenario is possibly different from that of the Kepler-56 system (Huber et al., 2013), whose host star's spin axis was recently discovered to be misaligned with its planetary orbital axes. The diversity can be an important key to reveal mysteries of planet formation mechanisms. Multicolor observations for deciding the color and therefore temperature of the companion candidate and common proper motion tests are necessary to confirm its boundness and the planet formation scenario.

B.7   Summary

We have focused on the multiple planetary system KOI-94 and conducted high-contrast direct imaging observations with Subaru/HiCIAO in order to examine a possibility of false positives. As a result of our classical ADI analysis, we have discovered a faint object at a separation of 0.6 arcsecs with a contrast of $\Delta H \sim 1 \times 10^{-3}$ to the north. Our estimates of its magnitude in Kp revealed that the insubstantial binary in the background can explain the depths of KOI-94.04 as a false positive. We have also excluded the possibility of a false positive of KOI-94.02 because the depths of KOI-94.02 is almost equal to or larger than the contrast of the faint object, assuming the companion candidate being a real companion or a background star with the typical color. On the other hand, our transit analyses show the limb darkening parameter of KOI-94.04 is consistent with those of the other planetary candidates in the KOI-94 system, suggesting that KOI-94.04 might orbit the same host star. Although we cannot conclude that KOI-94.04 is a planet from our results, we have demonstrated that the combination of the direct imaging and analysis of transit light curve can constrain the possibility of a false positive.

Our results also suggest that it is not enough to conclude the possibility of false positives by shallow or low-contrast direct imaging observations, which have been often conducted so far. Our results suggest to require deep observations with $\Delta m \gtrsim 10$ mag at a few arcsecs for the confirmation of a planet with its transit depth of $\lesssim 100$ ppm rather than conventional and shallow observations for excluding false positives. Furthermore, the discovery of the companion candidate B, if confirmed to be bound, gives an important clue to dynamical evolution of the planets in the KOI-94 system.

Bibliography

Adams, E. R., Dupree, A. K., Kulesa, C., & McCarthy, D.: 2013, *The Astronomical Journal* **146**, 9

Adams, F. C. & Laughlin, G.: 2006, *The Astrophysical Journal* **649**, 1004

Agol, E., Steffen, J., Sari, R., & Clarkson, W.: 2005, *Monthly Notices of the Royal Astronomical Society* **359**, 567

Albrecht, S., Winn, J. N., Johnson, J. A., Howard, A. W., Marcy, G. W., Butler, R. P., Arriagada, P., Crane, J. D., Shectman, S. A., Thompson, I. B., Hirano, T., Bakos, G., & Hartman, J. D.: 2012, *The Astrophysical Journal* **757**, 18

Anderson, D. R., Hellier, C., Gillon, M., Triaud, A. H. M. J., Smalley, B., Hebb, L., Collier Cameron, A., Maxted, P. F. L., Queloz, D., West, R. G., Bentley, S. J., Enoch, B., Horne, K., Lister, T. A., Mayor, M., Parley, N. R., Pepe, F., Pollacco, D., Ségransan, D., Udry, S., & Wilson, D. M.: 2010, *The Astrophysical Journal* **709**, 159

Anderson, D. R., Smith, A. M. S., Lanotte, A. A., Barman, T. S., Collier Cameron, A., Campo, C. J., Gillon, M., Harrington, J., Hellier, C., Maxted, P. F. L., Queloz, D., Triaud, A. H. M. J., & Wheatley, P. J.: 2011, *Monthly Notices of the Royal Astronomical Society* **416**, 2108

Bakos, G., Noyes, R. W., Kovács, G., Stanek, K. Z., Sasselov, D. D., & Domsa, I.: 2004, *Publications of the Astronomical Society of the Pacific* **116**, 266

Bakos, G. Á., Lázár, J., Papp, I., Sári, P., & Green, E. M.: 2002, *Publications of the Astronomical Society of the Pacific* **114**, 974

Bakos, G. Á., Torres, G., Pál, A., Hartman, J., Kovács, G., Noyes, R. W., Latham, D. W., Sasselov, D. D., Sipőcz, B., Esquerdo, G. A., Fischer, D. A., Johnson, J. A., Marcy, G. W., Butler, R. P., Isaacson, H., Howard, A., Vogt, S., Kovács, G., Fernandez, J., Moór, A., Stefanik, R. P., Lázár, J., Papp, I., & Sári, P.: 2010, *The Astrophysical Journal* **710**, 1724

Baraffe, I., Chabrier, G., Allard, F., & Hauschildt, P. H.: 1998, *Astronomy & Astrophysics* **337**, 403

Baraffe, I., Chabrier, G., Barman, T. S., Allard, F., & Hauschildt, P. H.: 2003, *Astronomy & Astrophysics* **402**, 701

Baranne, A., Mayor, M., & Poncet, J. L.: 1979, *Vistas in Astronomy* **23**, 279

Baranne, A., Queloz, D., Mayor, M., Adrianzyk, G., Knispel, G., Kohler, D., Lacroix, D., Meunier, J.-P., Rimbaud, G., & Vin, A.: 1996, *Astronomy & Astrophysics Supplement* **119**, 373

Barclay, T., Rowe, J. F., Lissauer, J. J., Huber, D., Fressin, F., Howell, S. B., Bryson, S. T., Chaplin, W. J., Désert, J.-M., Lopez, E. D., Marcy, G. W., Mullally, F., Ragozzine, D., Torres, G., Adams, E. R., Agol, E., Barrado, D., Basu, S., Bedding, T. R., Buchhave, L. A., Charbonneau, D., Christiansen, J. L., Christensen-Dalsgaard, J., Ciardi, D., Cochran, W. D., Dupree, A. K., Elsworth, Y., Everett, M., Fischer, D. A., Ford, E. B., Fortney, J. J., Geary, J. C., Haas, M. R., Handberg, R., Hekker, S., Henze, C. E., Horch, E., Howard, A. W., Hunter, R. C., Isaacson, H., Jenkins, J. M., Karoff, C., Kawaler, S. D., Kjeldsen, H., Klaus, T. C., Latham, D. W., Li, J., Lillo-Box, J., Lund, M. N., Lundkvist, M., Metcalfe, T. S., Miglio, A., Morris, R. L., Quintana, E. V., Stello, D., Smith, J. C., Still, M., & Thompson, S. E.: 2013, *Nature* **494**, 452

Baruteau, C. & Masset, F.: 2008, *The Astrophysical Journal* **672**, 1054

Batalha, N. M., Borucki, W. J., Koch, D. G., Bryson, S. T., Haas, M. R., Brown, T. M., Caldwell, D. A., Hall, J. R., Gilliland, R. L., Latham, D. W., Meibom, S., & Monet, D. G.: 2010, *The Astrophysical Journal Letters* **713**, L109

Batalha, N. M., Rowe, J. F., Bryson, S. T., Barclay, T., Burke, C. J., Caldwell, D. A., Christiansen, J. L., Mullally, F., Thompson, S. E., Brown, T. M., Dupree, A. K., Fabrycky, D. C., Ford, E. B., Fortney, J. J., Gilliland, R. L., Isaacson, H., Latham, D. W., Marcy, G. W., Quinn, S. N., Ragozzine, D., Shporer, A., Borucki, W. J., Ciardi, D. R., Gautier, III, T. N., Haas, M. R., Jenkins, J. M., Koch, D. G., Lissauer, J. J., Rapin, W., Basri, G. S., Boss, A. P., Buchhave, L. A., Carter, J. A., Charbonneau, D., Christensen-Dalsgaard, J., Clarke, B. D., Cochran, W. D., Demory, B.-O., Desert, J.-M., Devore, E., Doyle, L. R., Esquerdo, G. A., Everett, M., Fressin, F., Geary, J. C., Girouard, F. R., Gould, A., Hall, J. R., Holman, M. J., Howard, A. W., Howell, S. B., Ibrahim, K. A., Kinemuchi, K., Kjeldsen, H., Klaus, T. C., Li, J., Lucas, P. W., Meibom, S., Morris, R. L., Prša, A., Quintana, E., Sanderfer, D. T., Sasselov, D., Seader, S. E., Smith, J. C., Steffen, J. H., Still, M., Stumpe, M. C., Tarter, J. C., Tenenbaum, P., Torres, G., Twicken, J. D., Uddin, K., Van Cleve, J., Walkowicz, L., & Welsh, W. F.: 2013, *The Astrophysical Journal Supplement* **204**, 24

Bean, J. L., Seifahrt, A., Hartman, H., Nilsson, H., Wiedemann, G., Reiners, A., Dreizler, S., & Henry, T. J.: 2010, *The Astrophysical Journal* **713**, 410

Beaulieu, J.-P., Bennett, D. P., Fouqué, P., Williams, A., Dominik, M., Jørgensen, U. G., Kubas, D., Cassan, A., Coutures, C., Greenhill, J., Hill, K., Menzies, J., Sackett, P. D., Albrow, M., Brillant, S., Caldwell, J. A. R., Calitz, J. J., Cook, K. H., Corrales, E., Desort, M., Dieters, S., Dominis, D., Donatowicz, J., Hoffman, M., Kane, S., Marquette, J.-B., Martin, R., Meintjes, P., Pollard, K., Sahu, K., Vinter, C., Wambsganss, J., Woller, K., Horne, K., Steele, I., Bramich, D. M., Burgdorf, M., Snodgrass, C., Bode, M., Udalski, A., Szymański, M. K., Kubiak, M., Więckowski, T., Pietrzyński, G., Soszyński, I., Szewczyk, O., Wyrzykowski, Ł., Paczyński, B., Abe, F., Bond, I. A., Britton, T. R., Gilmore, A. C., Hearnshaw, J. B., Itow, Y., Kamiya, K., Kilmartin, P. M., Korpela, A. V., Masuda, K., Matsubara, Y., Motomura, M., Muraki, Y., Nakamura, S., Okada, C., Ohnishi, K., Rattenbury, N. J., Sako, T., Sato, S., Sasaki, M., Sekiguchi, T., Sullivan, D. J., Tristram, P. J., Yock, P. C. M., & Yoshioka, T.: 2006, *Nature* **439**, 437

Bechter, E. B., Crepp, J. R., Ngo, H., Knutson, H. A., Batygin, K., Hinkley, S., Muirhead, P. S., Johnson, J. A., Howard, A. W., Montet, B. T., Matthews, C. T., & Morton, T. D.: 2013, *ArXiv e-prints*

Benedict, G. F., McArthur, B. E., Forveille, T., Delfosse, X., Nelan, E., Butler, R. P., Spiesman, W., Marcy, G., Goldman, B., Perrier, C., Jefferys, W. H., & Mayor, M.: 2002, *The Astrophysical Journal Letters* **581**, L115

Benedict, G. F., McArthur, B. E., Gatewood, G., Nelan, E., Cochran, W. D., Hatzes, A., Endl, M., Wittenmyer, R., Baliunas, S. L., Walker, G. A. H., Yang, S., Kürster, M., Els, S., & Paulson, D. B.: 2006, *The Astronomical Journal* **132**, 2206

Bento, J., Wheatley, P. J., Copperwheat, C. M., Fortney, J. J., Dhillon, V. S., Hickman, R., Littlefair, S. P., Marsh, T. R., Parsons, S. G., & Southworth, J.: 2013, *ArXiv e-prints*

Bergfors, C., Brandner, W., Daemgen, S., Biller, B., Hippler, S., Janson, M., Kudryavtseva, N., Geißler, K., Henning, T., & Köhler, R.: 2013, *Monthly Notices of the Royal Astronomical Society* **428**, 182

Beuermann, K., Hessman, F. V., Dreizler, S., Marsh, T. R., Parsons, S. G., Winget, D. E., Miller, G. F., Schreiber, M. R., Kley, W., Dhillon, V. S., Littlefair, S. P., Copperwheat, C. M., & Hermes, J. J.: 2010, *Astronomy & Astrophysics* **521**, L60

Biller, B. A., Close, L. M., Masciadri, E., Nielsen, E., Lenzen, R., Brandner, W., McCarthy, D., Hartung, M., Kellner, S., Mamajek, E., Henning, T., Miller, D., Kenworthy, M., & Kulesa, C.: 2007, *The Astrophysical Journal Supplement* **173**, 143

Bond, I. A., Udalski, A., Jaroszyński, M., Rattenbury, N. J., Paczyński, B., Soszyński, I., Wyrzykowski, L., Szymański, M. K., Kubiak, M., Szewczyk, O., Żebruń, K., Pietrzyński, G., Abe, F., Bennett, D. P., Eguchi, S., Furuta, Y., Hearnshaw, J. B., Kamiya, K., Kilmartin, P. M., Kurata, Y., Masuda, K., Matsubara, Y., Muraki, Y., Noda, S., Okajima, K., Sako, T., Sekiguchi, T., Sullivan, D. J., Sumi, T., Tristram, P. J., Yanagisawa, T., Yock, P. C. M., & OGLE Collaboration: 2004, *The Astrophysical Journal Letters* **606**, L155

Borucki, W. J., Koch, D. G., Basri, G., Batalha, N., Brown, T. M., Bryson, S. T., Caldwell, D., Christensen-Dalsgaard, J., Cochran, W. D., DeVore, E., Dunham, E. W., Gautier, III, T. N., Geary, J. C., Gilliland, R., Gould, A., Howell, S. B., Jenkins, J. M., Latham, D. W., Lissauer, J. J., Marcy, G. W., Rowe, J., Sasselov, D., Boss, A., Charbonneau, D., Ciardi, D., Doyle, L., Dupree, A. K., Ford, E. B., Fortney, J., Holman, M. J., Seager, S., Steffen, J. H., Tarter, J., Welsh, W. F., Allen, C., Buchhave, L. A., Christiansen, J. L., Clarke, B. D., Das, S., Désert, J.-M., Endl, M., Fabrycky, D., Fressin, F., Haas, M., Horch, E., Howard, A., Isaacson, H., Kjeldsen, H., Kolodziejczak, J., Kulesa, C., Li, J., Lucas, P. W., Machalek, P., McCarthy, D., MacQueen, P., Meibom, S., Miquel, T., Prsa, A., Quinn, S. N., Quintana, E. V., Ragozzine, D., Sherry, W., Shporer, A., Tenenbaum, P., Torres, G., Twicken, J. D., Van Cleve, J., Walkowicz, L., Witteborn, F. C., & Still, M.: 2011, *The Astrophysical Journal* **736**, 19

Borucki, W. J., Koch, D. G., Batalha, N., Bryson, S. T., Rowe, J., Fressin, F., Torres, G., Caldwell, D. A., Christensen-Dalsgaard, J., Cochran, W. D., DeVore, E., Gautier, T. N., Geary, J. C., Gilliland, R., Gould, A., Howell, S. B., Jenkins, J. M., Latham, D. W., Lissauer, J. J., Marcy, G. W., Sasselov, D., Boss, A., Charbonneau, D., Ciardi, D., Kaltenegger, L., Doyle, L., Dupree, A. K., Ford, E. B., Fortney, J., Holman, M. J., Steffen, J. H., Mullally, F., Still, M., Tarter, J., Ballard, S., Buchhave, L. A., Carter, J., Christiansen, J. L., Demory, B.-O., Désert, J.-M., Dressing, C., Endl, M., Fabrycky, D., Fischer, D., Haas, M. R., Henze, C., Horch, E., Howard, A. W., Isaacson, H., Kjeldsen, H., Johnson, J. A., Klaus, T., Kolodziejczak, J., Barclay, T., Li, J., Meibom, S., Prsa, A., Quinn, S. N., Quintana, E. V.,

Robertson, P., Sherry, W., Shporer, A., Tenenbaum, P., Thompson, S. E., Twicken, J. D., Van Cleve, J., Welsh, W. F., Basu, S., Chaplin, W., Miglio, A., Kawaler, S. D., Arentoft, T., Stello, D., Metcalfe, T. S., Verner, G. A., Karoff, C., Lundkvist, M., Lund, M. N., Handberg, R., Elsworth, Y., Hekker, S., Huber, D., Bedding, T. R., & Rapin, W.: 2012, *The Astrophysical Journal* **745**, 120

Boss, A. P.: 2011, *The Astrophysical Journal* **731**, 74

Boss, A. P.: 2013, *The Astrophysical Journal* **764**, 194

Bowler, B. P., Liu, M. C., Dupuy, T. J., & Cushing, M. C.: 2010, *The Astrophysical Journal* **723**, 850

Bressan, A., Marigo, P., Girardi, L., Salasnich, B., Dal Cero, C., Rubele, S., & Nanni, A.: 2012, *Monthly Notices of the Royal Astronomical Society* **427**, 127

Bryden, G., Beichman, C. A., Carpenter, J. M., Rieke, G. H., Stapelfeldt, K. R., Werner, M. W., Tanner, A. M., Lawler, S. M., Wyatt, M. C., Trilling, D. E., Su, K. Y. L., Blaylock, M., & Stansberry, J. A.: 2009, *The Astrophysical Journal* **705**, 1226

Burgasser, A. J., Liu, M. C., Ireland, M. J., Cruz, K. L., & Dupuy, T. J.: 2008, *The Astrophysical Journal* **681**, 579

Burgasser, A. J., McElwain, M. W., Kirkpatrick, J. D., Cruz, K. L., Tinney, C. G., & Reid, I. N.: 2004, *The Astronomical Journal* **127**, 2856

Burrows, A., Hubeny, I., Budaj, J., Knutson, H. A., & Charbonneau, D.: 2007, *The Astrophysical Journal Letters* **668**, L171

Butler, R. P., Marcy, G. W., Williams, E., McCarthy, C., Dosanjh, P., & Vogt, S. S.: 1996, *Publications of the Astronomical Society of the Pacific* **108**, 500

Butler, R. P., Wright, J. T., Marcy, G. W., Fischer, D. A., Vogt, S. S., Tinney, C. G., Jones, H. R. A., Carter, B. D., Johnson, J. A., McCarthy, C., & Penny, A. J.: 2006, *The Astrophysical Journal* **646**, 505

Cameron, A. G. W.: 1962, *Icarus* **1**, 13

Campbell, B. & Walker, G. A. H.: 1979, *Publications of the Astronomical Society of the Pacific* **91**, 540

Canto Martins, B. L., Das Chagas, M. L., Alves, S., Leão, I. C., de Souza Neto, L. P., & de Medeiros, J. R.: 2011, *Astronomy & Astrophysics* **530**, A73

Carson, J., Thalmann, C., Janson, M., Kozakis, T., Bonnefoy, M., Biller, B., Schlieder, J., Currie, T., McElwain, M., Goto, M., Henning, T., Brandner, W., Feldt, M., Kandori, R., Kuzuhara, M., Stevens, L., Wong, P., Gainey, K., Fukagawa, M., Kuwada, Y., Brandt, T., Kwon, J., Abe, L., Egner, S., Grady, C., Guyon, O., Hashimoto, J., Hayano, Y., Hayashi, M., Hayashi, S., Hodapp, K., Ishii, M., Iye, M., Knapp, G., Kudo, T., Kusakabe, N., Matsuo, T., Miyama, S., Morino, J., Moro-Martin, A., Nishimura, T., Pyo, T., Serabyn, E., Suto, H., Suzuki, R., Takami, M., Takato, N., Terada, H., Tomono, D., Turner, E., Watanabe, M., Wisniewski, J., Yamada, T., Takami, H., Usuda, T., & Tamura, M.: 2013, *The Astrophysical Journal Letters* **763**, L32

Cayrel de Strobel, G., Soubiran, C., & Ralite, N.: 2001, *Astronomy & Astrophysics* **373**, 159

Chabrier, G., Baraffe, I., Allard, F., & Hauschildt, P.: 2000, *The Astrophysical Journal* **542**, 464

Chambers, J. E., Wetherill, G. W., & Boss, A. P.: 1996, *Icarus* **119**, 261

Chan, T., Ingemyr, M., Winn, J. N., Holman, M. J., Sanchis-Ojeda, R., Esquerdo, G., & Everett, M.: 2011, *The Astronomical Journal* **141**, 179

Charbonneau, D., Brown, T. M., Latham, D. W., & Mayor, M.: 2000, *The Astrophysical Journal Letters* **529**, L45

Charbonneau, D., Brown, T. M., Noyes, R. W., & Gilliland, R. L.: 2002, *The Astrophysical Journal* **568**, 377

Chatterjee, S., Ford, E. B., Matsumura, S., & Rasio, F. A.: 2008, *The Astrophysical Journal* **686**, 580

Christian, D. J., Pollacco, D. L., Skillen, I., Street, R. A., Keenan, F. P., Clarkson, W. I., Collier Cameron, A., Kane, S. R., Lister, T. A., West, R. G., Enoch, B., Evans, A., Fitzsimmons, A., Haswell, C. A., Hellier, C., Hodgkin, S. T., Horne, K., Irwin, J., Norton, A. J., Osborne, J., Ryans, R., Wheatley, P. J., & Wilson, D. M.: 2006, *Monthly Notices of the Royal Astronomical Society* **372**, 1117

Cochran, W. D., Hatzes, A. P., Butler, R. P., & Marcy, G. W.: 1997, *The Astrophysical Journal* **483**, 457

Collier Cameron, A., Guenther, E., Smalley, B., McDonald, I., Hebb, L., Andersen, J., Augusteijn, T., Barros, S. C. C., Brown, D. J. A., Cochran, W. D., Endl, M., Fossey, S. J., Hartmann, M., Maxted, P. F. L., Pollacco, D., Skillen, I., Telting, J., Waldmann, I. P., & West, R. G.: 2010, *Monthly Notices of the Royal Astronomical Society* **407**, 507

Cossou, C., Raymond, S. N., & Pierens, A.: 2013, *Astronomy & Astrophysics* **553**, L2

Croll, B., Lafreniere, D., Albert, L., Jayawardhana, R., Fortney, J. J., & Murray, N.: 2011, *The Astronomical Journal* **141**, 30

Currie, T., Burrows, A., Itoh, Y., Matsumura, S., Fukagawa, M., Apai, D., Madhusudhan, N., Hinz, P. M., Rodigas, T. J., Kasper, M., Pyo, T.-S., & Ogino, S.: 2011, *The Astrophysical Journal* **729**, 128

Currie, T., Debes, J., Rodigas, T. J., Burrows, A., Itoh, Y., Fukagawa, M., Kenyon, S. J., Kuchner, M., & Matsumura, S.: 2012, *The Astrophysical Journal Letters* **760**, L32

Daemgen, S., Hormuth, F., Brandner, W., Bergfors, C., Janson, M., Hippler, S., & Henning, T.: 2009, *Astronomy & Astrophysics* **498**, 567

D'Angelo, G., Lubow, S. H., & Bate, M. R.: 2006, *The Astrophysical Journal* **652**, 1698

de Mooij, E. J. W., Brogi, M., de Kok, R. J., Snellen, I. A. G., Kenworthy, M. A., & Karjalainen, R.: 2013, *Astronomy & Astrophysics* **550**, A54

Demarque, P., Woo, J.-H., Kim, Y.-C., & Yi, S. K.: 2004, *The Astrophysical Journal Supplement* **155**, 667

Díaz, R. F., Santerne, A., Sahlmann, J., Hébrard, G., Eggenberger, A., Santos, N. C., Moutou, C., Arnold, L., Boisse, I., Bonfils, X., Bouchy, F., Delfosse, X., Desort, M., Ehrenreich, D., Forveille, T., Lagrange, A.-M., Lovis, C., Pepe, F., Perrier, C., Queloz, D., Ségransan, D., Udry, S., & Vidal-Madjar, A.: 2012, *Astronomy & Astrophysics* **538**, A113

Dodson-Robinson, S. E., Veras, D., Ford, E. B., & Beichman, C. A.: 2009, *The Astrophysical Journal* **707**, 79

Donahue, R. A.: 1993, *Ph.D. thesis*, New Mexico State University, University Park.

Doyle, A. P., Smalley, B., Maxted, P. F. L., Anderson, D. R., Cameron, A. C., Gillon, M., Hellier, C., Pollacco, D., Queloz, D., Triaud, A. H. M. J., & West, R. G.: 2013, *Monthly Notices of the Royal Astronomical Society* **428**, 3164

Doyle, L. R., Carter, J. A., Fabrycky, D. C., Slawson, R. W., Howell, S. B., Winn, J. N., Orosz, J. A., Prša, A., Welsh, W. F., Quinn, S. N., Latham, D., Torres, G., Buchhave, L. A., Marcy, G. W., Fortney, J. J., Shporer, A., Ford, E. B., Lissauer, J. J., Ragozzine, D., Rucker, M., Batalha, N., Jenkins, J. M., Borucki, W. J., Koch, D., Middour, C. K., Hall, J. R., McCauliff, S., Fanelli, M. N., Quintana, E. V., Holman, M. J., Caldwell, D. A., Still, M., Stefanik, R. P., Brown, W. R., Esquerdo, G. A., Tang, S., Furesz, G., Geary, J. C., Berlind, P., Calkins, M. L., Short, D. R., Steffen, J. H., Sasselov, D., Dunham, E. W., Cochran, W. D., Boss, A., Haas, M. R., Buzasi, D., & Fischer, D.: 2011, *Science* **333**, 1602

Dupuy, T. J. & Liu, M. C.: 2011, *The Astrophysical Journal* **733**, 122

Duquennoy, A. & Mayor, M.: 1991, *Astronomy & Astrophysics* **248**, 485

Durisen, R. H., Boss, A. P., Mayer, L., Nelson, A. F., Quinn, T., & Rice, W. K. M.: 2007, *Protostars and Planets V* pp 607–622

Enoch, B., Anderson, D. R., Barros, S. C. C., Brown, D. J. A., Collier Cameron, A., Faedi, F., Gillon, M., Hébrard, G., Lister, T. A., Queloz, D., Santerne, A., Smalley, B., Street, R. A., Triaud, A. H. M. J., West, R. G., Bouchy, F., Bento, J., Butters, O., Fossati, L., Haswell, C. A., Hellier, C., Holmes, S., Jehin, E., Lendl, M., Maxted, P. F. L., McCormac, J., Miller, G. R. M., Moulds, V., Moutou, C., Norton, A. J., Parley, N., Pepe, F., Pollacco, D., Segransan, D., Simpson, E., Skillen, I., Smith, A. M. S., Udry, S., & Wheatley, P. J.: 2011, *The Astronomical Journal* **142**, 86

Fabrycky, D. & Tremaine, S.: 2007, *The Astrophysical Journal* **669**, 1298

Fabrycky, D. C. & Murray-Clay, R. A.: 2010, *The Astrophysical Journal* **710**, 1408

Fischer, D., Driscoll, P., Isaacson, H., Giguere, M., Marcy, G. W., Valenti, J., Wright, J. T., Henry, G. W., Johnson, J. A., Howard, A., Peek, K., & McCarthy, C.: 2009, *The Astrophysical Journal* **703**, 1545

Ford, E. B., Havlickova, M., & Rasio, F. A.: 2001, *Icarus* **150**, 303

Fortney, J. J., Marley, M. S., Saumon, D., & Lodders, K.: 2008, *The Astrophysical Journal* **683**, 1104

Fressin, F., Torres, G., Charbonneau, D., Bryson, S. T., Christiansen, J., Dressing, C. D., Jenkins, J. M., Walkowicz, L. M., & Batalha, N. M.: 2013, *The Astrophysical Journal* **766**, 81

Fulton, B. J., Howard, A. W., Winn, J. N., Albrecht, S., Marcy, G. W., Crepp, J. R., Bakos, G. A., Johnson, J. A., Hartman, J. D., Isaacson, H., Knutson, H. A., & Zhao, M.: 2013, *The Astrophysical Journal* **772**, 80

Gaudi, B. S. & Winn, J. N.: 2007, *The Astrophysical Journal* **655**, 550

Ghez, A. M., Neugebauer, G., & Matthews, K.: 1993, *The Astronomical Journal* **106**, 2005

Gibson, N. P., Aigrain, S., Barstow, J. K., Evans, T. M., Fletcher, L. N., & Irwin, P. G. J.: 2013, *Monthly Notices of the Royal Astronomical Society*

Girardi, L., Groenewegen, M. A. T., Hatziminaoglou, E., & da Costa, L.: 2005, *Astronomy & Astrophysics* **436**, 895

Goldreich, P. & Sari, R.: 2003, *The Astrophysical Journal* **585**, 1024

Goldreich, P. & Ward, W. R.: 1973, *The Astrophysical Journal* **183**, 1051

Gould, A. & Chanamé, J.: 2004, *The Astrophysical Journal Supplement* **150**, 455

Gould, A. & Loeb, A.: 1992, *The Astrophysical Journal* **396**, 104

Haisch, Jr., K. E., Lada, E. A., & Lada, C. J.: 2001, *The Astrophysical Journal Letters* **553**, L153

Hartman, J. D., Bakos, G. Á., Torres, G., Latham, D. W., Kovács, G., Béky, B., Quinn, S. N., Mazeh, T., Shporer, A., Marcy, G. W., Howard, A. W., Fischer, D. A., Johnson, J. A., Esquerdo, G. A., Noyes, R. W., Sasselov, D. D., Stefanik, R. P., Fernandez, J. M., Szklenár, T., Lázár, J., Papp, I., & Sári, P.: 2011, *The Astrophysical Journal* **742**, 59

Hartmann, M., Guenther, E. W., & Hatzes, A. P.: 2010, *The Astrophysical Journal* **717**, 348

Hashimoto, J., Tamura, M., Muto, T., Kudo, T., Fukagawa, M., Fukue, T., Goto, M., Grady, C. A., Henning, T., Hodapp, K., Honda, M., Inutsuka, S., Kokubo, E., Knapp, G., McElwain, M. W., Momose, M., Ohashi, N., Okamoto, Y. K., Takami, M., Turner, E. L., Wisniewski, J., Janson, M., Abe, L., Brandner, W., Carson, J., Egner, S., Feldt, M., Golota, T., Guyon, O., Hayano, Y., Hayashi, M., Hayashi, S., Ishii, M., Kandori, R., Kusakabe, N., Matsuo, T., Mayama, S., Miyama, S., Morino, J.-I., Moro-Martin, A., Nishimura, T., Pyo, T.-S., Suto, H., Suzuki, R., Takato, N., Terada, H., Thalmann, C., Tomono, D., Watanabe, M., Yamada, T., Takami, H., & Usuda, T.: 2011, *The Astrophysical Journal Letters* **729**, L17

Hauschildt, P. H., Allard, F., & Baron, E.: 1999a, *The Astrophysical Journal* **512**, 377

Hauschildt, P. H., Allard, F., Ferguson, J., Baron, E., & Alexander, D. R.: 1999b, *The Astrophysical Journal* **525**, 871

Hayano, Y., Takami, H., Guyon, O., Oya, S., Hattori, M., Saito, Y., Watanabe, M., Murakami, N., Minowa, Y., Ito, M., Colley, S., Eldred, M., Golota, T., Dinkins, M., Kashikawa, N., & Iye, M.: 2008, in *Society of Photo-Optical Instrumentation Engineers (SPIE) Conference Series*, Vol. 7015 of *Society of Photo-Optical Instrumentation Engineers (SPIE) Conference Series*

Hayashi, C.: 1981, *Progress of Theoretical Physics Supplement* **70**, 35

Hayashi, C., Nakazawa, K., & Nakagawa, Y.: 1985, in D. C. Black and M. S. Matthews (eds.), *Protostars and Planets II*, pp 1100–1153

Hebb, L., Collier-Cameron, A., Loeillet, B., Pollacco, D., Hébrard, G., Street, R. A., Bouchy, F., Stempels, H. C., Moutou, C., Simpson, E., Udry, S., Joshi, Y. C., West, R. G., Skillen, I., Wilson, D. M., McDonald, I., Gibson, N. P., Aigrain, S., Anderson, D. R., Benn, C. R., Christian, D. J., Enoch, B., Haswell, C. A., Hellier, C., Horne, K., Irwin, J., Lister, T. A., Maxted, P., Mayor, M., Norton, A. J., Parley, N., Pont, F., Queloz, D., Smalley, B., & Wheatley, P. J.: 2009, *The Astrophysical Journal* **693**, 1920

Hébrard, G., Bouchy, F., Pont, F., Loeillet, B., Rabus, M., Bonfils, X., Moutou, C., Boisse, I., Delfosse, X., Desort, M., Eggenberger, A., Ehrenreich, D., Forveille, T., Lagrange, A.-M., Lovis, C., Mayor, M., Pepe, F., Perrier, C., Queloz, D., Santos, N. C., Ségransan, D., Udry, S., & Vidal-Madjar, A.: 2008, *Astronomy & Astrophysics* **488**, 763

Hébrard, G., Désert, J.-M., Díaz, R. F., Boisse, I., Bouchy, F., Lecavelier Des Etangs, A., Moutou, C., Ehrenreich, D., Arnold, L., Bonfils, X., Delfosse, X., Desort, M., Eggenberger, A., Forveille, T., Gregorio, J., Lagrange, A.-M., Lovis, C., Pepe, F., Perrier, C., Pont, F., Queloz, D., Santerne, A., Santos, N. C., Ségransan, D., Sing, D. K., Udry, S., & Vidal-Madjar, A.: 2010, *Astronomy & Astrophysics* **516**, A95

Hirano, T., Narita, N., Sato, B., Takahashi, Y. H., Masuda, K., Takeda, Y., Aoki, W., Tamura, M., & Suto, Y.: 2012, *The Astrophysical Journal Letters* **759**, L36

Hirano, T., Suto, Y., Winn, J. N., Taruya, A., Narita, N., Albrecht, S., & Sato, B.: 2011, *The Astrophysical Journal* **742**, 69

Hodapp, K. W., Suzuki, R., Tamura, M., Abe, L., Suto, H., Kandori, R., Morino, J., Nishimura, T., Takami, H., Guyon, O., Jacobson, S., Stahlberger, V., Yamada, H., Shelton, R., Hashimoto, J., Tavrov, A., Nishikawa, J., Ukita, N., Izumiura, H., Hayashi, M., Nakajima, T., Yamada, T., & Usuda, T.: 2008, in *Society of Photo-Optical Instrumentation Engineers (SPIE) Conference Series*, Vol. 7014 of *Society of Photo-Optical Instrumentation Engineers (SPIE) Conference Series*

Høg, E., Fabricius, C., Makarov, V. V., Urban, S., Corbin, T., Wycoff, G., Bastian, U., Schwekendiek, P., & Wicenec, A.: 2000, *Astronomy & Astrophysics* **355**, L27

Høg, E., Kuzmin, A., Bastian, U., Fabricius, C., Kuimov, K., Lindegren, L., Makarov, V. V., & Roeser, S.: 1998, *Astronomy & Astrophysics* **335**, L65

Holman, M., Touma, J., & Tremaine, S.: 1997, *Nature* **386**, 254

Holman, M. J., Fabrycky, D. C., Ragozzine, D., Ford, E. B., Steffen, J. H., Welsh, W. F., Lissauer, J. J., Latham, D. W., Marcy, G. W., Walkowicz, L. M., Batalha, N. M., Jenkins, J. M., Rowe, J. F., Cochran, W. D., Fressin, F., Torres, G., Buchhave, L. A., Sasselov, D. D., Borucki, W. J., Koch, D. G., Basri, G., Brown, T. M., Caldwell, D. A., Charbonneau, D., Dunham, E. W., Gautier, T. N., Geary, J. C., Gilliland, R. L., Haas, M. R., Howell, S. B., Ciardi, D. R., Endl, M., Fischer, D., Fürész, G., Hartman, J. D., Isaacson, H., Johnson, J. A., MacQueen, P. J., Moorhead, A. V., Morehead, R. C., & Orosz, J. A.: 2010, *Science* **330**, 51

Howard, A. W., Bakos, G. Á., Hartman, J., Torres, G., Shporer, A., Mazeh, T., Kovács, G., Latham, D. W., Noyes, R. W., Fischer, D. A., Johnson, J. A., Marcy, G. W., Esquerdo, G. A., Béky, B., Butler, R. P., Sasselov, D. D., Stefanik, R. P., Perumpilly, G., Lázár, J., Papp, I., & Sári, P.: 2012, *The Astrophysical Journal* **749**, 134

Howell, S. B., Rowe, J. F., Bryson, S. T., Quinn, S. N., Marcy, G. W., Isaacson, H., Ciardi, D. R., Chaplin, W. J., Metcalfe, T. S., Monteiro, M. J. P. F. G., Appourchaux, T., Basu, S., Creevey, O. L., Gilliland, R. L., Quirion, P.-O., Stello, D., Kjeldsen, H., Christensen-Dalsgaard, J., Elsworth, Y., García, R. A., Houdek, G., Karoff, C., Molenda-Żakowicz, J., Thompson, M. J., Verner, G. A., Torres, G., Fressin, F., Crepp, J. R., Adams, E., Dupree, A., Sasselov, D. D., Dressing, C. D., Borucki, W. J., Koch, D. G., Lissauer, J. J., Latham, D. W., Buchhave, L. A., Gautier, III, T. N., Everett, M., Horch, E., Batalha,

N. M., Dunham, E. W., Szkody, P., Silva, D. R., Mighell, K., Holberg, J., Ballot, J., Bedding, T. R., Bruntt, H., Campante, T. L., Handberg, R., Hekker, S., Huber, D., Mathur, S., Mosser, B., Régulo, C., White, T. R., Christiansen, J. L., Middour, C. K., Haas, M. R., Hall, J. R., Jenkins, J. M., McCaulif, S., Fanelli, M. N., Kulesa, C., McCarthy, D., & Henze, C. E.: 2012, *The Astrophysical Journal* **746**, 123

Huber, D., Carter, J. A., Barbieri, M., Miglio, A., Deck, K. M., Fabrycky, D. C., Montet, B. T., Buchhave, L. A., Chaplin, W. J., Hekker, S., Montalbán, J., Sanchis-Ojeda, R., Basu, S., Bedding, T. R., Campante, T. L., Christensen-Dalsgaard, J., Elsworth, Y. P., Stello, D., Arentoft, T., Ford, E. B., Gilliland, R. L., Handberg, R., Howard, A. W., Isaacson, H., Johnson, J. A., Karoff, C., Kawaler, S. D., Kjeldsen, H., Latham, D. W., Lund, M. N., Lundkvist, M., Marcy, G. W., Metcalfe, T. S., Silva Aguirre, V., & Winn, J. N.: 2013, *ArXiv e-prints*

Ibukiyama, A. & Arimoto, N.: 2002, *Astronomy & Astrophysics* **394**, 927

Ida, S., Guillot, T., & Morbidelli, A.: 2008, *The Astrophysical Journal* **686**, 1292

Ida, S. & Lin, D. N. C.: 2004, *The Astrophysical Journal* **616**, 567

Ida, S., Lin, D. N. C., & Nagasawa, M.: 2013, *The Astrophysical Journal* **775**, 42

Ikoma, M., Nakazawa, K., & Emori, H.: 2000, *The Astrophysical Journal* **537**, 1013

Inutsuka, S.-i., Machida, M. N., & Matsumoto, T.: 2010, *The Astrophysical Journal Letters* **718**, L58

Ivanov, P. B. & Papaloizou, J. C. B.: 2004, *Monthly Notices of the Royal Astronomical Society* **353**, 1161

Ivezić, Ž., Sesar, B., Jurić, M., Bond, N., Dalcanton, J., Rockosi, C. M., Yanny, B., Newberg, H. J., Beers, T. C., Allende Prieto, C., Wilhelm, R., Lee, Y. S., Sivarani, T., Norris, J. E., Bailer-Jones, C. A. L., Re Fiorentin, P., Schlegel, D., Uomoto, A., Lupton, R. H., Knapp, G. R., Gunn, J. E., Covey, K. R., Smith, J. A., Miknaitis, G., Doi, M., Tanaka, M., Fukugita, M., Kent, S., Finkbeiner, D., Munn, J. A., Pier, J. R., Quinn, T., Hawley, S., Anderson, S., Kiuchi, F., Chen, A., Bushong, J., Sohi, H., Haggard, D., Kimball, A., Barentine, J., Brewington, H., Harvanek, M., Kleinman, S., Krzesinski, J., Long, D., Nitta, A., Snedden, S., Lee, B., Harris, H., Brinkmann, J., Schneider, D. P., & York, D. G.: 2008, *The Astrophysical Journal* **684**, 287

Janson, M., Brandt, T. D., Kuzuhara, M., Spiegel, D. S., Thalmann, C., Currie, T., Bonnefoy, M., Zimmerman, N., Sorahana, S., Kotani, T., Schlieder, J., Hashimoto, J., Kudo, T., Kusakabe, N., Abe, L., Brandner, W., Carson, J. C., Egner, S., Feldt, M., Goto, M., Grady, C. A., Guyon, O., Hayano, Y., Hayashi, M., Hayashi, S., Henning, T., Hodapp, K. W., Ishii, M., Iye, M., Kandori, R., Knapp, G. R., Kwon, J., Matsuo, T., McElwain, M. W., Mede, K., Miyama, S., Morino, J.-I., Moro-Martín, A., Nakagawa, T., Nishimura, T., Pyo, T.-S., Serabyn, E., Suenaga, T., Suto, H., Suzuki, R., Takahashi, Y., Takami, M., Takato, N., Terada, H., Tomono, D., Turner, E. L., Watanabe, M., Wisniewski, J., Yamada, T., Takami, H., Usuda, T., & Tamura, M.: 2013, *The Astrophysical Journal Letters* **778**, L4

Johnson, J. A., Winn, J. N., Albrecht, S., Howard, A. W., Marcy, G. W., & Gazak, J. Z.: 2009, *Publications of the Astronomical Society of the Pacific* **121**, 1104

Johnson, J. A., Winn, J. N., Bakos, G. Á., Hartman, J. D., Morton, T. D., Torres, G., Kovács, G., Latham, D. W., Noyes, R. W., Sato, B., Esquerdo, G. A., Fischer, D. A., Marcy, G. W., Howard, A. W.,

Buchhave, L. A., Fűrész, G., Quinn, S. N., Béky, B., Sasselov, D. D., Stefanik, R. P., Lázár, J., Papp, I., & Sári, P.: 2011, *The Astrophysical Journal* **735**, 24

Joshi, Y. C., Pollacco, D., Collier Cameron, A., Skillen, I., Simpson, E., Steele, I., Street, R. A., Stempels, H. C., Christian, D. J., Hebb, L., Bouchy, F., Gibson, N. P., Hébrard, G., Keenan, F. P., Loeillet, B., Meaburn, J., Moutou, C., Smalley, B., Todd, I., West, R. G., Anderson, D. R., Bentley, S., Enoch, B., Haswell, C. A., Hellier, C., Horne, K., Irwin, J., Lister, T. A., McDonald, I., Maxted, P., Mayor, M., Norton, A. J., Parley, N., Perrier, C., Pont, F., Queloz, D., Ryans, R., Smith, A. M. S., Udry, S., Wheatley, P. J., & Wilson, D. M.: 2009, *Monthly Notices of the Royal Astronomical Society* **392**, 1532

Kaib, N. A., Raymond, S. N., & Duncan, M.: 2013, *Nature* **493**, 381

Kalas, P., Graham, J. R., Chiang, E., Fitzgerald, M. P., Clampin, M., Kite, E. S., Stapelfeldt, K., Marois, C., & Krist, J.: 2008, *Science* **322**, 1345

Kaltenegger, L. & Traub, W. A.: 2009, *The Astrophysical Journal* **698**, 519

Kataoka, A., Tanaka, H., Okuzumi, S., & Wada, K.: 2013a, *Astronomy & Astrophysics* **557**, L4

Kataoka, A., Tanaka, H., Okuzumi, S., & Wada, K.: 2013b, *Astronomy & Astrophysics* **554**, A4

Kita, R., Rasio, F., & Takeda, G.: 2010, *Astrobiology* **10**, 733

Knutson, H. A., Charbonneau, D., Allen, L. E., Burrows, A., & Megeath, S. T.: 2008, *The Astrophysical Journal* **673**, 526

Kokubo, E. & Ida, S.: 2002, *The Astrophysical Journal* **581**, 666

Konopacky, Q. M., Barman, T. S., Macintosh, B. A., & Marois, C.: 2013, *Science* **339**, 1398

Kozai, Y.: 1962, *The Astronomical Journal* **67**, 591

Kraus, A. L. & Hillenbrand, L. A.: 2007, *The Astronomical Journal* **134**, 2340

Kuzuhara, M., Tamura, M., Kudo, T., Janson, M., Kandori, R., Brandt, T. D., Thalmann, C., Spiegel, D., Biller, B., Carson, J., Hori, Y., Suzuki, R., Burrows, A., Henning, T., Turner, E. L., McElwain, M. W., Moro-Martín, A., Suenaga, T., Takahashi, Y. H., Kwon, J., Lucas, P., Abe, L., Brandner, W., Egner, S., Feldt, M., Fujiwara, H., Goto, M., Grady, C. A., Guyon, O., Hashimoto, J., Hayano, Y., Hayashi, M., Hayashi, S. S., Hodapp, K. W., Ishii, M., Iye, M., Knapp, G. R., Matsuo, T., Mayama, S., Miyama, S., Morino, J.-I., Nishikawa, J., Nishimura, T., Kotani, T., Kusakabe, N., Pyo, T.-S., Serabyn, E., Suto, H., Takami, M., Takato, N., Terada, H., Tomono, D., Watanabe, M., Wisniewski, J. P., Yamada, T., Takami, H., & Usuda, T.: 2013, *The Astrophysical Journal* **774**, 11

Lafrenière, D., Marois, C., Doyon, R., Nadeau, D., & Artigau, É.: 2007, *The Astrophysical Journal* **660**, 770

Lagrange, A.-M., Bonnefoy, M., Chauvin, G., Apai, D., Ehrenreich, D., Boccaletti, A., Gratadour, D., Rouan, D., Mouillet, D., Lacour, S., & Kasper, M.: 2010, *Science* **329**, 57

Lagrange, A.-M., De Bondt, K., Meunier, N., Sterzik, M., Beust, H., & Galland, F.: 2012, *Astronomy & Astrophysics* **542**, A18

Lai, D., Foucart, F., & Lin, D. N. C.: 2011, *Monthly Notices of the Royal Astronomical Society* **412**, 2790

Latham, D. W., Bakos, G. Á., Torres, G., Stefanik, R. P., Noyes, R. W., Kovács, G., Pál, A., Marcy, G. W., Fischer, D. A., Butler, R. P., Sipőcz, B., Sasselov, D. D., Esquerdo, G. A., Vogt, S. S., Hartman, J. D., Kovács, G., Lázár, J., Papp, I., & Sári, P.: 2009, *The Astrophysical Journal* **704**, 1107

Lecavelier Des Etangs, A. & Vidal-Madjar, A.: 2009, *Astronomy & Astrophysics* **497**, 557

Lee, J. W., Kim, S.-L., Kim, C.-H., Koch, R. H., Lee, C.-U., Kim, H.-I., & Park, J.-H.: 2009, *The Astronomical Journal* **137**, 3181

Lin, D. N. C. & Papaloizou, J.: 1985, in D. C. Black and M. S. Matthews (eds.), *Protostars and Planets II*, pp 981–1072

Lufkin, G., Quinn, T., Wadsley, J., Stadel, J., & Governato, F.: 2004, *Monthly Notices of the Royal Astronomical Society* **347**, 421

Lyot, B.: 1939, *Monthly Notices of the Royal Astronomical Society* **99**, 580

Maciejewski, G., Dimitrov, D., Seeliger, M., Raetz, S., Bukowiecki, Ł., Kitze, M., Errmann, R., Nowak, G., Niedzielski, A., Popov, V., Marka, C., Goździewski, K., Neuhäuser, R., Ohlert, J., Hinse, T. C., Lee, J. W., Lee, C.-U., Yoon, J.-N., Berndt, A., Gilbert, H., Ginski, C., Hohle, M. M., Mugrauer, M., Röll, T., Schmidt, T. O. B., Tetzlaff, N., Mancini, L., Southworth, J., Dall'Ora, M., Ciceri, S., Zambelli, R., Corfini, G., Takahashi, H., Tachihara, K., Benkő, J. M., Sárneczky, K., Szabo, G. M., Varga, T. N., Vaňko, M., Joshi, Y. C., & Chen, W. P.: 2013, *Astronomy & Astrophysics* **551**, A108

Mamajek, E. E. & Hillenbrand, L. A.: 2008, *The Astrophysical Journal* **687**, 1264

Mandushev, G., O'Donovan, F. T., Charbonneau, D., Torres, G., Latham, D. W., Bakos, G. Á., Dunham, E. W., Sozzetti, A., Fernández, J. M., Esquerdo, G. A., Everett, M. E., Brown, T. M., Rabus, M., Belmonte, J. A., & Hillenbrand, L. A.: 2007, *The Astrophysical Journal Letters* **667**, L195

Marcy, G. W. & Butler, R. P.: 1992, *Publications of the Astronomical Society of the Pacific* **104**, 270

Marcy, G. W. & Butler, R. P.: 1996, *The Astrophysical Journal Letters* **464**, L147

Marley, M. S., Fortney, J. J., Hubickyj, O., Bodenheimer, P., & Lissauer, J. J.: 2007, *The Astrophysical Journal* **655**, 541

Marmier, M., Ségransan, D., Udry, S., Mayor, M., Pepe, F., Queloz, D., Lovis, C., Naef, D., Santos, N. C., Alonso, R., Alves, S., Berthet, S., Chazelas, B., Demory, B.-O., Dumusque, X., Eggenberger, A., Figueira, P., Gillon, M., Hagelberg, J., Lendl, M., Mardling, R. A., Mégevand, D., Neveu, M., Sahlmann, J., Sosnowska, D., Tewes, M., & Triaud, A. H. M. J.: 2013, *Astronomy & Astrophysics* **551**, A90

Marois, C., Lafrenière, D., Doyon, R., Macintosh, B., & Nadeau, D.: 2006, *The Astrophysical Journal* **641**, 556

Marois, C., Macintosh, B., Barman, T., Zuckerman, B., Song, I., Patience, J., Lafrenière, D., & Doyon, R.: 2008, *Science* **322**, 1348

Marois, C., Zuckerman, B., Konopacky, Q. M., Macintosh, B., & Barman, T.: 2010, *Nature* **468**, 1080

Marzari, F. & Weidenschilling, S. J.: 2002, *Icarus* **156**, 570

Mason, B. D., Hartkopf, W. I., Raghavan, D., Subasavage, J. P., Roberts, Jr., L. C., Turner, N. H., & ten Brummelaar, T. A.: 2011, *The Astronomical Journal* **142**, 176

Mason, B. D., Wycoff, G. L., Hartkopf, W. I., Douglass, G. G., & Worley, C. E.: 2001, *The Astronomical Journal* **122**, 3466

Masuda, K., Hirano, T., Taruya, A., Nagasawa, M., & Suto, Y.: 2013, *The Astrophysical Journal* **778**, 185

Mayor, M., Marmier, M., Lovis, C., Udry, S., Ségransan, D., Pepe, F., Benz, W., Bertaux, J. ., Bouchy, F., Dumusque, X., Lo Curto, G., Mordasini, C., Queloz, D., & Santos, N. C.: 2011, *ArXiv e-prints*

Mayor, M., Pepe, F., Queloz, D., Bouchy, F., Rupprecht, G., Lo Curto, G., Avila, G., Benz, W., Bertaux, J.-L., Bonfils, X., Dall, T., Dekker, H., Delabre, B., Eckert, W., Fleury, M., Gilliotte, A., Gojak, D., Guzman, J. C., Kohler, D., Lizon, J.-L., Longinotti, A., Lovis, C., Megevand, D., Pasquini, L., Reyes, J., Sivan, J.-P., Sosnowska, D., Soto, R., Udry, S., van Kesteren, A., Weber, L., & Weilenmann, U.: 2003, *The Messenger* **114**, 20

Mayor, M. & Queloz, D.: 1995, *Nature* **378**, 355

McCullough, P. R., Burke, C. J., Valenti, J. A., Long, D., Johns-Krull, C. M., Machalek, P., Janes, K. A., Taylor, B., Gregorio, J., Foote, C. N., Gary, B. L., Fleenor, M., García-Melendo, E., & Vanmunster, T.: 2008, *ArXiv e-prints*

McCullough, P. R., Stys, J. E., Valenti, J. A., Fleming, S. W., Janes, K. A., & Heasley, J. N.: 2005, *Publications of the Astronomical Society of the Pacific* **117**, 783

McLaughlin, D. B.: 1924, *The Astrophysical Journal* **60**, 22

Meru, F. & Bate, M. R.: 2011, *Monthly Notices of the Royal Astronomical Society* **411**, L1

Minowa, Y., Hayano, Y., Oya, S., Watanabe, M., Hattori, M., Guyon, O., Egner, S., Saito, Y., Ito, M., Takami, H., Garrel, V., Colley, S., Golota, T., & Iye, M.: 2010, in *Society of Photo-Optical Instrumentation Engineers (SPIE) Conference Series*, Vol. 7736 of *Society of Photo-Optical Instrumentation Engineers (SPIE) Conference Series*

Miyama, S. M., Hayashi, C., & Narita, S.: 1984, *The Astrophysical Journal* **279**, 621

Mizuno, H., Nakazawa, K., & Hayashi, C.: 1978, *Progress of Theoretical Physics* **60**, 699

Morton, T. D. & Johnson, J. A.: 2011a, *The Astrophysical Journal* **729**, 138

Morton, T. D. & Johnson, J. A.: 2011b, *The Astrophysical Journal* **738**, 170

Moya, A., Bouy, H., Marchis, F., Vicente, B., & Barrado, D.: 2011, *Astronomy & Astrophysics* **535**, A110

Mugrauer, M. & Neuhäuser, R.: 2009, *Astronomy & Astrophysics* **494**, 373

Nagasawa, M. & Ida, S.: 2011, *The Astrophysical Journal* **742**, 72

Nagasawa, M., Ida, S., & Bessho, T.: 2008, *The Astrophysical Journal* **678**, 498

Narita, N., Hirano, T., Sanchis-Ojeda, R., Winn, J. N., Holman, M. J., Sato, B., Aoki, W., & Tamura, M.: 2010a, *Publications of the Astrophysical Society of Japan* **62**, L61

Narita, N., Hirano, T., Sato, B., Harakawa, H., Fukui, A., Aoki, W., & Tamura, M.: 2011, *Publications of the Astrophysical Society of Japan* **63**, L67

Narita, N., Kudo, T., Bergfors, C., Nagasawa, M., Thalmann, C., Sato, B., Suzuki, R., Kandori, R., Janson, M., Goto, M., Brandner, W., Ida, S., Abe, L., Carson, J., Egner, S. E., Feldt, M., Golota, T., Guyon, O., Hashimoto, J., Hayano, Y., Hayashi, M., Hayashi, S. S., Henning, T., Hodapp, K. W., Ishii, M., Knapp, G. R., Kusakabe, N., Kuzuhara, M., Matsuo, T., McElwain, M. W., Miyama, S. M., Morino, J.-I., Moro-Martin, A., Nishimura, T., Pyo, T.-S., Serabyn, E., Suenaga, T., Suto, H., Takahashi, Y. H., Takami, M., Takato, N., Terada, H., Tomono, D., Turner, E. L., Watanabe, M., Yamada, T., Takami, H., Usuda, T., & Tamura, M.: 2010b, *Publications of the Astrophysical Society of Japan* **62**, 779

Narita, N., Sato, B., Hirano, T., & Tamura, M.: 2009, *Publications of the Astrophysical Society of Japan* **61**, L35

Narita, N., Sato, B., Hirano, T., Winn, J. N., Aoki, W., & Tamura, M.: 2010c, *Publications of the Astrophysical Society of Japan* **62**, 653

Narita, N., Takahashi, Y. H., Kuzuhara, M., Hirano, T., Suenaga, T., Kandori, R., Kudo, T., Sato, B., Suzuki, R., Ida, S., Nagasawa, M., Abe, L., Brandner, W., Brandt, T. D., Carson, J., Egner, S. E., Feldt, M., Goto, M., Grady, C. A., Guyon, O., Hashimoto, J., Hayano, Y., Hayashi, M., Hayashi, S. S., Henning, T., Hodapp, K. W., Ishii, M., Iye, M., Janson, M., Knapp, G. R., Kusakabe, N., Kwon, J., Matsuo, T., Mayama, S., McElwain, M. W., Miyama, S. M., Morino, J.-I., Moro-Martin, A., Nishimura, T., Pyo, T.-S., Serabyn, E., Suto, H., Takami, M., Takato, N., Terada, H., Thalmann, C., Tomono, D., Turner, E. L., Watanabe, M., Wisniewski, J. P., Yamada, T., Takami, H., Usuda, T., & Tamura, M.: 2012, *Publications of the Astrophysical Society of Japan* **64**, L7

Nordström, B., Mayor, M., Andersen, J., Holmberg, J., Pont, F., Jørgensen, B. R., Olsen, E. H., Udry, S., & Mowlavi, N.: 2004, *Astronomy & Astrophysics* **418**, 989

Noyes, R. W., Bakos, G. Á., Torres, G., Pál, A., Kovács, G., Latham, D. W., Fernández, J. M., Fischer, D. A., Butler, R. P., Marcy, G. W., Sipőcz, B., Esquerdo, G. A., Kovács, G., Sasselov, D. D., Sato, B., Stefanik, R., Holman, M., Lázár, J., Papp, I., & Sári, P.: 2008, *The Astrophysical Journal Letters* **673**, L79

Ohta, Y., Taruya, A., & Suto, Y.: 2005, *The Astrophysical Journal* **622**, 1118

Ohta, Y., Taruya, A., & Suto, Y.: 2009, *The Astrophysical Journal* **690**, 1

Paardekooper, S.-J. & Papaloizou, J. C. B.: 2008, *Astronomy & Astrophysics* **485**, 877

Pál, A., Bakos, G. Á., Torres, G., Noyes, R. W., Latham, D. W., Kovács, G., Marcy, G. W., Fischer, D. A., Butler, R. P., Sasselov, D. D., Sipőcz, B., Esquerdo, G. A., Kovács, G., Stefanik, R., Lázár, J., Papp, I., & Sári, P.: 2008, *The Astrophysical Journal* **680**, 1450

Peek, K. M. G., Johnson, J. A., Fischer, D. A., Marcy, G. W., Henry, G. W., Howard, A. W., Wright, J. T., Lowe, T. B., Reffert, S., Schwab, C., Williams, P. K. G., Isaacson, H., & Giguere, M. J.: 2009, *Publications of the Astronomical Society of the Pacific* **121**, 613

Perryman, M. A. C., Lindegren, L., Kovalevsky, J., Hoeg, E., Bastian, U., Bernacca, P. L., Crézé, M., Donati, F., Grenon, M., Grewing, M., van Leeuwen, F., van der Marel, H., Mignard, F., Murray, C. A., Le Poole, R. S., Schrijver, H., Turon, C., Arenou, F., Froeschlé, M., & Petersen, C. S.: 1997, *Astronomy & Astrophysics* **323**, L49

Pollack, J. B., Hubickyj, O., Bodenheimer, P., Lissauer, J. J., Podolak, M., & Greenzweig, Y.: 1996, *Icarus* **124**, 62

Pont, F., Hébrard, G., Irwin, J. M., Bouchy, F., Moutou, C., Ehrenreich, D., Guillot, T., Aigrain, S., Bonfils, X., Berta, Z., Boisse, I., Burke, C., Charbonneau, D., Delfosse, X., Desort, M., Eggenberger, A., Forveille, T., Lagrange, A.-M., Lovis, C., Nutzman, P., Pepe, F., Perrier, C., Queloz, D., Santos, N. C., Ségransan, D., Udry, S., & Vidal-Madjar, A.: 2009, *Astronomy & Astrophysics* **502**, 695

Queloz, D., Anderson, D. R., Collier Cameron, A., Gillon, M., Hebb, L., Hellier, C., Maxted, P., Pepe, F., Pollacco, D., Ségransan, D., Smalley, B., Triaud, A. H. M. J., Udry, S., & West, R.: 2010, *Astronomy & Astrophysics* **517**, L1

Raghavan, D., Henry, T. J., Mason, B. D., Subasavage, J. P., Jao, W.-C., Beaulieu, T. D., & Hambly, N. C.: 2006, *The Astrophysical Journal* **646**, 523

Raghavan, D., McAlister, H. A., Henry, T. J., Latham, D. W., Marcy, G. W., Mason, B. D., Gies, D. R., White, R. J., & ten Brummelaar, T. A.: 2010, *The Astrophysical Journal Supplement* **190**, 1

Rasio, F. A. & Ford, E. B.: 1996, *Science* **274**, 954

Raymond, S. N., Barnes, R., Armitage, P. J., & Gorelick, N.: 2008, *The Astrophysical Journal Letters* **687**, L107

Rein, H.: 2012, *Monthly Notices of the Royal Astronomical Society* **427**, L21

Rocha-Pinto, H. J. & Maciel, W. J.: 1998, *Monthly Notices of the Royal Astronomical Society* **298**, 332

Roell, T., Neuhäuser, R., Seifahrt, A., & Mugrauer, M.: 2012, *Astronomy & Astrophysics* **542**, A92

Rogers, T. M., Lin, D. N. C., & Lau, H. H. B.: 2012, *The Astrophysical Journal Letters* **758**, L6

Rossiter, R. A.: 1924, *The Astrophysical Journal* **60**, 15

Saffe, C., Gómez, M., & Chavero, C.: 2005, *Astronomy & Astrophysics* **443**, 609

Safronov, V. S.: 1969, *Evoliutsiia doplanetnogo oblaka.*

Sanchis-Ojeda, R., Fabrycky, D. C., Winn, J. N., Barclay, T., Clarke, B. D., Ford, E. B., Fortney, J. J., Geary, J. C., Holman, M. J., Howard, A. W., Jenkins, J. M., Koch, D., Lissauer, J. J., Marcy, G. W., Mullally, F., Ragozzine, D., Seader, S. E., Still, M., & Thompson, S. E.: 2012, *Nature* **487**, 449

Sanchis-Ojeda, R. & Winn, J. N.: 2011, *The Astrophysical Journal* **743**, 61

Santerne, A., Díaz, R. F., Moutou, C., Bouchy, F., Hébrard, G., Almenara, J.-M., Bonomo, A. S., Deleuil, M., & Santos, N. C.: 2012, *Astronomy & Astrophysics* **545**, A76

Santerne, A., Fressin, F., Díaz, R. F., Figueira, P., Almenara, J.-M., & Santos, N. C.: 2013, *Astronomy & Astrophysics* **557**, A139

Sari, R. & Goldreich, P.: 2004, *The Astrophysical Journal Letters* **606**, L77

Sato, B., Kambe, E., Takeda, Y., Izumiura, H., & Ando, H.: 2002, *Publications of the Astrophysical Society of Japan* **54**, 873

Schlaufman, K. C.: 2010, *The Astrophysical Journal* **719**, 602

Schneider, J., Dedieu, C., Le Sidaner, P., Savalle, R., & Zolotukhin, I.: 2011, *Astronomy & Astrophysics* **532**, A79

Skrutskie, M. F., Cutri, R. M., Stiening, R., Weinberg, M. D., Schneider, S., Carpenter, J. M., Beichman, C., Capps, R., Chester, T., Elias, J., Huchra, J., Liebert, J., Lonsdale, C., Monet, D. G., Price, S., Seitzer, P., Jarrett, T., Kirkpatrick, J. D., Gizis, J. E., Howard, E., Evans, T., Fowler, J., Fullmer, L., Hurt, R., Light, R., Kopan, E. L., Marsh, K. A., McCallon, H. L., Tam, R., Van Dyk, S., & Wheelock, S.: 2006, *The Astronomical Journal* **131**, 1163

Smith, A. M. S., Anderson, D. R., Skillen, I., Collier Cameron, A., & Smalley, B.: 2011, *Monthly Notices of the Royal Astronomical Society* **416**, 2096

Soummer, R., Brendan Hagan, J., Pueyo, L., Thormann, A., Rajan, A., & Marois, C.: 2011, *The Astrophysical Journal* **741**, 55

Southworth, J., Mancini, L., Browne, P., Burgdorf, M., Calchi Novati, S., Dominik, M., Gerner, T., Hinse, T. C., Jørgensen, U. G., Kains, N., Ricci, D., Schäfer, S., Schönebeck, F., Tregloan-Reed, J., Alsubai, K. A., Bozza, V., Chen, G., Dodds, P., Dreizler, S., Fang, X.-S., Finet, F., Gu, S.-H., Hardis, S., Harpsøe, K., Henning, T., Hundertmark, M., Jessen-Hansen, J., Kerins, E., Kjeldsen, H., Liebig, C., Lund, M. N., Lundkvist, M., Mathiasen, M., Nikolov, N., Penny, M. T., Proft, S., Rahvar, S., Sahu, K., Scarpetta, G., Skottfelt, J., Snodgrass, C., Surdej, J., & Wertz, O.: 2013, *Monthly Notices of the Royal Astronomical Society* **434**, 1300

Sozzetti, A., Torres, G., Charbonneau, D., Winn, J. N., Korzennik, S. G., Holman, M. J., Latham, D. W., Laird, J. B., Fernandez, J., O'Donovan, F. T., Mandushev, G., Dunham, E., Everett, M. E., Esquerdo, G. A., Rabus, M., Belmonte, J. A., Deeg, H. J., Brown, T. N., Hidas, M. G., & Baliber, N.: 2009, *The Astrophysical Journal* **691**, 1145

Spiegel, D. S., Burrows, A., & Milsom, J. A.: 2011, *The Astrophysical Journal* **727**, 57

Stevenson, K. B., Bean, J. L., Seifahrt, A., Desert, J.-M., Madhusudhan, N., Bergmann, M., Kreidberg, L., & Homeier, D.: 2013, *ArXiv e-prints*

Suzuki, R., Kudo, T., Hashimoto, J., Carson, J., Egner, S., Goto, M., Hattori, M., Hayano, Y., Hodapp, K., Ito, M., Iye, M., Jacobson, S., Kandori, R., Kusakabe, N., Kuzuhara, M., Matsuo, T., McElwain, M., Morino, J.-I., Oya, S., Saito, Y., Shelton, R., Stahlberger, V., Suto, H., Takami, H., Thalmann, C., Watanabe, M., Yamada, H., & Tamura, M.: 2010, in *Society of Photo-Optical Instrumentation Engineers (SPIE) Conference Series*, Vol. 7735 of *Society of Photo-Optical Instrumentation Engineers (SPIE) Conference Series*

Takeda, G., Ford, E. B., Sills, A., Rasio, F. A., Fischer, D. A., & Valenti, J. A.: 2007, *The Astrophysical Journal Supplement* **168**, 297

Takeda, G., Kita, R., & Rasio, F. A.: 2008, *The Astrophysical Journal* **683**, 1063

Takeda, G. & Rasio, F. A.: 2005, *The Astrophysical Journal* **627**, 1001

Tamura, M.: 2009, in T. Usuda, M. Tamura, and M. Ishii (eds.), *American Institute of Physics Conference Series*, Vol. 1158 of *American Institute of Physics Conference Series*, pp 11–16

Tamura, M., Fukagawa, M., Kimura, H., Yamamoto, T., Suto, H., & Abe, L.: 2006, *The Astrophysical Journal* **641**, 1172

Tamura, M., Suto, H., Nishikawa, J., Kotani, T., Sato, B., Aoki, W., Usuda, T., Kurokawa, T., Kashiwagi, K., Nishiyama, S., Ikeda, Y., Hall, D., Hodapp, K., Hashimoto, J., Morino, J., Inoue, S., Mizuno, Y., Washizaki, Y., Tanaka, Y., Suzuki, S., Kwon, J., Suenaga, T., Oh, D., Narita, N., Kokubo, E., Hayano, Y., Izumiura, H., Kambe, E., Kudo, T., Kusakabe, N., Ikoma, M., Hori, Y., Omiya, M., Genda, H., Fukui, A., Fujii, Y., Guyon, O., Harakawa, H., Hayashi, M., Hidai, M., Hirano, T., Kuzuhara, M., Machida, M., Matsuo, T., Nagata, T., Ohnuki, H., Ogihara, M., Oshino, S., Suzuki, R., Takami, H., Takato, N., Takahashi, Y., Tachinami, C., & Terada, H.: 2012, in *Society of Photo-Optical Instrumentation Engineers (SPIE) Conference Series*, Vol. 8446 of *Society of Photo-Optical Instrumentation Engineers (SPIE) Conference Series*

Thalmann, C., Carson, J., Janson, M., Goto, M., McElwain, M., Egner, S., Feldt, M., Hashimoto, J., Hayano, Y., Henning, T., Hodapp, K. W., Kandori, R., Klahr, H., Kudo, T., Kusakabe, N., Mordasini, C., Morino, J.-I., Suto, H., Suzuki, R., & Tamura, M.: 2009, *The Astrophysical Journal Letters* **707**, L123

Tinetti, G., Vidal-Madjar, A., Liang, M.-C., Beaulieu, J.-P., Yung, Y., Carey, S., Barber, R. J., Tennyson, J., Ribas, I., Allard, N., Ballester, G. E., Sing, D. K., & Selsis, F.: 2007, *Nature* **448**, 169

Todorov, K. O., Deming, D., Knutson, H. A., Burrows, A., Sada, P. V., Cowan, N. B., Agol, E., Desert, J.-M., Fortney, J. J., Charbonneau, D., Laughlin, G., Langton, J., Showman, A. P., & Lewis, N. K.: 2012, *The Astrophysical Journal* **746**, 111

Toomre, A.: 1964, *The Astrophysical Journal* **139**, 1217

Torres, G., Bakos, G. Á., Hartman, J., Kovács, G., Noyes, R. W., Latham, D. W., Fischer, D. A., Johnson, J. A., Marcy, G. W., Howard, A. W., Sasselov, D. D., Kipping, D., Sipőcz, B., Stefanik, R. P., Esquerdo, G. A., Everett, M. E., Lázár, J., Papp, I., & Sári, P.: 2010, *The Astrophysical Journal* **715**, 458

Torres, G., Konacki, M., Sasselov, D. D., & Jha, S.: 2004, *The Astrophysical Journal* **614**, 979

Triaud, A. H. M. J.: 2011, *Astronomy & Astrophysics* **534**, L6

Triaud, A. H. M. J., Collier Cameron, A., Queloz, D., Anderson, D. R., Gillon, M., Hebb, L., Hellier, C., Loeillet, B., Maxted, P. F. L., Mayor, M., Pepe, F., Pollacco, D., Ségransan, D., Smalley, B., Udry, S., West, R. G., & Wheatley, P. J.: 2010, *Astronomy & Astrophysics* **524**, A25

Tuomi, M. & Jenkins, J. S.: 2012, *ArXiv e-prints*

Valenti, J. A. & Fischer, D. A.: 2005, *The Astrophysical Journal Supplement* **159**, 141

Valenti, J. A. & Piskunov, N.: 1996, *Astronomy & Astrophysics Supplement* **118**, 595

van de Kamp, P.: 1963, *The Astronomical Journal* **68**, 515

van Leeuwen, F.: 2007, *Astronomy & Astrophysics* **474**, 653

Vogt, S. S., Marcy, G. W., Butler, R. P., & Apps, K.: 2000, *The Astrophysical Journal* **536**, 902

Ward, W. R.: 1986, *Icarus* **67**, 164

Weidenschilling, S. J.: 1977, *Monthly Notices of the Royal Astronomical Society* **180**, 57

Weiss, L. M., Marcy, G. W., Rowe, J. F., Howard, A. W., Isaacson, H., Fortney, J. J., Miller, N., Demory, B.-O., Fischer, D. A., Adams, E. R., Dupree, A. K., Howell, S. B., Kolbl, R., Johnson, J. A., Horch, E. P., Everett, M. E., Fabrycky, D. C., & Seager, S.: 2013, *The Astrophysical Journal* **768**, 14

West, R. G., Anderson, D. R., Gillon, M., Hebb, L., Hellier, C., Maxted, P. F. L., Queloz, D., Smalley, B., Triaud, A. H. M. J., Wilson, D. M., Bentley, S. J., Collier Cameron, A., Enoch, B., Horne, K., Irwin, J., Lister, T. A., Mayor, M., Parley, N., Pepe, F., Pollacco, D., Segransan, D., Spano, M., Udry, S., & Wheatley, P. J.: 2009, *The Astronomical Journal* **137**, 4834

Winn, J. N.: 2010, *ArXiv e-prints*

Winn, J. N., Fabrycky, D., Albrecht, S., & Johnson, J. A.: 2010a, *The Astrophysical Journal Letters* **718**, L145

Winn, J. N., Howard, A. W., Johnson, J. A., Marcy, G. W., Isaacson, H., Shporer, A., Bakos, G. Á., Hartman, J. D., Holman, M. J., Albrecht, S., Crepp, J. R., & Morton, T. D.: 2011, *The Astronomical Journal* **141**, 63

Winn, J. N., Johnson, J. A., Albrecht, S., Howard, A. W., Marcy, G. W., Crossfield, I. J., & Holman, M. J.: 2009, *The Astrophysical Journal Letters* **703**, L99

Winn, J. N., Johnson, J. A., Howard, A. W., Marcy, G. W., Isaacson, H., Shporer, A., Bakos, G. Á., Hartman, J. D., & Albrecht, S.: 2010b, *The Astrophysical Journal Letters* **723**, L223

Wolszczan, A.: 1994, *Science* **264**, 538

Wolszczan, A. & Frail, D. A.: 1992, *Nature* **355**, 145

Wood, P. L., Maxted, P. F. L., Smalley, B., & Iro, N.: 2011, *Monthly Notices of the Royal Astronomical Society* **412**, 2376

Wu, Y. & Murray, N.: 2003, *The Astrophysical Journal* **589**, 605

Wu, Y., Murray, N. W., & Ramsahai, J. M.: 2007, *The Astrophysical Journal* **670**, 820

Wuchterl, G., Guillot, T., & Lissauer, J. J.: 2000, *Protostars and Planets IV* p. 1081

Yan, Z., Shen, Z.-Q., Yuan, J.-P., Wang, N., Rottmann, H., & Alef, W.: 2013, *Monthly Notices of the Royal Astronomical Society* **433**, 162

Yi, S., Demarque, P., Kim, Y.-C., Lee, Y.-W., Ree, C. H., Lejeune, T., & Barnes, S.: 2001, *The Astrophysical Journal Supplement* **136**, 417

Zacharias, N., Monet, D. G., Levine, S. E., Urban, S. E., Gaume, R., & Wycoff, G. L.: 2004, in *American Astronomical Society Meeting Abstracts*, Vol. 36 of *Bulletin of the American Astronomical Society*, p. 1418

Zacharias, N., Urban, S. E., Zacharias, M. I., Wycoff, G. L., Hall, D. M., Germain, M. E., Holdenried, E. R., & Winter, L.: 2003, *VizieR Online Data Catalog* **1289**, 0